INFORMATION TO USERS

This manuscript has been reproduced from the microfilm master. UMI films the text directly from the original or copy submitted. Thus, some thesis and dissertation copies are in typewriter face, while others may be from any type of computer printer.

The quality of this reproduction is dependent upon the quality of the copy submitted. Broken or indistinct print, colored or poor quality illustrations and photographs, print bleedthrough, substandard margins, and improper alignment can adversely affect reproduction.

In the unlikely event that the author did not send UMI a complete manuscript and there are missing pages, these will be noted. Also, if unauthorized copyright material had to be removed, a note will indicate the deletion.

Oversize materials (e.g., maps, drawings, charts) are reproduced by sectioning the original, beginning at the upper left-hand corner and continuing from left to right in equal sections with small overlaps.

UMI®

University of Alberta

Measuring Desorption Kinetics from Chromatographic Packings via the Continuous-Monitoring Shallow-Bed Technique.

by

Robert Bujalski Ⓒ

A thesis submitted to the Faculty of Graduate Studies and Research in partial fulfillment of the

requirements for the degree of *Doctor of Philosophy*

Department of *Chemistry*

Edmonton, Alberta
Spring 2005

Canada

Dla moich rodziców

Abstract

The shallow-bed technique is used to measure sorption/desorption kinetics from particulate media. It involves an extremely short column (about 0.5 mm long and 2-3 mm in diameter) through which solutions are passed at high linear velocities (up to 60 cm/sec in this work), and the amount of solute sorbed/desorbed is measured as a function of time. This work presents the development and validation of an instrument which measures *desorption* kinetics from liquid-chromatographic packings. The experiments involve pre-equilibration of the particles with a solute-containing solvent, after which the flow is switched to that of pure solvent (a methanol/water mixture), and the concentration of the desorbing solute is monitored by a detector located as close as 1.5 mm downstream.

Two instruments are developed: The first is used to measure the desorption rate of naphthalene from a gel-like nonporous polymeric sorbent PRP-∞, which takes about 90 minutes to complete. The rate data are fitted with a spherical diffusion equation and the diffusivity obtained from the fit (5×10^{-11} cm^2/s) is compared with a literature value to validate the experimental approach. The second instrument can measure sub-second processes and is used to study the desorption kinetics of naphthalene and 1,2-dimethyl-4-nitrobenzene from the porous HPLC sorbents PRP-1 (10 μm diameter) and Luna C-18 (12 μm diameter), respectively. The desorption rate curves are fitted with a model accounting for particle diffusion combined with external film diffusion. The results are interpreted in terms of diffusion film thickness (0.3-0.5 μm), intraparticle mesopore diffusivities (on the order of 10^{-7} cm^2/s) and, for PRP-1, matrix diffusion ($\sim 10^{-15}$ cm^2/s).

The contribution of the measured intraparticle diffusion to bandbroadening in a 25-cm long chromatographic column of Luna C-18 is also studied.

For both shallow-bed instruments, experimental artifacts associated with extra-particle solute and instrument bandbroadening are overcome by subtraction and deconvolution with the desorption curve of an unretained-compound (phloroglucinol), which serves as an Impulse-Response-Function Marker.

Acknowledgements

I would like to thank Dr. Frederick Cantwell for his guidance, patience and support throughout the course of my studies. I also want to thank Eric Carpenter from the Department of Physics for writing the Labview programs which control my instruments, and for making the time to help me with numerous computer troubles which I encountered. I also want to acknowledge Dieter Starke and other staff members of the Chemistry Machine Shop for making the parts which I needed to conduct my studies. I am grateful to Dr. Monica Palcic for donating her stopped-flow apparatus, which has significantly simplified the designing of our instrument. I also thank Aaron Skelhorne, a fellow student, for taking confocal microscope images and for giving me a crucial piece of advice ("PDMS, I would recommend PDMS")

Finally, I would like to thank NSERC, University of Alberta, and, once again, my supervisor for financial support.

Table of contents

List of Tables

List of Figures

List of abbreviations and symbols

List of abbreviations

A.U	Absorbance Units (unitless)
DMNB	1,2-dimethyl-4-nitrobenzene
HMRAS DOSY	High Resolution Magic Angle Spinning - Diffusion Ordered Spectroscopy
HPLC	High Performance Liquid Chromatography
IRF	Impulse Response Function (a peak-shaped waveform)
IRF-Marker curve	used in subtraction and in obtaining IRF (not necessarily a peak)
MP	Mobile Phase (flowing solvent)
NMR	Nuclear Magnetic Resonance
NA	Naphthalene
ODS	Octadecylsilyl
PDMS	Polydimethylsiloxane elastomer
PFG-NMR	Pulsed-Field Gradient Nuclear Magnetic Resonance
PG	Phloroglucinol (1,3,5 trihydroxybenzene)
PRP-1	Mesoporous PS-DVB Stationary Phase, 10 micron diameter
PRP-∞	Nominally non-porous PS-DVB, 20 micron diameter
PS-DVB	Poly (styrene divinylbenzene) cross-linked copolymer
RP HPLC	Reverse Phase HPLC
S/N	Signal-to-Noise ratio
s.s.	Stainless Steel

List of Symbols

Latin alphabet symbols and symbols starting with Latin letters

$a_{DMNB,sorbed}$	area under the DMNB curve, defined in Section 5.3.3, Eq. 5.4
$a_{pore-PG}$	area under the PG curve, defined in Section 5.3.3, Eq. 5.4
A	Eddy Diffusion term in Van Deemter Equation
$A(t)$	absorbance as a function of time
$A(t)_{IRF}$	the instantaneous signal of the IRF-Marker
$A(t)_{observed\ IRF\ marker}$	the instantaneous signal of IRF-Marker being flushed out
$A_{i,0}$	the optical absorbance of the equilibration solution of i
$A_{0,\ IRF\ marker}$	the optical absorbance of the equilibration solution of IRF-Marker
B	the longitudinal diffusion term in Van Deemter Equation
C	the resistance-to mass transfer term in Van Deemter Equation
d	diameter of a cylindrical tube (unpacked)
d_p	particle diameter (cm)
D_i	diffusion coefficient inside the particle ($cm^2\ sec^{-1}$)
D_{matrix}	diffusion coefficient within a polymer matrix
D_{MP}	diffusion coefficient in the mobile phase ($cm^2\ sec^{-1}$)
D_P	diffusion coefficient inside the pores when there is no retention
f	ratio of porosities (Eq. 1.13)
$f(t)$	any function of time (any units)
$F'(v)$	the Fourier Transform of f(t); function of frequency (sec^{-1})

H	theoretical plate height
H_{couple}	the coupled H term due to resistance to lateral mass transfer
H_{Eddy}	H due to eddy diffusion
H_{film}	H due to film diffusion
$H_{intraparticle}$	H due to all the processes involved in sorption/desorption
H_{LD}	H due to longitudinal diffusion
H_{MP}	H due to diffusion mass transfer in the mobile phase
H_{obs}	H measured experimentally
H_S	H due to the actual chemical sorption/desorption step
H_{SM}	H due to diffusion inside the stagnant mobile phase plus surface diffusion
$H_{S,diff}$.	H due to diffusion in stationary phases with no stagnant mobile phase.
H_{Total}	the total combined plate height due to all the bandbroadening processes in the chromatographic column
Hindr	hindrance parameter: quantifies the retardation of diffusion in pores
i	symbol pertaining to solute i, also referred to as sample i.
$[i]_{MP}$	concentration of solute i in the mobile phase (moles/ L)
$[i]_{part}$	concentration of solute i in particle (moles/ $L_{Particle}$)
$[i_{pore}]_{part}$	conc. of un-sorbed solute i in the pores of a porous particle (moles/ $L_{Particle}$)
$[i_{sorbed}]_{part}$	concentration of sorbed i in the particle (moles/ $L_{Particle}$)

k'	capacity factor (also called retention factor), unit-less
k''	modified k' (Eqs. 1.19, 1.20)
k	rate constant for film diffusion controlled kinetics (sec^{-1}), Eq 2.6b
k_{ad}	first-order kinetic rate constant for adsorption onto surface (sec^{-1})
k_d	first-order kinetic rate constant for desorption from surface (sec^{-1})
k_f	the mass transfer coefficient in film (cm sec^{-1}) Eq.2.7
L	Parameter defined in Eq. 2.34-2.37. Also, a symbol used for 1 liter (1 liter = 1000 cm^3)
l	pathlength in absorbance measurement (cm)
m_{SB}	mass of the Shallow Bed particles (grams)
$n_{i,0}$	total moles of solute i at sorption equilibrium
$n_{i,0,fast}$	moles of solute at sorption equilibrium associated with the fast part of the desorption curve, See Section 4.3.2
$n_{i,0,film}$	total moles of solute i at sorption equilibrium associated with the PDMS film, Eq. 5.6
$n_{i,0,slow}$	moles of solute i at sorption equilibrium associated with the slow part of the desorption curve See Section 4.3.2
$n_{i,0,sph}$	total moles of solute i at sorption equilibrium with the spherical particle, Eq. 5.6
$n_i(t)$	moles of solute i adsorbed or desorbed by time t
r	particle radius or the radius of a hollow cylindrical tube, depending on the context (cm)
$r_{microsphere}$	the radius for the 'microspherical aggregate' within the particle

R	the ratio or the solute sorbed on the walls to that in the pores (unitless)
Re	Reynolds number for flow past spheres, Eq 2.8
R_c	Reynolds number for flow inside a tube, Eq 6.1
s	seconds
Sc	Schmidt number, Eq 2.10
sec	seconds
Sh	Sherwood number, Eq 2.11
t	time (sec)
t_{cg}	the center of gravity of a peak in time units, measured from the time that flow has started (Eq. 6.6)
t_d	the average time needed to pass through the detector cell
$t^`$	$t + t_c$
t_c	the center of gravity of function f(t)
t_{PG}	elution time of PG (phloroglucinol)
$t_{R,i}$	retention time of solute i (sec)
t_M	retention time of an unretained compound
u	velocity with which an unretained compound moves through the chromatographic column (cm sec^{-1})
u_{inter}	interstitial fluid velocity (cm sec^{-1})
u_s	superficial fluid velocity (cm sec^{-1})
U	average velocity of flow through a hollow tube
V	volume (L)

V_d	volume of the detection cell
V_{bath}	volume of the extra-particle liquid in an uptake/relese experiment
V_{HU}	hold-up volume
V_{SP}	volume of the particles in an uptake/release experiment
V_T	total volume in an uptake/release experiment: $V_{bath} + V_{SP}$
X	the Hellferich number, used to determine if particle diffusion or film diffusion are rate limiting
Z	the length of HPLC column.

Greek letter symbols and symbols starting with Greek letters

β	kinetic parameter of particle diffusion (sec^{-1})
β_{film}	kinetic parameter associated with diffusion in a plane sheet or film, Eq. 5.5 and 5.6
γ	obstruction factor for diffusion in the mobile phase in the column.
δ	thickness of the external diffusion film (cm)
δ_{expt}	δ determined by fitting experimental rate curves
$\delta_{predicted}$	δ predicted by correlations found in the literature
ε_i	the extinction coefficient (absorptivity) of solute i (L mol^{-1} cm^{-1})
ε_{inter}	interstitial porosity in a packed bed, expressed as volume fraction
ε_{intra}	intraparticle pore volume fraction in a packed bed
ε_{PP}	particle porosity: the volume fraction of the particle taken up by the pores.

ε_T	total porosity in a packed bed, expressed as volume fraction
η	viscosity (Poise: $g\ cm^{-1}\ s^{-1}$)
κ_i	the distribution coefficient of solute i between the stationary and mobile phase; ($L\ gram^{-1}$)
λ	packing factor (Eq. 1.5)
μm	micrometer (meter $\cdot 10^{-6}$)
ν	kinematic viscosity Eq 2.9
π	the number Pi
ρ	density (gram cm^{-3})
σ	standard deviation of a waveform (*e.g.* of a Gaussian elution peak)
σ^2	variance, or the second statistical moment, of a waveform
τ	tortuosity factor (unitless)
υ	frequency (Hz)
φ	volumetric phase ratio in an uptake/release experiment; Eq 2.21
ω	packing factor (Eq. 1.6)

Chapter 1:   Topic Introduction and Literature Review

1.1   High performance liquid chromatography

Reverse Phase High Performance Liquid Chromatography (RP HPLC) is a valuable and ubiquitous analytical tool, and it accounts for more than 90% of all liquid chromatographic analytical separations of small molecules [1]. RP HPLC is generally performed with porous silica particles, 10 µm in diameter or less, the surface of which is modified by covalently bonding different alkyl groups, the most common of which is octadecyl silane (ODS). RP HPLC is sometimes performed with porous polymeric particles, such as those made from poly (styrene-divinylbenzene), which also provide a hydrophobic surface. The two types of reverse-phases are shown in Fig.1.1.

The separation process occurs in a column packed with the porous particles. The sample molecules distribute themselves between the stationary phase and the mobile phase (solvent). In the case of ODS silica, the stationary phase (SP) is the thin layer (1-2 nm) of the bonded silane, while for polymeric packings the stationary phase is the surface of PS-DVB, and, in some cases, the bulk of the PS-DVB matrix. The mobile phase is composed of the liquid flowing in between the particles, and the stagnant liquid inside the small pores. The process of entering the stationary phase is called sorption and the process of leaving the stationary phase is desorption. Compounds interacting more

1

strongly with the stationary phase (stronger sorption) spend a smaller fraction of their time in the mobile phase. This leads to different velocities for different compounds, and the separation between the zone-centers of individual compounds increases linearly with column length.

Unfortunately, associated with the separation of zone centers is the tendency of each zone to broaden due to several dynamic phenomena. The band broadening (also called dispersion or spreading) due to these phenomena increases with only the square root of the column length, as compared to the linear rate associated with the separation of zone centers. This makes separation feasible. However, it is always desirable to improve separation, and this involves minimizing the band broadening phenomena.

2

Column wall

Packing particles

Flowing MP

polymeric

SP (matrix)

ODS silica

Silica support

SP

SM

Sorption/
Desorption
Onto/into
ODS

Adsorption/
Desorption
Onto matrix
walls

Sorption/
Desorption
into matrix
(not always)
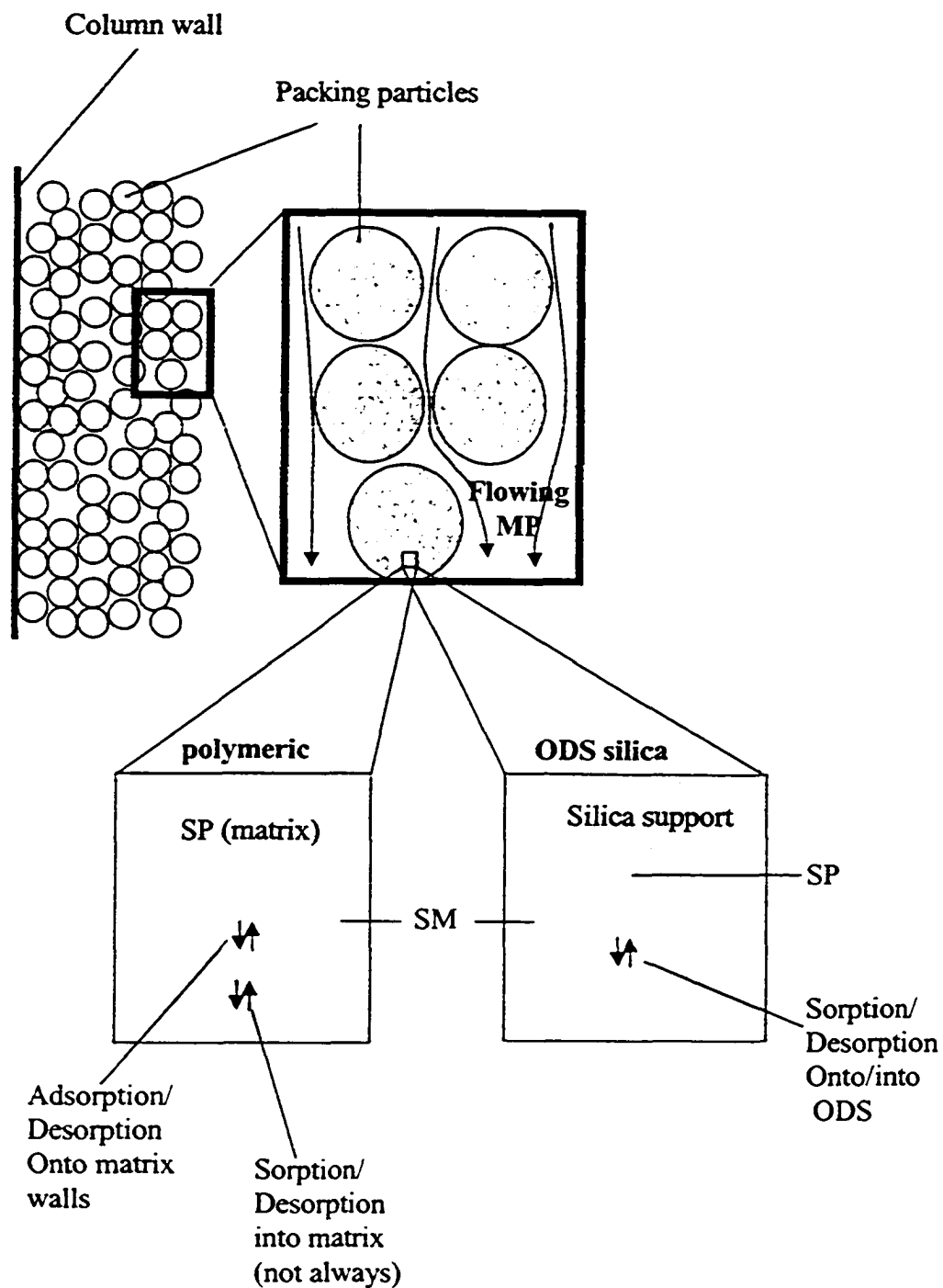
Fig 1.1   Column packed with porous packing particles and the possible sorption
processes which can occur in the two types of Stationary Phases (SP): ODS-
silica (and other bonded phase silicas) and polymeric.

3

1.2   Band broadening sources in HPLC

1.2.1 Quantifying band broadening.

The phenomenon of band broadening in a packed column has been treated extensively in literature [1-11]. The theoretical plate height model is the standard way to describe broadening in chromatography. Elution peak width can be described by the variance of the peak, σ^2, which is a square of its standard deviation. The plate height, H, is the variance of the peak per unit length of column, Z:

$$H = \frac{\sigma^2}{Z}$$
(1.1)

In a chromatographic column there are several, independent spreading processes, such as longitudinal (axial) diffusion, flow non-uniformity in the mobile phase, and non-equilibrium due to finite rate of sorption/desorption kinetics. For independent spreading processes, the variances generated by each one are additive in the time domain. They are also additive in the distance domain if the linear velocity is constant throughout the system, as is true in liquid chromatography [3]

$$\sigma^2_{Total} = \sum_{j=1} \sigma^2_j$$
(1.2)

and

$$H_{Total} = \sum_{j=1} H_j$$
(1.3)

4

1.2.2 Longitudinal diffusion in the mobile phase

When an infinitely narrow zone (band) of sample is injected onto the top of a column and migrates down the column, molecules diffuse axially away from the narrow band both forward and backward from the center of the band due to random thermal motion. After a short time, the resulting profile of the sample is Gaussian and the variance of the band increases proportionally to time. Therefore, the higher the flowrate through the column, the less time there is for molecular diffusion to act as a broadening phenomenon. The resulting plate height equation, based on a modified Einstein equation is [1, 3, 5, 6, 10]:

$$H_{LD} = \frac{2\gamma D_{MP}}{u} \tag{1.4}$$

where D_{MP} is the diffusion coefficient of the solute in the mobile phase (cm^2/sec) and u is the linear velocity of the mobile phase (*i.e.* the velocity with which an unretained component moves axially through the column). The obstruction factor, γ, is about 0.5 to 0.8 in packed columns and accounts for the fact that the diffusion pathway between the particles is not straight [1, 3, 5, 6, 10] . The magnitude of the H_{LD} is inversely proportional to the velocity of the mobile phase, which is consistent with the fact that the less time that is available for axial diffusion, the smaller the contribution of this phenomenon to band broadening. For the range of linear velocities normally used in HPLC longitudinal diffusion is negligible, as compared to other sources of band broadening, which will be discussed below. Under some circumstances, longitudinal diffusion can occur while the solute (sample) is sorbed in the stationary phase, and will thus add to the overall plate height [10, 12]. The extent of such diffusion is usually smaller than in the mobile phase, because of the smaller diffusion coefficient inside the

5

stationary phase. Therefore, the axial diffusion inside the stationary phase can also be neglected.

In newer HPLC columns, such as those packed with particles of 3 μm or less, the longitudinal diffusion contribution to plate height often cannot be ignored [13, 14]. This is because the other contributions to band broadening decrease with particle size, while H_{LD} is independent of the particle size [13, 14]. Such cases will not be discussed further here, however.

1.2.3 Eddy "Diffusion"

The eddy diffusion term arises from the non-uniformity of the packing of particles across the column, and the resulting differences in the interparticle channel diameters. Non-uniformity is aggravated by differences in particle sizes, but even if the particles were of uniform size, the randomness of packing structure would cause the inter-particle channels to differ in diameter. The velocity of the mobile phase is proportional to the square of the channel diameter, thus giving rise to different relative velocities in different channels [3], which is the cause of band broadening. According to Giddings, there are five types of flow non-uniformities in the bed. (1). Trans-channel, where there is a flow velocity distribution across a single channel in which the velocity distribution approaches a parabolic profile, due to viscous flow. (2). Trans-particle, where there are different average velocities in the channels on different sides of the particle. (3). Short range inter-channel, where there are different velocities across a small number of particles. (4). Long

6

range inter-channel, where there are velocity differences between larger regions of the packed bed. (5). Finally, there is the trans-column non-uniformity, due to the fact that the packing structure near the walls of the column is different (usually looser) than the packing structure in the center. This results in different average velocities near the walls as compared to the center of column. All these non-uniformities are relaxed by the fact that every time the mobile phase exits a flow channel, it is split between a number of other flow streams, where the velocities are unrelated to those experienced in the former channel. This is called lateral convective mass transfer (as opposed to lateral diffusive mass transfer), also referred to as eddy diffusion. If the column is sufficiently long, the band will have a Gaussian shape and the plate-height associated with eddy diffusion is [1, 3]:

$$H_{Eddy} = \lambda d_p \tag{1.5}$$

where λ is a packing parameter, which decreases with greater uniformity of packing. For well packed HPLC columns , λ is usually between 2.5 and 5 [1]. H_{Eddy} is independent of the mobile phase velocity.

1.2.4 Resistance to Mass Transfer in the flowing Mobile Phase

As discussed above, there are several flow non-uniformities in a packed bed, and they can be relaxed by lateral convection, which is included in the eddy term as discussed in section 1.2.3. However, lateral diffusion can also relax the non-uniform flow pattern.

7

In lateral diffusion molecules move across the column, and thus move among mobile phase flow streams having various axial linear velocities. They thus acquire different velocities in an ever-changing, random fashion, which relaxes the effect of flow non-uniformities. If lateral diffusion occurred infinitely fast, all molecules would experience the same average velocity, and there would be no band broadening due to non-uniformity of flow (though there would be infinite band broadening from longitudinal diffusion). However, lateral diffusion occurs at a finite rate so that there is a net band broadening effect. For a long column, the plate height contribution from the lateral diffusion in the mobile phase is [3, 6]:

$$H_{MP} = \frac{\omega\, d_p^2\, u}{D_{MP}} \qquad (1.6)$$

where ω is a packing factor, similar to λ from section 1.2.3, and its value is also close to 5. It also decreases with improved uniformity of packing.

1.2.5 Coupling of the eddy and the lateral diffusion term

Both lateral convection and lateral diffusion act to relax the non-uniform flow patterns in a packed bed. Thus they both decrease the band broadening associated with them. Their associated plate-heights cannot be simply added, because they are not statistically

8

independent of one another. Giddings has combined the two contributions into a coupled plate height term H_{couple} [3]:

$$H_{couple} = \left(\frac{1}{H_{Eddy}} + \frac{1}{H_{MP}}\right)^{-1} = \left(\frac{1}{\lambda\,d_p} + \frac{D_{MP}}{\omega\,d_p^2\,u}\right)^{-1} \tag{1.7}$$

This means that the magnitude of H_{couple} is always smaller than the magnitude of either H_{Eddy} or H_{MP} alone. The smallest term thus dominates, similar to the parallel-resistances model of electricity. This coupling term is not a rigorous solution to the combination of the two steps, but is a simplified way of the combining of the two processes. Furthermore, while in principle each of the five flow non-uniformities listed in section 1.2.3 would require its own coupling term [3], this is not done in practice, in which Eq. 1.7 is employed.

1.2.6 Non-equilibrium effects due to sorption-desorption kinetics in the packing particles

Before a molecule is sorbed onto the stationary phase, it must go through several processes, with intra-particle diffusion being usually the most important of them. The diffusion into and out of the packing particles is not infinitely fast, and it takes some time to achieve equilibrium between the solute (sample) in the mobile phase flowing past the particles and the solute in the stationary phase. As the sample molecules in the mobile phase are migrating down the column, there is always an excess concentration (above that

9

dictated by equilibrium) of solute in the leading half of the band in the flowing mobile phase, because there is not enough time for the sorption process to have reached equilibrium. Naturally, the situation in the stationary phase is the opposite, because there is a solute deficiency in the stationary phase for the leading half of the sample zone. In the trailing half of the band in the flowing mobile phase, the mobile phase contains a lower concentration of sample, causing net desorption to occur from the stationary phase. Sample transport from the inside of the packing particles also takes some time, so that the sample concentration in the particles is higher than that dictated by equilibrium after the mobile phase concentration maximum has passed.

The slower the intraparticle sorption/desorption kinetics, the greater the band broadening at the front and rear of the band of solute. Increasing the mobile phase velocity has the same effect as slower intraparticle kinetics. For sufficiently long columns, Gaussian peaks will be observed [3, 15]. In general, the plate height equation for Gaussian peaks due to non-equilibrium is :

$$H_{intraparticle} = \frac{(constant) \cdot u}{k_{intraparticle}} \tag{1.8}$$

where $k_{intraparticle}$ is the equivalent of first-order kinetic parameter for the process of sorption-desorption.

Thus, in terms of sections 1.2.2 – 1.2.6, the overall plate height H_{Total} in Eq 1.3 has the form.

10

$$H_{Total} = H_{LD} + H_{intraparticle} + \left(\frac{1}{H_{Eddy}} + \frac{1}{H_{MP}} \right)^{-1} \qquad (1.9)$$

Often, the term $H_{intraparticle}$ is seen as the sum of plate heights due to resistance to mass transfer in the stationary phase, H_s, and the resistance to mass transfer in the stagnant mobile phase, H_{SM} [2, 3, 6]. It is now apparent why the rates of sorption and desorption into and out of particulate stationary phases are a subject of interest to chromatographic sciences. Any excessively slow sorption/desorption behavior will greatly reduce column efficiencies, yielding excessively broad, or even tailed peaks. Conversely, any phenomenon which acts to speed up the kinetics of sorption/desorption can increase the performance of chromatographic columns. A detailed understanding of intraparticle mechanisms of mass transfer can advance efforts to create more efficient separation media.

11
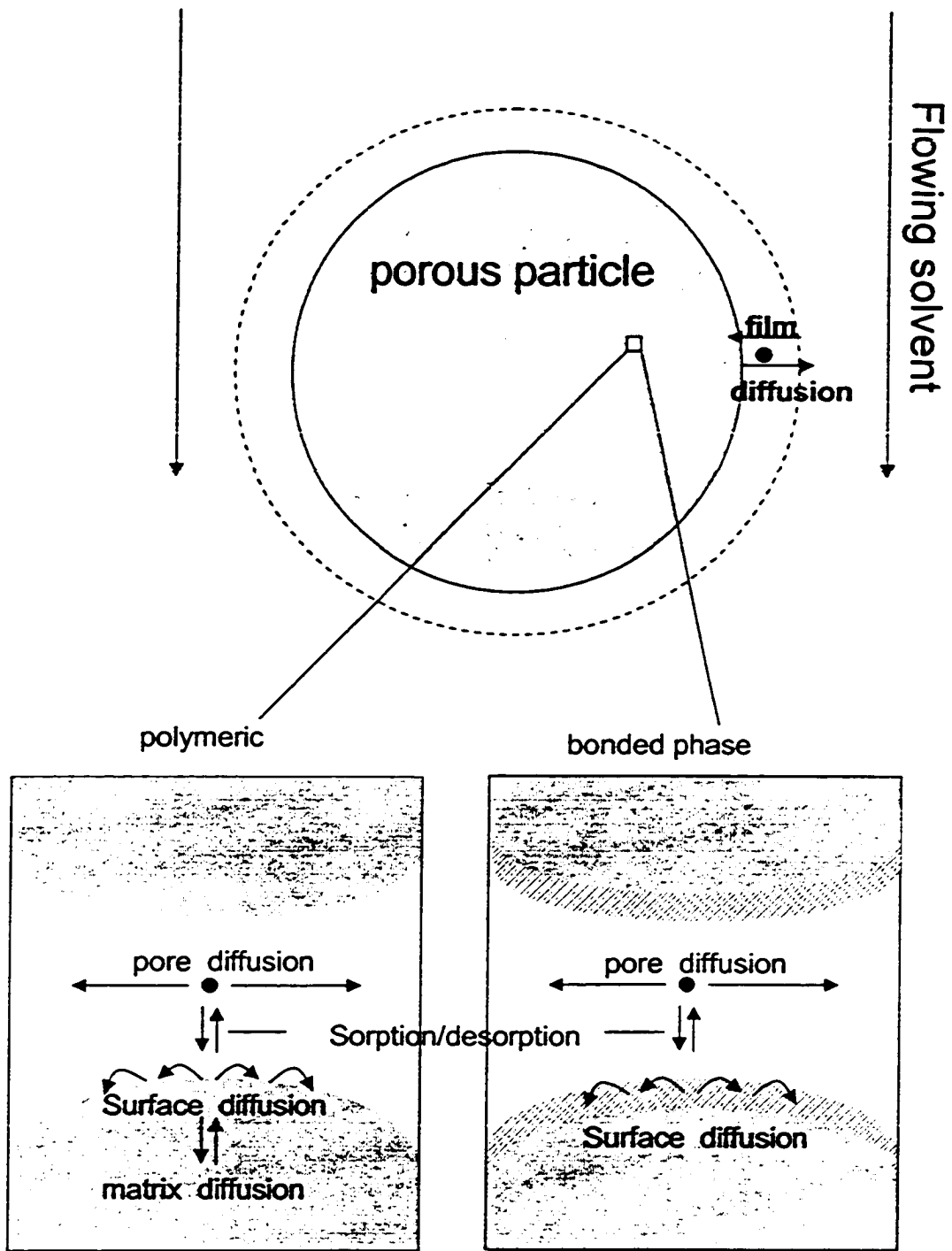
Fig. 1.2. Kinetic Processes which can take place in a porous particle during sorption/desorption

1.3 Mechanisms of sorption/desorption kinetics in packing particles

The subject of this thesis is the measurement and characterization of sorption/desorption kinetics associated with chromatographic band broadening. There are several steps which the sorbing molecules go through in order to equilibrate with porous HPLC packing. These processes are all depicted in Fig.1.2. The first of these is the mass transfer from the flowing solution to the particles, which occurs through a stationary film of liquid surrounding the particles, and is referred to as external film diffusion. (External film diffusion through the mobile phase is not treated by Eq. 1.6 for H_{MP}) This is followed by the radial diffusion (in case of spherical particles) through the pores towards the centre of the particle. (For most HPLC packing the pore size is so small that effectively no flow occurs in the particle, and the transport occurs through diffusion only.) There are also kinetics associated with the actual adsorption from the pore solution onto the pore walls. Once adsorbed onto the pore walls, the solute can diffuse along the pore surface; this can serve as another mode of transport towards the centre of particle. In polymeric particles, such as PS-DVB and related polymeric supports, sorption may involve not only the adsorption onto the surface lining the pores, but it could include the diffusion into the matrix which makes up the skeleton of the particle. Matrix diffusion does not happen in ODS silica used in HPLC, however. The desorption process follows the same steps in reverse. Each one of these three steps: film diffusion, intraparticle diffusion, and the sorption-desorption step onto/into the stationary phase, can be rate

13

limiting, depending on the specifics of the solute, the stationary phase, and the mobile phase.

1.3.1 The chemical adsorption/desorption step

Kinetics of the actual adsorption/desorption step onto the walls of the packing can be rate-limiting when specific recognition of analyte is involved, such as in affinity and chiral chromatography [16-18]. The plate height associated with this process is [3]:

$$H_s = \frac{2k'u}{(1+k')\,k_d} \tag{1.10}$$

where k' is the capacity factor, also known as the retention factor of the solute i. It is defined as the ratio of solute sorbed to that in the mobile phase. The parameter k_d is the desorption rate constant. In deriving this equation, the reversible adsorption/desorption process is assumed to follow a first order rate law.

When non-specific sorption is involved, such as in RP HPLC, the actual physical adsorption/desorption step is often very fast [19-24] (although exceptions do exist [25]). Thus, the solute in the pore liquid can be assumed to be in local equilibrium with solute on the pore walls, and a single molecule is expected to undergo the adsorption-desorption step a large number of times during its stay in the particle. For all the systems studied in this work the kinetics of the sorption-desorption step are assumed to be the fastest step, and therefore they are negligible and not rate-limiting to the overall sorption/desorption process. In this case, the sorption/desorption inside of the chromatographic particles is limited by diffusional mass transfer.

14

1.3.2 Particle diffusion

Mass transfer inside porous particles, both toward and away from the centre, can occur through both pore diffusion (in liquid filling the pores) and surface diffusion (along the pore wall). Since these are parallel processes, the faster one contributes more to the mass transfer rate. The combined intraparticle diffusion coefficient, D_i, can be expressed as follows [26-29]:

$$D_i = \frac{D_P + R\,D_S}{1+R} \qquad (1.11)$$

Where D_P is the pore diffusion coefficient (*i.e.* for the diffusion in the stagnant mobile phase which fills the intra-particle pores), D_S is the surface diffusion coefficient, R is the equilibrium ratio of the moles of solute sorbed in the stationary phase to the moles of solute in the pore liquid. R can be calculated from k' by:

$$R = k'/f \qquad (1.12)$$

$$f = \varepsilon_{intra}/\varepsilon_T \qquad (1.13)$$

where ε_{intra} is the intraparticle porosity, defined as the pore volume per unit volume of an HPLC column, and ε_T is the total porosity of a column per unit volume. It includes ε_{intra},

15

as well as ε_{inter}, known as the interparticle porosity, defined as the fraction of the column volume occupied by interparticle spaces.

$$\varepsilon_T = \varepsilon_{intra} + \varepsilon_{inter} \tag{1.14}$$

The pore diffusion coefficient is related to the free liquid diffusion coefficient D_{MP} by the expression [27-29]:

$$D_P = \frac{D_{MP} \cdot Hindr}{\tau} \tag{1.15}$$

where Hindr is the hindrance parameter, also referred to as the constrictivity or restrictivity factor, which accounts for an additional drag on the solute caused by a more viscous liquid in the presence of the nearby walls of the small pores. It ranges in value from 0 to 1. For example, Hindr is equal about 0.8 when the solute diameter is 20 times smaller than the pore radius, 0.6 when ten times smaller, and it quickly approaches very small values as the solute diameter grows closer to the pore diameter [27, 30, 31]. It is convenient at this point to define the terms used to describe the diameter of the pores. The IUPAC convention is to call pores having widths ≥ 50 nm as macropores, and those having widths between 2 and 50 nm mesopores, while pores having diameters ≤ 2nm are called micropores. Since small molecules of molecular weight 100-600 Daltons have molecular diameters between 0.5 and 1 nm, diffusion through micropores is extremely hindered, and can be a source of very slow mass transfer, leading to excessive band broadening. For this reason, most HPLC packings have their pore diameters on the order

16

of 10 nm or larger. The other parameter in Eq. 1.15 is the tortuosity, τ, and it accounts for the fact that the pores aren't straight, so the diffusion distance is, in effect, longer than in pure liquid. Tortuosity is in fact the square of the increase of the diffusion path, since diffusion time is proportional to the square of the diffusion distance [3, 27]. It is difficult to predict tortuosity *a priori*, but several experimental studies report that for porous HPLC packings τ falls in the range of 2 ± 0.5. [32-36].

In some cases, as in the diffusion of cations in porous silica gel (non - alkylated), surface diffusion is likely negligible, and the solute travels by sorption-retarded pore diffusion (SRPD), a process where the effective diffusion coefficient is the pore-diffusion coefficient multiplied by the fraction of time that the molecule is not adsorbed, and is thus free to diffuse [37-39]. The equation for SRPD is easily obtained from Eqs 1.11 and 1.15 by substituting $D_S = 0$.

$$D_{i,SRPD} = \frac{D_P}{1+R} = \frac{D_{MP} \cdot Hindr}{\tau(1+R)} \qquad (1.16)$$

In other cases, such as on ODS reverse phase packing, surface diffusion along the pore walls can occur at the same time as pore diffusion, and thus it can speed up the intra-particle rate process [40-43]. When surface diffusion occurs along the pore walls, its path is also tortuous, with a value $\tau_{surface}$ that is expected to be greater than the one for pore diffusion, since the diffusing molecule is forced to follow the contours of the walls. In the Eq. 1.11, the value of $\tau_{surface}$ is lumped into the overall effective surface diffusion D_S.

For a sufficiently long column, the elution peak shape due to stagnant mobile phase diffusion and simultaneous surface diffusion would be Gaussian, and the plate height associated with stagnant mobile phase diffusion through the pores plus the associated surface diffusion is [6, 44].

$$H_{SM} = \frac{(1-f+k')^2}{30(1-f)(1+k')^2} \frac{d_P^2 u}{(D_P + \frac{k'D_S}{f})}$$

(1.17)

In the case of polymeric packings, such as poly(styrene-divinylbenzene) (PS-DVB), other modes of diffusion are possible. For a macro/mesoporous particle both surface diffusion and pore diffusion can occur inside the larger pores. However, the matrix of the polymeric packing is made up of cross linked monomers [28, 45-47]. When the degree of cross-linking is very high, the matrix is incapable of swelling and is very rigid. However, rigid micropores do exist in such a network, and slow, hindered diffusion will occur inside such highly cross-linked matrix. Hindered diffusion can also occur in microporous inorganic material substrates, such as zeolites, and in poorly-prepared porous graphite stationary phases [48].

In certain cases, the polymeric particle does not have macro/mesopores where the mobile phase can enter, and they are made up of a continuous matrix. This matrix can be viewed as either microporous or a gel. If the degree of cross-linking is high, micropores are seen as discussed above. If the degree of cross linking is small, the polymer matrix can swell (when exposed to a proper solvent) and the spaces between the polymer strands open up.

18

It is common for those two types of matrix to be seen in a single particle. In either case, when the mobile phase is an aqueous/organic solvent mixture, the solvent composition within the matrix is different than that outside the particles, since wetting solvents are more enriched inside the particles. This is often the case in gel-type ion exchangers made up of sulfonated PS-DVB. In such a particle no stagnant mobile phase is thought to exist, and an unretained compound is also excluded from the particle (in meso/macroporous particles unretained components do not sorb onto the stationary phase, but can still enter the stagnant mobile phase. Therefore, unretained compounds do enter the particle space of and are not excluded from macro/mesoporous particles). The intraparticle diffusion coefficient D_i through the gel often may not be correlated to D_{MP} in the mobile phase because of the different environment inside the gel. Correlations to estimate D_i in gels do exist, but will not be reviewed here [49]. The plate height expression associated with diffusion into such a gel-type stationary phases is:

$$H_{s,diff} = \frac{k'}{30\,(1+k')^2} \frac{d_P^2 u}{D_i} \tag{1.18}$$

where D_i is the diffusion coefficient inside the particle.

1.3.3 Film diffusion

The influence of external mass transfer through the mobile-phase liquid surrounding the packing particles can be an important contributor to the overall resistance-to-mass

19

transfer under some chromatographic conditions. This phenomenon is physically very complex, but can be well approximated by a very simple model [50]. When a fluid flows through a bed of particles, or through any channel, it is stationary at the walls, but its velocity increases gradually away from them, reaching a maximum in the middle of a channel. Consider a situation where the solute "disappears" when it touches the walls of a channel. Such a possibility exists in the case of an electrochemical reaction at a surface, or when sorbent particles have a very strong affinity (*i.e.* large k') and a large capacity for the solute. The depleted solute can be replaced in two ways. First, the flowing solution can deliver fresh solute from upstream of the channel, which is called convective mass transport. The second, usually slower, process of delivering new solute to the walls is by diffusion of unreacted molecules along the direction normal to the surface from the regions further away from the walls. Regions with the highest velocity, in the middle of the channel, experience the highest rate of solute replenishment. Convectional mass transfer is thus highest in the middle of flow channels, where it is much faster than diffusional mass transfer. However, the convectional transfer diminishes continually as the particle surface is approached, and diffusive mass transfer of solute from the outer layers of the flowing solution from above becomes more and more important. An analogous situation exists for particles suspended in a stirred beaker, except that convectional mass transfer takes place by the particle itself moving to new regions of the stirred bath [51].

The model of a Nernst diffusion layer, or the Nernst diffusion film, is a very practical idealization of the convective/diffusive situation just described [51-53]. It replaces that

20

situation with a layer of thickness δ, where no convection takes place, and a sharp

boundary which separates it from a solution where convective mass-transfer is infinitely

fast and any depleted solute is replaced immediately. Even though not physically correct,

this simplification has been shown to be very successful when compared both to

experimental results and to rigorous theoretical models [51].

The plate-height contribution arising from transport through a hypothetical Nernst

diffusion film, H_{film} can be derived from reference [51], assuming that the concentration

gradient through the film is linear, and that the column is long enough to give a Gaussian

peak shape:

$$H_{film} = \left(\frac{k''}{k''+1}\right)^2 \frac{2d_p \, \delta \, u_{inter}}{3 D_{MP}}$$ (1.19)

where u_{inter} is the interstitial fluid velocity, and k' is the equilibrium ratio of moles of

solute in the particle, including in the pore liquid, to the moles in the mobile phase

outside of the particles. For non-porous particles, such as gel ion exchangers, $k'' = k'$, and

$u_{inter} = u$, since unretained solutes don't enter the particle region at all. For porous

particles:

$$k'' = \frac{k'' \varepsilon_T}{\varepsilon_{inter}} + \varepsilon_{intra}$$ (1.20)

$$u_{inter} = \frac{u \varepsilon_T}{\varepsilon_{inter}}$$ (1.21)

21

Other authors cite H_{film} to be [2, 17] :

$$H_{film} = \frac{\xi(k_0 + k' + k_0 k')^2}{(1 + k_0)^2 (1 + k')^2} \frac{d_p^{5/3} u_{inter}^{2/3}}{D_{MP}^{2/3}}$$ (1.22)

where ξ is a packing factor, and k_0 is defined as the ratio of the intraparticle and interparticle porosities.

$$k_0 = \frac{\varepsilon_{intra}}{\varepsilon_{inter}}$$ (1.23)

In Eq. 1.22 , the effect of δ is incorporated into d_p, D_{MP}, u_{inter}, and ξ. The effect of these parameters on δ is discussed in more detail in Chapter 2.

1.4 Extra-column band broadening

In addition to the band broadening (dispersion) caused by the individual physical processes present in a column, there are also band broadening effects from the extra-column components such as the injector, connecting tubing, fittings, detector cell and the electronic readout system [54, 55].

For example, connecting tubing is known to display a non-uniform velocity distribution due to the laminar flow profile, usually parabolic in shape. As well, a sudden increase in tube diameter creates a mixing-chamber effect, which increases band-spreading significantly, making Gaussian peaks look like exponential decay curves under the worst of circumstances. Related mixing behavior can also occur in any dead pockets with no

22

direct flow through them. Slow response time of the detector also has a distorting, broadening effect which results in asymmetry.

The additional dispersion produced by the extra-column devices adds to the observed broadness of the peak as:

$$\sigma_{obs}^2 = \sigma_{column}^2 + \sigma_{extra}^2 \tag{1.24}$$

Therefore, narrow, short tubing, zero-dead volume connectors, and fast detector response-time are a must in high efficiency chromatography. Extra-column band broadening will be dealt with in more detail in Chapter 6.

1.5 Methods of studying sorption/desorption kinetics in packing particles

Sometimes, as when characterizing new column packings, it is desired to study sorption/desorption kinetics and their relative contribution to column band broadening. As well, the study of kinetics of sorption/desorption can lend deeper insight into the physical properties of the existing stationary phases. Nevertheless, sorption/desorption kinetics have been the subject of relatively few scientific investigations. The approaches previously employed to experimentally measure particle sorption/desorption rates on chromatographic packings can be grouped into three categories: column chromatography; spectroscopy; and uptake measurements.

23

1.5.1 Column Chromatography

In the column chromatographic approach, elution chromatograms are obtained for the solute on a column of the packing being studied. The observed plate heights, H_{obs}, are then calculated from the observed elution peak, by obtaining the variance of peaks using the method of moments [44] or by approximating the peaks as exponentially-modified Gaussian [25]. The plate heights are plotted versus the linear velocity of the mobile phase and these plots are evaluated in terms of a theoretical equation, involving a summation of terms, such as given in Eqs. 1.3 and 1.9, which relate them to physical properties such as particle size and diffusion coefficients [56, 57]. A literature example of such an equation this given by Horvath is [2]:

$$H_{obs} = \frac{2\gamma D_{MP}}{u_{inter}} + \frac{2\lambda d_p u_{inter}^{1/3}}{u_{inter}^{1/3} \omega (D_{MP}/d_p)^{1/3}} + \frac{\xi (k_0 + k' + k_0 k')^2}{(1+k_0)^2 (1+k')^2} \frac{d_p^{5/3} u_{inter}^{2/3}}{D_{MP}^{2/3}} +$$

$$\frac{\alpha (k_0 + k' + k_0 k')^2}{30 k_0 (1+k_0)^2 (1+k')^2} \frac{d_p^2 u_{inter}}{D_{MP}} + \frac{2 k' u_{inter}}{(1+k_0)(1+k')^2 k_d}$$

$$(1.25)$$

where the first term is H_{LD}, the second is an alternative way to express H_{couple}, the third is H_{film}, the fourth is H_{SM} and the fifth is H_S. The form of the equation is slightly different because it is written as a function of u_{inter} instead of u.

The column chromatography can also be carried out by the frontal approach, where, instead of injecting the solute, the solution containing it is continuously fed into the column, until the front breaks through at the outlet. The shape of the edge of the front also contains information about the band spreading of the elution peak [56].

24

The column chromatographic method is quite convenient, because it uses the standard equipment of liquid chromatography and, when the intraparticle kinetics are so slow that they are the major contributors to chromatographic band broadening, the column chromatographic approach can be readily used. For example, Muller and Carr have studied the slow kinetics of dissociation of sugar derivatives by using silica particles containing immobilized concanavalin A, a known lectin, in affinity chromatography columns. They correlated the variance of the elution peak with the kinetics of sorption (*i.e.* complex formation)/desorption (*i.e.* dissociation) step via a simple relationship. They didn't need to make large corrections for other band broadening processes occurring in the column. In addition, they found a convenient way to measure the other band broadening processes experimentally by performing a run with a sugar of the same molecular weight, but with no affinity for the immobilized ligand [16-18]. McGuffin and coworkers have also studied slow kinetics of sorption of selected compounds onto ODS silica, and determined the kinetic parameters from the peak shapes [25].

The column chromatographic approach becomes problematic when the intraparticle processes are fast enough that they do not dominate the band broadening. Under such conditions, the variance and shape of the observed peak or front are the result of several band broadening processes occurring in the column, as shown, for example in Eq. 1.25. These include the eddy dispersion coupled with the mobile–phase mass transfer resistance, the external stagnant film diffusion, and longitudinal diffusion, and even extra-column band broadening, as discussed in sections 1.2 and 1.4. Each of these other contributions, whether they be measured experimentally or estimated through theoretical

25

equations, will have an uncertainty associated with them. All of these contributions to band broadening must be subtracted from the overall peak variance in order to obtain the intra-particle contribution by difference [2, 8, 11, 47]. This is particularly problematic when the intra-particle kinetics are responsible for only a small fraction of the peak variance.

Miyabe and Guichon have published close to thirty articles in which they study the intraparticle kinetics on reverse phase octadesylsilane (ODS) silica gel packings. They have recently reviewed their work [44]. Their main conclusion is that the intraparticle mass transport in porous ODS silica occurs via surface diffusion along the walls covered with the C-18 chains. Their analysis, however, suffers from the problems listed above, which can lead to large uncertainties. Thus, it would be beneficial to confirm their result by other methods. A large part of the work in this thesis is devoted to the study of kinetics in porous ODS particles, and, as will become apparent, the results are in qualitative agreement with those of Miyabe and Guichon.

1.5.2 Spectroscopic Methods

Nuclear magnetic resonance

Nuclear magnetic resonance (NMR) has been used for the measurement of self-diffusivity. Also NMR is now routinely used to measure diffusion rates in polymer systems [58]. The pulsed-field gradient (PFG) method has been used for kinetic studies of mass transfer inside stationary phase particles [32-36], and in columns. It has been

26

applied for the study of the monolithic columns as well, and it is a powerful tool for studying fluid dynamics in porous media.

The most important contribution of PFG NMR studies to intraparticle kinetics is the measurement of tortuosity factors inside chromatographic stationary phases. For example, tortuosity factors inside porous silica, porous zirconia, and PS-DVB have been obtained in several studies and numerous data indicate that the tortuosity factors fall within the range of 1.5 to 2.5 [32-36]. This is an important result, since there are various theoretical equations for predicting tortuosity factors based on the particle porosity, but they can vary in their predictions. For example the theoretically predicted value of tortuosity can vary as much as an order of magnitude for the case when the particle porosity is 0.5 [27]. Experimental measurements that narrow that range down are thus indispensible. To the best of the author's knowledge, with the exceptions noted below, the solutes used for the kinetic studies were usually unretained, so NMR studies generally have not been used to study the kinetics of sorbed compounds, which is obviously of more interest from the point of view of chromatographers. In one case, diffusion of retained molecules in zeolites has been reported [59]. In another example of a recent study using high resolution magic angle spinning diffusion-ordered spectroscopy (HRMAS-DOSY) diffusion was measured under retentive conditions in ODS silica, in deuterated ethanol [60], and the obtaining of such kinetic information by NMR under conditions typical of RP HPLC (aqueous/organic) may yet be possible.

27

Another limitation to measurements of intraparticle diffusivity is the fact that high

magnetic field is required to measure small diffusion coefficients in porous polymers (D_i

$< 10^{-8}$ cm^2/sec). Measurement of diffusion in porous polymers is additionally

challenging if two or more diffusion coefficients having very different values exist [45,

58].

Luminescence

Luminescence methods, involving pressure jump [20, 21], temperature jump [23], and

photon-induced dipole jump [24], are used to study the kinetics of the actual sorption

from the solution to the walls of C-18 – derivatized silica. These techniques study only

the chemical adsorption/desorption step described in Section 1.3.1 and do not provide

detailed information about other mechanisms in Section 1.3. The pressure- and

temperature jump methods involve a perturbation of the equilibrium and kinetic

constants, while the photon-induced dipole jump leaves them unchanged. Usually, the

solute has to be strongly fluorescent or phosphorescent, and often flat fused silica

surfaces are used as substrates, though silica gel particles have been successfully studied

as well [19]. The main results of these studies relating to RP HPLC is that for small

molecules the adsorption/desorption kinetics are fast enough that the actual

adsorption/desorption step from the pore solution to the C-18 derivatized wall is diffusion

limited (in the sense of a homogenous reaction) ; *i.e.* the process is as fast as the diffusion

of the solute to and from the pore wall.

28

Fluorescence methods, such as fluorescence autocorrelation, fluorescence recovery after photobleaching, and excimer formation have also been used to study surface diffusion coefficients on ODS silica substrates, and valuable information has been obtained. The diffusion coefficients observed for small molecules diffusing laterally across a C-18 surface range from about $2 \cdot 10^{-7}$ to $6.5 \cdot 10^{-6}$ cm^2/sec, with only a few cases exhibiting lower diffusion coefficients [19, 40-43]. In this regard they provided the first measurements of surface diffusion in RPLC.

Other fluorescence-based techniques are fluorescence imaging [22] and single molecule spectroscopy [43], which both have been used to study the unwanted strong adsorption of cations onto the active silanol sites in silica gel. As well, confocal laser scanning microscopy has been used to study intraparticle mass-transfer kinetics in 200 μm porous beads [61]. The Fluorescence imaging and confocal laser scanning microscopy methods could be classified both as being fluorescence methods and uptake/release methods, which are discussed in the next section.

1.5.3 Uptake/ Release Methods

These experiments involve some way of monitoring the approach to equilibrium after the solvent surrounding the particles is suddenly changed to have a different concentration of solute. Generally, uptake/release techniques do not change the equilibrium constants, since only the concentration of the sample changes, while the solvent remains the same. They can be performed either in a batch mode or a shallow-bed mode. The obtained sorption/desorption rate curves are then fit to theoretical equations, which describe the

29

uptake/release as either first or second order chemical reactions, spherical diffusion, film diffusion, or a combination thereof. (*i.e.* any process described in Section 1.3 which potentially contributes to rate control of sorption/desorption onto the particle). The kinetic parameters, such as the chemical rate constants, diffusion coefficients inside the particles, or the thickness of the diffusion film are obtained as the fitting parameters of those equations.

Batch Mode

Kinetic uptake experiments are performed in a batch mode by placing sorbent particles in a stirred solute-containing solution and measuring the amount of solute taken-up as a function of time [29, 50, 62-64]. The release kinetics are measured by placing sorbent particles that have previously been pre-equilibrated with a solute into a stirred, solute-free solvent and measuring the depletion of the solute in the particles as a function of time. The measurement can be made by removing some of the sorbent particles, eluting the sorbed solute and quantifying it; or it can be done by removing some of the mobile phase, determining the concentration of the solute, and calculating, the amount of solute that has been sorbed or desorbed. In the case of uptake experiments the concentration in the solution would decrease as a function of time, and in the case of the release experiments the solute concentration in solution would increase with time. A plot of the amount of solute sorbed versus time is the sorption-rate curve, and the plot of the amount of solute desorbed versus time is the desorption rate curve. (Note that the fraction of the solute desorbed from a sorbent equals 1 minus the fraction of the original solute still remaining in the sorbent). The obtained (de)sorption rate curves are then fit to theoretical equations,

30

which describe the uptake/release as either first order chemical reactions, spherical diffusion, film diffusion, or a combination thereof.

If the slurry is stirred sufficiently fast, the Nernst diffusion layer around the particles can be made very thin, so that intra-particle sorption processes determine the overall sorption rate curve. If during the uptake experiment, the fraction of solute sorbed out of the solution is very small, then solute concentration in the solution is essentially constant and the batch sorption-rate experiment is said to have been performed with an "infinite solution volume" or under "infinite bath" conditions. For the release experiments, infinite bath conditions mean that the solute that desorbs into the solution does not raise the concentration there significantly from zero. It follows that under infinite bath conditions the sorption or desorption rates must be done by measuring the amount of solute in the sorbent, and not the solvent phase. On the other hand, if the fraction of solute sorbed from the solution is significant, the experiment has been performed with a "finite bath volume" or under "limited bath" conditions. Under limited bath conditions the rates of reaction may be monitored in either the sorbent or the solvent phases.

In a variation of this technique a single sorbent particle is contacted with the solution or with the solvent and the concentration of solute in the particle itself is measured as a function of time. This has usually been performed without stirring in solution, and under infinite bath conditions [37, 65].

31

The stirred batch mode and single particle uptake/release measurements usually apply to relatively large particles, with diameters ranging from 50 μm to several millimeters or, more generally, to cases where the intraparticle uptake/release rates are excessively slow. This is because, under even efficient stirring, the Nernst diffusion film is relatively thick. For small particles in a stirred bath the uptake/release rate would almost invariably be controlled by film diffusion. However, it is small particles with diameters < 10μm which are useful for HPLC.

The Shallow Bed Method

Uptake/release studies can also be performed in the shallow bed column mode (which also has been called differential reactor, differential contactor, and zero-length column). In this method, the sorbent particles are packed as an extremely short bed in a tube [28, 45, 46, 50, 62, 64, 66-74]. To measure the sorption rate, a solution of solute is caused to flow at a high linear velocity, such that, at all times, the concentration of solute in the effluent solution is nearly identical to that in the influent solution. All of the sorbent particles in the shallow bed are therefore bathed in a solution containing, essentially, the inflowing concentration of the solute. This creates infinite bath conditions if only fresh solution is delivered. If the solute is recycled, then finite bath conditions are created [75]. Furthermore, if the linear velocity of solution is high enough, the Nernst diffusion film surrounding the particles in the shallow bed will be very thin, much thinner than in the stirred bath conditions, so that intra-particle sorption rate will likely determine the observed sorption rate. (There are examples, however, where shallow-bed and shallow-bed like studies were used to measure the sorption/desorption kinetics under conditions

32

where film diffusion was the rate limiting step [62, 64, 76].) The flow of solution is allowed to proceed for various periods of time, after each of which the amount of solute sorbed is measured.

Sorption rate curves have been obtained from shallow-bed measurements for the sorption of naphthalene by the mesoporous PS-DVB HPLC sorbent Hamilton PRP-1 [28, 46]. Rate curves have also been obtained for the sorption of naphthalene by the nominally nonporous PS-DVB sorbent Hamilton PRP-∞ [28, 71]. It was shown that in both cases the rate of sorption is controlled by diffusion through the polymer matrix, and that this slow diffusion is the cause of the excessive band broadening that these packings exhibit with polyaromatic compounds such as naphthalene.

From the uptake/release methods, only shallow bed studies proved capable of measuring kinetics inside HPLC packings [28, 46]. The shallow bed technique is attractive because it can be applied to a wide variety of solutes, since the detection of the amount of solute is done after it has been eluted from the sorbent. A disadvantage of operating in the sorption mode is the labor- intensive and time-consuming nature of the experiments. Each experiment yields the amount of solute sorbed at only a single loading time. The shallow-bed technique can also be used to measure particle desorption rates. The particle-packed bed is first pre-equilibrated with a solution of the solute and then solute-free solvent is caused to flow through the bed to desorb the solute. By placing a detector downstream of the bed the entire plot of the desorbed solute concentration vs time is

33

obtained in one experiment as the detector signal decays toward zero with time [62, 64, 66].

There is a challenge in adapting the continuous monitoring desorption method to the study of fast kinetics. As the solute travels between the shallow-bed and the detector, the instrument components through which this flow occurs (e.g. bed outlet frit, connecting tubing, detector cell, detector time constant) produce instrument (*i.e.* extra-column) band broadening. Therefore, the solute concentration detected may be very different from that which actually leaves the bed. This effect will not be very important if the process studied is relatively slow, with half-lives on the order of tens of seconds and more; but to study faster kinetics this effect needs to be minimized. The subject of this work is to develop the instrumentation and the data analysis to minimize the effect of this extra-column solute zone dispersion, in order to advance the shallow-bed desorption method to the study of fast, sub-second, intraparticle desorption kinetics.

The first part of the work is to develop the appropriate data processing steps and to confirm the feasibility of the technique (Chapter 3). The desorption of naphthalene from 20 μm polymeric particles of PRP-∞ in 70/30 MeOH/H$_2$O is chosen as the solute-sorbent-solvent system to be studied. The reasons are that the diffusion coefficient of naphthalene inside PRP-∞ particle is slow, and that it was previously measured. This makes the design of the instrument simpler and allows comparison of the observed intraparticle diffusion coefficient to the literature value. The digital data processing techniques (Section 2.2) such as deconvolution and filtering allow corrections for

34

experimental artifacts due to instrument band broadening and extra-particle solute, after running a separate desorption experiment on an unretained, excluded compound, phloroglucinol. The results are fit with a spherical diffusion model (Eq. 2.1), and the measured particle diffusivity of 5×10^{-11} cm^2 sec^{-1} is found to be statistically indistinguishable from the observed literature value. This successfully demonstrates the feasibility of the instrumental and data-processing approach.

The second, more difficult part of the work is to develop an instrument capable of measuring sub-second desorption kinetics, in order to further advance the shallow-bed method. Some of the challenges include placing the detector very close to the shallow bed (about a millimeter), while maintaining dependable seals. Other issues to be addressed include the partial automation of the instrument, rapid data acquisition, as well the development of proper preparation (packing) of the shallow bed, in order to yield reproducible and reliable data. As well, the new instrument requires a modified approach to data processing (described in Section 2.2.5). The basic instrument design (Chapter 4) is based on a modified stopped-flow apparatus, interfaced with a solvent-delivery system (constant pressure pumps) via an array of computer-controlled electronic valves. The shallow-bed is prepared through a packing procedure which includes the use of microfabricated grids, the purpose of which is to stabilize the packing structure.

The first solute / particle / solvent studied with the second instrument is naphthalene / PRP-1 / 85% MeOH (Chapter 4). PRP-1 is an HPLC polymeric sorbent, 10 μm particle diameter. The kinetic data reveal that there are two intraparticle diffusivities. The faster

35

process is found due to mass transport through the mesopores of PRP-1, though extra-particle film diffusion is identified as partially rate limiting. The slower process, taking about 60 seconds to complete, involves matrix diffusion through the skeleton made up of microspherical aggregates of the cross-linked polymer.

The second and final solute / particle / solvent system studied is 1,2-dimethyl-4-nitrobenzene /Luna C-18 (12 μm)/ 50% aqueous MeOH (Chapter 5). Luna C-18 is a porous ODS packing, with a particle diameter of 12 μm. The desorption of the 1,2-dimethyl-4-nitrobenzene is completed in about 0.5 sec and the kinetic data indicate that particle and film diffusion are both rate-limiting under the conditions studied. It is determined that surface diffusion comprises more than 90% of intraparticle transport for a compound with a high retention factor. Finally, the effect of surface diffusion on band broadening of elution peaks in column chromatography is studied to reveal that surface diffusion can significantly decrease band broadening due to intraparticle mass transport.

To complete this work, Chapter 6 is an investigation into the sources of bandbroadening in the newly developed shallow-bed apparatus. This work identifies ways in which the extra-shallow bed distortions can be minimized in the future.

36

Chapter 2:   Theory for uptake/release kinetics

In this chapter are described the mathematical aspects of uptake/release experiments, and in particular of shallow-bed desorption experiments. A novel aspect of this work is the use of an "impulse response function marker" (IRF-Marker) to correct desorption rate curves for instrumental artifacts by means of subtraction and deconvolution.

2.1   Sorption/Desorption Rate Curves

It is assumed that in all cases the equilibrium conditions occur in the linear part of the sorption isotherm: i.e. that the equilibrium ratio of sorbed solute concentration to the concentration of solute in solution is a constant.

2.1.1 Spherical Particle Diffusion

Nowadays, the majority of packings used in HPLC have a spherical, as opposed to irregular, shape due to their better performance when packed in a column [1]. This is advantageous for uptake/release kinetic studies, because the process of diffusion in a sphere is rather easily described by mathematical equations. The equation below is the theoretical cumulative (integral) rate equation which describes intra-particle diffusion into or out of a spherical particle under infinite-bath conditions, which were described in Section 1.5.3, above [51, 77]. In this equation $n_i(t)$ is both the number of moles of solute that has diffused into the particle by time t during a sorption experiment, and the number

37

of moles of solute that has diffused out of the previously equilibrated particle by time t during a desorption experiment.

$$n_i(t) = n_{i,0}\left(1 - \frac{6}{\pi^2}\sum_{j=1}^{\infty}\frac{1}{j^2}e^{-j^2\beta t}\right)$$
(2.1)

The parameter $n_{i,0}$ is the total number of moles of solute in the particle at sorption equilibrium which can be expressed in terms of the distribution coefficient for the solute κ_i (L/gram), the mass of the packing in the shallow-bed, m_{SB}, and the concentration of the solute i in the mobile phase (solvent) $[i]_{MP}$.

$$n_{i,0} = \kappa_i\,[i]_{MP}\,m_{SB}$$
(2.2)

For the uptake experiment, $[i]_{MP}$ simply means the concentration kept in the solvent during the uptake, while for the release experiments, $[i]_{MP}$ is the concentration of the solute in the mobile phase (solvent) used to pre-equilibrate the sorbent.

The parameter β (s^{-1}) is related to the intra-particle diffusion coefficient D_i $(cm^2\,sec^{-1})$ and to the radius of the spherical particle r (cm) as follows:

$$\beta = \frac{\pi^2 D_i}{r^2}$$
(2.3)

38

This is true for both diffusion through pores and diffusion through a gel. The expression for D_i in porous particles is given in terms of solution- and surface- diffusion coefficients by Eq 1.11- 1.16. Expressions relating D_i for a gel to free-volume inside the gel are reviewed in the literature [49, 71]. When spherical diffusion is the process which controls the observed sorption/desorption rate then the experimental plot of $n_i(t)$ vs t can be fit with Eq 2.1 using non-linear regression. The two fitting parameters are β and $n_{i,0}$.

In certain cases, the intraparticle diffusion occurs with two diffusion coefficients. This can sometimes happen with polymeric sorbents when a particle has macro/meso pores through which diffusion is relatively unhindered, and the matrix consists of micropore and/or gel regions where diffusion is severely hindered. In such polymeric sorbents the polymer matrix is present as agglomerates of fused microspheres. The micropores and gel are in the agglomerates while the macro/meso pores are spaces between the agglomerates [49, 71]. Mathematically, this case is difficult to solve unless the two processes differ widely in time scales, such as when the macro/meso pore diffusion is so much faster than the micropore diffusion that equilibrium for the former process is achieved almost instantaneously on the time scale of the slower process. Then the overall cumulative (integral) sorption/desorption rate curve will be the sum of two spherical diffusion processes. Assuming that the agglomerates have a roughly spherical shape and are relatively uniform in size, $n_i(t)$ is approximated by the expression [28, 78]:

$$n_i(t) = n_{i,01}\left(1 - \frac{6}{\pi^2}\sum_{j=1}^{\infty}\frac{1}{j^2}e^{-j^2\beta_1 t}\right) + n_{i,02}\left(1 - \frac{6}{\pi^2}\sum_{j=1}^{\infty}\frac{1}{j^2}e^{-j^2\beta_2 t}\right) \qquad (2.4)$$

where $n_{i,01}$ is the number of moles of solute sorbed onto the walls of macro/mesopores in the particle at sorption equilibrium, and $n_{i,02}$ is the moles of solute sorbed within the matrix at sorption equilibrium. β_1 is the same as in Eq. 2.3, where D_i is described by Eq. 1.11 which applies to diffusion within the macro/mesopores. β_2 is defined as:

$$\beta_2 = \frac{\pi^2 D_{matrix}}{r_{microsphere}^2} \qquad (2.5)$$

where $r_{microsphere}$ is the radius for the 'microspherical aggregate' within the particle, and D_{matrix} is the diffusion coefficient within the matrix that makes up the microspherical aggregate. As for Eq. 2.1, Eq. 2.4 applies under infinite bath conditions.

2.1.2 Film Diffusion

When sorption/desorption is controlled by the external mass transfer through the Nernst diffusion film, a rigorous analytical solution which describes the rate of uptake/release is available under the steady-state assumption, i.e. assuming a linear concentration gradient through the film. This assumption is valid after a very short lag time (i.e. several orders of magnitude less than the half time of film diffusion controlled uptake/release) which is needed to establish the steady-state conditions across the film [51]. The uptake/ release cumulative rate curve has a form of a simple exponential under these conditions:

$$n_i(t) = n_{i,0} (1 - e^{-kt}) \qquad (2.6a)$$

40

$$k = \frac{3 D_{MP} [i]_{MP}}{r \delta [i]_{part}}$$
(2.6b)

where $[i]_{part}$ is the equilibrium molar concentration inside the particle in the sorption experiment and the pre-equilibrium concentration in the desorption experiment (in units of moles solute in particle per unit volume of particle). The rate of the process is thus proportional to the diffusion coefficient in the film and to the concentration of solute in the mobile phase, and is inversely proportional to the film thickness, the particle radius, and the equilibrium concentration of solute in the particle. Thus, even though the mass transfer is limited by the external film diffusion, properties of the particle itself also have an effect on the rate of sorption/desorption.

The thickness of the diffusion film (δ) can be derived theoretically only for selected cases, such as flow around a single sphere, or flow over a planar surface, or flow inside a cylindrical tube [53, 79, 80]. In other cases it has to be deduced from empirical correlations. For packed columns, several empirical correlations have been developed, mostly found in the chemical engineering literature. These treatments are briefly reviewed here.

Instead of δ, chemical engineers use the dimensionless Sherwood number (Sh) [51, 53]:

$$Sh = \frac{2 k_f r}{D_{MP}} = \frac{2r}{\delta}$$
(2.7)

41

where k_f (cm s^{-1}) is the mass transfer coefficient through the film. This quantity is also often used by engineers and is defined as [51, 53]

$$k_f = \frac{D_{MP}}{\delta} \qquad (2.8)$$

To calculate the Sherwood number, it is first necessary to obtain the Reynolds number (Re) and the Schmidt number (Sc).

The Reynolds number, in the case of flow past a sphere is defined as [51, 53]

$$Re = \frac{2 u_s r}{v} \qquad (2.9)$$

where u_s is the superficial velocity calculated as simply the volumetric flowrate divided by the cross-sectional area of the column (without regard for porosity), and v is the kinematic viscosity defined as the viscosity of the solvent divided by its density.

$$v = \frac{\eta}{\rho} \qquad (2.10)$$

The Schmidt number is independent of flowrate and is defined as [51, 53]

42

$$Sc = \frac{\nu}{D_{MP}}$$

$$(2.11)$$

For packed beds, textbooks quote the following expression of Sh, proposed by Wilson and Geankoplis [53, 81]

$$Sh = \frac{1.09 \, (Re \cdot Sc)^{1/3}}{\varepsilon_{inter}} = \frac{1.09}{\varepsilon_{inter}} \left(\frac{2 \, u_s \, r}{D_{MP}} \right)^{1/3} \; ; Re \cdot Sc >> 1, \, or \, 0.0015 < Re < 55 \qquad (2.12)$$

However, other correlations have also been developed. Kataoka et al. proposed [82]

$$Sh = 1.85 \left(\frac{1 - \varepsilon_{inter}}{\varepsilon_{inter}} \right)^{1/3} (Re \cdot Sc)^{1/3} = 1.85 \left(\frac{1 - \varepsilon_{inter}}{\varepsilon_{inter}} \right)^{1/3} \left(\frac{2 \, u_s \, r}{D_{MP}} \right)^{1/3} \qquad (2.13)$$

These correlations are the most modern of the ones reviewed. They have the same dependence on the velocity and particle diameter. The effect of kinematic viscosity is cancelled when the Re and Sc numbers are multiplied. The only difference in these relationships is the dependence of the proportionality constant preceding $(Re \cdot Sc)^{1/3}$ on the interstitial porosity. For example, for $\varepsilon_{inter} = 0.4$, which is most common for particulate HPLC columns, these values preceeding '$(Re \cdot Sc)^{1/3}$' are 2.7 and 2.1 for the Wilson-Geankoplis and Kataoka relationships, respectively.

43

In the classic book by Helfferich equations for δ proposed by Gilliland [51, 83], and by Glueckauf [51, 84] are cited. However, the results are considered less accurate than those of the two more recent equations cited above.

There is no easy way to choose whether one should use the Wilson or the Kataoka equation for δ. They both have the same relationship with respect to fluid velocity, particle size, *etc*, except for the porosity of the packed bed. Their magnitudes differ by approximately 25 %. The approach used in this thesis is to average the two values which are obtained from Eq 2.12 and 2.13.

2.1.3 Intermediate range between film and particle diffusion

A rough criterion for the relative contribution of intra-particle diffusion and external film diffusion to sorption/desorption rate is [50, 51].

$$X = \frac{[i]_{part} \, D_{MP} \, \delta}{[i]_{MP} \, D_i \, r} \tag{2.14}$$

When $X \ll 0.13$, particle diffusion is rate–limiting, and when $X \gg 0.13$, film diffusion is limiting. When the value of X is approximately 0.13 both processes significantly contribute to the mass transfer control.

44

At first glance, the influence of the resistance to-mass transfer through the external film of solvent surrounding the particles may seem to be minor. This is because in a particulate HPLC column the thickness of the film (δ) is thought to not exceed 20% of the particle radius (r) [50, 51, 81, 82, 84], and also because the diffusion across the film is unhindered and non-tortuous. When compared to the flux due to sorption-retarded pore diffusion (SRPD, see Eq. 1.16) film resistance is indeed expected to be minor. However, when the mass transfer inside the packing is supplemented with an additional process like surface diffusion, the situation could reverse [44].

When both particle and film diffusion contribute to diffusion rate control an analytical solution has been offered, again assuming linear concentration profiles in the film. It only applies to the case of infinite solution volume (infinite bath conditions) [50, 51]. The expression for the cumulative rate curve is:

$$n_i(t) = n_{i,0} \frac{6\theta^2}{r^2} \sum_{n=1}^{n=\infty} \frac{A_n \sin^2(m_n r)}{m_n^4} e^{(-D_i m_n^2 t)}$$

(2.15 a)

where

$$\theta = \frac{[i]_{MP} D_{MP}}{[i]_{part} D_i \delta}$$

(2.15 b)

$$A_n = \frac{(m_n r)^2 + (\theta r - 1)^2}{(m_n r)^2 (\theta r - 1) \theta r}$$

(2.15 c)

the quantities m_n are the roots of the equation

$$m_n r = (1 - \theta r) \tan(m_n r)$$

(2.15 d)

45

Another way to solve this problem is to do numerical modeling of the situation [56, 76, 77]. This technique doesn't make any assumptions as to the concentration profiles in the film; however, it will not be used in this work.

2.1.4 Chemical kinetic control

The "chemical" reaction of interest to chromatography is the actual step of adsorption/desorption onto the surface of the stationary phase from the mobile phase adjacent to it. For example, in ODS the chemical adsorption step occurs when a molecule of solute i in the pore liquid immediately adjacent to the C-18 stationary phase enters that phase. In affinity chromatography, this adsorption step is when the solute i molecule in the pore liquid binds to the immobilized ligand. Analytical chromatography usually occurs under trace conditions, or in the linear region of the sorption isotherm, which is to say that the concentration of free surface sites is much larger that the concentration of the sites occupied by the bound solute i. Thus, adsorption kinetics occur under pseudo first-order conditions. This discussion will only relate to reactions that follow first order kinetics. Consider a porous particle at equilibrium, where, by definition:

$$k_d \, [i_{sorbed}]_{part} = k_{ad} \, [i_{pore}]_{part} \qquad (2.16)$$

where, k_{ad} and k_d are adsorption and desorption constants (s^{-1}) for the sorption step and $[i_{pore}]_{part}$ is the equilibrium concentration of solute i in the particle pores, in units of moles

46

of i per volume of particle, and $[i_{sorbed}]_{part}$ is the sorbed concentration, also in units of moles per volume of particle. This makes:

$$\frac{[i_{sorbed}]_{part}}{[i_{pore}]_{part}} = \frac{k_{ad}}{k_d} = R \qquad (2.17)$$

where R was previously defined as the ratio of moles sorbed to moles in the particle pores, at equilibrium.

If an uptake/release experiment were to be performed on a particle where the chemical adsorption/desorption step is rate-limiting, the following equations give the cumulative sorption/desorption rate curves:

$$n_i(t) = n_{i,0} \left\{ 1 - \frac{R}{R+1} \frac{V_{bath}}{V_T} \exp\left[-\left(1 + \frac{RV_{SP}}{V_T}\right) k_d t \right] \right\} \quad ; \text{ limited bath} \qquad (2.18a)$$

$$n_i(t) = n_{i,0} \left\{ 1 - \frac{R}{R+1} \exp[- k_d t] \right\} \qquad\qquad ; \text{ infinite bath} \qquad (2.18b)$$

where V_{SP}, V_{bath}, and V_T are the volume of the porous particles, volume of the bath surrounding the particles, and the total combined volume, respectively [77]. The previous sections considered sorption/desorption rate curves under only infinite bath conditions, but both infinite bath and finite bath cases are considered in Eq. 2.18 to better illustrate the difference between homogenous and heterogeneous kinetics. From homogenous kinetics, one would expect the observed rate constant to be [85, 86] :

47

$$k_{observed,homogenous} = k_{ad} + k_d \qquad (2.19)$$

However, this is not the case in heterogeneous kinetics. Eq 2.18a is analogous to that for a reversible chemical reaction. The apparent rate constant for Eq 2.18a is $(1 + RV_{SP}/V_T)k_d$. Its value depends on the volumetric ratio of V_{SP}/V_T. Only if V_{SP}/V_T is equal to 1, which is when there is no extra-particle fluid, would $k_{observed}$ equal $k_{observed,homogenous}$. Of course, under these conditions no sorption/desorption would occur at all. When a shallow-bed experiment is carried out under infinite bath conditions, where V_{SP}/V_T is equal to zero, the observed rate constant will always equal k_d, as in Eq 2.18b. This is true for the sorption as well as the desorption experiment [77]. Thus, the fact that a sorption/desorption process is observed to have the same kinetic parameter for both sorption and desorption reactions, is not evidence that the process is mass-transfer limited.

2.1.5 Intermediate range between chemical control and particle diffusion

This case has been treated extensively by Crank and the references therein [77]. A discussion of this topic will not be carried out here, since the rate laws become very complex, and the results are not of direct interest here.

48

2.2 Observed Rate Curves and Data Processing

In this thesis desorption rate experiments are performed in two different designs of the shallow-bed instrument, Type I and Type II. Fig. 2.1 shows a Type I shallow-bed instrument, based on a slider valve. The shallow-bed of particles is placed in a slider, which can move between two flow channels. Channel 1 contains the solution of solute in the solvent (mobile phase) while channel 2 contains the mobile phase alone. The shallow-bed is pre-equilibrated with solute i in channel 1, but the detector is in channel II, where only the solute- free solvent flows. This situation is shown in Fig. 2.1 A. The shallow-bed must be physically moved from channel 1 to channel 2 as shown in Fig. 2.1 B, after which the flowing solvent can start the desorption run.

In the second case, the shallow-bed is pre-equilibrated with solute i in the same channel as the detector, as shown in Fig. 2.2. Here both channels 1 and 2 meet just upstream of the shallow-bed. In this case, the shallow-bed is not moved, but the flow is controlled by remote valves (not shown). The shallow-bed is pre-equilibrated with solute i by only allowing flow through channel 1. This is followed by replacing the solution of i with the solvent alone by allowing the flow to go from channel 2 into channel 1 as shown in Fig. 2.2 B, again by using remote valves. The final step, shown in Fig. 2.2 C is to flow the solvent solution from channel 2 through the bed and towards the detector.

49

A

Channel 1
(solution of solute
in solvent)

Channel 2
(solvent alone)

Slider
valve

slider

Shallow bed of particles

To
detector

B

Channel 1   Channel 2

To
detector
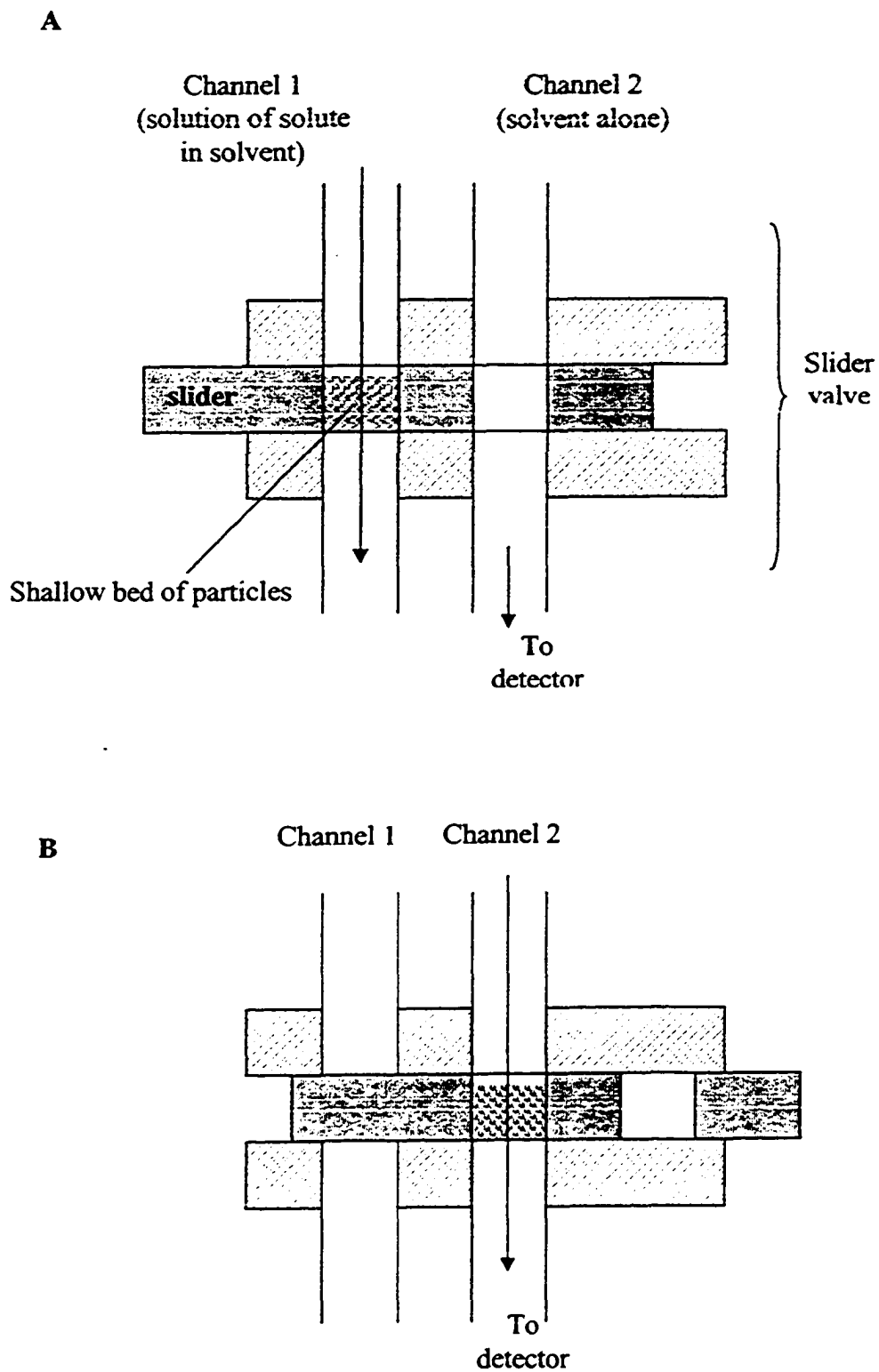
Fig 2.1 Type I Shallow-bed desorption instrument. (A) loading. (B) desorption

50
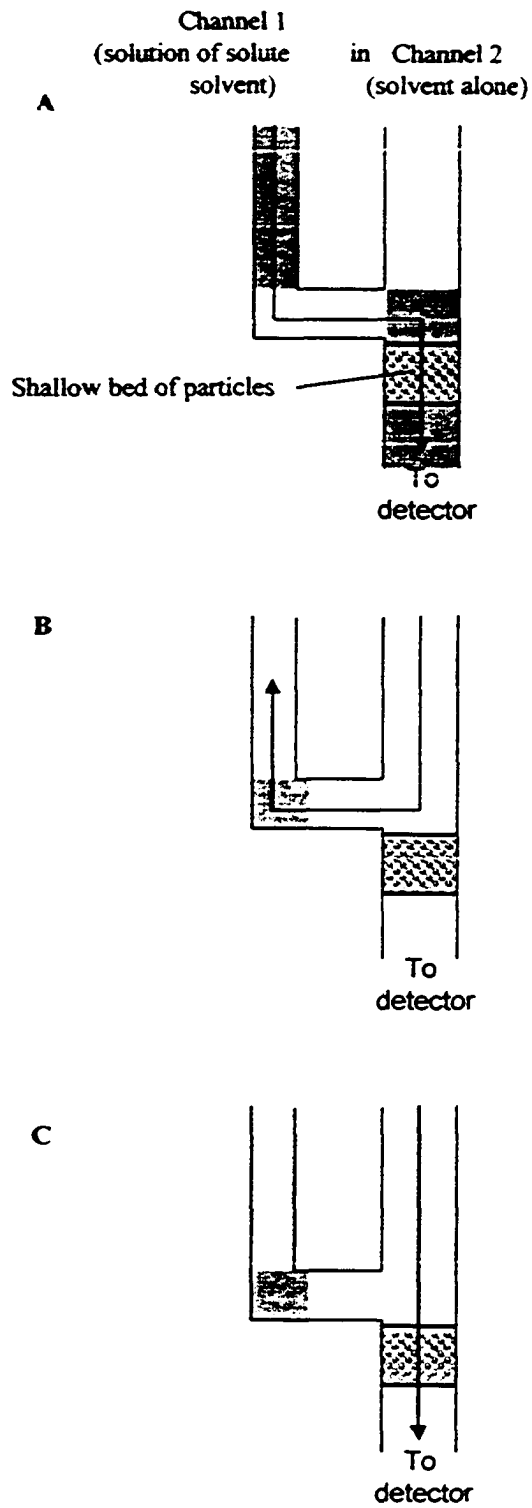
Fig. 2.2 Type II shallow-bed desorption experiment. (A) load step. (B) flush-out step.

(C) Desorption Step.

The most important difference between Type I and Type II shallow-bed instruments is what happens once the desorption steps starts. With the Type I instrument, in Fig 2.1 B, the solute in the pre-equilibrated shallow-bed from Fig 2.1 A can be thought of as being injected into a stream of solvent when the slider is switched. With the Type II instrument, in Fig 2.2 C, switching of the liquids upstream initially finds solute i in the pre-equilibrated shallow-bed, the outlet tubing, and the detector, and this is followed by flowing of pure solvent into them. These two cases are discussed in more detail in subsequent sections.

2.2.1 Effects of band broadening in Type I shallow-bed instrument

Fig. 2.3A shows an idealized version of the instantaneous (differential) rate curve which can be expected when a shallow-bed, previously equilibrated with solute i, is placed in a flowing stream of eluent (solvent or mobile phase), such as depicted in Fig 2.1. At time zero, the desorption starts and the solute leaving the bed travels to the detector (e.g an absorbance detector). Because the flow velocity is necessarily high in order to achieve shallow-bed conditions, the portion of solute which is washed from the extra particle spaces would appear as a very narrow absorbance spike which is labeled as I in Fig. 2.3A. On the other hand, the portion of solute which is desorbed from within the particles would appear as a decaying absorbance signal. This is shown as the line bounding the shaded part of Fig. 2.3A and is labeled as II. Only curve II is related to the desorption rate. The more strongly sorbed the solute (larger value of distribution coefficient κ_i) the smaller is the ratio of moles in the spike to moles desorbed.

52
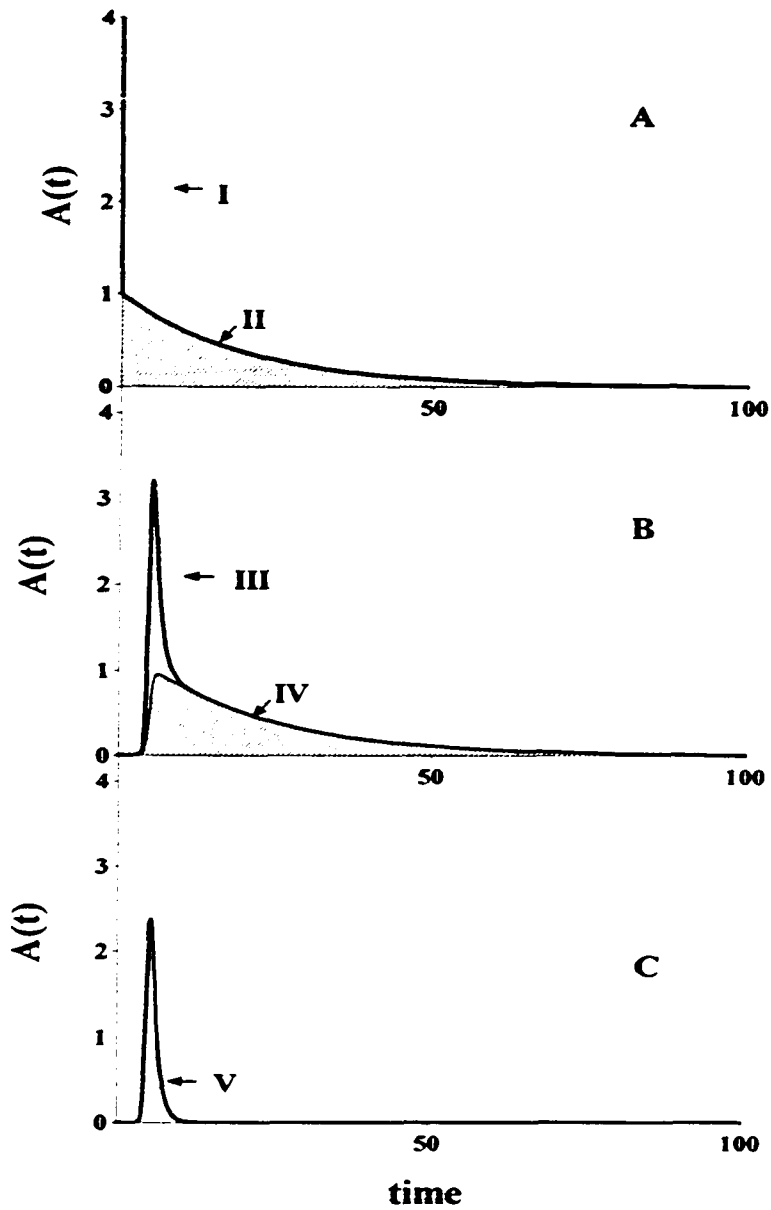
Fig 2.3 Simulations of curves associated with continuously monitored instantaneous

desorption rate of solute i from a shallow-bed in the type I instrument. (A) Idealized rate

curve including the spike of i from extraparticle spaces (I) and the curve for desorbed i

(II). (B) Observed rate curve showing displacement and band broadening of the spike

(III) and of the desorbed solute i (IV). (C) Observed peak for the IRF-Marker (V).

53

Figure 2.3 A is idealized. In reality the flow of solute between bed and detector requires time and, more importantly, the instrument components through which this flow occurs (*e.g.* bed outlet frit, connecting tubing, detector cell, detector time constant) produce instrument band broadening (*i.e.* solute zone dispersion) [54, 55]. The result of this is the solid line bounding the whole area in Fig. 2.3 B. The part of this plot that is associated with the desorbed portion of solute is shaded, just as it is in Fig. 2.3A, and it is labeled IV. The part associated with the broadened spike is not shaded and is labeled III.

2.2.2 Correcting for band broadening in Type I shallow-bed instrument

In order to obtain curve II from the whole of curve (III + IV) in Fig. 2.3B, the following strategy is employed. The desorption experiment described above is performed also on a solute which does not enter the particles in the bed and is not sorbed by them. Such a solute can be called the "impulse response function marker" (IRF-Marker). Curve V in Fig. 2.3 C is a simulated plot of A(t) *vs* t such as might be observed for an IRF-Marker. The center of gravity of this somewhat asymmetric peak is displaced from zero along the time axis by the transit time between the bed and the detector. It has a non-zero width as a result of the same instrument band broadening processes that are experienced by solute i. The IRF peak is used in two ways after its A(t) values are rescaled *via* multiplication by Eq. 2.22.

54

$$\text{Scaling factor} = \frac{V_{hu}[i]_{MP}\,\varepsilon_i}{V_{hu}[IRF]_{MP}\,\varepsilon_{IRF}}$$

(2.20)

In this equation V_{hu} is the hold-up volume of solution between the particles in the bed (it has the same value for both solute i and IRF-Marker); ε_i and ε_{IRF} are the molar absorptivities; and $[i]_{MP}$ and $[IRF]_{MP}$ are the concentrations of solute i and of IRF-Marker in the mobile phases that were used to pre-equilibrate the bed and which are therefore present in the hold-up volume at the beginning of the desorption step.

The re-scaled values of the IRF peak are first subtracted from the A(t) values of solute i in Fig. 2.3 B at corresponding times. The remaining difference is curve IV. The second use of the IRF peak is to deconvolve curve IV as described in the next subsection. Deconvolution yields curve II, which is the desired quantity.

2.2.3 Convolution and Deconvolution

Many signal-distorting effects which occur in nature and in instrumentation, can be described by mathematical convolution [87-90]. For example, when an unretained compound is injected as a very narrow zone into an HPLC column, it undergoes band broadening by several processes, such as longitudinal diffusion, non-linear flow profile in the channels between the packed particles, nonlinear flow profile in the connecting tubing and in the detector cell, etc. so that its elution is recorded by the detector not as a narrow

55

spike, but as a broader peak, often slightly asymmetric. Similar band broadening

processes occur when a solute leaves the shallow-bed and flows towards the detector,

though their relative contributions are different from those in an HPLC column.

Consider a sample zone which has some initial distribution of concentration vs. time $f_1(t)$

passing through a device which causes band broadening of the mathematical form $f_2(t)$.

Function $f_1(t)$ is the input function, while $f_2(t)$ is the impulse response function (IRF),

which is also called the instrument response function or the system response function.

The IRF describes the concentration-time distribution (or waveform) that would exit the

system if the input function had been an impulse, or a waveform of zero width. If the

input function $f_1(t)$ is not an impulse, but both it and the IRF, $f_2(t)$, are known beforehand,

then the shape of the waveform exiting the system through $C_{overall}(t)$ can be predicted by

performing the convolution of the two functions:

$$C_{overall}(t) = \int_{-\infty}^{\infty} f_1(t') f_2(t - t') dt' \qquad (2.21)$$

where

$$t' = t + t_c$$

and t_c is the center of gravity of the function f_2.

If one is dealing with experimental data in digital form, convolution can be performed

numerically. In this case the data for $f_1(t)$ and $f_2(t)$ should be obtained at equal time

increments Δt. The most computationally efficient way to perform convolution involves

the use of the Fourier transforms. Two functions can be convolved by taking the Fourier

56

transforms of $f_1(t)$ and $f_2(t)$, symbolized as $F_1(\upsilon)$ and $F_2(\upsilon)$, multiplying the two

transforms together, and then performing an inverse Fourier transform on the product to

obtain $C_{overall}(t)$. This operation is shown in Eq. 2.22 [87-90].

$F_1(\upsilon) \cdot F_2(\upsilon) = F_{overall}(\upsilon)$ (2.22a)

$F_{overall}(\upsilon) \rightarrow$ inverse FT $= C_{overall}(t)$ (2.22b)

Conversely, if one knows the IRF function $f_2(t)$, and the final waveform $C_{overall}(t)$, but one

doesn't know the input function $f_1(t)$, it is possible to obtain $f_1(t)$ by the process of

deconvolution. Deconvolution of digital data is also performed efficiently through

Fourier transformations. In this case the Fourier transform of $C_{overall}(t)$ is divided by the

Fourier transform of f_2 to obtain the Fourier transform of $f_1(t)$. An inverse transformation

then yields the input function $f_1(t)$ [87-90].

$F_{overall}(\upsilon)/ F_2(\upsilon) = F_1(\upsilon)$ (2.23a)

$F_1(\upsilon) \rightarrow$ inverse FT $\rightarrow = f_1(t)$ (2.23b)

This procedure can also be applied to obtain $f_2(t)$ when only $C_{overall}(t)$ and $f_1(t)$ are known.

Convolution of two functions of areas a1 and a2 will result in $C_{overall}(t)$ with the area

which is the product of a1 and a2. Likewise, during deconvolution of $C_{overall}(t)$ with $f_2(t)$,

the resulting area will be the result of division of the area of $C_{overall}(t)$ by area $f_2(t)$, a2.

57

Therefore, the area under the curve of the IRF, or $f_2(t)$, should be made equal to 1 before convolution/deconvolution is done.

In the case considered in the previous section, it is curve IV of Fig 2.3 B which is considered as the $C_{overall}(t)$, while the IRF, or $f_2(t)$, is obtained by injecting a pulse of an IRF-marker compound, exemplified by curve V in Fig 2.3C. We can therefore extract $f_1(t)$, which is curve II of Fig 2.1A by deconvolving curve IV with curve V of Fig 2.3 C. Prior to deconvolution, we have to normalize curve V so that its area is equal to one.

Frequency filtering in Deconvolution

One problem encountered in performing deconvolution is the effect of noise. Fig. 2.4 A shows an observed waveform for a desorbed solute, and Fig. 2.4 B shows an experimentally measured IRF waveform, normalized to make its area equal to 1. Shown in panels 2.4 C and 2.4 D are the absolute magnitudes of their respective Fourier transforms. (Fourier transforms yield complex numbers; *i.e.* numbers with real and imaginary terms. For simplicity only the overall magnitude is shown in Fig 2.4. The magnitude is obtained by multiplying each complex number by its complex conjugate and taking the root of the product.) We see that a typical FT has its largest value at frequency of zero Hz (which corresponds to the area under the curve in the time domain), and it decays slowly towards zero at higher frequencies. Every measurement carries with it a random uncertainty, or noise, which is also present in its Fourier transform. When the amplitude of the Fourier Transform falls towards zero, noise dominates it, and

58
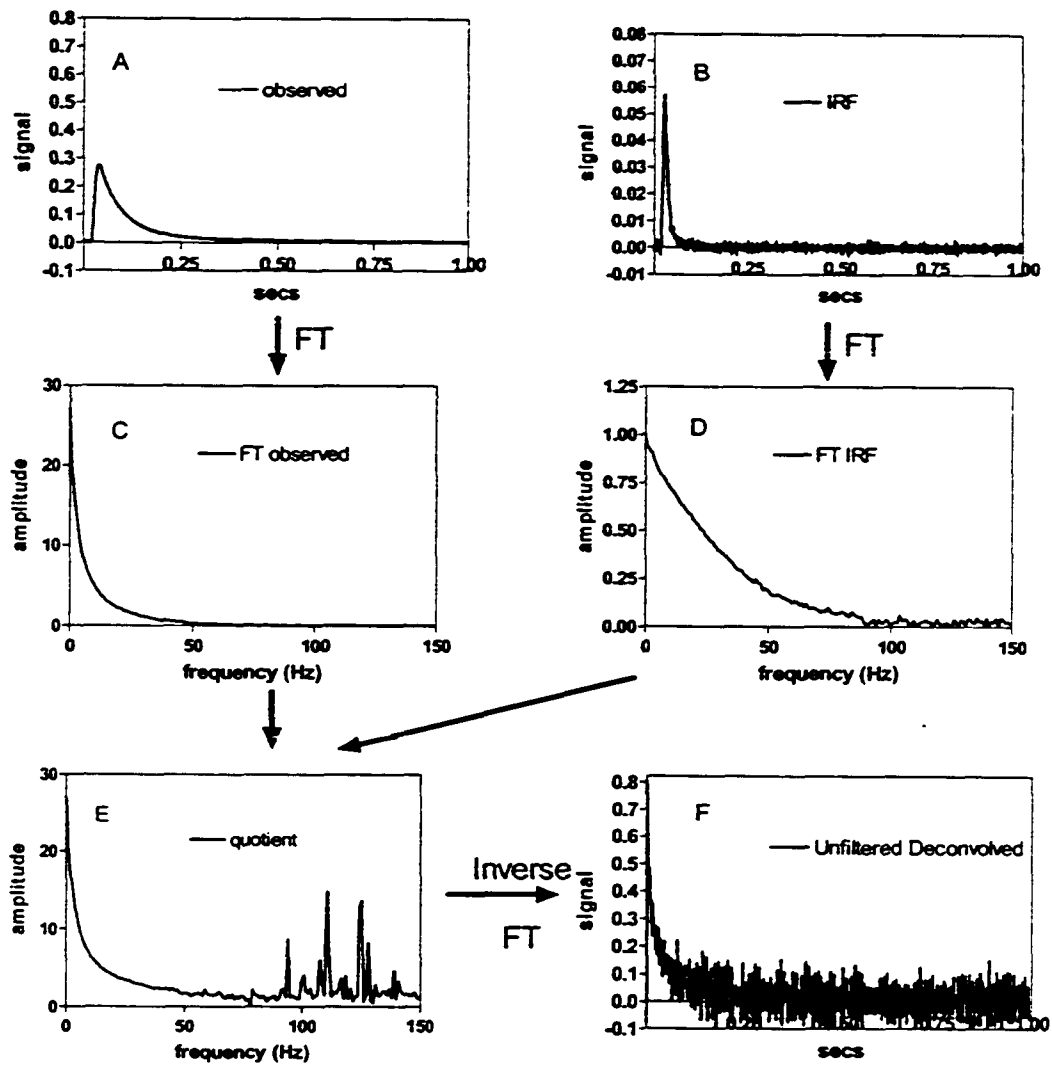
Fig 2.4. Deconvolution using Fourier transformation (FT) without filtering. (A)

experimental C(t)overall. (B) experimental IRF peak $f_2(t)$ normalized to give area of 1.

(C) and (D) Amplitudes of the Fourier Transforms of panels A and B, respectively. (E)

the result of the division of FT from panel C by FT from panel B; (F) The result of

inverse FT of the quotient, the amplitude of which is shown in panel E. All Fourier

spectra have been cut off at 150 Hz for better viewing, but they go up to 1000 Hz.

59

the amplitudes range from zero to some upper value in a random fashion (i.e. independent of the frequency value). The problem in deconvolution arises when one spectrum is divided by another, because in some cases division by very small numbers takes place, giving rise to very large magnitudes at (random) high frequencies. This is illustrated in Fig 2.4 E, where the results of the division show random high values at frequencies above 70 Hz and, especially, after 90 Hz. When such a noisy quotient is taken through the inverse FT, the resulting function is plagued by high - frequency noise, as seen in Fig 2.4 F. This is the reason why frequency filtering has to be performed in the Fourier domain. Fig 2.5 shows the exact same steps as Fig 2.4, up to and including panel E. Shown in Fig. 2.5 F is a frequency filter with which the noisy FT in Fig 2.5 E will be multiplied. The filter has a value of 1 until the frequency of 50 Hz, after which the values decrease in a linear fashion until they become zero at 70 Hz. This is called a trapezoidal filter, and it can be described mathematically by the coordinates of its corner points {(0, 1) ; (0, 1) ; (50,1) ; (70, 0) }, where the first number denotes the frequency and the second number denotes the filter value at that frequency [88]. After applying (multiplying by) this filter, low frequencies are unchanged, while the parts of the FT where noise dominates are multiplied by zero. The product of this multiplication can be seen in Fig 2.5 G. When the inverse FT is performed on it, the resulting deconvolved function is much smoother than in the absence of filtering (*i.e.* compare Fig 2.5 G with Fig 2.4 F).

The reason why the filter is a trapezoidal function and not a simple square cut-off, such {(0, 0) ; (0, 1) ; (50,1) ; (50 , 0) } is because the trapezoidal works better in the sense that

60
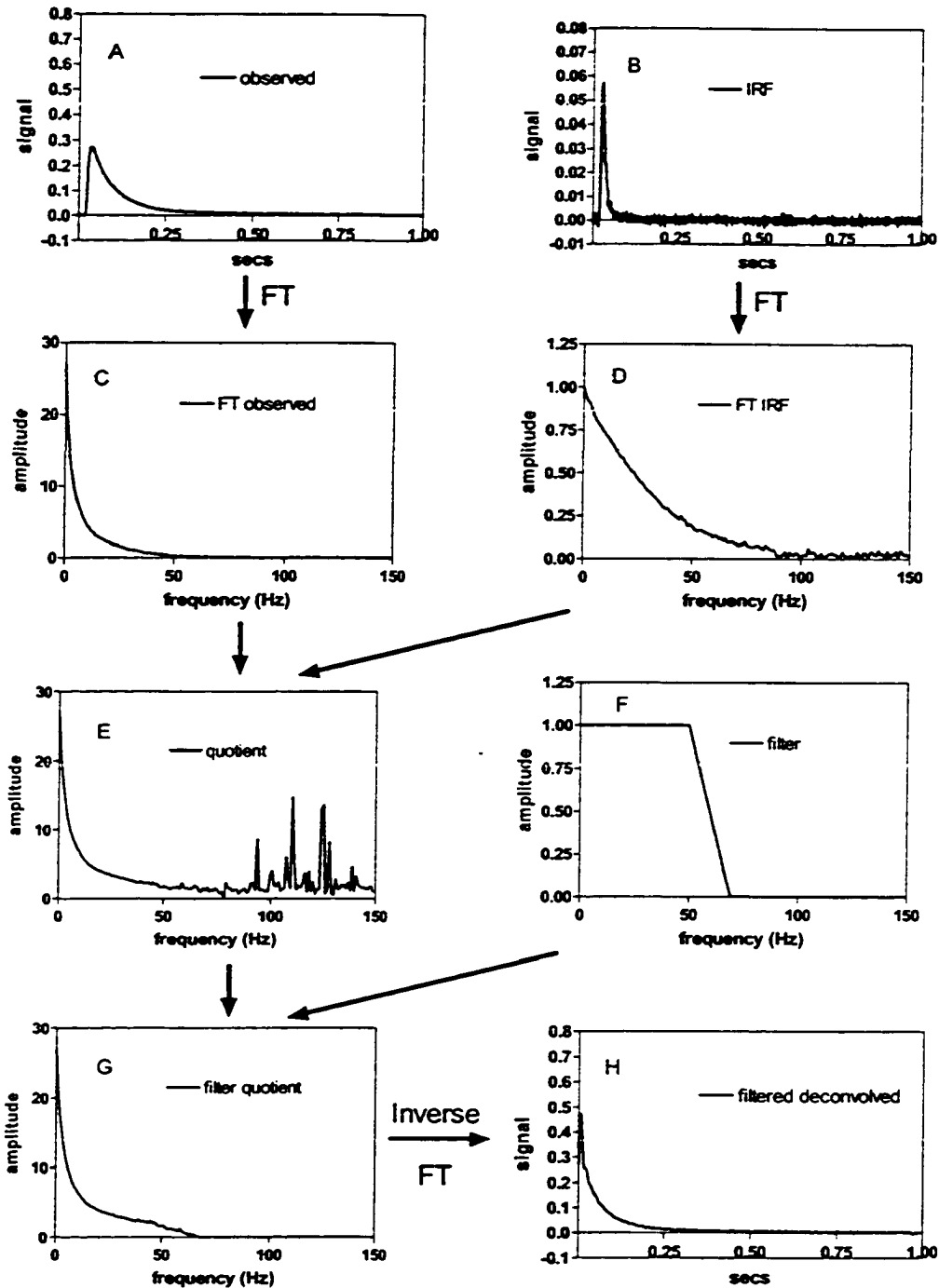
Fig 2.5. Deconvolution using Fourier transformation (FT) and frequency filtering. (A-E)
Exactly the same as in Fig 2.4. (F) The spectrum frequency filter function (only made up
of real numbers). (G) The result of complex multiplication of the quotient in panel E by
the filter in panel F (H) The result of inverse FT of the filtered quotient, the amplitude of
which is shown in panel G. All Fourier spectra have been cut off at 150 Hz for better
viewing, but they go up to 1000 Hz.

61

a sharp cutoff filters generate "ringing noise" in the deconvolved function[87] while trapezoidal filters reduce this.

2.2.4 Effects of band broadening in Type II Shallow-bed Instrument

In Fig. 2.6 is shown an idealized version of the observed instantaneous rate curve which can be expected under conditions shown in Fig 2.2. In this version of the desorption experiment the solute is passed through the shallow-bed and the detector until equilibrium is achieved. During this equilibration step, the signal rises until it reaches a plateau, corresponding to the full concentration of solute passing through the shallow-bed and detector. (The rise in concentration until plateau is reached is not shown in Fig. 2.6.) Then, the flow is switched by means of an upstream valve system so that instantly solute-free solvent starts flowing through the bed (start time). The pure solvent displaces the solute-containing solution that is present around the packing particles in the shallow-bed and in the tube between the shallow-bed and the detector, and it initiates desorption of solute from inside the particles. Fig. 2.6 A shows what the detector would see in a system where band broadening would be absent. It takes a finite time (e.g. tens of milliseconds) for the solvent front to reach the detector. Until then, even though the fluid is moving past the detector, the concentration passing through it is still at its plateau value. At the time where the front of solvent reaches the detector, the concentration of solute originally present outside of the particles would rapidly decrease to zero. This time should be marked as the zero time for the kinetic run, and the amount of time between the start time and zero time can be called the delay time.

62
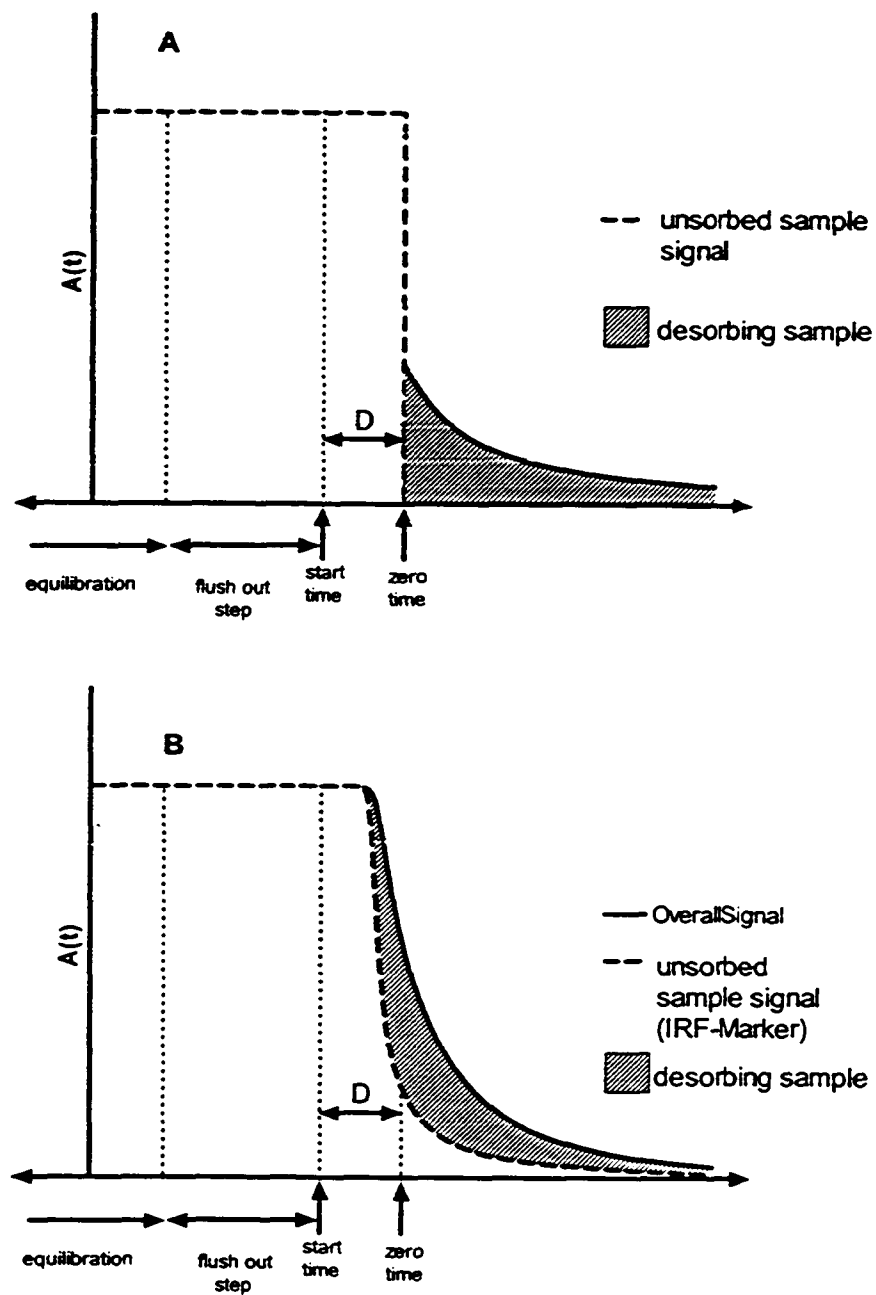
Fig 2.6 Simulations of curves associated with continuously monitored instantaneous desorption rate of solute i from a Type II shallow-bed instrument. (A) Idealized rate curve including the drop-off of i from extraparticle spaces (dashed line) and the curve for desorbed i (shaded area). (B) Observed rate curve showing displacement and band broadening of the drop off (dashed line) and of the desorbed solute i (shaded area)

As the extra-particle solute is displaced from the shallow-bed, the solute inside the packing starts desorbing and is carried by the solvent towards the detector. In the imagined system with no band broadening, this desorption signal would get to the detector at the same time as when the signal from the displaced solute dropped down to zero. Overall, after the "start time"one would see a delay time where the signal would remain at the plateau value, followed by a sudden drop, after which the only signal seen would be the desorption signal. In such and idealized, dispersion-less system neither the solute molecules originally present between the particles nor those originally present between the shallow-bed and the detector interfere with the signal from the actual desorbing solute. The real life situation includes dispersion, where both the sharp drop-off in signal and the desorption signal are broadened with respect to time. This causes the signal from the desorbing molecules to overlap with the signal from the sample present outside of the packing. Furthermore, the true zero time is not visually identifiable anymore. Such a more realistic example is shown in Fig. 2.6 B.

2.2.5 Correcting for band broadening in Type II shallow-bed experiment, including deconvolution

In order to obtain the shaded part of Fig 2.6 A (*i.e.* the desorption curve) from the whole of Fig. 2.6 B, the following strategy is employed. The desorption experiment described above is performed at the same flowrate on an IRF-Marker, just as in case 1. The desorption curve of the IRF-Marker (*i.e.* IRF-Marker curve) will look like the dashed curve in Fig. 2.6 B, provided that it is first scaled as shown by Eq. 2.24 :

$$\text{Scaling factor} = A_{0,i} / A_{0,IRF\ marker} \tag{2.24}$$

where $A_{0,i}$ is simply the absorbance of the equilibrating solution of solute i, and $A_{0,IRF}$ is the absorbance of the equilibrating solution of the IRF marker. These values are easily obtained by measuring the difference between the plateau absorbance at the start time and the baseline absorbance value which is obtained at the end of the run. (NOTE: the end of the run is not shown in Fig. 2.6) The IRF-Marker curve is used in two ways. First, after re-scaling, it is subtracted from the overall A(t) values of the solid-line curve for solute i in Fig. 2.6 B at corresponding times. This subtraction gives the shaded part of Fig. 2.6 B, which is the broadened desorption signal. This step is analogous to what is done for data from the Type I instrument.

The second use of the dashed IRF-Marker curve is to generate an IRF (*i.e.* a peak) in order to deconvolve the shaded part of Fig. 2.6 B. The IRF-Marker curve cannot be used directly as the IRF, because it wasn't injected into the system, such as in the Type I instrument, but rather it is the rear boundary of a frontal zone. In engineering literature, the shape of a frontal chromatogram resulting from a step input, which is normalized so that its plateau value is equal to 1, is called the F-curve [55, 91]. The shape of the IRF (which is called the E-curve, or the C-curve in engineering literature [55, 91]) is mathematically related to the F-curve by the expression :

$$IRF = (E\text{-}curve) = \frac{d(F\text{-}curve)}{dt} \tag{2.25}$$

65

In other words, since an elution peak is proportional to the E-curve and a frontal breakthrough is proportional to the F-curve, an elution peak is proportional to the derivative of a breakthrough curve. In our case, however, the IRF–Marker curve is analogous to the reverse edge of the breakthrough curve in frontal chromatography, so a negative sign is needed:

$$F\text{-curve} = (-1) \cdot IRF\text{-Marker curve} \qquad (2.26)$$

Equation 2.26 is valid when the IRF-Marker curve is scaled in such a way that the plateau value is equal to 1 and the final value is equal to zero [55, 91].

Thus, to obtain the IRF:

$$IRF = (E\text{-curve}) = (-1) \cdot \frac{d\,(IRF\text{-Marker curve})}{dt} \qquad (2.27)$$

Once the IRF is obtained via Eq. 2.27, deconvolution and filtering are carried out on the shaded part of Fig 2.6 B, as described in section 2.2.3 in order to obtain the shaded part of Fig 2.6 A which is the corrected desorption rate curve. The deconvolution process is the same as what is done for data from the Type I instrument.

2.2.6 Obtaining a cumulative (integral) desorption rate curve from the corrected instantaneous rate curve

So far in section 2.2, for both the Type I and Type II instruments, the topic has been to correct the observed instantaneous desorption curve of A(t) vs t for the effects of band broadening and noise. As discussed, the proper way to extract the true instantaneous desorption curve is to perform the same experiment on an unretained, excluded solute, called the IRF-Marker. The IRF peak is then used to perform two tasks. In the first operation it is subtracted, after appropriate scaling from the overall observed curve. In the second step it is used to deconvolve the difference of the subtraction. These two operations yield the true desorption absorbance signal A(t) as it would be observed if no band broadening were present.

This corrected absorbance signal is a function of the instantaneous (i.e. differential) molar desorption rate of the solute (dn_i/dt), of the molar absorptivity of the solute ε (L $mol^{-1}cm^{-1}$), of the pathlength of the detector cell l (cm) and of the flowrate F (L/sec) through the bed as shown in Eq. 2.28:

$$A(t) = \frac{\dfrac{dn_i(t)}{dt} \times \varepsilon l}{F}$$

(2.28)

In order to transform a corrected, instantaneous, experimentally-measured plot of A(t) vs t into a cumulative (i.e. integral) desorption rate curve it is necessary to integrate Eq. 2.28, as shown in Eq. 2.29. Here $n_i(t)$ is moles of i desorbed by elapsed time t, which increases with time.

67

$$n_i(t) = \frac{F}{\varepsilon l} \int_0^t A(t)dt \tag{2.29}$$

It is after this operation that we obtain the cumulative sorption/desorption rate curves which can be fit by the rate equations of Section 2.1

2.3 Effect of experimental factors on the experimental instantaneous desorption rate curves

In the following section we discuss the issue of how the absorbance signal observed in a continuous monitoring experiment is affected by various parameters, such as the strength of retention, flowrate, the diffusion coefficient inside the particles and the particle radius. We will consider the case where the desorption process is governed by spherical diffusion. In order to predict the effects of various experimental parameters on the observed plot of A(t) vs t when spherical diffusion prevails, Eqs. 2.1, 2.2 and 2.28 can be combined to give:

$$A(t) = \frac{6 \beta \kappa_i [i]_{MP} m_{SB} \varepsilon_i l}{F\pi^2} \sum_{j=1}^{\infty} e^{-j^2\beta t} \tag{2.30}$$

Equation 2.30, like Eq. 2.1, contains the sum of an infinite series of exponential terms. The accuracy with which Eq. 2.30 represents A(t) at shorter and shorter times improves with the number of terms employed. Here it should be noted that if an infinite number of terms could be used Eq. 2.30 would give a numerical value of infinity for A(t) at time zero. It is of course impossible to calculate an infinite number of terms, so a sufficiently large, but finite number of terms must be employed. The value of infinity for the

68

instantaneous desorbing concentration at time zero is also physically impossible, since film diffusion is never negligible at very short times, so it would become the rate-determining process [50, 51].

Examples of the predicted effects of various experimental parameters on the instantaneous rate curve are shown in Fig. 2.7. The parameters are chosen so that the resulting absorbance closely matches that which is experimentally seen in a system studied in Chapter 3, where the desorption is slow and it takes more than 90 minutes to go to completion. For that system, the use of the first twenty terms in Eq. 2.30 assures that the values of A(t) at and above 15 seconds time have negligible error. Thus, the plots in Fig 2.7 all begin 15 seconds after the start of desorption, as justified by the use of twenty terms in Eq. 2.30. In Fig. 2.7A it is seen that the value of A(t) at any given time is directly proportional to the value of κ_i. The same is true of A(t) with respect to the parameters $[i]_{MP}$, m_{SB}, ε_i and l, all of which appear in the numerator of Eq. 2.30. In Fig. 2.7 B it is seen that a slower flow rate gives a larger signal. Although the area under the curve changes inversely with the flow rate, this change does not reflect the amount of solute in the packing since it is compensated by F in the denominator of Eq. 2.30.

The effects of solute diffusion coefficient (Fig. 2.7 C) and of particle radius (Fig. 2.7 D) are mediated *via* the parameter β, which is defined in Eq. 2.3. A larger value of D_i produces both a higher concentration of desorbed solute and a sharper drop off of A(t) with time. At later desorption times the curves for solutes with higher values of D_i cross over those with lower values since the faster desorption processes decay to zero earlier

69
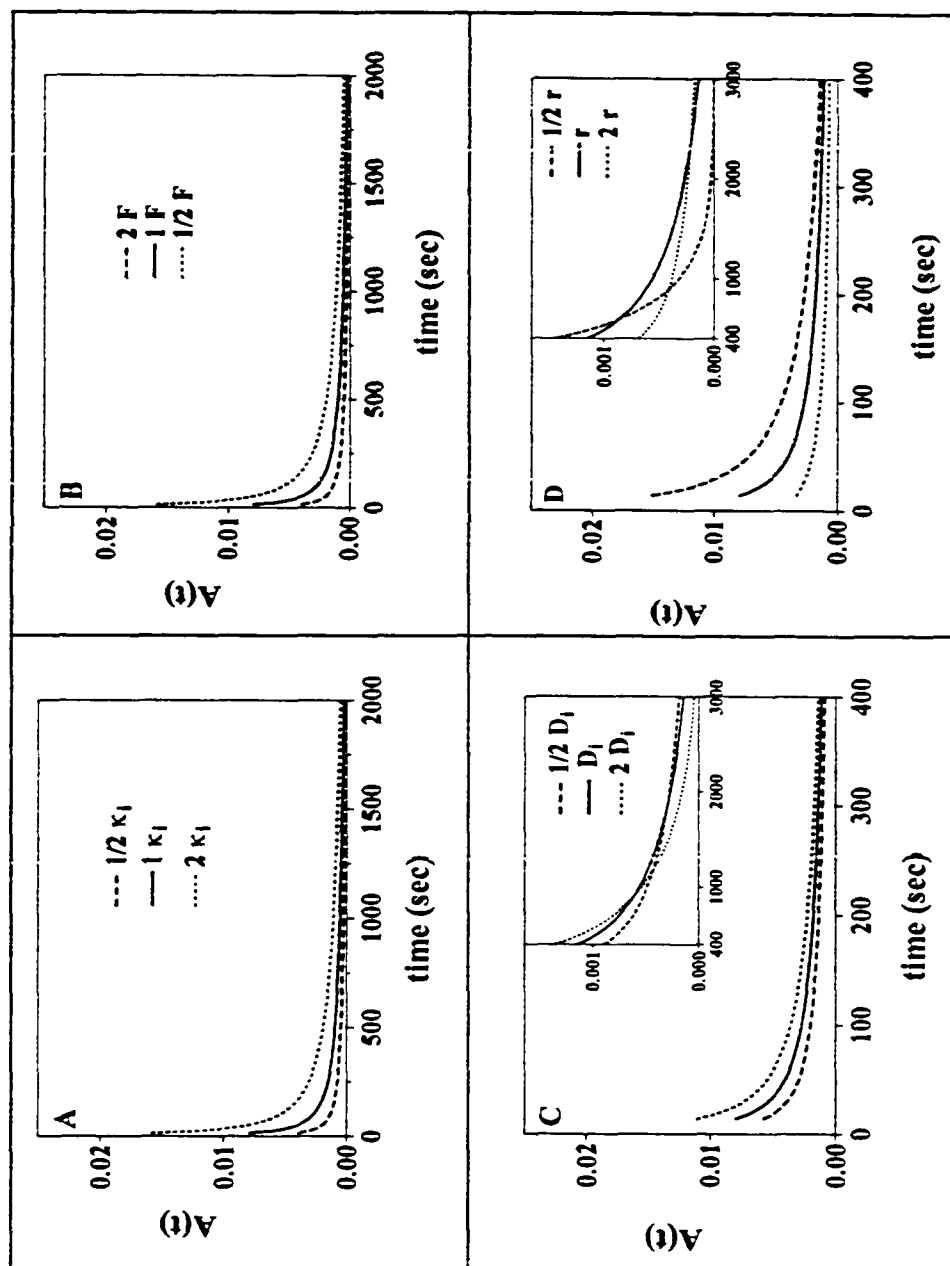
Fig 2.7. Predicted effects of varying experimental parameters on instantaneous desorption rate curves calculated with Eq.2.30. The parameters with their default values are as follows: (A) κ_i (0.1 L/g), (B) F (0.0833 mL/sec through a 0.3-cm diameter bed); (C) D_i (6.0 × 10^{-11} cm^2/sec); (D) r (1.0 × 10^{-3} cm). In each panel the solid line is calculated using all default values. Values of non-varied parameters are m_{SB} (2.5 mg); $[i]_{MP}$ (1.6 × 10^{-4} M); ε_i (5000 M^{-1} cm^{-1}); detector cell pathlength, l (1.00 cm). Points from the first 15 sec of each curve are omitted because only 20 terms were used in Eq. 2.32.

70

than the slower ones. This is portrayed in the inset in Fig. 2.7 C. A smaller radius of the packing particles, r, increases β by an inverse square relationship (Eq. 2.3). The resulting effect, shown in Fig. 2.7 D, is more pronounced than that of D_i because r is squared. The area under the A(t) vs t curve is independent of both D_i and r.

If the particle desorption rate was governed by film-diffusion, the combination of Eqs 2.6, 2.2 and 2.28 would yield a decay curve of only a single exponential:

$$A(t) = \frac{k\,\kappa_i\,[i]_{MP}\,m_{SB}\,\varepsilon_i}{F}\,e^{-kt} \tag{2.31}$$

where k is given by Eq. 2.6b. The effect of κ_i and flowrate on the absorbance signal would be the same as above in Fig 2.7 A. The diffusion coefficient inside the stationary phase D_i is absent because it is not involved when film-diffusion is rate controlling. Instead, the diffusion coefficient in the mobile phase D_{MP} assumes its role. The effect of D_{MP} will be analogous to that of D_i, as seen in Fig 2.7 C. The effect of the film thickness δ and radius, predicted by k from Eq. 2.6b, is analogous to the effect of r in Eq. 2.30, but not as pronounced, since there is no inverse square relationship.

2.4 Non-ideal shallow bed conditions

Ideally, the achievement of shallow-bed conditions for a desorption process requires that the eluent leaving the bed should contain zero concentration of solute i. Of course this

71

condition cannot be met because the desorbed solute molecules produce a non-zero solute concentration in the flowing eluent. Furthermore the technique depends on this concentration becoming high enough to be experimentally measurable. In practice, shallow-bed conditions can be closely approximated by ensuring that the maximum solute concentration in the flowing eluent never exceeds a small fraction of the concentration that was used initially to produce sorption equilibrium, also called the loading concentration (*i.e.* $[i]_{MP}$ in Eqs 2.2, 2.20 and 2.30). However, when the flow-rate becomes too low, the desorbing solute is not removed fast enough and its concentration in the mobile phase increases to high values, which decreases the driving force for the desorption process. This has the effect of slowing down the observed desorption rate. When studying very fast desorption rates, it can be difficult to achieve flowrates fast enough that the solute concentration in the flowing eluent doesn't exceed a small fraction of the feed concentration. Therefore, the observed curve may be slower than the true process – i.e. the kinetic parameters obtained by fitting the desorption curve with theoretical equations such Eq. 2.1 will be smaller than the true values.

The expression below gives the shape of the cumulative rate curve which applies for spherical particles whether the flowrate is sufficiently fast or not. It was developed under the assumption that the solute concentration in the solvent flowing past the bed is the same everywhere in the bed [72-74, 77]:

$$n_i(t) = n_{i,0}\left(1 - \sum_{n=1}^{\infty} \frac{6\,L^2 \exp\left(-\alpha_n^2\,D_i\,t/r^2\right)}{\alpha_n^2\left[\alpha_n^2 + L(L-1)\right]}\right)$$

(2.32)

72

where α_n is given by the roots of the equation:

$$\alpha_n \cot(\alpha_n) + L - 1 = 0 \qquad (2.33)$$

and

$$L = \frac{F[i]_{MP} \, r^2}{3 \, n_{i,0} \, D_i} \qquad (2.34)$$

The parameter L above is simply a measure of the ratio of the flowrate through the shallow bed to the desorption rate constant in the spherical particle. If L is a large number, the flow through the shallow bed is able to remove the desorbing solute almost instantly, and Eq. 2.32 reduces to the same form as Eq. 2.1. In other words, large values of L mean that shallow bed conditions are met. A small value of L signifies failure to meet shallow-bed conditions, where the flow cannot remove the solute leaving the particle fast enough and the whole process is slowed down. Simple experimental ways to increase the value of L are either to increase the flowrate, or to decrease the value of $n_{i,0}$ by decreasing the amount of stationary phase in the shallow bed.

There is an important second case however, where fitting the cumulative rate curve data to Eq. 2.32 can yield low values of L even if shallow-bed conditions *are* met. The phenomenon of film diffusion, discussed in Section 2.1.2, can also slow down the desorption rate and thus can independently give rise to the low value of L. In this case L is redefined as [72, 73]:

$$L = \frac{Sh\,[i]_{MP}\,D_{MP}}{2[i]_{part}\,D_i}$$

(2.35)

In Eq. 2.35 L is a measure of relative resistances to mass transfer of intraparticle diffusion to film diffusion, and it is related to parameter X of Eq. 2.14 and parameter θ in Eq. 2.15. If L is high, it means that film diffusion is negligible (fast) comparing to intraparticle diffusion. Conversely, a low value of L means that film diffusion significantly contributes to desorption rate control. If film diffusion is the major cause of the slow-down of the desorption process, then the value of L can be predicted, by substituting the expression for Sh from Eq. 2.12, or 2.13. Thus the value of L can be predicted as:

$$L = \frac{1.09}{\varepsilon_{inter}} \left(\frac{2\,u_s\,r}{D_{MP}} \right)^{1/3} \frac{[i]_{MP}\,D_{MP}}{2[i]_{part}\,D_i}$$

(2.36)

if Eq.2.12 is used for Sh, or:

$$L = \frac{1.09}{\varepsilon_{inter}} \left(\frac{2\,u_s\,r}{D_{MP}} \right)^{1/3} \frac{[i]_{MP}\,D_{MP}}{2[i]_{part}\,D_i}$$

(2.37)

if Eq. 2.13 is used for Sh. The only way to increase L is to increase the Sherwood number by increasing the flowrate (which is proportional to velocity u_s in the above equations). However, the Sherwood number is proportional to only $(velocity)^{1/3}$.

If Eq. 2.32 is fit to desorption rate data and a low value of L is obtained, it may be of interest to determine whether the low value of L is due to failure to meet shallow bed

74

conditions or film diffusion. This can be done by obtaining desorption rate data at several flowrates, fitting with Eq. 2.32 to obtain the value of L at each flowrate, and plotting L vs. flowrate. If slow flowrate is the cause, then the value of L should be directly proportional to flowrate, in accordance with Eq. 2.34. If film diffusion is the cause then L should be proportional to (flowrate)$^{1/3}$ in accordance with the Eq 2.36 or Eq. 2.37. Also, if film diffusion is the cause of low L, the magnitude of the predicted value of L, according to Eq 2.36 or Eq. 2.37 above, should be close (i.e. within experimental error) to the value of L obtained from fitting the kinetic data with Eq. 2.32. In the case where film diffusion is the main distorting mechanism, Eq. 2.32 and 2.35 can serve as an alternative to Eq. 2.15.

Fig. 2.8 shows the effect of L on the observed, cumulative desorption curves of a process which proceeds via spherical diffusion, with a value of β = 1. Curves are calculated for different values of L via Eq. 2.32. When the value of L is greater than about 25, the observed curve matches Eq. 2.1 closely, but lower values of L show significant deviations. Table 2.1 shows the results of fitting the curves calculated with Eq. 2.32 to Eq 2.1, and the errors involved with such an analysis. For example, when L = 6, the R^2 value for the goodness of fit is only 0.983, and the best fit value of β is only 55 % of its true value. When L = 25, the R^2 value is about 0.999 and the best fit value of β is about 87% of the true value.

75
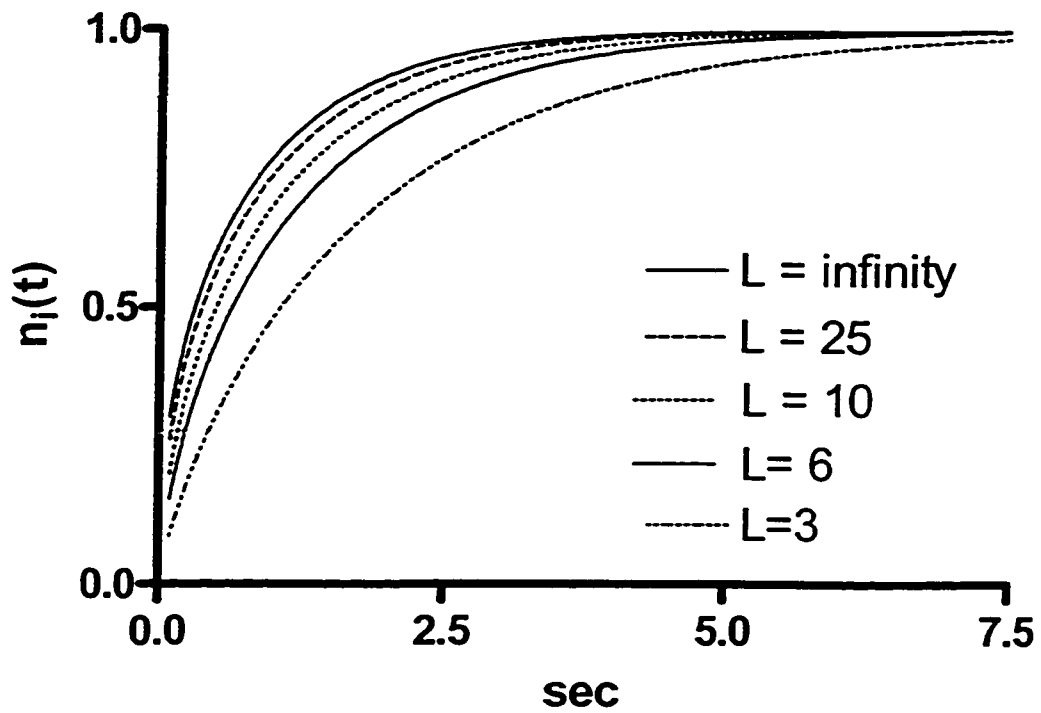
Fig. 2.8. Effect of parameter L in Eq. 2.32 on the cumulative desorption rate curve. The top curve follows Eq 2.1 (L = infinity) with a value of $\beta=1$. More details are given in the text and Table 2.1

76

Table 2.1. Errors arising from fitting data simulated by Eq 2.32, shown in Fig. 2.8, with Eq. 2.1 for different values of L.

L	$D_{i,fit} / D_{i,true}$ [a, b]	$n_{i,0,fit} / n_{i,0,true}$	R^2
3	0.313	1.05	0.9746
6	0.5569	1.012	0.9877
10	0.6933	1.005	0.9944
16	0.7936	1.003	0.9974
25	0.8635	1.002	0.999
∞	1	1	1

[a] The subscript true, signifies the value of D_i which was input into Eq. 2.32 to generate a set of simulated data. The subscript "fit" is the resulting fitting parameters from fitting Eq. 2.1 to the simulated data.

[b] The "fit" parameters will vary slightly with different ranges of time-values chosen to be fit.

Chapter 3.[a] Desorption rate of naphthalene from PRP-∞ using Type I instrument

This chapter describes in detail the Type I shallow-bed apparatus for the continuous measurement of slow desorption kinetics, and the results obtained for the desorption of naphthalene (NA) from polymeric particles of PRP-∞ in 70/30 methanol/water solvent. The purpose of this work is to apply the theoretical ideas from section 2.2 and 2.3 to a real system. As well, the desorption-rate data obtained are compared with the sorption-rate data from literature in order to validate the method.

3.1 Introduction

3.1.1 Structure of PRP- ∞

PRP - ∞ is a spherical, polymeric sorbent made up of a solid, nominally nonporous matrix of PS-DVB. This matrix is heterogeneous with respect to crosslinking density, chain density and swelling properties. The following structure has been proposed [47, 49, 71]: there is a very large number of very small, closely spaced nuclei (or "nodules") throughout the polymer particle. The cross-linking density is highest within the nuclei

---

[a]   Most of Chapter 3 is taken from "Continuous Desorption Rate Measurement from a Shallow-bed of PS-DVB Particles With Correction for Experimental Artifacts", R. Bujalski, and F.F. Cantwell, J. Chromatogr. A (2004) Volume 1048, pages 173-181.

78

and decreases with distance from the nuclei. There is thus a gradient of crosslinking density from the center of each nucleus to the internuclear region. Because the cross-linking density is highest within the nodules, they have the greatest rigidity and contain a larger number of permanent micropores. The internuclear regions have a much lower crosslinking density and are much more flexible. They are referred to as a gel. Thus PRP- ∞ displays both micropore regions and gel regions. In the dry state, with no sorbed organic solvent, the gel regions of the matrix collapse completely so that there are the smallest possible spaces between the individual chains. Micropore regions, however, are unable to collapse and retain their permanent structure. Once an organic solvent is added though, the gel regions become swollen and have larger interchain pore spaces than do the micropore regions, which do not swell appreciably.

3.1.2 Diffusion of NA in PRP - ∞ matrix

The nominally nonporous matrix of PRP - ∞ is accessible to solutes whose solubility parameter (sol. par.) is similar to that of PS-DVB (sol. par. = 18.6-19.0 $(MPa)^{1/2}$) [49, 71, 92, 93]. NA, with a solubility parameter of 20.2 $(MPa)^{1/2}$ [49] can enter the polymer matrix and diffuse within it. Polar compounds have high solubility parameters (e.g. H_2O sol. par. = 47.9 $(cal\ cm^{-3})^{1/2}$ [47, 71]) and do not enter the PS-DVB matrix.

As described above, PRP - ∞ is actually heterogeneous with regard to crosslinking density, swelling, and the amount of permanent microporosity. NA can thus diffuse through roughly two types of environments – microporous and gel like. However, the

79

distances between the centers of the polymer nuclei are so small that an average value of D_i has been observed [28, 71], showing that, on the scale of the whole particle, the matrix can be assumed to be a homogenous medium.

3.1.3 Reasons for choosing the desorption of NA from PRP - ∞

The kinetics of sorption of naphthalene into the polymeric sorbent PRP-∞ from methanol/water solutions have been studied by the shallow-bed method in the literature [28, 71], and are known to proceed through slow intraparticle diffusion. The fact that the diffusion of NA inside the PS-DVB is slow means that it is relatively easy to build an apparatus capable of measuring it. The extra-column band-broadening can be relatively large, because the duration of the desorption process (more than 90 minutes for completion) is much larger than the duration of the effects of band broadening (the width of the IRF in the experimental section will be seen to be on the order of 10 seconds). The contribution of extra-shallow-bed band broadening can thus be easily accounted for by deconvolution, even if only limited steps have been taken to limit the extra-bed band broadening.

The fact that the sorption kinetics of NA on PRP-∞ are well characterized is an added advantage, because previously obtained kinetic data serve as a check on the results obtained with the present, desorption technique. The sorption rate curve of NA onto PRP-∞ fits the spherical diffusion equation (Eq. 2.1) [28, 71]. The kinetics of desorption are expected to proceed through the same process in reverse and to yield the same kinetic

80

data, *i.e.* the desorption will proceed through spherical diffusion with the same intraparticle diffusion coefficient, provided that the mobile-phase in which the PRP-∞ is bathed is the same. If the desorption data agree with the sorption data, it will be taken as evidence for the validity both of the method of continuous monitoring of desorption from the shallow-bed and of the data processing steps involved.

3.2 Experimental

3.2.1 Reagents, solvents and resin

NA (Coleman and Bell, Norwood, OH) was recrystallized from methanol. Phloroglucinol (PG) (1,3,5-trihydroxybenzene, Fisher) was recrystallized from water. Methanol (MeOH) (certified ACS grade, Fisher) was distilled before use. Water was distilled and deionized with a NANO-pure System (Barnstead, Boston, MA). The eluting solvent, 7/3 MeOH/H$_2$O, was prepared by combining solvent volumes in this ratio. NA and PG solutions were also prepared in 7/3 MeOH/H$_2$O with the individual concentrations of NA as given in Table 3.1 (See Section 3.3.3). The PG concentration was 11.0 mM. The batch of PRP-∞ sorbent employed in this study has a diameter of 19 ± 1 μm [28, 71, 94] (batch EE2, Hamilton, Reno, NV, USA).

81

3.2.2 Apparatus and procedure

Plots of A(t) *vs* t were measured using a Type I continuous monitoring shallow-bed apparatus, the schematic of which is described in Chapter 2, section 2.2 and Fig 2.1. In the Type I instrument, the shallow-bed is equilibrated with the solute-carrying solvent in one flow channel, and then the slider containing the shallow-bed is moved to a second flow channel, which carries only the pure solvent. The flow of the pure solvent causes desorption and the eluent flows towards the detector. The details of the apparatus are shown in Figs. 3.1 and 3.2. Pump P1, which delivers the NA solution, and pump P2, which delivers the eluent, are pulseless constant-pressure pumps operated at 50 psi (3.4 bar) [95]. Pump P3, which delivers the PG solution, is an HPLC pump (Waters 591, Milford, MA). All pumped solutions were thermostated at $25 \pm 0.5°C$. The slider valve, V_{SB}, which is shown in Fig. 3.2, contains the shallow-bed of PRP-∞ (between 2 and 3 mg accurately weighed). It is a modified version of a valve that was previously used in sorption rate studies [28, 46, 71]. In the present modification the left outlet flow channel has been tapered at an angle of 30 degrees from 3.0-mm i.d. to 0.75-mm i.d. starting at a distance 1 cm below the bed. This was done in order to reduce the volume between the shallow-bed and the detector while at the same time maintaining parallel flow streamlines of eluent through the bed during desorption. V_{SB} enables switching of the bed between the loading and the desorption positions.

82
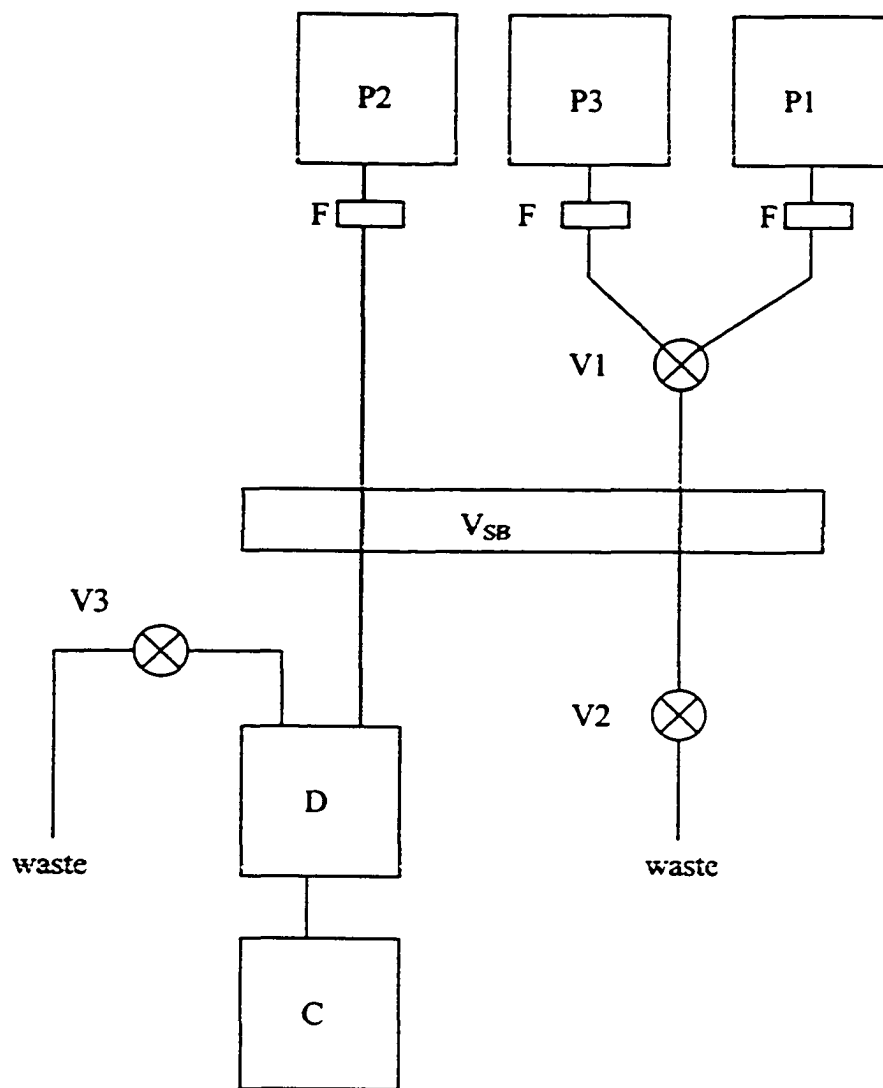
Fig 3.1 Schematic diagram of the continuous monitoring shallow-bed desorption apparatus. P1, P2 and P3 are pumps, F is an in-line filter (0.45 μm), V1, V2 and V3 are valves, V_{SB} is the slider valve containing the shallow-bed (see Fig. 3.2), D is the detector, C is the computer. See text for details.

83
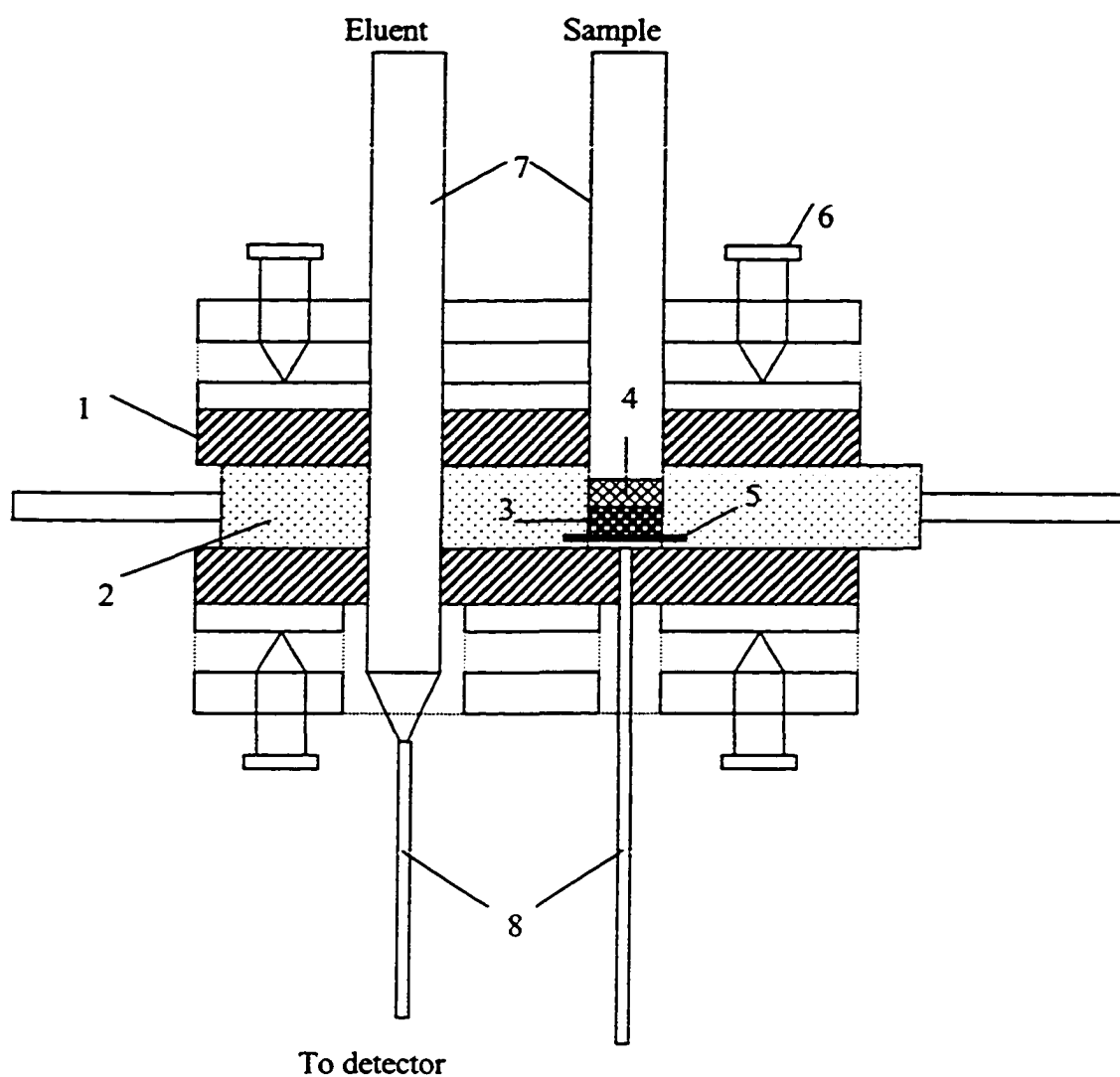
Figure 3.2 Schematic diagram of the slider valve V_{SB}. (1) Teflon face plate, (2) Kel-F insert in S.S. slider, (3) bed of PRP-∞, (4) porous Teflon disk, (5) S.S. screen, (6) tension adjustment screw, (7) 3 mm i.d. S.S. tubing, (8) 0.75 mm i.d. (left) and 0.55 mm i.d. (right) S.S. tubing. See text for details.

The NA desorption experiment starts with the slider in the loading position as shown in Fig. 3.2 in which NA solution passes through the bed for at least 2 hours at a flow rate of about 1 mL/min in order to establish sorption equilibrium unambiguously. Meanwhile the eluent solution from P2 passes through the empty hole in the slider valve and flushes out the HPLC detector (Waters Lambda Max 481, 1 cm pathlength, with the wavelength set to 276 nm). The detector signal is recorded using a data acquisition program written in Labview on a Pentium 166 MHz PC equipped with a PCI-MIO-16XE-50 input/output board (National Instruments, Austin, TX) (See Appendix 1). The signal gain is 10 in order to decrease the bit noise introduced by the I/O board. After the bed is equilibrated with NA a sequence of three steps, which take about 10-15 seconds to complete, is performed in order to initiate desorption of NA: (i) flows of both NA and eluent are stopped by closing V2 and V3 which are both Cheminert on/off valves (Valco, Houston, Texas, Part #4142410); (ii) the slider in V_{SB} is switched left; (iii) eluent flow from P2 is restarted by opening V3. During desorption the flow rate was measured as the time necessary to fill a specified volume of a burette situated downstream of V3. The major resistance to flow during the desorption step is the detector cell with its connecting tubing. The shallow-bed accounts for about 20% of the total resistance.

The PG experiments were performed immediately after the naphthalene experiments using the same sequence of steps with three minor differences. First, the equilibrium (loading) time was only a few minutes since this step had only to ensure that V_{SB} and the tubing were fully flushed. Second, since a constant displacement HPLC pump was used to deliver PG, the flow from P3 was stopped and started simply by turning that pump off

85

and on. Third, the solution carrying PG from the HPLC pump to V_{SB} was first passed through a coil immersed in the thermostated water bath in order to bring it to the same temperature as the liquids from pumps 1 and 3.

The molar absorptivity (ε_i) of NA (5.00×10^3 L mol^{-1}cm^{-1}) in 70/30 MeOH/H$_2$O was obtained by measuring absorbances of several solutions having concentrations between 1 $\times 10^{-6}$ and 1×10^{-5} mol/L while flowing through the HPLC detector at a flow rate of 5.0 mL/min. The molar absorptivity of PG at 276 nm (262 L mol^{-1}cm^{-1}) was obtained in a separate experiment.

3.2.3 Deconvolution and Filtering

The A(t) vs t data for both NA and PG were saved as Microsoft Excel® spreadsheet files. Prior to deconvolution the PG curve in Fig. 3.3 B was normalized to make the area under it equal to one (curve not shown). Deconvolution and digital filtering in the Fourier domain were performed by the following steps [88-90]: complex division of the Fourier transform of curve 3.3 C by the Fourier transform of the normalized PG curve; multiplication of the quotient of this complex division by the filter function ({0,1}, {0,1}, {0.3,1}, {0.4,0}) [88] in order to remove high frequency noise (>0.4 Hz); and inverse Fourier transformation to produce the deconvolved data in the time domain.

86

3.3 Results and Discussion

The following topics are considered: the choice of PG as an IRF-Marker, the observed and the corrected instantaneous rate curves, the cumulative rate curve. The cumulative rate curve is quantitatively interpreted in terms of theory. Finally the attainment of shallow-bed conditions is discussed.

3.3.1 IRF-Marker

As discussed in section 3.1.2, solutes such as NA which possess a similar solubility parameter to that of the PS-DVB polymer are adsorbed onto the polymer surface and also diffuse into the polymer matrix [28, 71, 92, 93]. In contrast, polar-hydrophilic solutes such as PG neither adsorb onto nor diffuse into a PS-DVB polymer matrix [28, 71]. Furthermore, since PRP-∞ particles are free of meso- and macro-pores, PG cannot enter the particle *via* that route. Hence PG meets the IRF-Marker criterion of non-entry into the particles. A secondary criterion is that the IRF-Marker should have a free-solution diffusion coefficient that is the same as that of solute i (*i.e.* NA in this case) because free-solution diffusion may be involved in some of the processes that contribute to instrument band broadening [55, 96-98]. PG is satisfactory also in this regard. The diffusion coefficients for NA and PG at 298K in 7/3 MeOH/H$_2$O are 6.0×10^{-6} cm^2/sec and 6.9×10^{-6} cm^2/sec, respectively with an estimated uncertainty of 0.7×10^{-6} cm^2/sec for each based on calculations employing the Wilke-Chang equation [99].

3.3.2 Instantaneous desorption rate curve for NA

Data for the first 100 sec in a typical experiment on NA (Run 1) and on PG are shown in Fig. 3.3. The insets show the remainder of the data from 100 to 6400 sec. Figure 3.3A is the observed curve of A(t) vs t for the desorption of NA. Figure 3.3B is the IRF peak for PG scaled by Eq. 2.20. Figure 3.3C results from subtracting Fig. 3.3B from Fig. 3.3A. Figure 3.3D shows the result of deconvolution and frequency filtering. In order to clarify their significance, the curves in panels A, B, C, and D of Fig. 3.3 may be compared respectively to the corresponding simulated curves (III + IV), V, IV and II in Chapter 2, Fig. 2.3.

Deconvolution and digital filtering in the Fourier domain were performed by the following steps, described in more detail in chapter 2 section 2.3 [88-90]: complex division of the Fourier transform of curve 3.3C by the Fourier transform of the normalized PG curve; multiplication of the quotient of this complex division by the trapezoidal filter function ({0,1}, {0,1}, {0.3,1}, {0.4,0}) [88] in order to remove high frequency noise (>0.4 Hz); and inverse Fourier transformation to produce the deconvolved data in the time domain.

The "ringing" noise, which is evident in the first 100 sec of the corrected instantaneous desorption rate curve in Fig. 3.3D is a result of truncation in the Fourier domain by using the filter function described above. The ringing observed with this trapezoidal filter function is less than would be observed for a square-cut function, but could not be
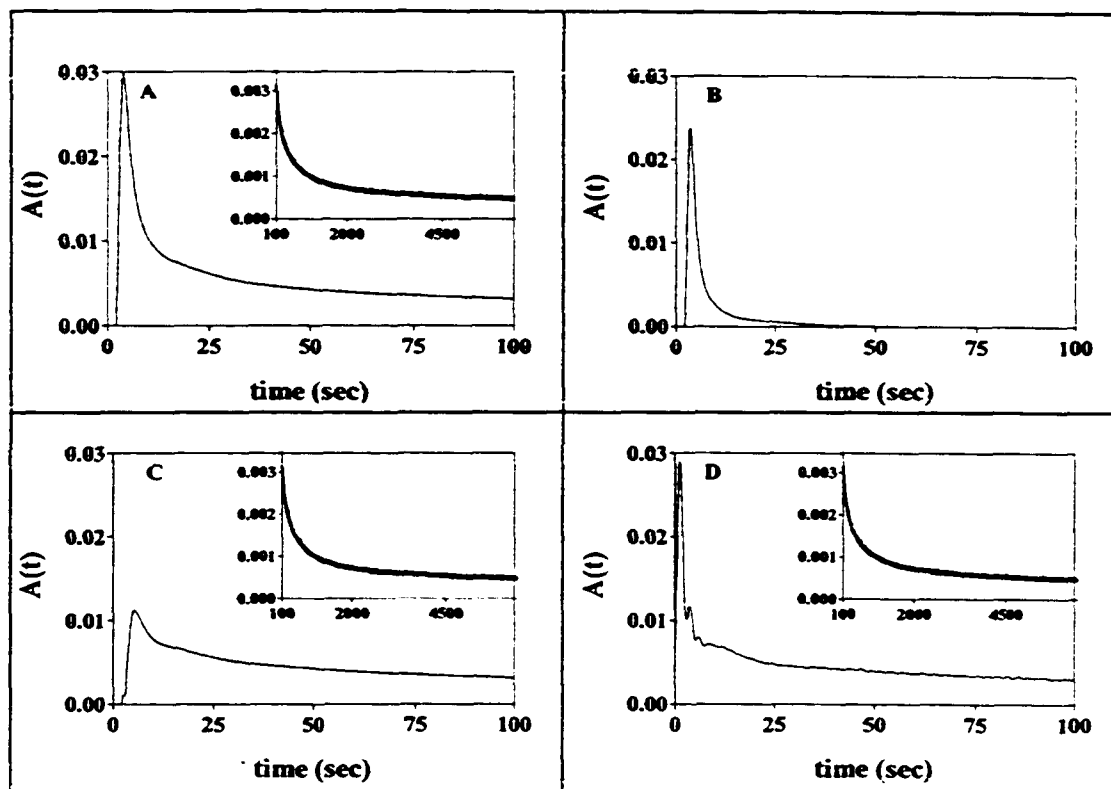
Figure 3.3. Instantaneous desorption rate curves for NA (Run 1) and PG. Acquisition frequency was 10 Hz. There are 64,000 data points over the 6400 sec. The first 100 sec are shown in the large panels, with the remaining 100 to 6400 sec given in the inserts. (A) Observed NA curve, (B) IRF peak for PG scaled by Eq. 2.20, (C) difference between curves in (A) and (B), (D) result of deconvolution of curve in (C) with normalized version of curve in (B).

89

entirely eliminated [87]. Comparison among the curves presented in panels A, C and D reveals that at times longer than about 50 sec they are identical to one another (*i.e.* absorbances at corresponding times agree within 1% relative). This is true for all of the NA runs listed in Table 3.1, which will be discussed in section 3.3.3 below. Its significance is that after about 50 sec the distorting effects of extra particle NA and of band broadening become negligible.

3.3.3 Cumulative rate curve for NA

The instantaneous rate curves (*e.g.* Fig. 3.3D) were digitally integrated between 0 and 6400 sec for all four experimental runs using Excel software. The average absorbance between 6000 and 6400 sec was taken as baseline and the results of the integrations were multiplied by $F/\varepsilon_i l$ in order to obtain the cumulative rate curves for desorption of NA, as described by Eq. 2.29. The curves for Runs 1-4 are shown in Fig. 3.4 as solid lines, each one of which is actually composed of 6400 data points, corresponding to every tenth one of the 64,000 acquired data points. Prism Software Version 4.00 (GraphPad Software, San Diego, CA) was used to fit Eq. 2.1, describing spherical diffusion, as well as Eq. 2.6, describing film diffusion, to all of the points starting at 15 sec in these cumulative rate curves using nonlinear regression.

90
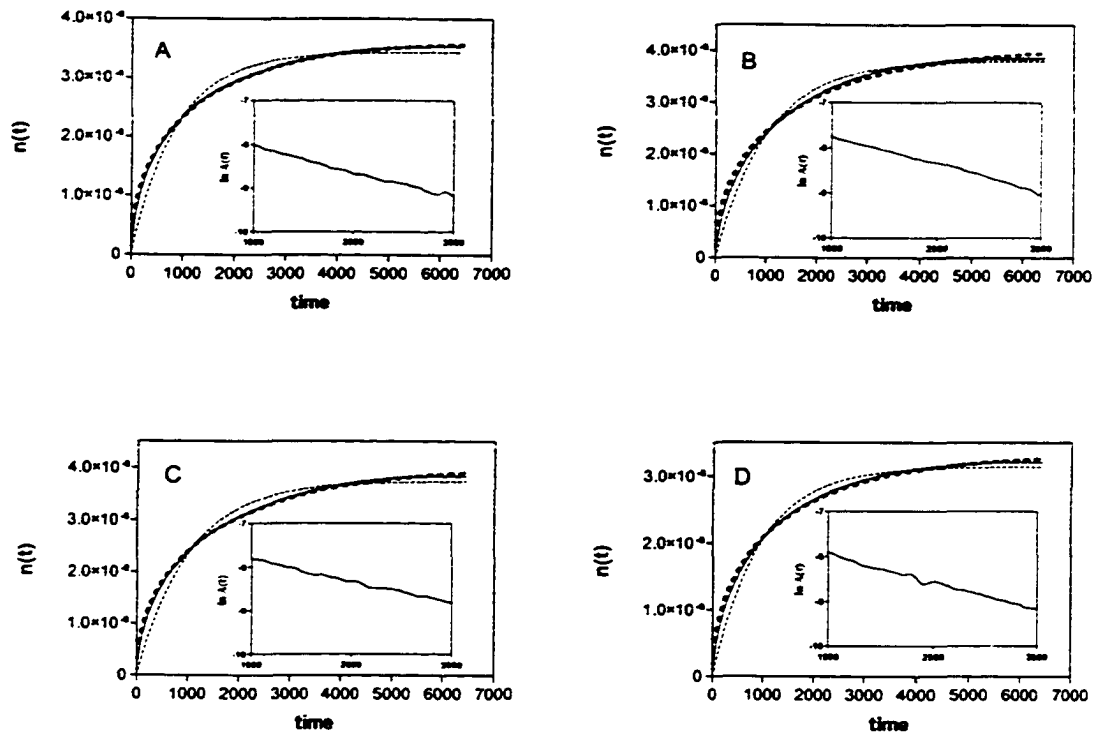
Figure 3.4 Cumulative desorption rate curves for NA. The apparently solid line is 6400 of the 64,000 experimental points from integration of the points in curve D in Fig. 3.3 using Eq. 2.29. The thin dashed line is the regression fit-line for the film diffusion model (Eq. 2.6). The thick dashed line is the regression fit-line for the spherical diffusion model (Eq. 2.1).

91

Table 3.1. Parameters from non-linear regression fit of Eq. 2.1 for spherical diffusion to the cumulative desorption rate curves of NA ($n_{i,0}$ and β are fitting parameters).

Result/Parameter	Run 1	Run 2	Run 3	Run 4
m_{SB} ($\times 10^3$ g)	2.53	2.53	2.48	2.48
$[i]_{MP}$ ($\times 10^4$ mol/L)	1.83	1.83	1.36	1.36
F ($\times 10^5$ L/s)	8.58	8.47	7.88	7.88
$n_{i,0}$ ($\times 10^8$ mol)	3.63	4.11	4.05	3.35
β ($\times 10^4$ s^{-1})	5.7	4.6	4.6	5.2
D_i ($\times 10^{11}$ cm^2/s)^a	5.7	4.6	4.6	5.2
R^2	0.9985	0.9925	0.9982	0.9955

[a]The diffusion coefficient for NA is obtained from β via Eq. 2.3 using 1.0×10^{-3} cm for particle radius.

The regression fit-lines of Eq. 2.6 to the data for Runs 1-4 are shown with a thin dashed line in Fig. 3.4. The correlation coefficient (R^2) values are 0.9601, 0.9799, 0.9636, and 9739 for runs 1 through 4, respectively, which indicates a relatively poor fit to the data points. The non-linear regression fit-lines of Eq. 2.1 (spherical diffusion) to the data for Runs 1-4 are shown with thick dashed lines in Fig. 3.4. Fitting parameters $n_{i,0}$ and β and other parameters for all four runs are summarized in Table 3.1. Correlation coefficients (R^2) are all high suggesting that Eq. 2.1 describes the data well. The intra-particle diffusion coefficient D_i is obtained from β *via* Eq. 2.3. The average value of D_i, with standard deviation, is $(5.0 \pm 0.6) \times 10^{-11}$ cm^2 s^{-1} (n = 4). Comparison of this value *via* the t-test with the value $(7.1 \pm 0.8) \times 10^{-11}$ cm^2 s^{-1} (n = 3), which previously was obtained from shallow-bed **sorption** rate experiments [71], shows that these two measured values of D_i are in agreement with one another at the 99% confidence level.

There is an alternative way to obtain D_i which involves using the data from the differential (instantaneous) rate curves such as the one shown in the inset in Fig 3.3 D. A plot of the natural logarithms of A(t) *vs* time for only the data at very long times is expected to be linear because Eq. 2.30 (describing instantaneous absorbance observed downstream from a shallow-bed where desorption is proceeding via spherical diffusion) reduces to a single exponential term as the higher order terms become negligible [51, 72, 73]. The data from Fig. 3.3D between 1500 and 3500 sec, after smoothing by the running average of 100 points and subtracting the baseline absorbance, is presented as the semilog plot in the insets of Fig. 3.4. The slope of the linear regression line of this plot gives the value of β in Eq. 2.3, from which D_i can be extracted as described above. The average value of D_i from the four runs is $(5.8 \pm 0.6) \times 10^{-11}$ cm^2/s and the R^2 values for the four

runs range from 0.9930 to 0.9962. (Inclusion of data much beyond 3500 sec would have decreased R^2 for the linear fit due to the lower signal-to-noise ratio and was therefore not included in the semi-log plot.) The t-test shows that this average value of D_i agrees with both $(5.0 \pm 0.6) \times 10^{-11}$ cm^2/s and $(7.1 \pm 0.8) \times 10^{-11}$ cm^2/s at the 95% confidence level. It is important to note, however, that there is an advantage to fitting data from the entire cumulative rate curve with Eq 2.1 as opposed to fitting only the long-time data with the semi-log plot. A good fit of the entire rate-curve shows that spherical intraparticle diffusion (defined by Eqs 2.1 and 2.30) is the rate-controlling process, while a good fit to only the data at long times does not. For example, spherical diffusion in a biporous particle is described by an equation containing two diffusion coefficients (see section 2.1.1, Eqs 2.4 and 2.5, as well as Chapter 4) [28]. Plotting only the long time data would yield only the value of the smaller diffusion coefficient.

The fact that the desorption process is controlled by particle diffusion, and not film diffusion, is further supported by evaluating the relative contributions of the two processes with Eq. 2.14. For NA, D_{MP} is 6.0×10^{-6} cm^2 s^{-1} and D_i is 5.0×10^{-11} cm^2 s^{-1} (see above), the density of PS-DVB is about 1 g/mL [1], and the distribution coefficient κ for NA on PRP-∞ from 7/3 MeOH/H$_2$O is 0.106 L g^{-1} [71]. The ratio $[i]_{part}/[i]_{MP}$ is calculated from κ and the density to be about 100. If ε_{inter} is assumed to be approximately 0.4 and the flowrate is taken to be 0.000083 L s^{-1} (average from Table 3.1), a value of δ = 1.1 μm is calculated using the average of Eq. 2.12 and 2.13. The value of X from Eq. 2.14 is about 1.0×10^{-4} which is 3 orders of magnitude smaller than 0.13. This shows that the desorption rate is controlled by intra-particle diffusion.

94

The same theoretical spherical diffusion equation describes both the sorption [28, 71] and desorption rate curves and in both cases yields the same value for the diffusion coefficient of NA. This result is consistent with the expectation that pure intra-particle diffusion control, free of any significant contribution from film-diffusion control, is the rate-determining process for both sorption and desorption of NA in PRP-∞ in these shallow-bed experiments. The mechanism by which NA diffuses through the PRP-∞ polymer matrix can be treated either as "pore diffusion" through the liquid which fills the micropores, in which case D_i would be an "effective" diffusion coefficient [28], or as diffusive movement among the entangled and crosslinked polymer chains, the structure of which ranges from rigid microporous to soft gel [71]. Previous solvent-sorption and polymer swelling studies would seem to favor the latter [71]. Thus, the continuous monitoring of desorption yields kinetic data equivalent to that obtained by a shallow-sorption rate method.

3.3.4 Shallow-bed conditions and linear isotherm

Ideally the achievement of shallow-bed kinetic conditions for a desorption process requires that the eluent leaving the bed should contain zero concentration of solute i. Of course this condition cannot be met because the desorbed solute molecules produce a non-zero solute concentration in the flowing eluent and furthermore the technique depends on this concentration becoming high enough to be experimentally measurable. In practice, shallow-bed conditions can be closely approximated by ensuring that the maximum solute concentration in the flowing eluent never exceeds a very small fraction

95

of the concentration that was used initially to produce sorption equilibrium (*i.e.* $[i]_{MP}$ in Eq. 2.20 and 2.30). In the present case, $[i]_{MP}$ for the naphthalene loading solution was 1.7 $\times$ 10^{-4} M, while the highest absorbance observed in curve D of Fig. 3.3 (*i.e.* about 0.03 AU) corresponds to a maximum concentration of only 6×10^{-6} M NA in the eluent. After 3-4 seconds A(t) has become smaller than 0.01 AU which corresponds to a concentration of less than 2×10^{-6} M NA. This is two orders of magnitude smaller than its concentration in the loading solution. Therefore the requirement of zero solute concentration is effectively achieved after the first few seconds in the present experiments.

The attainment of this condition may also be tested in another way. Eqs 2.1 and 2.31 represent a particular case of a more general zero-length column equation, Eq. 17 in reference [72], which has been developed for desorption over a broad range of flow-rates. When the parameter L in that equation has a very large value it means that the flow of the mobile phase effectively takes away the desorbing solute as soon as it exits the particle. The average magnitude of L for the present experimental conditions, calculated from Eq. 17 in ref. [72] is $2.1 \cdot 10^{3}$ which is very large. This is another way of proving that correcting the observed differential desorption rate curve of NA by subtraction and deconvolution with the IRF-Marker effectively eliminates the effect of the holdup volume on the NA curve.

The sorption isotherm of NA from 7/3 MeOH/H_2O onto PRP-∞ is linear with a distribution coefficient of 0.106 L/g up to a solution concentration of about 2×10^{-4}

mol/L [71]. Since the loading step of PRP-∞ was done with solutions containing less than this concentration, all experiments were performed in the linear region of the NA isotherm.

3.3.5 Minimizing Experimental artifacts

Continuous monitoring of the entire time course of desorption of solute from a shallow-bed in a single experiment is convenient. The present work identifies the several artifactual sources of systematic error that cause inaccuracies in this technique and it demonstrates the ways, including deconvolution, in which corrections can be made for them. If these systematic errors cause relatively small distortions of the rate curves as is true in the present case, correction for them in this way yields an accurate corrected rate curve. However, if the systematic errors are relatively much larger it becomes necessary to reduce their magnitude by modification of the experimental details. For example, this would be necessary in the measurement of desorption rates from HPLC packing materials such as 10 μm diameter particles of an alkylsilyl bonded phase [35, 36] for which desorption rates would be much faster (*i.e.* half-time <0.5 sec) because particle radius is smaller (r in Fig. 2.7 D) and because intra-particle diffusion coefficients are larger (D_i in Fig. 2.7 C). Faster desorption rates give higher concentrations of solute in the early stages of the experiment which would necessitate the use of higher flow rates (F in Fig. 2.7 B) to attain shallow-bed conditions (*i.e.* very low concentration of i in the effluent). A higher flow rate and a smaller r both require a higher pump pressure, the latter because the permeability of the bed is inversely proportional to r^2 [1].

97

Also, for such a packing material the true instantaneous desorption rate curve would be much narrower than the one that is now seen in Fig. 3.3 D and the observed desorption rate curve would be only slightly broader than the IRF peak. This would make it virtually impossible to accurately extract the true rate curve from the observed rate curve solely by deconvolution because of the uncertainty introduced by the unavoidable presence of noise in the data [87]. It would be necessary to reduce instrument band broadening by reducing the volume of the instrument components that are located between the bed and the outlet end of the detector. For porous particles it would be also necessary, in principle, to distinguish the amount of solute in the pores from that between the particles because the former amount should not be subtracted from the observed rate curve. These experimental modifications are all feasible. Their implementation will be the subject of the Chapters 4 and 5, in which are reported desorption rate curves of solute, both from porous 10 μm diameter PS-DVB particles and from porous 12 μm diameter, silica-based, octadecylsilyl (C_{18}) bonded-phase particles.

98

Chapter 4: Desorption rate of naphthalene from PRP-1 using Type II instrument

In chapter 3, it was shown that the continuous monitoring shallow-bed technique, combined with corrections for experimental artifacts by subtraction of and deconvolution with the IRF-marker run is a valid method for the measurement of desorption kinetics. However, the amount of band broadening taking place in the apparatus used (standard deviation of the IRF is around 10 sec) is too large for studying more rapid desorption processes which occur on the time scale of seconds and milliseconds, not hours. In such cases deconvolution is not able to correct for instrument band broadening, because the IRF is much broader than the time scale of the fast desorption process. For this reason, it is necessary to build an apparatus with drastically reduced band broadening by reducing the volume of the instrument components that are located between the bed and the outlet end of the detector. This chapter describes the design and validation of such a low-band broadening shallow-bed apparatus for the continuous measurement of *fast* desorption kinetics. The basic design chosen is the Type II apparatus, and the process studied is the desorption of NA from polymeric particles of PRP-1, an HPLC sorbent, in 85/15 methanol/water solvent. As well, the desorption-rate data obtained are compared with the sorption-rate data from the literature in order to validate the new shallow-bed apparatus.

99

4.1 Introduction

4.1.1 Structure of PRP-1 and intraparticle diffusion of NA

PRP - 1 is a spherical, polymeric HPLC sorbent made up of PS-DVB. It possesses mesopores, the diameter of which averages around 10 nm (100 Å) where diffusion can occur either through sorption-retarded pore diffusion or surface diffusion along the pore walls. Its PS-DVB matrix also exhibits porosity, and solutes with a solubility parameter close to that of PS-DVB can enter it, as discussed in Chapter 3, sections 3.1.1 and 3.1.2. It is not certain whether the matrix of PRP-1 is composed mainly of micropores or of gel-like regions. However, for two reasons, it is likely that it is dominated by the microporous regions. First, PRP-1 does not exhibit appreciable swelling or shrinkage when solvents are changed from 100% organic to 100% aqueous solvents, whereas PRP-∞ (less-highly cross-linked PS-DVB packing discussed in Chapter 3) exhibits changes of up to 12% [71]. The inability to swell is attributable to permanent micropores. Second, the diffusion coefficient in the matrix of PRP-1 ($D \approx 10^{-12}$ cm^2 sec^{-1}) has been shown to be at least 3 orders of magnitude lower than the diffusion coefficient inside the matrix of PRP-∞ ($D = (4\pm1) \cdot 10^{-9}$ cm^2 sec^{-1}) in the same mobile phase of 85/15 MeOH/H$_2$0 [28]. Whether PRP-1 possesses micropores or gel regions or both, NA has been shown to enter its matrix and to go through a severely hindered diffusion, in addition to the relatively rapid diffusion through the mesopores [28, 46]. Thus, the diffusion of NA inside PRP-1 is described by two different diffusion coefficients.

100

4.1.2 Reasons for study of NA desorption from PRP-1

One of the reasons this system was chosen as the first to be measured with the Type II desorption apparatus is because it is a well known system, which has been characterized previously [28, 46]. Because the Type II apparatus design is completely new and the data analysis methods for minimizing its experimental artifacts (sections 2.3 and 2.4) have not been previously applied in shallow-bed kinetic experiments, it is desirable to study a sorbent whose kinetic properties are known. In addition, PRP-1 is a popular HPLC porous polymeric packing, often used in analytical determinations. [100-103].

4.2 Experimental

4.2.1 Reagents, solvents, and sorbent

Naphthalene (NA) (Coleman and Bell, Norwood, OH, USA) was recrystalized from methanol. Phloroglucinol (PG) (1,3,5 trihydroxybenzene, Fluka, $\geq$99%) was used without further purification. The solvent (mobile phase, or eluent) used in this study, both for making solutions of NA and PG, was 85/15 MeOH / H_2O v/v, which was prepared by mixing pre-measured volumes of HPLC grade MeOH (Fisher Scientific) and filtered, deionized H_2O.

The solvent and its NA and PG solutions were sparged with helium before the kinetic experiments. The concentrations of NA used were around 5×10^{-5} M, which is the maximum concentration that still falls within the linear range of the sorption isotherm

101

[46]. The concentration of PG used was about 0.052 g/L, chosen to nearly match the absorbance of the 5×10^{-5} M NA solution at 222 nm.

The mesoporous PS-DVB sorbent PRP-1 (Lot No. 334, Hamilton Co., Reno, NV, USA) has the following characteristics listed by the manufacturer: spherical shape with 10 µm particle diameter (95% within the range 8-12 µm), specific pore volume of particles 0.79 cm^3 g^{-1}, average pore diameter 75 Å, specific surface area of 415 m^2 g^{-1}, and a particle porosity of 0.48 mL of pores per mL of a particle [46].

4.2.2 Apparatus

4.2.2.1   Overview of the shallow-bed apparatus

The diagram of a Type II apparatus shown as Fig. 2.2 in Chapter 2 is partial and highly simplified. Figure 4.1 is a more detailed schematic of the entire apparatus which is a modification of a stopped-flow device manufactured by the Union Giken company, described in Section 4.2.2.2 below. Fig. 4.2 enlarges the shallow-bed assembly (SBA) containing the flow-channel block and the cuvette block in which are contained the shallow-bed and the flow-cuvette with the detection window. P1, P2, and P3 in Fig. 4.1 are constant pressure pumps [95] carrying the NA solution, the PG (unretained compound) solution, and the pure solvent (mobile phase), respectively. V1 -V3 are solenoid valves (Part # 009-0616-900, Parker Hannifin, General Valve Division,

102

A V1(u)

Waste

V2(u)

SBA

V3(u)

V4

F F F

(NA soln) (PG soln) (solvent)

P1 P2 P3

B V1(e)

Waste

V2(e)

SBA

V3(e)

V4

F F F

(NA soln) (PG soln) (solvent)

P1 P2 P3
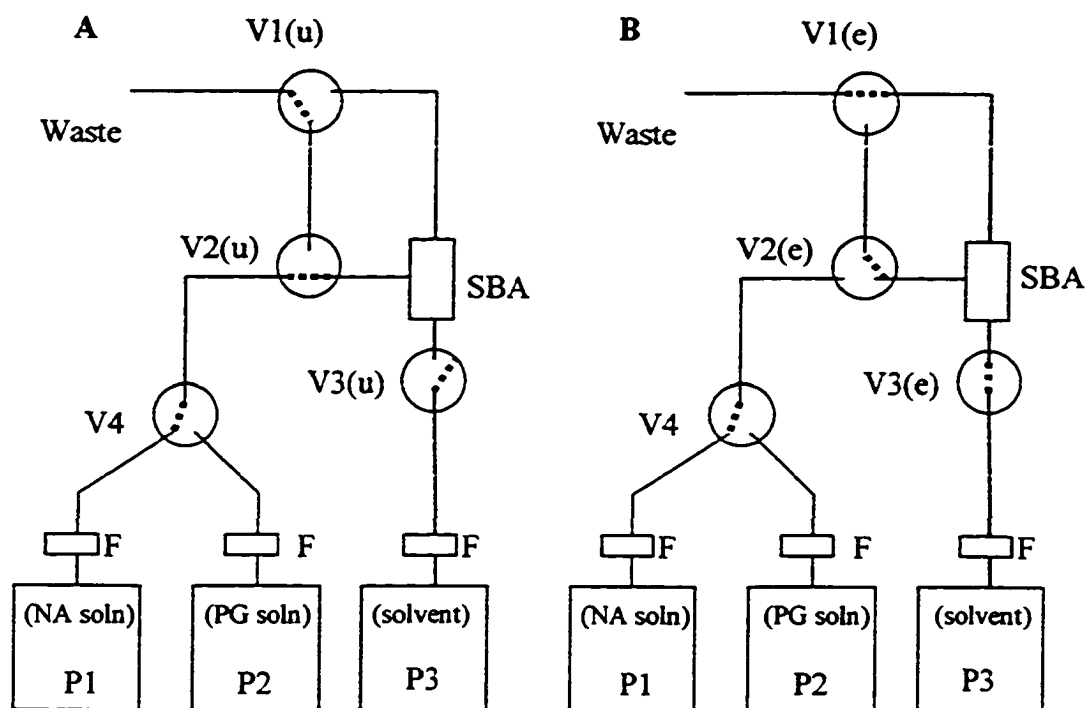
C

Step name	V1	V2	V3
default (no flow)	u	u	u
equilibration	e	u	u
time-out	u	u	u
flush	u	e	e
desorption	e	e	e

Fig 4.1 Overview of the Type II shallow bed kinetics apparatus. P1-P3 are pumps. V1-V3 are electronic valves; the dashed lines in valves connect the valve ports between which solvent flow can occur through the valve. V4 is a manual 3-way valve. F is an inline filter. SBA = Shallow-Bed Assembly, which includes the flow-channel block, the shallow bed, and the cuvette block (See Fig 4.2). Panel A (no flow): valves V1-V3 are in the unenergized position (u). Panel B(desorption): valves V1-V3 are in the energized position (e). Panel C. Table indicating the valve states during one cycle of operation.

103
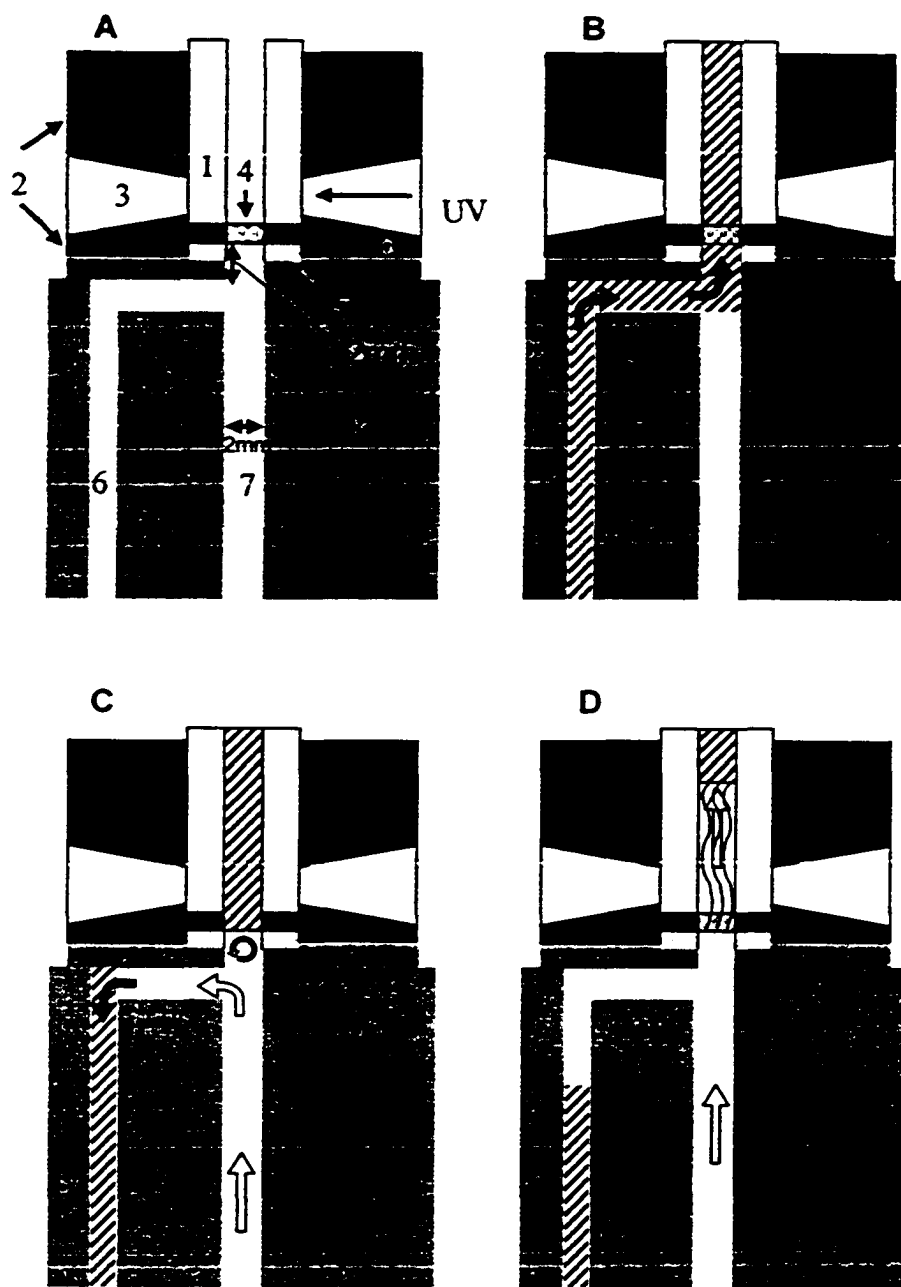
Fig. 4.2 Close - up schematic of the shallow-bed assembly (SBA) showing the flow of solutions during the desorption experiment. Not to scale. A: the assembly before the experiment; B: Equilibration step, C: Flush step; D: Desorption step; Labels: 1: quartz cuvette, 2mm ID(2mm pathlength), 6mm OD; 2: Cuvette-block; 3: Aperture that defines detection window on cuvette (2 mm, circular); 4: the shallow bed (shown in more detail in Fig. 4.4); 5: PEEK spacer; 6: sample delivery channel; 7: pure solvent channel, 2 mm diameter, 30 mm long; 8: Kel-F flow-channel block.

104

Fairfield, NJ), each controlled by Valve Drivers (Part #090-0022-100-1 Parker Hannifin, General Valve Division, Fairfield, NJ), which in turn are computer controlled. V1 and V2 are 3-way valves, and V3 serves as an ON/OFF valve. During the experiment, all of the valves are kept at the same pressure, because they are all connected to the same high-pressure helium gas tank. The letters in the brackets beside the valve numbers on the figure represent the un-energized (u) and energized (e) states of the solenoid valves. V4 is a manual 3 way valve, (Cheminert, Valco Instruments, Co. Inc., Houston, TX) used to select between the NA and PG solutions. The whole system has a maximum pressure rating of 250 psi.

Computer control has a dual function in this apparatus. The first function, as already mentioned, is to control and time the flow sequences, while the second is to acquire the spectrometric data obtained by the detector. The computer program to control the flow and acquire the spectrometric data was written in LabVIEW® (National Instruments, Austin, TX, USA) and the Valve Drivers are interfaced to a 166 MHz PC via a National Instruments I/O board (part # PCI-MIO-16XE-50), and an additional external circuit. The LabVIEW program is shown in Appendix 2. A diagram showing which pins on the three valve drivers connect with which pins on the I/O board, along with the external circuit is also given in Appendix 2.

The SBA shown in Figure 4.2 is the "heart" of the system, where the sample and solvent lines meet just upstream (below) the shallow-bed, which in turn is just upstream of the detector window. The design is meant to limit sample dispersion between the shallow-

105

bed and the detector during the desorption step. The pure solvent flow channel is in-line

with, and of the same diameter (*i.e.* 2.0 mm) as, the shallow-bed and the cuvette

downstream (above it). The reason for this is to maintain a straight velocity profile, with

no stagnant zones or recirculation zones [104-106]. The flow channel which delivers the

sample is at a right angle to the solvent flow channel, because sample dispersion does not

need to be limited during the equilibration (*i.e.* loading) step. The 90 degree angle

allows one to place the junction very close to the shallow-bed, which makes for easy

washing out of the sample during the flush step.

A nut is used from above to apply pressure on all the parts of the assembly from the top,

which is necessary to enable a seal (not shown in Fig. 4.2).

4.2.2.2   Union Giken Stopped Flow Device

The Union Giken stopped flow [85, 86] device (RA – 401) is a pressure-driven system,

which is used to study the rates of fast homogeneous chemical reactions. The schematic

of the flow system in the factory-supplied instrument is shown in Fig. 4.3. Before the

stopped flow experiment starts, the two 5 mL reservoirs are filled with solutions

containing the reactants. Both of the reservoirs are pressurized by an inert gas from one

pressure tank; the gas space above the solutions in the reservoirs is connected via a hole

just above the solutions as shown in Fig. 4.3 A. The flow is started and stopped *via* a

Flow Stop Valve seen on the right of Fig. 4.3 A which is a gas-pressure-driven on/off

valve with an electromagnetic actuator. When the valve is open the pressurized solutions

106

A

B
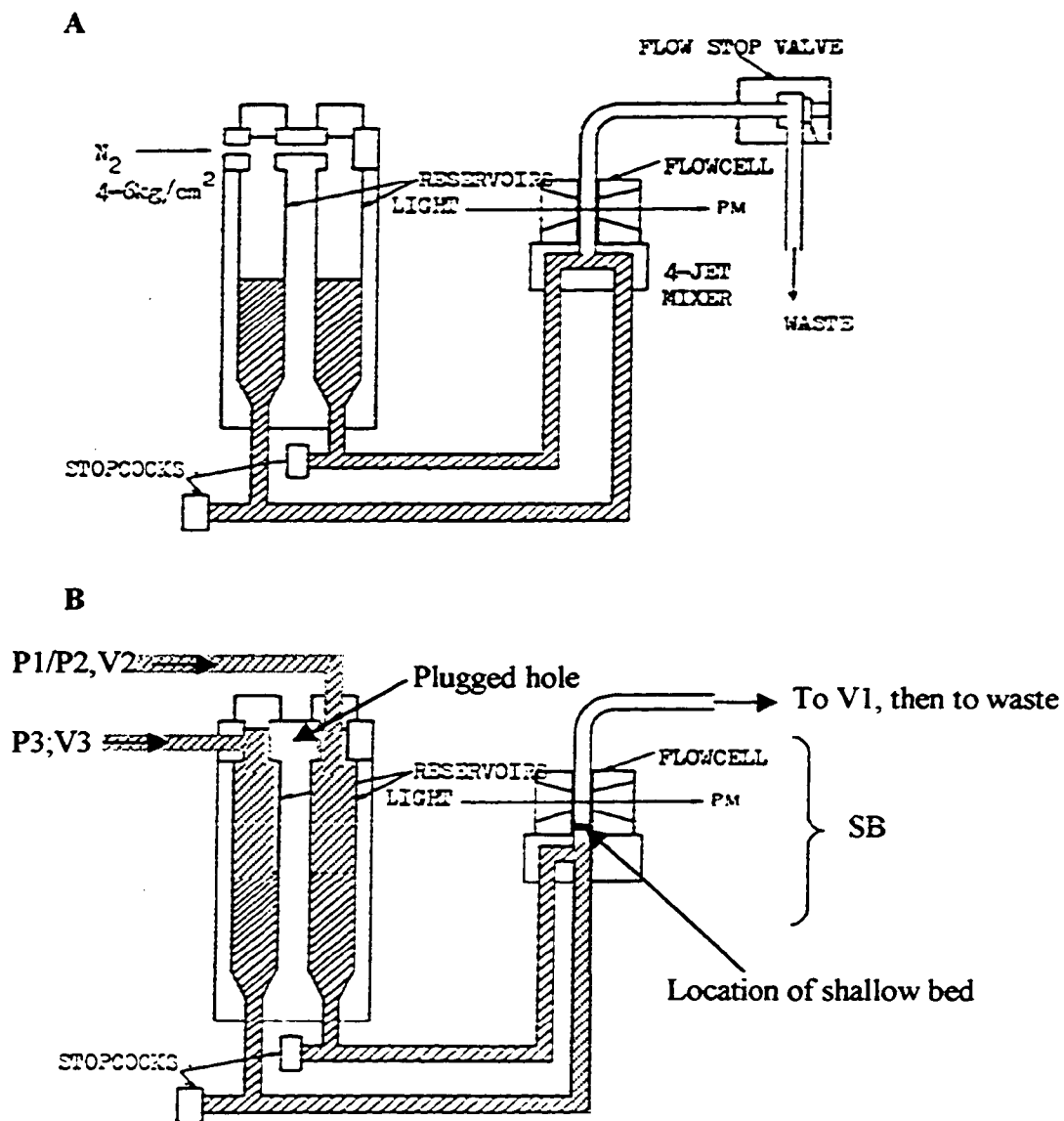
Fig 4.3.   Modification of the stopped flow apparatus to obtain a shallow-bed Type II instrument A: The schematic of the flow assembly of the Union Giken apparatus scanned from the user manual; PM = photomultiplier. B: the modifications done to enable the study of desorption kinetics from a shallow bed; P1, P2, P3, V1, V2, V3, and SBA are the pumps, valves and the location of the shallow-bed assembly from in Fig. 4.1.

107

from the reservoirs flow downstream at a very high velocity. The solutions from the two reservoirs meet at the 4 jet mixer, where they rapidly mix. The mixed solution is carried towards the flowcell located 2-5 mm above the point of mixing. The flow-cell is a 2 mm ID synthetic quartz tube which is put into a plastic (Daiflon®) holder, in which 2 mm-high windows are drilled out. When the flow is stopped, the changing absorbance of one of the reactants or products is monitored as a function of time. A stopped-flow device was chosen to be modified for the study of intraparticle kinetics because it has the capabilities of measuring rapidly changing absorbances in the UV and Visible regions. This Union Giken apparatus was a gift from Dr. Monica Palcic of the Chemistry Department at the University of Alberta.

The detection system includes the cylindrical quartz cuvette, 6 mm O.D and 2 mm ID and its holder, which are both shown in Fig. 4.2. It also includes UV (deuterium) and visible (tungsten) lamps, a monochromator, and a photomultiplier (PM in Fig. 4.3), a system controller (not shown in Fig. 4.3), and the assembly containing the lenses enabling light-focusing on the region of the quartz cuvette defined by the windows (also not shown in Fig. 4.3). The system controller enables voltage control to the PM, and it outputs the PM signal in absorbance or transmittance units (absorbance mode was used in all experiments). It also enables the setting of the time constant from 0.1 to 30 milliseconds, (time constant set at 1 ms for all experiments), and signal amplification (gain) from 0.1 to 100, (gain = 10 was used for all experiments in this chapter).

108

The modifications to the Union Giken system involved primarily the flow control of the system, and are schematized in Fig. 4.3. B. The overall goal of the modifications is to place a shallow-bed in between the flow cell and the mixer from the Fig 4.3 A, and to change the delivery of solutions so that instead of the two solutions being delivered at the same time, the solutions can be delivered one at a time in a controlled fashion. The detection system is left intact. The plumbing was modified by treating the reservoirs not as containers but as simply a part of the tubing/channel system connecting the solutions from the constant pressure pumps to the detection system. This involves filling the reservoirs completely with liquid and connecting one of them to P1/ P2 (solvent carrying either the solute or IRF-Marker) and valve V2, while connecting the other one to P3 (pure solvent) and valve V3 from Fig. 4.1. This also requires that the hole connecting the two reservoirs be plugged, as shown in Fig 4.3 B, which was done by the chemistry machine shop. The block to replace the 4-jet mixer was also redesigned because it has to contain the shallow-bed in between the point where the channels meet and the detection window. The schematic of this flow-channel block, which was made in the chemistry machine shop, has already been described as Fig. 4.2, and the schematic of the washers and other parts immediately attached to the shallow-bed is shown in Fig. 4.4. The change of the 4-jet mixer is also symbolized in Fig. 4.3 B by the changed geometry of the delivery channels compared to Fig. 4.3. A.

Since the original deuterium lamps are not in production anymore, new lamps with the same optical characteristics were employed (L2D2, Type L 6310, Hamamatsu, Middlesex, NJ, USA) along with a new power supply (Model C1518, Hamamatsu).

109

4.2.2.3　Further close-up of the of the shallow-bed parts

The shallow-bed is located in the SBA as shown in Fig. 4.2 in between the flow-channel block and the quartz cuvette. The close-up of all the parts in between the flow-channel and quartz-cuvette is shown in Fig. 4.4. The shallow-bed itself is 0.6 mm high and 2 mm in diameter and it is contained in a stainless steel (s.s.) washer 0.6 mm high, 2 mm ID, and 6 mm OD (center washer in Fig. 4.4). The particles are actually packed into silicon grids which fit into this washer. These silicon grids are micro-fabricated perforated plates, with square through-holes 200 μm on a side, and 40 μm thick walls. Each silicon grid is also 200 μm high, so there are three plates stacked in the s.s. washer containing the shallow-bed. They serve to stabilize the bed during the flow experiments, so that no gaps or channels develop in the packing. Just above and below the shallow-bed are nickel meshes (7.5 μm hole size and 5 μm thick, Internet, Minneapolis, MN, Part # BM 2000-01-N) which retain the packing in place. On either side of the shallow-bed there is one more, empty, silicon grid, further followed by a s.s. screen (2 μm pore size, ca. 75 μm thick, Anspec, Ann Arbor, MI, USA). The purpose of such an arrangement is to ensure that the Nickel meshes are flush with the top and bottom of the packing, while at the same time providing structural support to hold the assembly in place during the high flows employed.

Since a good seal cannot easily be formed between flat stainless steel surfaces, a soft gasket must be placed between them. However, it is required in this assembly that the s.s. washers are as close together as possible to keep the thin nickel meshes flush with

110
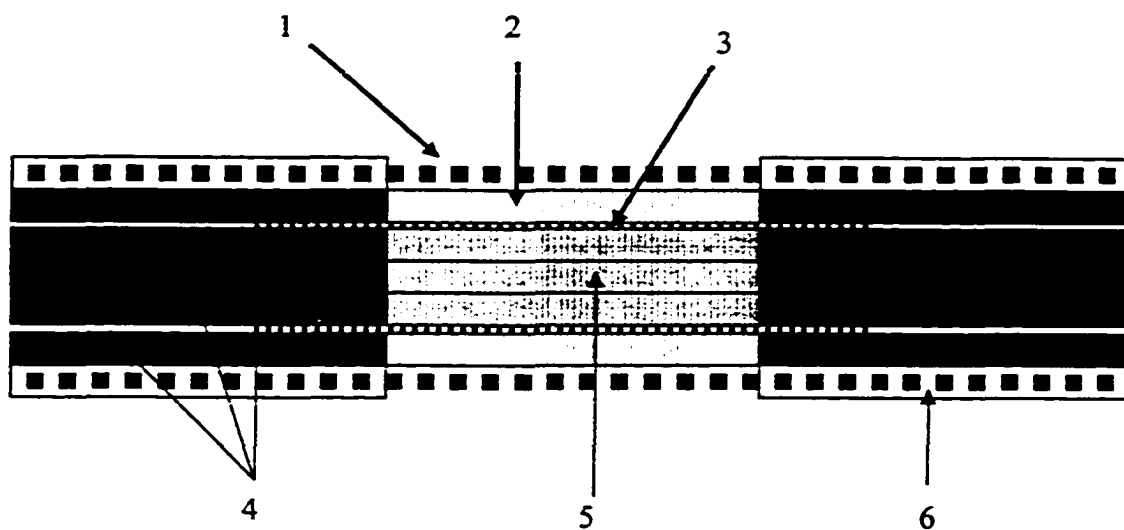
Fig. 4.4: Schematic of the particle-packed shallow-bed and other parts located in between the flow channel block and the quartz cuvette of Fig. 4.2. Not to scale. 1; woven s.s. screen, 2; empty silicon microgrid (200 μm high); 3: nickel mesh, 5 μm thick, 7.5 μm hole size; 4: s.s. washers 6 mm OD, 2 mm ID. Centre washer is 600 μm high while the outside washers are 200 μm high; 5: packed shallow bed consisting of PRP-1 packed into 3 silicon microgrids, each 200 μm high; 6: teflon membrane pressed into the s.s. screen.

111

the shallow-bed. The seal is achieved by putting a thin layer of Polydimethylsiloxane (PDMS) elastomer on the sealing surfaces. To do this, a thin film of a liquid polymerization mixture, with 10:1 ratio of elastomer to curing agent, (Sylgard 184 from Dow Corning) is simply deposited on the s.s. washers, followed by curing for at least 24 hours at room temperature.

The woven stainless steel screen is, of course, permeable in the direction perpendicular to its face, from top to bottom. In addition, however, it is also permeable laterally, through the plane of the screen, which causes the system to leak if the screen is used as-is. This condition is also remedied by impregnating the outer margin of the s.s. screen with the polymerization curing mixture just described. The fluid mixture travels a short distance into the screen through capillary action, and fills up the spaces in between the woven wires. After several hours of curing at room temperature, the mixture solidifies, leaving a non –porous region of the s.s. screen. The screens were impregnated with the PDMS elastomer in the region between the outside edge and 1.5 mm from the edge - leaving the centre of the screens porous and permeable to through -flow.

A thin washer, made of porous Teflon membrane (Zitex, 10-20 μm pore size) is placed on either sides of the woven s.s. screen as shown in Fig. 4.4. Even though the porous membrane is 0.005" thick (125 μm), it collapses upon pressure to yield a non-porous material, which is much thinner. It is used to protect the fragile quartz cuvette from being damaged by contact with a hard , uneven surface of the woven s.s. screen (The amount of

112

the PDMS elastomer, with which the s.s. screen is impregnated, is assumed to be too thin to risk direct pushing against the quartz cuvette).

It should be noted that not all the items mentioned in the design of the shallow-bed may be essential. However, the described arrangement was the first one tested that yielded reliable seals along with a stable shallow-bed. It was also found that the length of the shallow-bed cannot be much shorter than 0.6 mm. Experiments carried out on shallow-beds which were 0.2 mm thick, for example, always yielded extremely noisy desorption curves. The reasons for this phenomenon were not investigated; however, channeling is a possible explanation.

4.2.2.4 Packing of the shallow-bed

The shallow-bed is packed in a separate, temporary assembly, by vacuum-driven slurry packing. The procedure is schematized in Fig. 4.5. The silicon grids are put into the 0.6 mm thick s.s. washer (the same washer as the center one in Fig. 4.4), which is covered on the bottom side with the nickel mesh, to trap the packing. The Ni mesh sticks to the s.s. washer because it is partially pressed into the PDMS elastomer film. The unpacked shallow-bed is then placed on top of a woven, s.s. screen which serves as support. The whole assembly is connected to vacuum from underneath, via a specially-made manifold. The top surface of the washer is temporarily connected to a s.s. tube, (2 mm ID, 6 mm OD, 20 mm long) using the PDMS elastomer film, as described earlier. A 50 μL Eppendorf pipette tip is placed into the top of the tube to serve as a reservoir for the

113
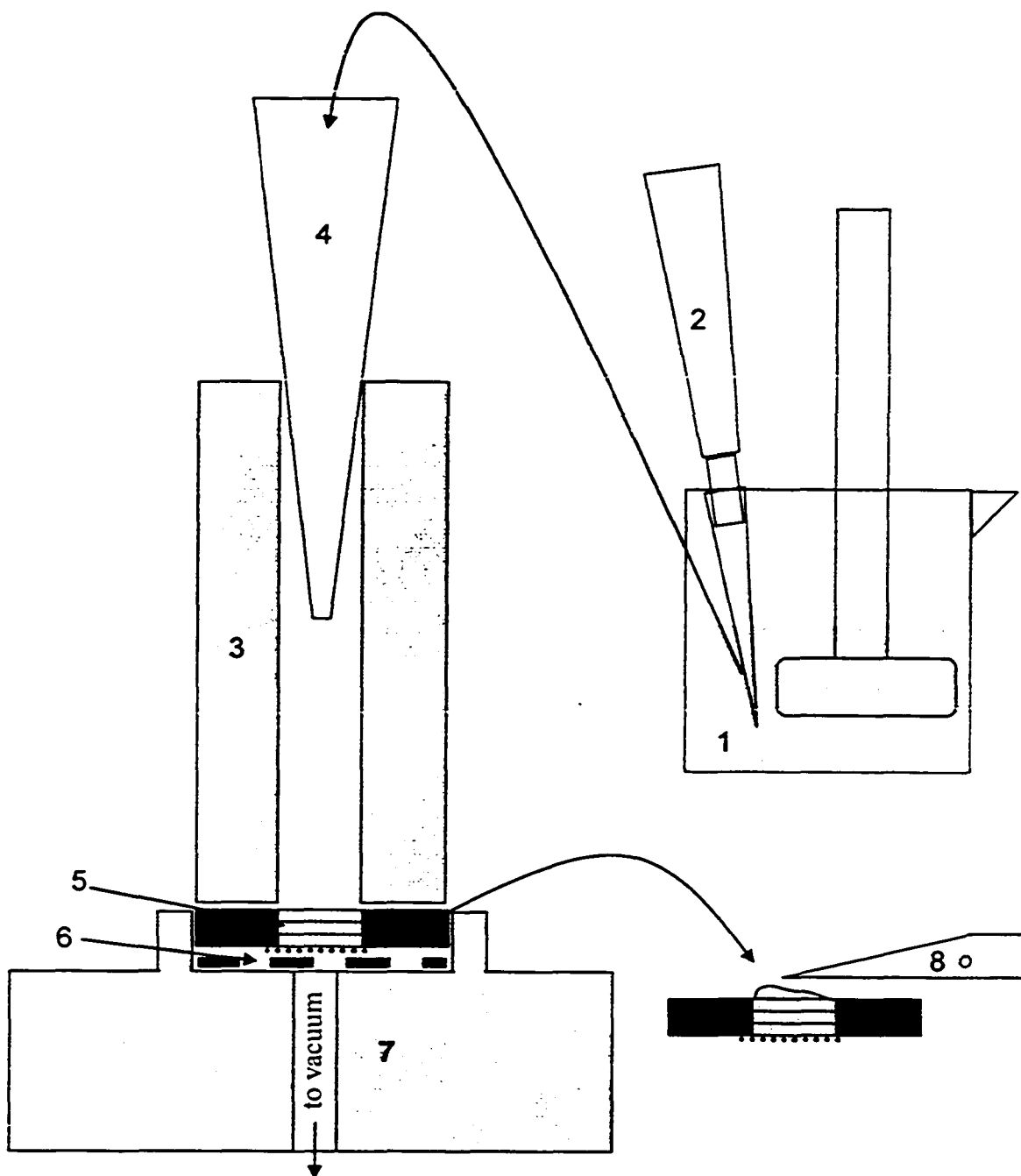
Fig. 4.5.   Slurry packing procedure for the shallow bed. The stirred slurry from the beaker (1) is aspirated into a micropipette (2) and transferred into the s.s. tube (3). Another pipette tip (4) serves as a slurry reservoir on top of the s.s. tube to facilitate the transfer. The shallow bed to be packed is made up of the s.s. washer filled with 3 silicon grids plus one Ni mesh on the bottom (5) it is placed on top of a s.s. screen (6), which in turn sits in a well in the packing manifold (7) which is connected to the house vacuum. After slurry packing, the washer with the silicon grids and Ni mesh is taken out and extra particles are removed with a surgical blade (8).

114

slurry solution. A slurry of PRP-1 in ethanol, (about 0.02% by mass) is pipetted into this reservoir using a micropipette. The beaker from which the slurry is aspirated by the micropipette is continually sonicated and stirred during the packing process. Usually, about 5 mL of the slurry are needed to fill in the shallow-bed. It takes about 10 refills of the micropipette and about 15 min to fill the bed. After filling the bed, the s.s. tube is taken away, the excess packing is removed, and the top Ni mesh is put in place. This is followed by placing the packed bed in the shallow-bed apparatus.

4.2.2.5   Fabrication of the silicon grids

The microfabricated silicon grids help in the packing of the shallow-bed by preventing the shifting of the packing by currents which develop as the pipetted slurry wets the packing and then passes through. They are also thought to stabilize the bed during the kinetic experiments, again by preventing the shifting of the packing. They essentially serve as fences, preventing particles from shifting; it was found that, because of the fast flows and changing pressures in the described apparatus, the packed shallow-bed has to be structurally robust in order to maintain a relatively uniform permeability to flow throughout its area. Normally, high packing stability is achieved by using high pressure slurry packing techniques. However, packing such a short column volume using the conventional slurry packing technique can be difficult, and an apparatus for packing such beds is not commercially available. In addition, a densely packed bed may exhibit smaller permeability to flow than a more loosely packed one, which is not necessarily

115

desirable for the shallow-bed experiment. Thus, a slurry packing technique using only the house vacuum line was developed as described above, and the silicon grids were found to stabilize the shallow-beds packed by this technique.

The silicon grids were fabricated at the University of Alberta Nanofab facility. The pattern was designed in L-Edit, and allowed fabrication of 27 such grids per 4" silicon wafer. The pattern was etched onto a chrome mask, using standard procedures. Each 200 μm–thick silicon wafer (Plane: <100>; resistivity: 1-20 ohm/cm; Virginia Semiconductor, Frederickburg, VA) was exposed to water vapor-saturated flowing nitrogen gas in an oven at 1100 °C to make a 1.2 μm thick film of silicon dioxide. The wafers were then coated with a layer of HPR 504 photoresist, and exposed photolithographically to the grid pattern on the mask. The exposed photoresist was washed away, leaving the bare silicon dioxide surface. The wafer in turn was bathed in a buffered oxide etch, containing HF, for 25 minutes, to leave the original Si over places on the surface where the grid holes were to be created. Deep Reactive Ion Etching (DRIE) was then performed to "drill" the through-holes and free the grid from the rest of the wafer. An Oxford Instruments System 100 DRIE (Bristol,UK) operating the Bosch process with an ICP power of 500 W was used. Etching was done at 20 W for 10 s (SF$_6$ flow rate75 sccm), followed by 10 W for 7 s (C$_4$F$_8$ flow rate 50 sccm) during the polymer deposition step. Between 320 and 350 cycles were needed to etch all the way through the wafer. The square holes have the diameter of either 100 μm or 200 μm and the walls have thicknesses of either 30 μm or 40 μm, respectively. The silicon grid, packed with PRP-1 particles, is shown in Fig. 4.6

116
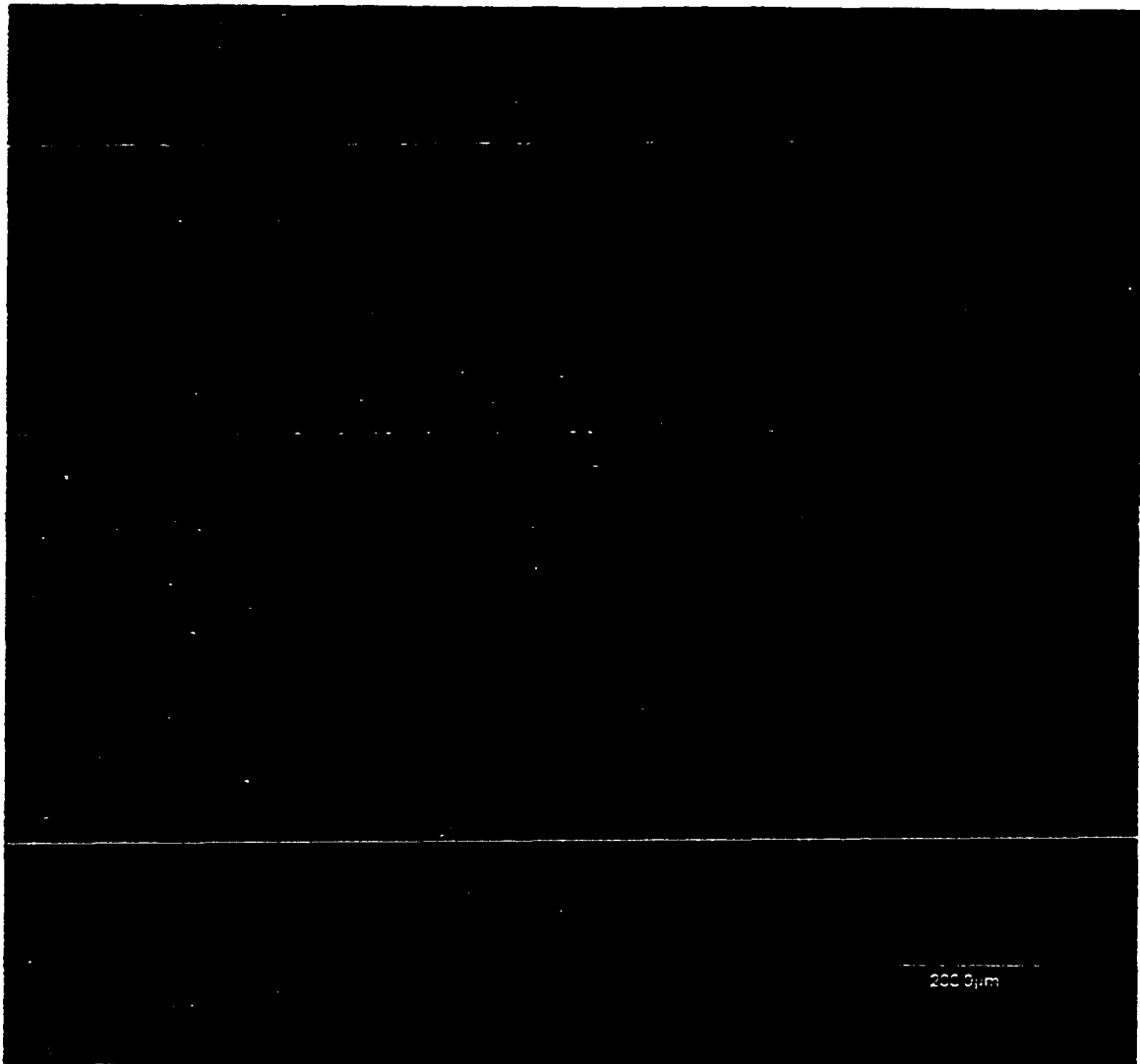
Fig 4.6 Confocal image of the surface of a part of a Silicon Grid packed with PRP-1.
The image is 1.4 mm on a side. Each hole is 200 μm by 200 μm wide, and the grid is 200 μm deep. In the top left corner is visible a part of the s.s. washer in which the grid is placed. The yellow line at the bottom right corner is 200 μm. The black piece in the hole second from the top and second from the right is a broken–off piece of the silicon wall from elsewhere in the grid formed during the packing procedure.

117

4.2.3 Procedure for Desorption Rate Measurement

The flow sequence is controlled by the states of the three solenoid valves shown in Fig. 4.1. There are five distinct steps per cycle, and the valve states during each of the steps are tabulated in the table underneath Fig. 4.1. At first, as in Fig. 4.1 A and 4.2 A, all the solenoid valves are in the un-energized state, and their arrangement is such that there is no flow, even though the constant-pressure pumps are pressurized. The next step is the equilibration of the shallow-bed with the sample solution, and it starts when V1 becomes energized and the solution of either NA or PGL flows through the shallow-bed, as in Fig. 4.2 B. The equilibration step lasts at least 70 seconds, which is more than enough time for sorption equilibrium to occur. (The results are independent of equilibration time in the range studied.) Next, V1 becomes un-energized again, and the valves return briefly to the same state as in Fig. 4.1 A. This step can be called the time-out, and it has no purpose in the experiment, other than that it is required for the proper functioning of the timing sequence of the clocks on the I/O board. The fourth step is called the flush step, during which sample is flushed from just upstream of the shallow-bed by energizing valves V2 and V3, but leaving V1 in its resting state. The solvent from P3 pushes the sample back through the sample channel in the mixer and out to waste as seen in Fig. 4.2 C. The flush step is always one second long. The final step is the desorption, where all the valves are energized and the solvent from P3 flows directly through the shallow-bed, as in Fig. 4.1 B and Fig. 4.2 D.

118

The purpose of the flush step is to remove all of the solute from underneath (upstream of) the shallow-bed, while leaving the sample solution surrounding the particles in the bed undisturbed. The liquid right underneath the bed, but above the junction of the sample and solvent delivery channels is not swept out directly. However, it is expected that the recirculation zone present in that cavity, shown as a circular arrow in Fig. 4.2 C, contributes to the flushing out of the solute from that region.

Since the sequence is computer controlled, the cycle portrayed in Fig. 4.1 can be repeated any desired number of times. The entire cycle is repeated five times, with the help of the computer-controlled program to form a set of cycles. Sets of cycles for the sorbed solute NA and for the IRF-Marker PG are run alternately. The flow-rate is measured after each five-cycle set by determining the time it takes for the solvent (from P3) flowing through the shallow-bed to fill a volumetric flask. This is done by manually switching the solenoid valves to the position in Fig. 4.1 B. (or position in Fig. 4.2 D). If necessary, the pressure applied to the constant-pressure pumps in Fig. 4.1 is increased to compensate for the change in flow-rate. The flowrates for the NA and PG sets are matched to less then 1%.

4.2.4 Deconvolution and filtering

Deconvolution and filtering are performed the same way as described in Chapter 3, Section 3.2.3. The sole difference is in the frequency filters used. They are ({0,1}, {0,1}, {21.97,1}, {31.49,0}); ({0,1}, {0,1}, {24.90,1}, {29.78,0}); ({0,1}, {0,1}, {23.68,1}, {33.45,0}); ({0,1}, {0,1}, {26.86,1}, {36.62,0}) for runs 1 through 4,

119

respectively. The different vertices of the trapezoidal filters stem from the fact that different flowrates were used for the 4 runs.

4.3 Results and Discussion

The following topics are considered: the choice of PG as an IRF-Marker, the observed and the corrected instantaneous rate curves, and the cumulative rate curve. The cumulative rate curve is quantitatively interpreted in terms of theory. Finally the attainment of shallow-bed conditions is discussed.

4.3.1 The choice of PG as an IRF-Marker

The 'desorption' rate curve for the IRF-Marker serves two purposes. First, it is subtracted from the solute run (NA) in order obtain the signal of the actual desorbing solute from that of the solute in between the shallow-bed and detector. Second, its derivative, according to Eq. 2.27 quantifies the effects of band broadening in a Type II shallow-bed instrument. The use of an unretained compound (PG) as the IRF-marker presents problems both with the subtraction step and with obtaining the IRF. Both problems stem from the fact that PG enters the pores of the PRP-1 packing and their origin is discussed in the next two paragraphs.

First, the desorption process of a solute (NA) from a porous particle should include all of that solute that was in the particle, whether by sorption onto or into the walls. or by its

120

presence in the stagnant mobile phase in the pores of the particle. If the PG run (scaled by Eq. 2.24) is subtracted from the NA solute run, an amount of NA equal to that which was in the particle pores is included in the subtraction. This is an error. However, for the desorption of NA from PRP-1, the amount of the solute present in the pores is less than 2 percent of the NA which is sorbed. This can be shown by the following numbers. The retention factor of NA on PRP-1 in 85/15 MEOH/H$_2$O is determined to be 28.5 by column chromatography [46]. Since, for $\varepsilon_{intra} = 0.31$ and $\varepsilon_{inter} = 0.33$ [46], the ratio R, defined as the moles of NA sorbed to the moles of NA in the pores of the particles, is calculated to be equal to 55.3 via Eq. 1.12, and the quantity (100% · 1/55.3) is less than 2%. Thus, the solute in the pores represents a small fraction of the total amount of NA in the particle. Furthermore, the desorption of PG from the pores of the particles takes place very quickly (under 0.1 sec) when compared to the entire desorption process of NA from PRP-1 (about 60 sec). Thus, the error introduced by subtracting this imperfect IRF-Marker is important only at small times and is small in magnitude, and PG can be used without employing any correction.

The second problem has to do with the use of the IRF peak in deconvolution, in order to correct for band broadening. The IRF-curve should arise only from the processes giving rise to the dispersion between the particles of the shallow-bed and the detector. Since the PG which is present in the stagnant mobile phase in the pores of the particles has to diffuse out to the surface of the particle before it is carried away, this pore diffusion of the non-sorbed PG also contributes to the observed band broadening. This creates an error in the determination of the IRF. However, it will be shown in Chapter 5 that the

121

effect of the PG in the pores distorts the shape of the true IRF-curve to a negligible degree; overall this effect, as well as the effect described above, together are expected to introduce an error of less than 5% in the determination of the fast kinetic parameters. Furthermore, and again, the distortion due to the instrument band broadening is important only at short times (approximately 3 s) in this instrument. As stated above, the overall desorption process lasts approximately 60 seconds, and distortions in the early part of the curve are not critically important.

Because of these reasons, the errors introduced by the use of PG as an IRF-Marker are not deleterious to overall information obtainable from the kinetic data. Therefore, it was decided to proceed with the deconvolution using PG, an unretained, but not excluded compound. In Chapter 5, however, kinetic processes lasting only 0.5 seconds to complete take place, and it will be more critical to correct for the fact that PG is not excluded.

4.3.2 Instantaneous Desorption Rate Curves

Four NA desorption runs were performed. The A(t) vs t data for each run were obtained by averaging 4-7 sets of 5 cycles (20-35 cycles) for NA and the same number of cycles for PG, all at the same flowrates (within less than 1% relative). Run 1 was performed with shallow-bed #1, while Runs 2-4 were performed with bed #2.

Data for the first 2 sec in a typical experiment (Run 1) on NA and on PG are shown in Figs. 4.7 and 4.8. Figure 4.7A shows the observed curve of normalized A(t) vs t for the desorption of NA as well as the curve for the IRF-Marker PG. Figure 4.7 B repeats the A(t) vs t curve for the IRF-Marker curve, and also shows the negative derivative of this curve which serves as the IRF in accordance with the discussion of section 2.2.5. All curves have been normalized so that the absorbance of the plateau at the start of the experiment is equal to 1. Figure 4.7 C results from subtracting the dashed line in Fig. 4.7 A from the solid line in Fig. 4.7 A. Figure 4.7 D shows the result of deconvolution of 4.7 C with the solid line in 4.7 B. In order to clarify their significance, the solid curve in panel A, the dashed curve in panel A and B, the curve in C, and the curve in D of Fig. 4.7 may be compared respectively to the corresponding simulated curves: solid line in Fig. 2.6 B, the dashed line in Fig 2.6 B, the shaded part in Fig 2.6 B, and the shaded part in Fig 2.6 A respectively.

Deconvolution and digital filtering in the Fourier domain were performed by the following steps, which are described in more detail in Chapter 2, Section 2.3 [88-90]: complex division of the Fourier transform of curve 4.7 C by the Fourier transform of the solid line in 4.7 B (the normalized PG curve) multiplication of the quotient of this complex division by the trapezoidal filter function ({0,1}, {0,1}, {21.97,1}, {31.49,0}) [88] in order to remove high frequency noise (>31.49 Hz); and inverse Fourier transformation to produce the deconvolved data in the time domain in Fig 4.7 D.

123
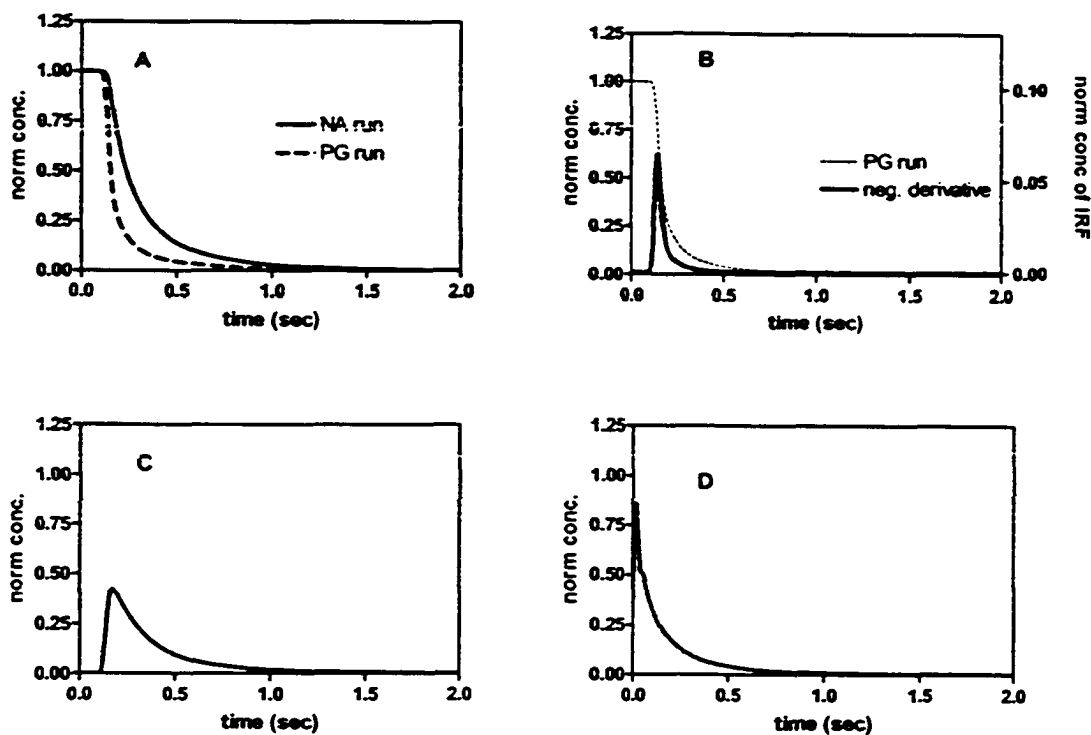
Fig 4.7. Correction for experimental artifacts of the instantaneous desorption rate curve for Run 1. Panel A contains the normalized A(t) values (or normalized concentrations in the detector) observed for the NA run (solid line, average of 20 cycles) and the PG run (dashed line also an average of 20 cycles). Fig 4.7 B shows the PG run again (thin dashed line) and its negative derivative which is used as the IRF (solid line, the y-axis scale for this line is on the right of the panel) Fig 4.7 C shows the difference of the subtraction of the PG curve from the NA curve from panel A. Fig 4.7 D shows the result of the deconvolution of the difference curve in panel C with the IRF in panel B. All runs are shown from 0-2 sec.

124

Fig 4.8 shows a portion of the difference curve and the deconvolved curve from Fig. 4.7 C and D, respectively, for times between 1 sec and 4 sec. Both curves were smoothed by the Savitzky-Golay [107] method in order to facilitate visual comparison. Since the deconvolved curve is automatically corrected for time delay, the difference curve is also plotted on the corrected time axis. The correction is to subtract the center of gravity of the IRF-curve (the first statistical moment) from the time axis of Fig 4.7 C. The center of gravity of IRF is 0.208 sec for run 1, so the time of 0.208 sec in Fig 4.7 C becomes 0.000 in the corrected axis of Fig 4.8. Comparison between the two curves reveals that at times longer than about 3.0 sec they become identical to one another (*i.e.* absorbances at corresponding times agree within 1% relative). This is true for all of the NA runs listed in Table 4.1 (Table 4.1 is found in Section 4.3.3). The significance of Fig. 4.8 is that after about 3 sec the distorting effects of extra particle NA and of band broadening become negligible. The deconvolved curve is noisier because of the small amount of ringing noise associated with deconvolution, which could not be totally reduced by smoothing.

Fig 4.9 shows the deconvolved A(t) *vs* t curves for runs 1-4 using data from 0 to 2 sec. The insets show the deconvolved A(t) *vs* t curves for longer times (*i.e.* for 2 - 69.5 sec). It is quite apparent from the long-time curves that the S/N ratio is low for data much beyond 10 seconds, after which the signal becomes quite small. The baseline exhibits low frequency noise (less than about 0.5 Hz), the magnitude of which was determined to be around $\pm 1 \cdot 10^{-4}$ absorbance units, which is on the order of the A(t) signal from about 20 seconds onward.

125
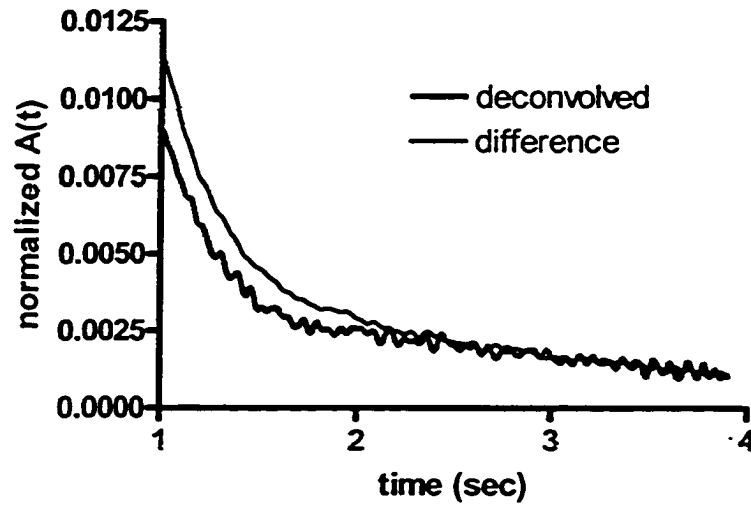
Fig. 4.8. Comparison of the difference curve (plotted vs. corrected time) and the deconvolved curve for Run 1, from 1 to 4 sec. At times beyond 3 seconds, the deconvolved curve (the grey line) from Fig 4.7 D and the difference curve from Fig 4.7 C (black line) are within 1% relative on averaged. The deconvolved curve is noisier because of the ringing noise introduced by a frequency filter during deconvolution.

126
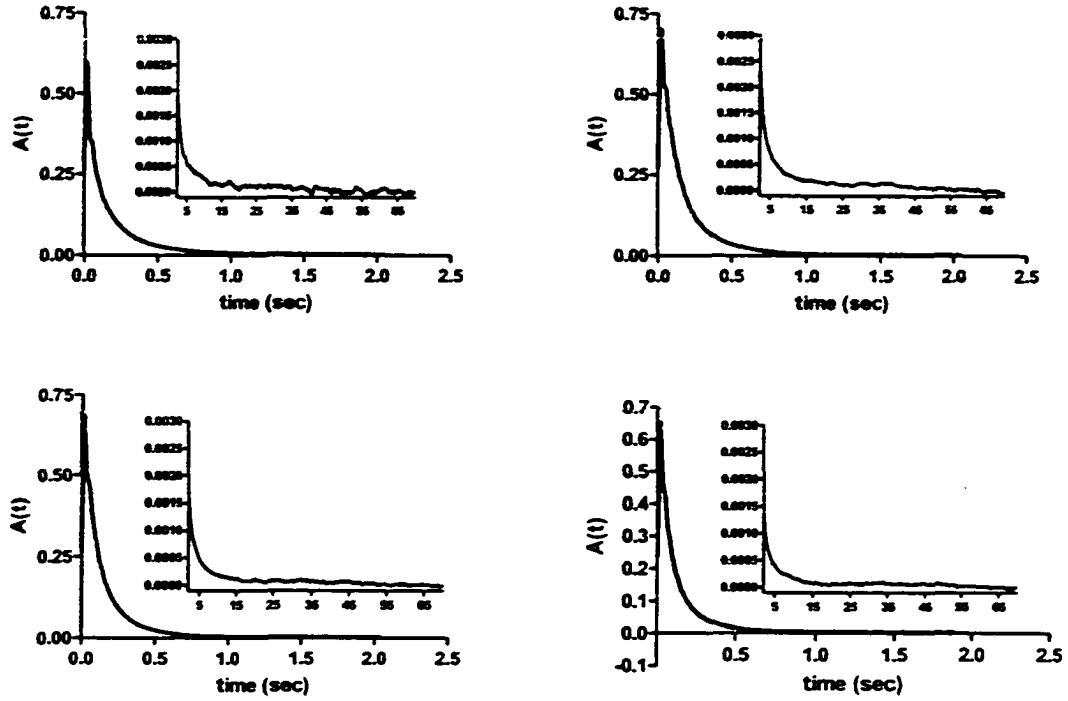
Fig. 4.9. Deconvolved A(t) vs. t curves for the desorption of NA from PRP-1. Panels A-D contain Runs 1-4 respectively. The main part of each panel shows the deconvolved curve from 0-2 sec, while the insets show the desorption curve from 2 seconds onward.

127

4.3.3 Cumulative desorption rate curve for NA

The deconvolved instantaneous rate curves (e.g. Fig. 4.9) were digitally integrated between 0 and 69.5 sec for all four experimental runs using Excel software. The average absorbance between 60 and 70 sec was taken as baseline and the results of the integrations were multiplied by $F/\varepsilon_i l$ in order to obtain the cumulative rate curves for desorption of NA, as described by Eq. 2.29. The cumulative rate curves for Runs 1-4 are shown in Fig. 4.10 as solid lines, each one of which is actually composed of 17500 data points. Prism Software Version 4.00 (GraphPad Software, San Diego, CA) was used to fit Eq. 2.1, describing spherical diffusion (20 exponential terms), as well as Eq. 2.4, describing biporous spherical diffusion (11 terms each for the fast and slow process), to all of the points starting at 0.024 sec. The use of 11 terms in Eq. 2.4 does not allow for fitting times shorter than 0.024 sec.

The non-linear regression fit-lines of Eq. 2.1 (spherical diffusion) to the data for Runs 1-4 are shown with a thin dashed line in Fig. 4.10. The correlation coefficient (R^2) values are 0.768, 0.744, 0.769, and 0.693 for Runs 1 through 4, respectively, which indicates a bad fit to the data points. The non-linear regression fit-lines of Eq. 2.4 (biporous spherical diffusion) to the data for Runs 1-4 are shown with thick dashed lines in Fig. 4.10. Fitting parameters $n_{i,0}$ and β and other parameters for all four runs are summarized in Table 4.1. Correlation coefficients (R^2) are much higher (though not very high) suggesting that Eq. 2.4 describes the data much better than Eq. 2.1. The average values, with standard deviations (n =4), of parameters β_1 (fast desorption rate constant, Eq. 2.3) and β_2 (slow

128
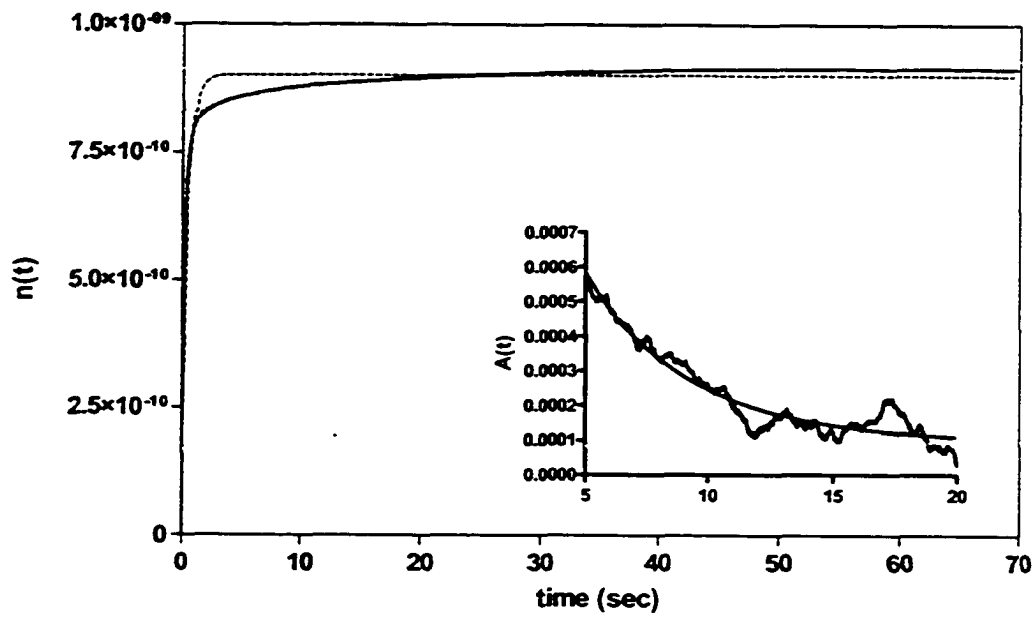
Fig 4.10 A. Fits of Eq 2.1(thin dashed line) and 2.4 (grey line) to the cumulative NA desorption curve from PRP-1 for Run 1, integrated from 0-69.5 sec. Inset: Fit of Eq. 2.30 to the instantaneous A(t) vs t data from 5-20 secs using non-linear regression.

129
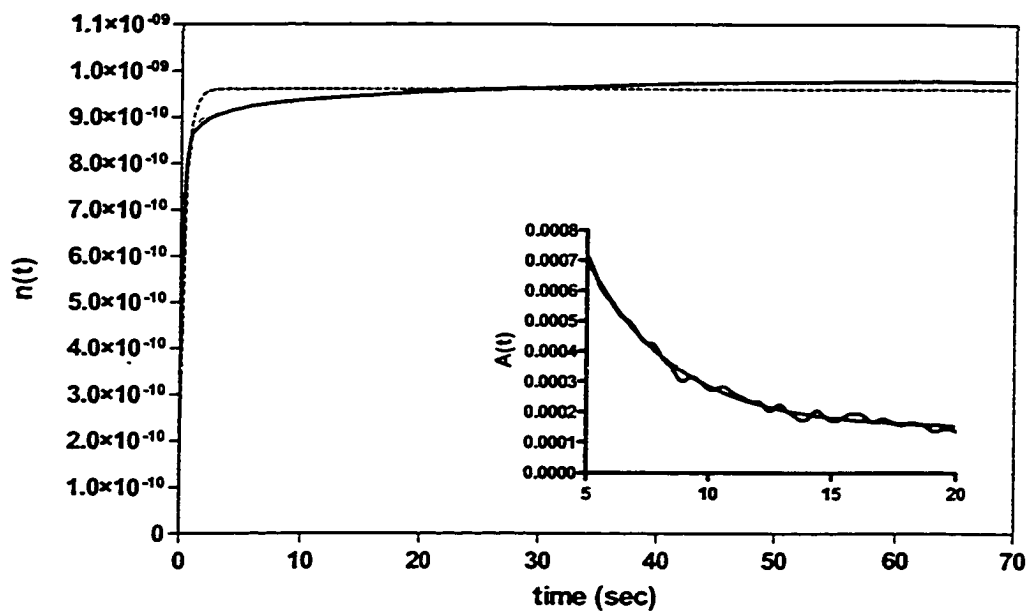
Fig 4.10 B. Fits of Eq 2.1 and 2.4 to the cumulative NA desorption curve from PRP-1 for Run 2, integrated from 0-69.5 sec. Inset: Fit of Eq. 2.30 to the instantaneous A(t) vs t data from 5-20 secs using non-linear regression.

130
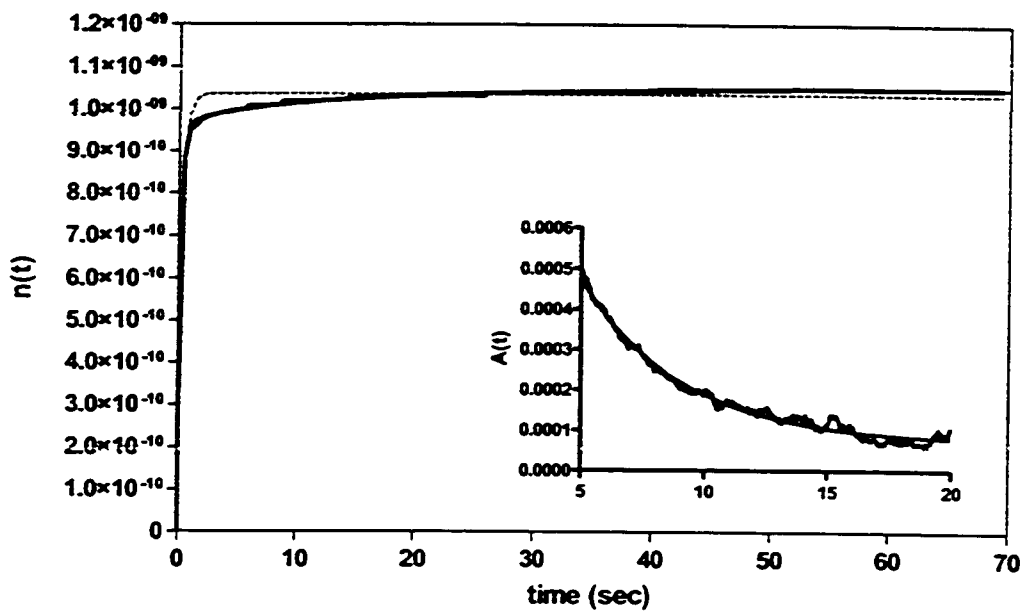
Fig. 4.10 C. Fits of Eq 2.1 and 2.4 to the cumulative NA desorption curve from PRP-1 for Run 3, integrated from 0-69.5 sec. Inset: Fit of Eq. 2.30 to the instantaneous A(t) vs t data from 5-20 secs using non-linear regression.

131
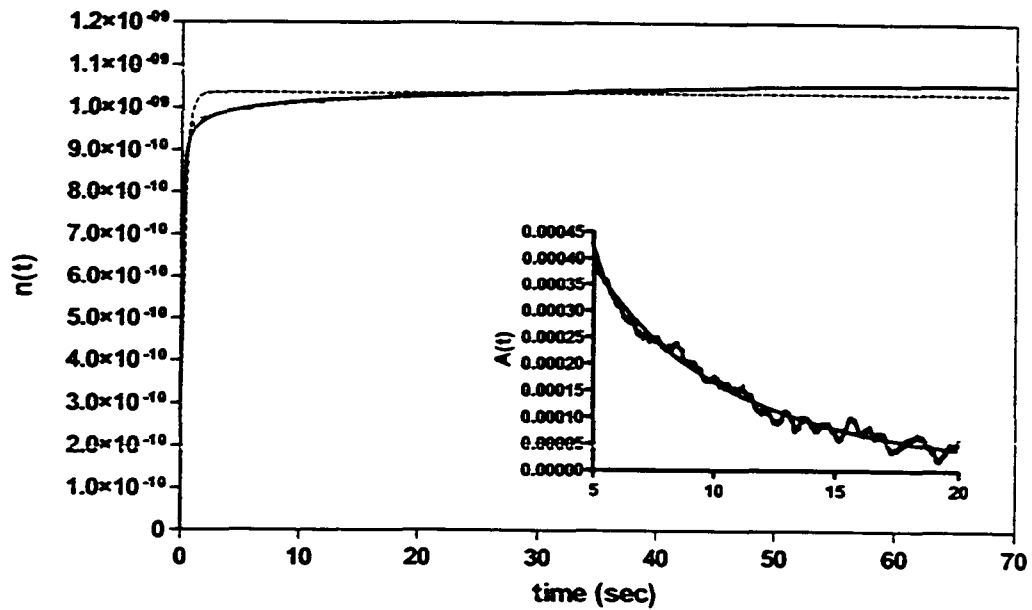
Fig 4.10 D. Fits of Eq 2.1 and 2.4 to the cumulative NA desorption curve from PRP-1 for Run 4, integrated from 0-69.5 sec. Inset: Fit of Eq. 2.30 to the instantaneous A(t) vs t data from 5-20 secs using non-linear regression.

132

Table 4.1. Parameters from non-linear regression fit of Eq. 2.4 for biporous spherical diffusion to the cumulative desorption rate curves of NA ($n_{i,0,fast}$, $n_{i,0,slow}$, β_1 and β_2 are fitting parameters).

Result/Parameter	Run 1[a]	Run 2[b]	Run 3[b]	Run 4[b]
m_{SB} ($\times 10^3$ g)	0.505	0.51	0.51	0.51
$[i]_{MP}$ ($\times 10^4$ mol/L)	0.493	0.499	0.499	0.499
F ($\times 10^5$ L/s)	14.3	10.9	14.4	17.5
$n_{i,0,fast} + n_{i,0,slow}$ ($\times 10^{10}$ mol)	9.2	9.8	10.5	10.6
$n_{i,0,fast} / n_{i,0,slow}$	0.16	0.14	0.11	0.12
β_1 (s^{-1})	3.2	3.4	4.0	4.4
β_2 (s^{-1})	0.069	0.050	0.061	0.038
R^2	0.9943	0.9883	0.9831	0.9862

[a] Run 1 was performed on shallow Bed # 1, and it is an average of 20 NA cycles subtracted from 20 PG cycles

[b] Runs 2-4 are performed with Bed # 2. Runs 2 and 3 are both average of 25 cycles of NA and PG, while Run #4 is an average of 35 cycles.

desorption rate constant, Eq. 2.5) for the two diffusion processes, with standard

deviations, are $\beta_1 = 3.7 \pm 0.5$ s^{-1} and $\beta_2 = 0.055 \pm 0.013$ s^{-1}. The value for D_i in the

mesopores (fast process) is calculated from β_1 *via* Eq. 2.3 to be $(9.4 \pm 1.3) \cdot 10^{-7}$ cm^2 s^{-1}.

The value for D_i inside the PRP-1 matrix will be discussed below in Section 4.3.7,

because its calculation from β_2 requires knowledge of the microspherical aggregate

radius. The ratio of the equilibrium moles sorbed into the matrix to the moles adsorbed

onto the pore walls is, $n_{i,0,slow}/n_{i,0,fast}$, $= 0.13 \pm 0.02$. Previously reported values for these

parameters which were obtained from shallow-bed **sorption** rate experiments [28], are β_1

$= 1.7 \pm 0.3$ s^{-1}, $\beta_2 = 0.086 \pm 0.007$ s^{-1} and $n_{i,0,slow}/n_{i,0,fast} = 0.1 \pm 0.03$, based on 4 kinetic

runs. The comparison of the present values with the sorption values reveals that both β_1

(and D_i for the mesoporous diffusion, which is proportional to β_1), and β_2 fail the t-test at

the 99% level, while the values for $n_{i,0,slow}/n_{i,0,fast}$ pass the t-test at the 95% confidence

level. The diffusion parameter for mesopores is more than 2 times higher in the present

case, while the diffusion parameter in the micropores is about 35% lower. The ratio of

moles in the matrix to that adsorbed on the mesopore walls, obtained from fitting the

present data to the biporous equation is statistically indistinguishable from the previous

results.

4.3.4 Linear Isotherm

The sorption isotherm of NA from 85/15 MeOH/H$_2$O onto PRP-1 has been previously

found to be linear up to a solution concentration of about 5×10^{-4} mol/L, with a

distribution coefficient of 0.039 L/g [28, 46]. Since the loading step of PRP-1 was done

134

with solutions containing this concentration or less, all experiments were performed in the linear region of the NA isotherm.

4.3.5 Shallow-bed conditions

The requirements which need to be met for the achievement of shallow-bed conditions have already been discussed in Section 2.4 and Section 3.3.4. In short, shallow-bed conditions can be effectively achieved if the maximum desorbing solute concentration never exceeds a very small fraction of the feed-solution concentration. For this purpose it is useful to refer to Fig 4.7, which has been normalized so that the absorbance (or concentration) of the feed solution is equal to 1. The plot of the normalized, deconvolved desorbing concentration is shown in Fig 4.7 D. It is apparent that at small times the desorbing concentration is almost equal to the feed concentration. Therefore the requirement of zero solute concentration is clearly not achieved in this case. This is true for all the runs.

Whenever failure to meet shallow-bed conditions is suspected, it is useful to fit the desorption data with an equation which accounts for this effect. Eq. 2.32 takes into account non-shallow bed conditions and/or film diffusion, and the magnitude of one of its fitting parameters, L, is indicative of the presence of one or both of these retarding effects on the desorption rate. When the parameter L in that equation has a small value (less than ~ 25) it signifies either a failure to meet shallow bed conditions and/or a significant

135

presence of film diffusion. However, Eq. 2.32 can be applied only to spherical particles with a single intraparticle diffusivity (monoporous), while the PRP-1 particles studied here are biporous. While a solution to this problem will be attempted in a later section, it is useful here to estimate whether shallow-bed conditions, though not met rigorously, are approximately met by using known experimental parameters and conditions. Eq. 2.34 relates the value of L to the flowrate, the amount sorbed, and the kinetic parameters of a sphere [72]:

$$L = \frac{F[i]_{MP} \, \pi}{3 \, n_{i,0} \, \beta} \tag{2.34}$$

When Eq. 2.34 is applied to the fast-sites (using the values of F, $n_{i,0,fast}$, and β_1 from Table 4.1) the average magnitude of L is only about 6, which is not large. (Compare this value to the value $2.1 \cdot 10^3$ from the conditions in Chapter 3). Therefore, according to this criterion also, it is expected that shallow-bed conditions are not met. This means that the values of β_1 in Table 4.1 have a systematic error. In contrast, when Eq. 2.34 is applied to the slow sites, the average value of L increases to more than 3000, meaning that the values of β_2 are free of such systematic error. That is, while shallow-bed conditions are not met for the purpose of quantifying the kinetic parameters for fast desorption of NA from the mesopore walls, they are met for the purpose of quantifying the kinetic parameters for slow desorption from the polymer matrix.

The effect of flowrate at short times can be seen in Fig. 4.11 A, which shows the data points for the cumulative curves for Runs 1-4 plotted from 0 to 0.05 seconds. They are normalized so that the y-axis units are the fraction of the total moles desorbed in order to

136
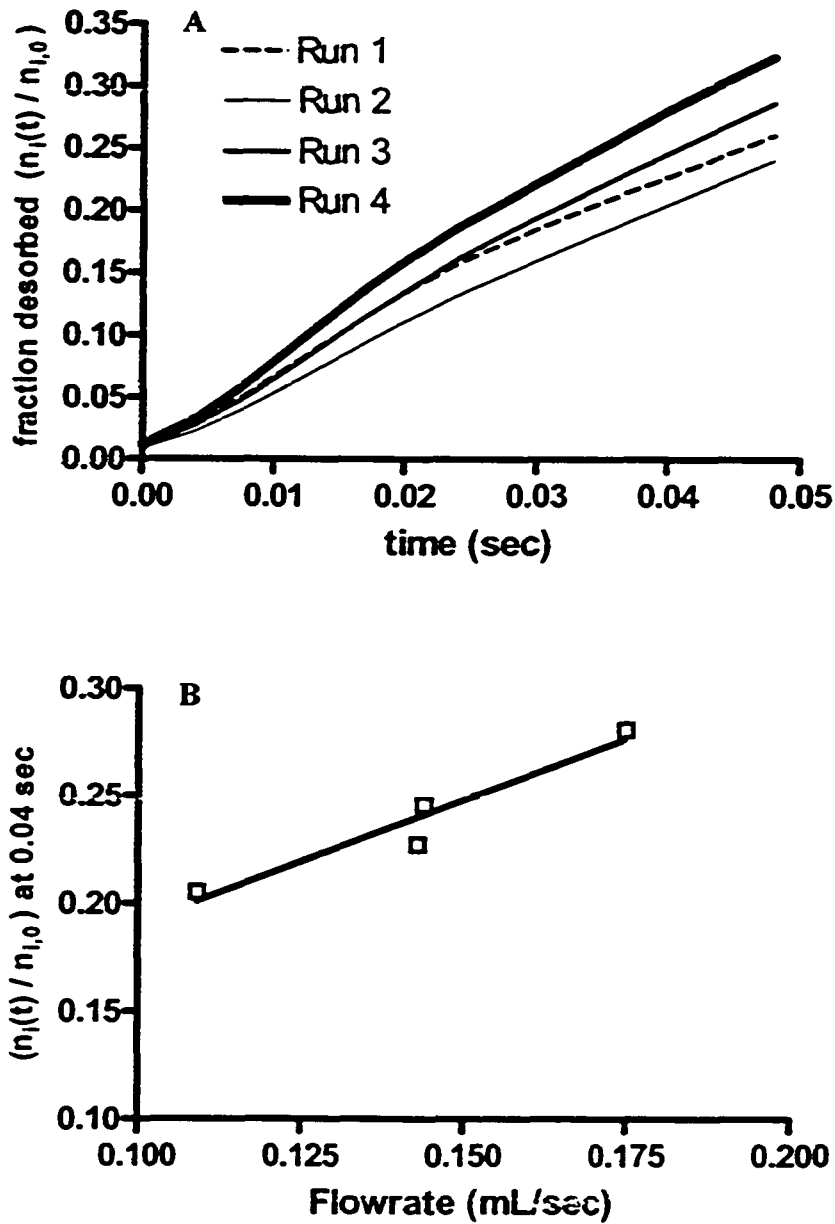
Fig 4.11. Effect of flowrate on the fraction desorbed at small times. Panel A shows the fraction desorbed vs. time for Runs 1-4. Run 1, which is performed with a separate bed from Runs 2-4, is shown as a dashed line. For runs 2-4 the flowrates used are in ascending order (Run 2 has the slowest flowrate and Run 4 the fastest). The flowrate in Run 1 is nearly identical to that for Run 3. See Table 4.1 for details. Panel B shows the fraction desorbed at 0.04 sec. vs. flowrate.

137

account for the minor differences in the $n_{i,0}$ values in Table 4.1. The trend in the figure is that the desorption rate at these short times is faster for runs carried out at larger flowrate. Fig 4.11 B shows the fraction desorbed at 0.04 sec vs flowrate, and it is evident that there is a positive dependence on the flowrate. This is consistent with the low value of the parameter L for the fast sites.

4.3.6 Slow particle diffusion

The value of the parameter ($\beta_2 = 0.055 \pm 0.013$ s^{-1}) obtained from Fig 4.10 is statistically different from the value of 0.086 ± 0.007 s^{-1}, obtained in the sorption experiment [28], at the 99% confidence level, according to the t-test. The primary reason for this discrepancy is the effect of the relatively large baseline noise, which makes it difficult to determine accurately the kinetic parameters through fitting to Eq. 2.4. As seen in Chapter 3, another way to measure β_2 involves using long time data from the differential (instantaneous) rate curves such as the one shown in the inset in Fig 4.9. A plot of the natural logarithms of A(t) vs time for only the data at very long times is expected to be linear because Eq. 2.30 (describing instantaneous absorbance observed downstream from a shallow-bed where desorption is proceeding via spherical diffusion) reduces to a single exponential term as the higher order terms become negligible. This approximation is allowed when the value of $t \cdot \beta_2/\pi^2 > 0.05$ to 0.1, depending on different authors [27, 51]. Assuming that the value of β_2 is either 0.05 or 0.1, the times after which this approximation may apply is either 5 or 10 seconds. When the semilog plot is fit from 5 to 20 seconds (plots not shown) the results among the four runs are $\beta_2 = 0.12 \pm 0.02$ s^{-1},

138

but the R^2 values are low (0.795, 0.9196, 0.9386, 0.9418 for Runs 1-4, respectively), which is mainly due to the rather low S/N ratio which can be seen in Fig 4.9 at t > 10 sec.

An alternative approach is to directly fit the A(t) vs. t data at long times in Fig 4.9 with Eq 2.30 by means of non-linear regression. The advantage of fitting the full Eq 2.30 is that it does not rely on the validity of the assumption that all but the first exponential term are negligible. The times fit are greater than 5 seconds, to insure that there is no contribution from the fast desorbing sites, and smaller than 20 seconds, to ensure an acceptable S/N ratio. Ten terms are actually used in fitting Eq. 2.30 (which has an infinite number of terms), but 10 terms are more than enough to represent the curve at times longer than 5 seconds. These data are shown as insets in Fig 4.10. The fitting results obtained are $\beta_2 = 0.13 \pm 0.02 \text{ s}^{-1}$, with $n_{i,0,slow} = 1.2 \cdot 10^{-10}$, $1.08 \cdot 10^{-10}$, $0.97 \cdot 10^{-10}$, and $1.02 \cdot 10^{-10}$ for runs 1-4 respectively, and R^2 values of 0.9155, 0.9582, 0.9706, and 0.9831. This value of $n_{i,0,slow}$ and the value $n_{i,0,fast}$ from Table 4.1 yield a ratio of $n_{i,0,slow}/n_{i,0,fast} = 0.12 \pm 0.02$, which is in agreement with both the values obtained from the cumulative desorption curves (0.13 ± 0.02) and the values obtained from sorption rate experiment (0.1 ± 0.03) in reference [28]. The value β_2 is, however, more than twice that obtained by fitting the cumulative data with Eq. 2.4. As well the R^2 values are still relatively low, most likely due to the presence of low frequency noise.

Table 4.2 shows the values of parameter β_2 obtained via different methods described above. From these data, it seems that the best way to express this value, along with a

Table 4.2. Parameters for the slow particle diffusion process obtained by different means.

Method used to obtain parameters	$\beta_2 (s^{-1})$	$n_{i,0,slow}/ n_{i,0,fast}$ [a]
Fit of cumulative desorption curve to Eq. 2.4 (from Table 4.1, and Fig. 4.10)	0.055±0.013	0.13±0.02
Fit of instantaneous desorption curve to Eq. 2.30 (5-20 sec, from insets of Fig. 4.10)	0.13±0.02	0.12±0.02
Linear fit of a semilog plot of instantaneous desorption curve (5-20 sec)	0.12±0.02	0.12±0.02
Fit of cumulative sorption curve to Eq. 2.4 (reference [28])	0.086±0.007	0.1±0.03

[a] The value of $n_{i,0,fast}$ used is the average from Table 4.1.

140

95% confidence interval , is $\beta_2 = 0.1 \pm 0.05$ s^{-1}. This means that there is 95% chance that β_2 lies between 0.05 and 0.15 s^{-1}.

The diffusion coefficient inside the matrix of PRP-1 can be estimated from the value of $\beta_2 = 0.1$ s^{-1} and the radius of the microspherical aggregates in PRP-1 by rearranging Eq. 2.5.

$$\beta_2 = \frac{\pi^2 D_{matrix}}{r^2_{microsphere}} \qquad (2.5)$$

The $r_{microsphere}$ can be estimated as follows: In porous particles used for HPLC the pore-size (10 nm for PRP-1) is of the same order of magnitude as the diameter of the microspherical aggregates in between which the pores exists [1]. Therefore, the value of $r_{microsphere}$ can be assumed to have a value of approximately 5 nm. Rearrangement of Eq. 2.5 gives a value of the $D_{matrix} \sim 3 \cdot 10^{-15}$ cm^2 sec^{-1}.

4.3.7 Estimating the value of D_i for the fast sites.

The discussion from Section 4.3.5 suggests that while shallow-bed conditions are met for the slow sites, they are *not* met here for the fast sites of PRP-1. When this is the case, an erroneous value of D_i is obtained from fitting with Eq. 2.4, because it doesn't account for the effect of slow flowrate. It is thus desirable to fit the data with Eq. 2.32 which does account for effect of slow flowrate [72]. However, Eq. 2.32 assumes that the spherical particles are monoporous (have only one intraparticle diffusion coefficient) while PRP-1

141

is a biporous particle, (displays slow and fast intraparticle diffusion coefficients). It is therefore desirable to subtract the contribution of the slow-sites before fitting with Eq. 2.32 , so that only the data relating to the fast-sites remain. The best fit values of β_2 and $n_{i,0,slow}$ for Runs 1-4 from Table 4.1 were used to model the slow part via Eq. 2.1, and the modeled curves were subtracted from the overall desorption rate curves for Runs 1-4. The resulting difference represents the fast sites only and is shown from 0 to 1 seconds as the solid line (actually 250 data points) in Fig 4.12 for Run 1. The fit of Eq. 2.32 to this fast-site-only curve for Run 1 is shown in Fig 4.12 as the thick grey line. The fit to Eq.2.32 is very good with a high R^2 value ($R^2 = 0.9993$). The best fitting parameters for the fast sites of all the Runs 1-4 are shown in Table 4.3: the average mesoporous diffusion coefficient for all the runs is determined to be $D_i = (3.0 \pm 0.7) \times 10^{-7} \text{ cm}^2 \text{s}^{-1}$ while the values of L range from 2.0 to 4.5. Also shown in Fig 4.12 is a fit of the spherical diffusion equation (Eq. 2.1) to the same data, represented as a thin dashed line. This fit is much poorer, with an R^2 value of 0.9826. Similar R^2 values (~0.98) are obtained for all four runs. It is apparent from the smaller R^2 value and from visual inspection that, for times shorter than 1 sec, Eq. 2.1 does not fit the data as well as Eq. 2.32 does, and therefore, that the desorption data are not described by spherical diffusion alone, but the effects of film diffusion and/or non-shallow bed conditions are also important. It is thus more likely that the true mesoporous diffusion coefficient is closer to the values obtained by fitting the fast-only rate-curve with Eq. 2.32 [$D_i = (3.0 \pm 0.7) \times 10^{-7} \text{ cm}^2 \text{s}^{-1}$], than to the value of D_i obtained in Section 4.3.3 by fitting the entire cumulative rate curve with the biporous model of Eq. 2.4 ($D_i = 9.4 \times 10^{-8} \text{ cm}^2 \text{s}^{-1}$).
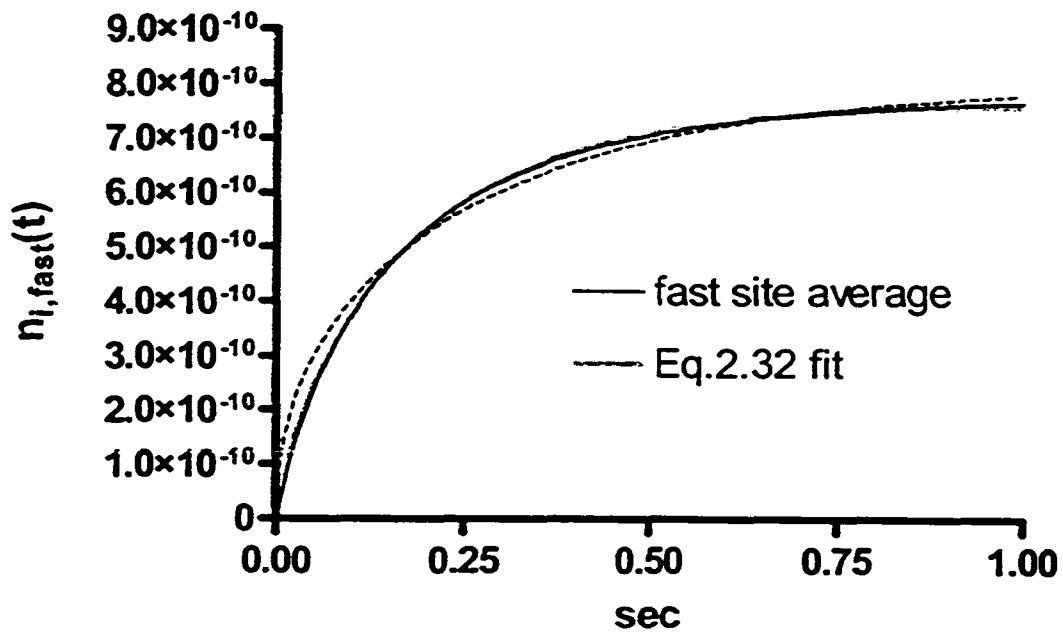
Fig. 4.12. The averaged desorption cumulative data for fast sites for Run 1, corrected by subtracting the contribution of slow sites. Solid line is the corrected data, actually made up of 250 data points. The thick gray line is the fit to Eq. 2.32, while the thin dashed line is the fit to Eq. 2.1.

143

Table 4.3. Parameters from non-linear regression fit of Eq. 2.32 to the cumulative desorption rate curves for mesoporous diffusion only (fast sites), after subtracting the slow part ($n_{i,0,fast}$, D_i, and L are fitting parameters).

Result/Parameter	Run 1[a]	Run 2[b]	Run 3[b]	Run 4[b]
m_{SB} ($\times 10^3$ g)	0.505	0.51	0.51	0.51
$[i]_{MP}$ ($\times 10^4$ mol/L)	0.493	0.499	0.499	0.499
F ($\times 10^5$ L/s)	14.3	10.9	14.4	17.5
$n_{i,0,fast}$ ($\times 10^{10}$ mol)	7.7	8.3	9.1	9.1
D_i ($\times 10^7$ cm^2 s^{-1})[c]	1.9	3.5	3.4	3.1
L	4.5	2.0	2.6	3.6
R^2	0.99934	0.999114	0.99887	0.99848

[a]   Run 1 was performed on shallow bed#1, and it is an average of 20 NA cycles subtracted from 20 PG cycles

[b]   Runs 2-4 are performed with bed #2. Runs 2 and 3 are both average of 25 cycles of NA and PG, while Run #4 is an average of 35 cycles.

[c]   Mean value for Runs 1-4 is $D_i = (3.0 \pm 0.7) \times 10^{-7}$ cm^2 s^{-1}

144

The effects of the failure to meet shallow bed conditions and/or external film diffusion were not accounted for in the previous **sorption** studies, described in Reference [28] for which a similar value of L ($\sim$ 6), can be calculated using Eq. 2.34. The mesopore diffusion coefficient reported from previous work by sorption is $(4.2 \pm 0.8) \cdot 10^{-8}$ cm^2 s^{-1}. This value was obtained by fitting the **sorption** rate data to Eq. 2.4, which is not correct in view of the above discussion. However, the reported sorption rate value should still be in agreement with the current value obtained by fitting the **desorption** rate data to Eq 2.4 [$D_i = (9.4 \pm 1.3) \cdot 10^{-8}$ cm^2 s^{-1}]. Yet they are statistically different and fail the t-test at the 99% confidence level. One plausible explanation for this fact is that the **sorption** data suffers from undersampling at short times. In the **sorption** study, there were only three data points collected in the first 2 seconds, while in the present case there are 500 data points in the first 2 seconds. The combination of poor fit of Eq. 2.4 to the data at short times combined with undersampling and the effect of data scatter likely accounts for this discrepancy.

The relative contributions of particle diffusion and film diffusion to the desorption rate from the fast sites of PRP-1 can be estimated by evaluating the relative contributions of the two processes with Eq. 2.14. For NA, D_{MP} is 1.1×10^{-5} cm^2 s^{-1} and D_i is 3×10^{-7} cm^2 s^{-1} (value obtained after accounting for small value of L), the ratio $[i]_{part} / [i]_{MP}$ is calculated from $\kappa = 0.039$ L/g and the density of 0.61 L/g [28, 46] to be about 25.5. If ε_{inter} (between the particles) is assumed to be approximately 0.4, and the fraction of the shallow-bed taken up by the grids (100 μm holes and 30 μm walls) is approximately 0.41, a value of $\delta = 0.34$ μm is calculated for the fastest flowrate (Run 4, 0.17 mL s^{-1}), while δ

145

= 0.40 μm is calculated for the slowest flowrate (Run 2, F = 0.11 mL s^{-1}). The value of δ

is calculated using the average of Eq. 2.12 and 2.13 for the Sherwood number. The value

of X from Eq. 2.14 ranges from 0.11 for the slowest to 0.10 for the highest flowrates used

in Table 4.1. These values are only slightly smaller than 0.13. This shows that the

desorption rate is significantly retarded by film diffusion, in addition to the already

existing distortion due to the failure to meet shallow-bed conditions. This reinforces the

fact that some error is to be expected in the determination of the diffusion coefficient by

fitting the desorption curve with purely intraparticle diffusion equations, neglecting film

diffusion, which is consistent with the results of Section 4.3.5

4.3.8 Mesoporous diffusion

The diffusion coefficient for NA in the mesopores obtained from fitting Eq. 2.32 to the

cumulative desorption rate curve is $D_i = 3.0 \cdot 10^{-7}$ cm^2 s^{-1} (Table 4.3). If NA was to

diffuse inside the mesopores of PRP-1 via sorption-retarded pore diffusion (SRPD), the

expected diffusion coefficient for NA in the mesopores of PRP-1 can be calculated via

Eq. 1.16 as follows. The parameter $D_{MP} = (1.1 \pm 0.2) \cdot 10^{-5}$ cm^2 s^{-1} for NA in 85/15

MeOH/H$_2$O (from the Wilke-Chang correlation [99]), the parameter R in Eq. 1.16, for the

fast step, which the ratio of NA in the pores to the moles adsorbed on the pore walls but

not sorbed into the matrix, can be calculated as approximately $0.9 \cdot R = 49.7$ (R has

already been calculated in section 4.3.1 to be 55.3). Tortuosity is assumed to have the

value of 2 ± 0.5, as discussed in sections 1.3.2 and 1.5.2. The hindrance parameter for

NA (molecular diameter of 6.2 Å) inside the mesopores of PRP-1 (average pore size of

75 Å) is estimated to be 0.7 ± 1 [27, 30, 31]. The estimated diffusion coefficient for NA assuming SRPD mechanism is then calculated *via* Eq. 1.16 to be $(7.6 \pm 2) \cdot 10^{-8} \ cm^2 \ s^{-1}$. This value is 4 times lower than the D_i value obtained from the fit with Eq. 2.32. It is thus likely that the majority of NA diffusive flux is occurring via surface diffusion, with a surface diffusivity of $D_S \sim 2 \cdot 10^{-7} \ cm^2 \ s^{-1}$ (calculated from Eq. 1.11).

4.3.9 Summary of sources of error

There are several possible sources of error in the determination of the kinetic parameters in this chapter.

(1). The error from using PG as an IRF Marker. The fact that PG enters the pores of PRP-1 makes it a potentially problematic IRF-Marker, as discussed in section 4.3.1. The error that this contributes to estimating the diffusion coefficient inside PRP-1 is fully treated in Chapter 5, where it is determined that the use of PG as the IRF-Marker gives errors of less than 5% in the value of D_i. In Chapter 5, the solute in the pores comprises 3% of the solute inside the particle at sorption equilibrium. In this chapter, the solute in the pores makes up an even smaller fraction of the total solute in the particle – less than 2%. Therefore, this error will be even smaller here.

(2). Error in estimating the fast-site rate curve by subtracting the second term from Eq. 2.4. In Section 4.3.7, it was necessary to approximate the shape of the cumulative

desorption rate curve due only to the mesoporous diffusion (fast sites). To do this, the effect of the slow sites was subtracted from the overall cumulative rate curve, based on their best-fit parameters for β_2 and $n_{i,0,slow}$, to the biporous diffusion equation (Eq. 2.4). However, the best fit values of β_2 show a considerable amount of variability between runs, and they also vary depending on the method used to obtain them (See Table 4.2) showing that this parameter is not known very accurately. In addition, the assumption that there are only two types of sites in PRP-1 is an oversimplification. There likely exists some sort of gradient between the fast and the slow sites, which means that they cannot be fully described by two distinct diffusion coefficients. Moreover, Eq. 2.4 is strictly valid only when the ratio of $\beta_1/\beta_2 > 1000$, which is the point where the two parameters become roughly independent of each other [78]. However, Table 4.1 shows that the ratio of $\beta_1/\beta_2 \sim 70$ in this case. This suggest that at small times the slow component desorption rate is actually affected by the presence of the faster component and its desorption rate would not strictly follow spherical diffusion.

(3). Effect of slow flowrate and extraparticle effects on estimating the mesoporous diffusion coefficient. The second source of error, in addition to that associated with subtraction of the slow part of the rate curve above, is that the magnitude of extraparticle effects is large (*i.e.* the value of L in Table 4.3 is low – from L = 2 to L =4.5). Therefore extraparticle effects have a major contribution to the observed shape of the desorption rate curve associated with mesoporous diffusion. Obtaining D_i from the fitting of such desorption data to Eq. 2.32, corrects for this in principle but, in practice, it is prone to errors analogous to when a minor component is calculated by subtraction of larger components from an overall sum. The best way to reduce this effect is to flow faster or

148

to use less stationary phase in the shallow bed (in order to increase parameter L from Eq. 2.32 through Eq. 2.35), however, this decreases the S/N ratio (See Eq. 2.30).

(4). Error in estimating the slow sites from the whole rate curve. As discussed above in the second source of systematic error there are likely to be sites having intermediate rates between the fast and the slow sites, and their time constants are likely not completely independent. This not only causes error in the estimation of the fast-site rate curve, but also in the determination of the slow–site rate curve. Such error is at least partially remedied by fitting only the data after 5 seconds, were there is much less influence from the faster sites, as shown in the insets of Fig. 4.10. As can be seen in Table 4.2 values estimated in this way are larger (0.13 ± 0.02 s^{-1}) than the values estimated from fitting the whole curve (0.055 ± 0.13). However, as can be see in the insets of Fig. 4.9 and Fig 4.10, at these longer times, the S/N is relatively low. This random error reduces the precision with which β_2 can be measured.

The S/N could be increased by lowering the flowrate. If the flowrate is slower the concentration desorbing is higher which increases the signal observed, while the magnitude of the instrumental noise remains roughly the same. Together this increases the S/N ratio would reduce the uncertainty in the value of β_2. However, decreasing the flowrate would be detrimental to measuring the fast-site rate since it would decrease the value of parameter L.

To sum up, the flowrate used is too slow to determine the diffusion coefficient in the mesopores with good accuracy (because of small value of L), and yet it is also too fast to accurately determine the slow diffusion kinetic parameter (low S/N). Separate experiments would be required for the fast and slow processes. Even if that was done, it

149

has to be remembered that the assumption of two diffusion coefficients inside the PRP-1 is a simplification; the border between the fast and slow diffusion sites may not be sharp and there could be a continuum of sites between them.

4.4 Summary

The low extra-bed band broadening Type II instrument was designed to study desorption kinetics from small HPLC-sorbent particles via the continuous monitoring shallow bed technique. The use of an IRF-Marker, deconvolution, and other data-processing methods corrects for the band broadening effects which remain. The technique allows for the monitoring of the desorption rate with a very high sampling frequency to give a large number of data points. The data obtained were fit to a conventional biporous diffusion model [28, 78] and the results show that the sorption/desorption rate of NA into/from PRP-1 involves both a fast and a slow diffusion process, with a majority of the capacity belonging to the fast sites. In addition, systematic sources of error, such as failure to meet shallow bed conditions and the presence of external film diffusion have been identified, and their effects have been compensated for by using an appropriate theoretical model. The compensated results show that the intraparticle mesopore diffusion coefficient is faster than that originally measured. This suggests that surface diffusion could play an important role in the intraparticle mass transfer of NA inside PRP-1.

Chapter 5: Fast desorption of 1,2-dimethyl-4-nitrobenzene from Luna C-18 using Type II instrument

In Chapter 4 the Type-II shallow-bed instrument was used for continuous monitoring of desorption from the mesoporous polymeric HPLC packing PRP-1, which contains both fast and slow diffusion regions. The flowrate could not be made large enough to closely approach shallow bed conditions for the fast sites due to several experimental limitations such as the need to have a large amount of packing, which caused a large resistance to flow. In this chapter the Type-II apparatus is applied to the measurement of desorption kinetics from an ODS HPLC packing, which exhibits only fast desorption. Small modifications to the apparatus, procedure, and data processing are carried out in order to increase flowrates and enable the study of sub-second desorption processes. The data are interpreted in terms of pore and surface diffusion.

5.1 Introduction

Luna C-18 is a porous ODS HPLC packing. Intraparticle mass-transfer inside can proceed through two parallel processes: pore diffusion through the liquid-filled pores and surface diffusion of the adsorbed solute along the walls, which are lined with an octadecyl silane (ODS) monolayer. To date, a limited number of studies have been devoted to intraparticle mass transfer inside ODS HPLC packings. They include luminescence studies and column chromatography, which are described in Chapter 1, section 1.5. Evidence gathered through luminescence studies [19-24] suggests that surface diffusivity along the C-18 derivatized silica can be almost as large as that in free

151

solution and can range between $2.5 \cdot 10^{-7}$ to $6.5 \cdot 10^{-6} \text{cm}^2/\text{sec}$ (free solution diffusion coefficients are typically $4 \cdot 10^{-6}$ to $10 \cdot 10^{-6} \text{cm}^2/\text{sec}$ [27, 52, 99]). As well, column chromatography studies (see Chapter 1, Section 1.5.1) suggest that surface diffusion is the dominating mode of intraparticle transfer in ODS silica, with the values of surface diffusion coefficients falling in a similar range ($3 \cdot 10^{-7}$ to $5 \cdot 10^{-6} \text{cm}^2/\text{sec}$) depending on the mobile phase used and the strength of retention (with more viscous eluents and more retained compounds leading to lower surface diffusivities[56]). However, because of experimental difficulties associated with fast heterogenous kinetics, no studies have been carried out that directly measure the overall uptake/release rates (which could include film or intraparticle diffusion, or slow chemical kinetics) of **microparticulate** ODS packings. For example, temperature jump and pressure jump methods [20, 21, 23, 24] measure only the rate processes discussed Section 1.3.1. This chapter reports, for the first time, the direct measurement of desorption kinetics from ODS packings used in HPLC, and the relative importance of surface diffusion, pore diffusion, and external film diffusion is quantified.

5.2 Experimental

5.2.1 Reagents, solvents, and sorbent

1, 2, Dimethyl-4-nitrobenzene (DMNB) (Sigma-Aldrich #R 45943), phloroglucinol (PG) (1,3,5 trihydroxybenzene, Fluka, $\geq 99\%$), and Blue Dextran (Sigma-Aldrich #D 5751) were used without further purification.

152

The solvent (mobile phase, eluent) used in this study, for making solutions of both DMNB and PG, was 50/50 MeOH / H$_2$O v/v, and was prepared by mixing pre-measured, equal volumes of HPLC grade MeOH (Fisher Scientific) and water, which was distilled and deionized with a NANO-pure system (Barnstead, Boston, MA)

The mobile phase and its DMNB and PG solutions were sparged with helium before the kinetic and chromatographic experiments. The concentrations of DMNB used were around 6×10^{-5} M, which is in the linear range of its sorption isotherm. The concentration of PG used was about 5×10^{-5} M, chosen to nearly match the absorbance of the 6×10^{-5} M DMNB solution at 222 nm.

The monomeric ODS HPLC sorbent studied was Luna 15u C18(2), having a 12.3 μm diameter, 16% carbon load, pore volume of 1.0 mL/gram and a pore diameter of 10 nm. It was purchased from Phenomenex®, Torrence, CA (part #04G-4273, batch 5303-15). A 250 x 4.6 mm HPLC column packed with the same batch of Luna 15u C18(2) was used in the chromatographic studies (part # 00G-4273-EO).

Glass beads (used to "dilute" the Luna C-18 sorbent inside the shallow bed) were non-porous beads, 10-20 μm diameter, purchased from Small Parts, Inc., Miami Lakes, FL, USA, part # ADGB-SF

153

5.2.2 Elution and frontal HPLC studies

The HPLC equipment for elution studies consisted of the mobile phase reservoir, Waters Chromatography Pump (model 6000A), Rheodyne injection valve (Part # 8125) with a 5 µL injection loop, a 25-cm Luna C-18 column described above, and a UV-vis detector (Waters Lambda-Max LC Spectrophotometer, model 481) set at 263 nm. Elution chromatograms were run in 50/50 MeOH/H$_2$O, which was sparged with helium prior to the experiment. The samples (DMNB, PG, and Blue Dextran) were also prepared in 50/50 MeOH/H$_2$O.

Frontal chromatography employed all the components described above for elution chromatography, but also involved the use of an extra mobile phase reservoir, which carried a solution of 6.1·10^{-5} M DMNB eluent (50/50 MeOH/H$_2$O), in addition to the reservoir carrying the pure eluent. The inlet of the HPLC pump is equipped with a solvent selection valve, which allows for switching between the two reservoirs. As well, an extra solvent selection valve (Rheodyne, 6 port valve part # 7060) was placed in between the outlet of the pump and the injector. The outlet of the pump was the inlet of this valve; one of the 6 outlets is connected to the column, while another directs the fluid to waste, and the remaining outlets are not used. The column was first equilibrated with the pure eluent, and then the pump was flushed with the DMNB solution with the six port valve switched to waste. This was done to eliminate band broadening in the pump, since the DMNB travels through the pump in the frontal chromatography set-up used. Once the flushing was complete, the 6-port valve was switched back to direct flow through the

154

column. The flowrate through the column was always 2 mL/min, regardless of whether elution or frontal chromatography was done.

The following measurements were made – the interstitial volume of the column (the volume of the liquid-filled spaces between the particles); the total-porosity volume (the sum of both the interstitial volume and the volume of the pores inside the particles of the column); the retention factor (k') of DMNB on Luna C-18. The determination of the interstitial volume and the total porosity volume was done by simultaneous elution chromatography of Blue Dextran (interstitial volume marker – see Section 5.3.1) and PG (the total liquid volume marker), respectively. The determination of the k' for DMNB was done both by elution and frontal chromatography. In both cases, PG was used as the unretained compound.

5.2.3 Shallow bed apparatus and packing procedures

The apparatus used in this study is based on the one described in Chapter 4. The modified Union Giken apparatus is exactly the same as described in Sections 4.2.2.1 - 4.2.2.2, and 4.2.2.5, and shown in Fig. 4.1 – Fig. 4.4. Thus, the overall plumbing, the computer program used to control the valve sequence, and the shallow bed structure are identical. The only differences, which are described in Sections 5.2.3.1 through 5.2.3.3, are a slightly modified packing procedure and an additional step in the preparation of the shallow bed - the removal of a residual film of PDMS polymer present on the inside wall of the s.s. washers that contain the bed.

155

5.2.3.1 Packing procedure

The shallow-bed is packed in a separate, temporary assembly, by vacuum-driven slurry packing, in a way very similar to that described in Chapter 4, section 4.2.2.4 and Fig. 4.5. The present procedure is shown in Fig. 5.1. The major difference is with the reservoir for the slurry solution just above the bed. The only reason for the use of the new reservoir is that it is easier and faster to position on top to the shallow bed and to remove after the shallow bed is filled with particles. The slurry in the beaker is a mixed-particle slurry of glass beads and Luna C-18 in ethanol, (about 2% by mass), which is further described in a subsequent section. Usually, about 1.5 mL of the slurry are needed to fill the shallow-bed. It takes about 3 refills of the micropipette and about 5 min to accomplish the filling. All other steps and parts are exactly the same as in Fig. 4.5.

5.2.3.2 Mixed particle slurry

The slurry used in this study is a mixed-particle slurry of LUNA C-18(2) and non-porous glass beads. Bed 1 was packed with a slurry with 1: 4.17 mass ratio of ODS to glass beads, while Bed 2 was packed with a separately-made slurry of 1: 4.21 mass ratio. This translates to a volume ratio of about 1: 1.9 of ODS to glass beads. The reason for adding the glass beads is twofold. First, the resistance of a 0.6 mm-long bed packed with purely LUNA C-18 particles proved to be too high, which made it impossible to achieve the high flowrates necessary to approach shallow bed conditions. As mentioned in Chapter 4, this problem could not be fixed by decreasing the length of the shallow bed, because unstable desorption signals resulted, probably due to channeling. For this reason, the ODS particles were mixed with glass particles of higher diameter. The bed of the porous

156
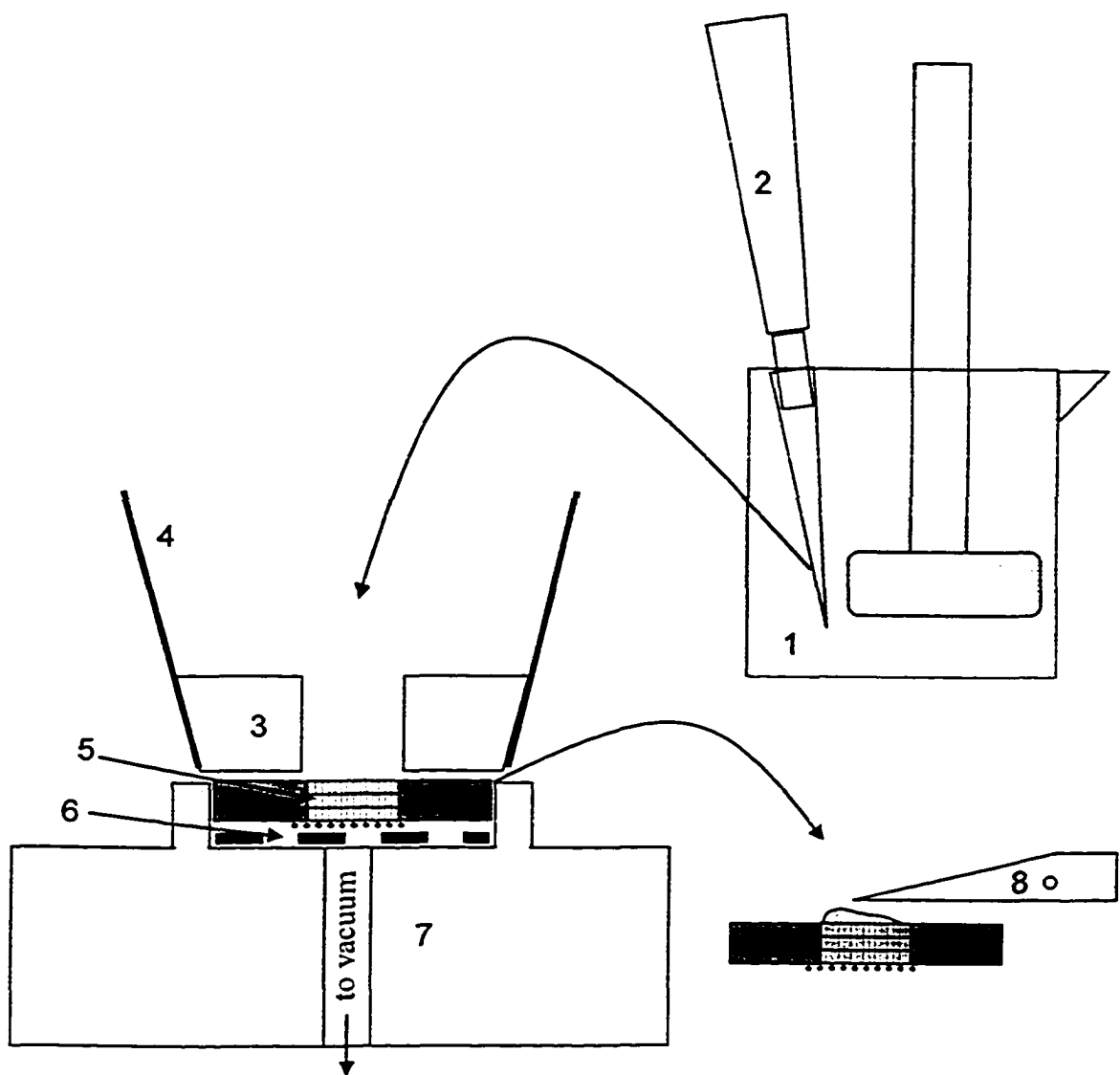
Fig. 5.1. Slurry packing procedure. The stirred slurry from the beaker (1) is aspirated into a micropipette (2) and transferred into the shallow bed *via* a temporary reservoir made up of a PDMS washer (~ 2.1 mm ID, 6 mm OD, and 1 mm thick) (3), encased in a ¼ inch s.s. ferrule (4). The shallow bed to be packed is made up of the s.s. washer filled with 3 silicon grids plus one Ni mesh on the bottom (5). It is placed on top of a s.s. screen (6), which in turn sits in a well in the packing manifold (7) which is connected to the house vacuum. After slurry packing, the washer with the silicon grids and Ni mesh is taken out and extra particles are removed with a surgical blade (8).

157

glass beads alone has a resistance more than an order of magnitude lower than that of a same-length bed of Luna C-18 particles. For beds packed using a mixed slurry such as Bed 1 and Bed 2 the permeability is observed to be greater than that of bed of pure ODS by a factor of 3-4 (data not shown). The second reason for using the mixed-particle slurry is that a bed packed with purely Luna C-18 particles exhibits a slow increase of the resistance to flow, possibly due to consolidation (tighter packing) of the hydrophobic particles in a water-rich solvent. This phenomenon is known to occur in loosely-packed columns of hydrophobic packings when they are exposed to highly aqueous solutions [108], and it did occur with the polymeric PRP-1 sorbent as well (see Chapter 4). As a result, in such beds the pressure needs to be constantly adjusted (increased) to maintain a relatively constant flowrate through the bed. This phenomenon does not occur in beds packed with glass beads only. It is also eliminated in beds packed with the mixed particle slurry. The constant permeability makes operation much easier in an apparatus which uses constant pressure pumps, and allows one to use the bed for an indefinite number of cycles (since flowrate does not decrease with time).

One characteristic of the mixed particle slurry and the present packing procedure, is that it is not possible to know the mass of ODS particles in the bed. The particle slurry of LUNA C-18 mixed with glass beads is transferred to the shallow bed as described in section 4.2.2.3 and Fig. 5.1. The beaker from which the slurry was aspirated by the micropipette was continually sonicated and stirred, except at the time of aspiration. The larger size and density of the glass beads made them settle more rapidly than ODS. Also, a significant fraction of the slurry particles stick onto the walls of the beaker and there is

no reason to assume that the glass beads and ODS do so to the same extent. Thus, it is

not possible to know the exact mass of the C-18 silica used. From microscopic

observation however, it seems that proportionally more C-18 transfers into the actual bed

than the glass beads. Based upon microscopic examination after disassembling the beds

the volume percentage of the C-18 beads in the bed could be as high as 60 – 70 % of the

total volume taken up by the particles, compared to about 35% by volume in the slurry

used.

5.2.3.3   Removing excess PDMS from the s.s. washers

As described in section 4.2.2.3, the s.s. washers are covered with a thin layer of PDMS.

To do this, a thin film of a liquid polymerization mixture, with 10:1 ratio of elastomer to

curing agent is deposited on the top and bottom faces of s.s. washers, followed by curing

for at least 24 hours at room temperature. The deposition is done by first spreading a thin

liquid film of the polymerization mixture on a piece of parafilm and then gently pressing

the s.s. washers on the parafilm for a few seconds. However, during the deposition the

liquid polymerization mixture creeps into the inside of the s.s. washers. This is

undesirable as will be shown in Results and Discussion section. In order to minimize the

amount of PDMS inside the s.s. washers, the PDMS was scraped off from that area. As

well, PDMS was carefully scraped off from the area up to 0.2 mm from the inside edge of

the washers. This is shown in Fig. 5.2. The removal of PDMS was performed for Bed 2,

but not for Bed 1.

159
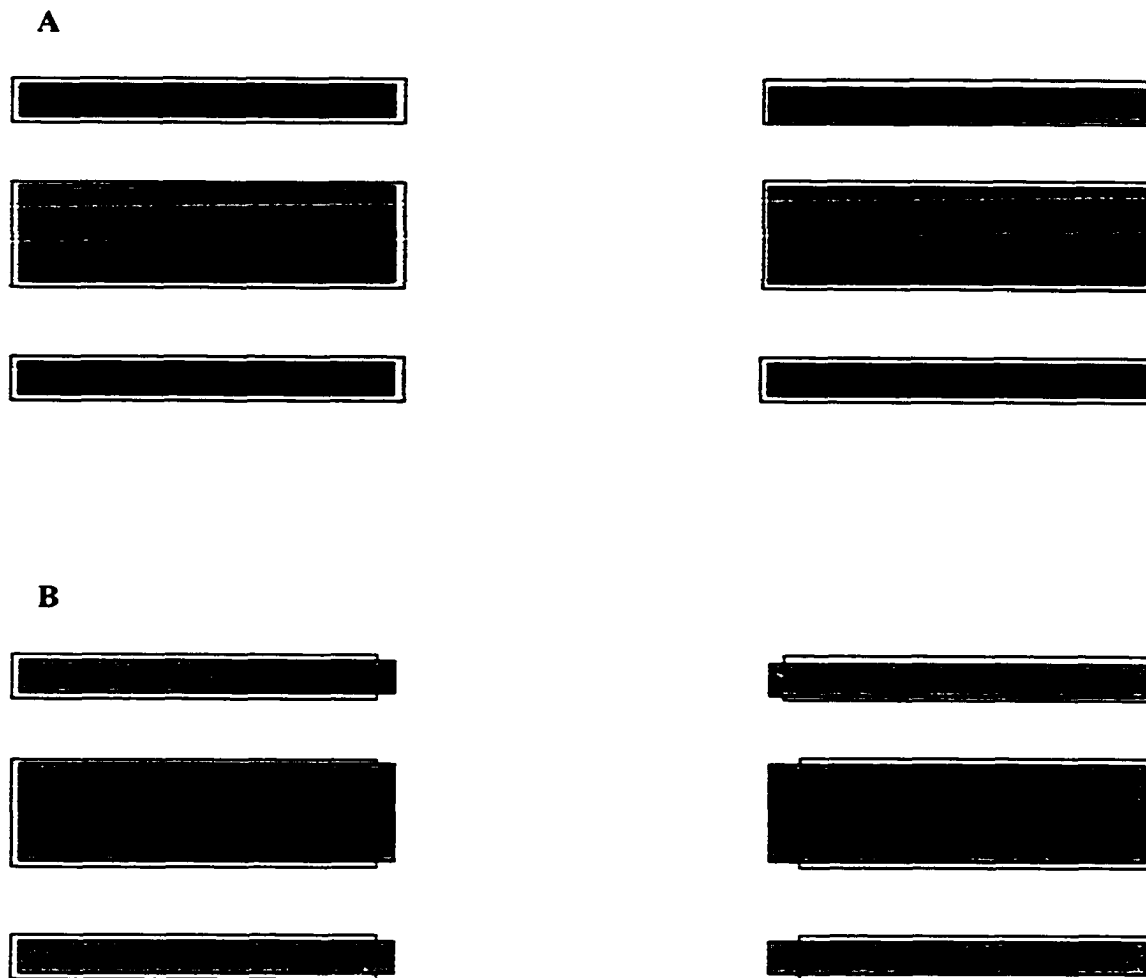
Fig. 5.2: Schematic of the presence of PDMS film around. s.s. washers. The dark rectangles are cross-sections of the s.s. washers (top washer, 200 µm thick, middle washer to contain the shallow bed, 600 µm thick, and bottom washer is 200 µm thick. All washers are 2 mm ID and 6 mm OD). The light gray regions show where PDMS films were present before scraping (panel A) and after scraping (panel B). The thickness of the film is exaggerated (it is thought not to be thicker than 10-20 µm). The distance of scraped PDMS from the inside edge is not uniform around a washer, but it is small enough to still afford a large enough area for pressing the Ni screen (See Fig. 4.4)

160

5.2.4 Procedure for desorption rate measurement.

The flow sequence is the same as described in section 4.2.3, except that the times required for each step differ. Equilibration times were usually 12 seconds, but in certain cases were extended to 36 seconds, while desorption times were 10 seconds. The time-out and flush time were 1 sec each, as before.

5.2.5 Deconvolution and filtering

Deconvolution and filtering are performed the same way as described in Chapter 3, section 3.2.3. The sole difference is in the frequency filters used. For Bed 1 , Runs 1 and 3 they are ({0,1}, {0,1}, {49.80,1}, {68.34,0}); while for Run 2 they are ({0,1}, {0,1}, {40.03,1}, {64.45,0}). For Bed 2, Run 1 they are ({0,1}, {0,1}, {49.80,1}, {68.34,0}); while for both Run 2 and Run 3 they are ({0,1}, {0,1}, {69.34,1}, {88.87,0}). The different vertices of the trapezoidal filters stem from the fact that different flowrates were used for the different runs, and also from the fact that each run has its own idiosyncratic frequency distribution requiring slightly different filters.

161

5.3 Results and discussion

5.3.1 Particle porosity of Luna-C18 and linear isotherm of DMNB

It will be important to obtain the values of the particle porosity of Luna C-18, which will be used to obtain the ratio of $[i]_{part} / [i]_{MP}$, used later in the chapter. This value is not given by the manufacturer, but can be obtained by the following equation.

$$\varepsilon_{PP} = \varepsilon_{intra} / (1 - \varepsilon_{inter}) \qquad (5.1)$$

where ε_{PP} is the particle porosity (the volume fraction of the particle taken up by the pores) and ε_{intra} is the intraparticle porosity of the column (the volume fraction of the packed column taken up by the pores), and ε_{inter} is the interstitial porosity of the column (volume fraction of the packed column taken up by the spaces in between the porous particles). The value of ε_{inter} can be determined by performing an elution chromatogram with an excluded compound, a solute which does not enter the pores of the particles and is not sorbed on the outside surface of the particles. The sum of $\varepsilon_{inter} + \varepsilon_{intra}$ can be obtained by performing an elution chromatogram with an unretained compound as the analyte. PG is used as the unretained compound, while Blue Dextran, a 2,000,000 Da polymer is used as the excluded compound, because the diameter of the individual molecule (at least 180 Å) is larger than the pore size of Luna C-18(100 Å).

The total volume of the column is calculated from its length and its inner diameter. The interparticle volume is calculated from the retention time of Blue Dextran and the

162

volumetric flowrate. The value of ε_{inter} is obtained by dividing the interparticle volume by the total volume of the column. The same is done with the retention time of PG in order to calculate the sum of $\varepsilon_{inter} + \varepsilon_{intra}$.

From triplicate measurements, $\varepsilon_{inter} = 0.369\pm0.003$, $\varepsilon_{total} = 0.688\pm0.002$. Subtraction of ε_{inter} from ε_{total} gives $\varepsilon_{intra} = 0.318\pm0.004$. The value of ε_{PP} calculated via Eq. 5.1 is thus equal to 0.505 ± 0.009. The chromatogram showing elution of Blue Dextran and PG are presented in Fig. 5.3.

The retention factor k' of DMNB is obtained by performing an elution chromatogram of DMNB and PG on the Luna column. The retention times are measured by calculating the first statistical moment of the retention peaks [54, 55, 57, 91], and the retention factor is calculated by

$$k' = (t_R - t_{PG}) / t_{PG} \qquad (5.2)$$

The retention factor for DMNB on the Luna C-18 column in 50/50 MeOH/H$_2$O is 15.07 ± 0.04 based on 3 replicates of the elution chromatograms. The linearity of the sorption isotherm is confirmed by running a frontal chromatogram of $6.1\cdot10^{-5}$ M DMNB and by injecting 5 μL of the same solution in the elution mode. In frontal chromatography, the concentration of the solute in the mobile phase is always the actual concentration in the feed solution. Thus the concentration is always $6.1\cdot10^{-5}$ M which is

163
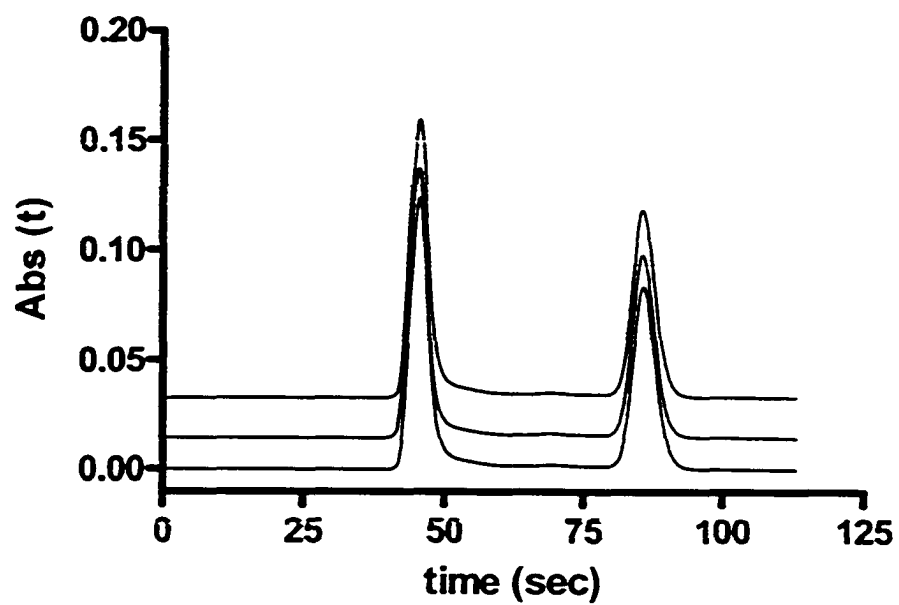
Fig 5.3. Elution chromatograms of an excluded compound (Blue Dextran) and an unretained compound (PG) on 4.6 mm ID, 25 cm, Luna C-18 column in 50/50 MeOH/H₂O. The first peak is the excluded compound.

164

the concentration we are trying to test for linearity. However, when only 5 µL of the solution are injected in elution chromatography, the concentration of DMNB drops dramatically to a very low level (since k' is 15, this concentration drops first by a factor of 15, and it further decreases because of the band broadening processes in the column). In effect frontal chromatography provides retention information at the concentration of interest, while elution chromatography provides retention information at concentrations about 2 orders of magnitude lower. If the value of k' from frontal chromatography is the same as that from elution chromatography, it must mean that the isotherm is linear up to the concentration tested. The retention times for the frontal chromatograms were calculated as follows. First the derivative of the frontal chromatography data is taken according to Eq. 2.25, in order to transform the frontal data into the form of an elution peak (not shown). The first statistical moment of the resulting peak-shaped derivative is calculated in the same way which was used for elution data. The reverse frontal chromatogram is treated the same way, except that the derivative is multiplied by (-1), according to Eq. 2.26 or 2.27. The values of k' obtained with elution chromatography are 15.07 ± 0.04, while the value obtained for frontal chromatography is 15.2 ± 0.1. Both are shown in Fig. 5.4.

From the values obtained from HPLC studies, the parameters obtained for the column are $\varepsilon_{inter} = 0.369 \pm 0.003$, $\varepsilon_T = 0.688 \pm 0.002$, $\varepsilon_{intra} = 0.318 \pm 0.004$, $\varepsilon_{PP} = 0.505 \pm 0.009$, and k' = 15.0 ± 0.1. This allows calculating two important parameters. The first of them is R, the ratio of moles DMNB sorbed onto ODS-coated walls of Luna C-18 to the moles in the pores of Luna C-18. It is calculated, according to equation 1.12, to be R = 32.4 ± 0.6. The
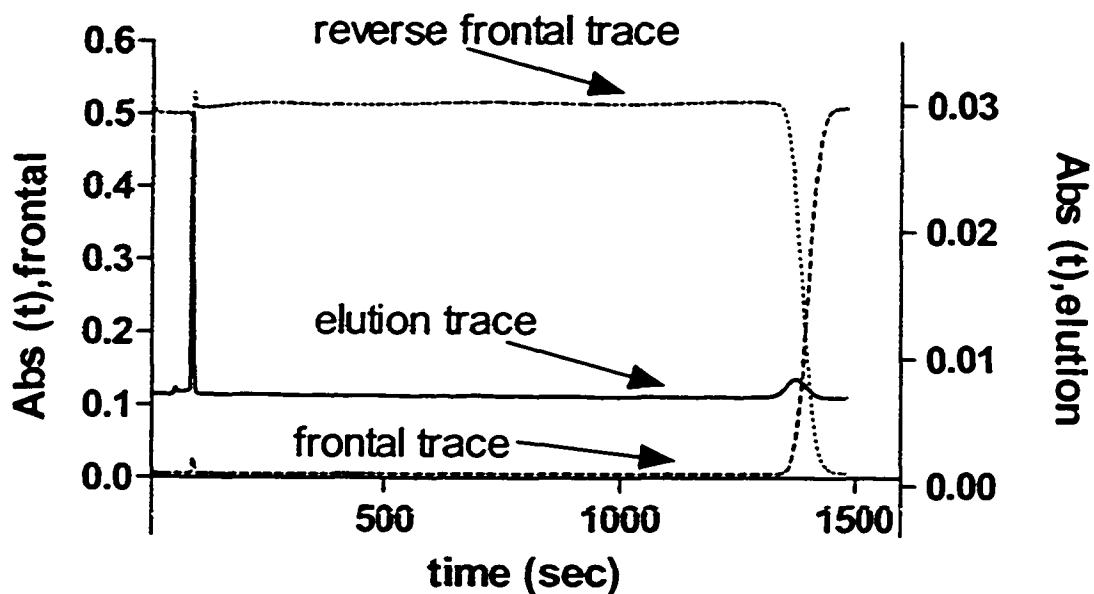
Fig 5.4. The superposition of elution chromatogram on DMNB (the middle trace, with the large spike corresponding to the unretained compound PG), and frontal chromatograms of 0.061 mM DMNB (frontal chromatography has been done both in the leading-front, and the reverse-front mode). Note that the different scales for frontal and elution chromatograms.

166

second parameter is the ratio of $[i]_{part} / [i]_{MP}$. It, or its reciprocal, is used in equations such as 2.6, 2.14, 2.15, and 2.32. There are different ways to calculate this ratio, as seen in Chapters 3 and 4, but here it is obtained by the following relationship:

$$[i]_{part} / [i]_{MP} = (1+R) \cdot \varepsilon_{PP} \qquad (5.3)$$

This ratio has the value of 16.9 ± 0.5.

5.3.2 The choice of PG as the IRF-Marker

The 'desorption' rate curve for the IRF-Marker serves two purposes. First, it is subtracted from the solute run (DMNB) in order obtain the signal of the actual desorbing solute separate from that of the solute between the shallow-bed and detector. Second, its derivative, according to Eq. 2.27, quantifies the effects of band broadening in a Type II shallow-bed instrument. For both of these purposes, an ideal marker would be an excluded molecule which does not enter the pores of the packing itself. Thus, high molecular-weight polymers, on the order of 1 million Daltons, which have molecular diameters greater than the pore size of the packing (10 nm in this case) seem like an obvious choice for an IRF marker. There are, however, three limitations to the use of such polymers as effective IRF markers: (i) The first arises from the fact that the polymer has to be both soluble in the solvent used (50% MeOH) and a good absorber of UV-visible light. The one, commonly used co-polymer that fits those criteria is blue Dextran (2,000,000 Daltons) which is a cross linked dextrose polymer with groups present to give it an absorptivity. The fact that the absorbing groups are interspersed between the glucose monomers gives Blue Dextran a low absorbance per unit mass. For

167

example, one needs a concentration of 0.2 grams per Liter to obtain an absorbance of 0.075 in our present system. Because of its high molecular weight, Blue Dextran actually increases the viscosity of the mixture[109]; viscosity increased by as much as 2-4% in the present case (careful determination has not been carried out). Since constant pressure pumps are used in this apparatus, this creates the need to adjust the pressure manually every time one switches between the solute and the IRF marker solutions to maintain the same flowrate. (ii) A second limitation to the use of Blue Dextran is that, for reasons that were not investigated further, it causes a marked decrease in the permeability of the bed packed with the mixed slurry of C-18 and glass beads. (Though it does not have that effect in beds packed with pure glass beads.) The resistance can increase as much as 30% after performing a single set of 5 cycles, and the loss in permeability is not reversible. Under such conditions, it is very difficult to keep the flowrates constant and thus to obtain useful data. (iii) The third limitation is the fact that the Blue Dextran has a very low diffusion coefficient. This means that the Blue Dextran present in the diffusion film around the particles is going to diffuse out more slowly than a small molecule would, which could affect the shape of the IRF marker curve. Therefore, for practical reasons, the use of Blue Dextran as an IRF marker is abandoned.

Another approach to obtaining IRF information is to use an unretained compound (such as PG) as the IRF-marker, but this presents problems both with the subtraction step and with obtaining the IRF. Both problems stem from the fact that PG enters the pores of the LUNA C-18 packing. Their origin is discussed in the next two paragraphs.

168

First, the desorption process of a solute (DMNB) from a porous particle should include all of that solute that was in the particle, whether by sorption onto or into the walls, or by its presence in the stagnant mobile phase in the pores of the particle. If the PG run (scaled by Eq. 2.24) is subtracted from the DMNB solute run, an amount of DMNB equal to that which was in the particle pores is included in the subtraction. This is an error. However, for the desorption of DMNB from LUNA C-18, the amount of the solute present in the pores is less than 3 percent of the sorbed DMNB. This can be shown by the following numbers. The ratio R, defined as the moles of DMNB sorbed to the moles of DMNB in the pores of the particles, is shown above to be equal to 32.4 via Eq. 1.12, and the quantity is approximately 3%. Thus, the solute in the pores represents a small fraction of the total amount of DMNB in the particle. Though the magnitude of this error is not large, a correction for it will be developed in the following section 5.3.3.

The second problem has to do with the use of the IRF peak in deconvolution, in order to correct for band broadening. The IRF-curve should arise only from the processes giving rise to the dispersion between the particles of the shallow-bed and the detector. Since the PG which is present in the stagnant mobile phase in the pores of the particles has to diffuse out to the surface of the particle before it is carried away, this pore diffusion of the non-sorbed PG also contributes to the observed band broadening. This creates an error in the determination of the IRF. Although it will be shown in section 5.3.3 that the PG from the pores distorts the shape of the true IRF-curve only slightly, nevertheless, a correction for it too is developed in the next section.

169

5.3.3 The Pore-PG Correction for Luna C-18

When unretained PG enters Luna C-18 during the equilibration step, it is present in its pores but is not sorbed on the pore walls. The PG present in the stagnant mobile phase of Luna C-18 can be called pore-PG. During the desorption step, this pore-PG diffuses out of the particles and adds an undesirable contribution to the observed PG curve. However, if the amount of pore-PG present in the pores is known, and if the shape of this desorbing PG which is observed at the detector is known, it is possible to subtract the pore-PG curve from the overall observed PG curve, yielding only the curve of extra-particle PG.

The first task is to determine the amount of pore-PG in the pores. Normally, this is readily done if the mass of ODS is known, because it can be used with the specific pore volume given by the manufacturer and the (scaled) concentration of the feed PG solution. However, as stated in section 5.2.3.2, it is impossible to exactly measure the mass of ODS in the shallow bed, because of the mixed slurry used in the packing. There is another way to calculate the amount of PG in the pores, which is just as precise, assuming that the ODS under study is the only sorptive material in the shallow bed (This will be a relevant point when discussing the residual film of PDMS in the shallow bed). Fig. 5.5 A shows both the experimentally observed PG and DMNB curves for Run 1 obtained with Bed 2. They are both averages of 20 desorption cycles and are normalized so that the plateau absorbance (absorbance of the feed solutions used for equilibration) is equal to 1. The difference between the DMNB and PG curves in Fig. 5.5 A is the shaded area. The area of this shaded region corresponds to the normalized absorbance of the DMNB which is *sorbed* onto the stationary phase, not including DMNB present in the pores of ODS.

170
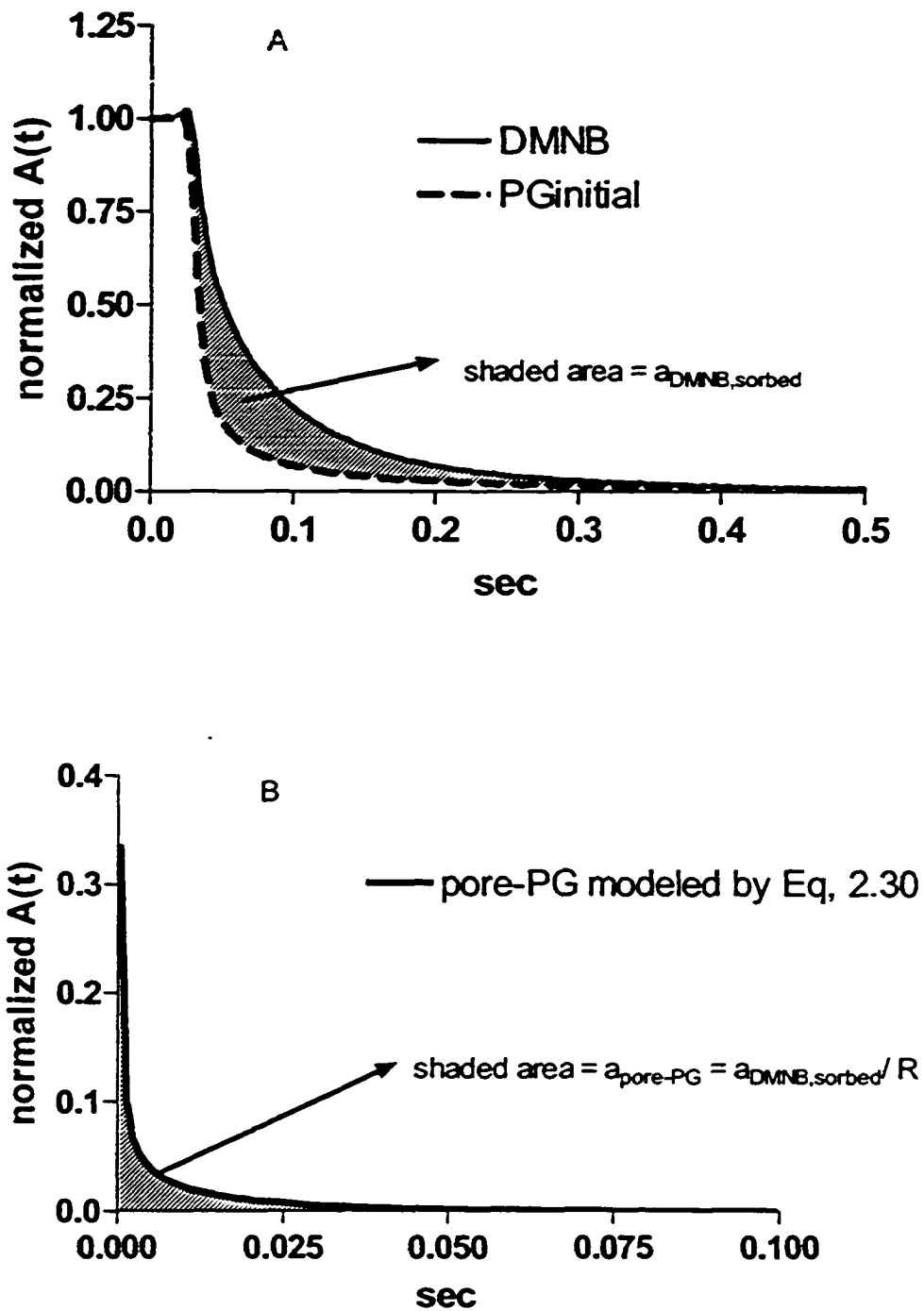
Fig 5.5. Predicting the shape and magnitude of pore-PG. A: Visualizing the amount of sorbed DMNB for experimentally observed curves of Run 1, Bed 2. B: The estimated shape of the desorption curve of pore-PG. The normalized A(t) values are such that the area under the curve in panel B is equal to the shaded area from panel A divided by R.

171

This area is given a symbol $a_{DMNB, sorbed}$. From chromatography data (section 5.3.1) R, the ratio of moles of DMNB sorbed on the walls to DMNB in the pores, is determined to be 32.4. This ratio is necessarily the same as the ratio of the sorbed DMNB to PG in the pores (both curves have been normalized). When $a_{DMNB, sorbed}$ is divided by the value of R, the result is the area due to the DMNB in the pores, which is equal to the area that should belong to PG in the pores. Therefore, regardless of the shape of the desorbing PG from the pores, its area, $a_{pore-PG}$ is:

$$a_{pore-PG} = a_{DMNB, sorbed} / R \qquad (5.4)$$

The second task is to obtain the shape of the curve of pore-PG observed by the detector. First, an educated guess can be made as to whether it is particle or film diffusion which is the rate-limiting step in the desorption process.

For PG, D_{MP} is 6.0×10^{-6} cm^2 s^{-1}, calculated via the Wilke-Chang correlation [99] and the pore diffusion coefficient D_P is about 2.4×10^{-6} cm^2 s^{-1} (using Eq. 1.15, and assuming a tortuosity of 2 ± 0.5, and hindrance of 0.8 ± 1). The ratio of $[i]_{part}/[i]_{MP} = 0.5$ (which for an unretained compound is simply the value of the particle porosity; see Eq. 5.3). If ε_{inter} in the shallow bed is assumed to be approximately 0.4, and the open fraction of the shallow bed about 0.7 (area in between the walls of the silicon grids) a value for the thickness of the external diffusion film ranging from $\delta = 0.29$ μm to 0.35 μm is calculated for the flowrates used with Bed 2 (from 0.27 mL/sec for Run 1 to 0.49 mL/sec for Run 3) using the average of Eq. 2.12 and 2.13. When these values are put into Eq. 2.14, in order to

172

estimate the relative importance of film vs. particle diffusion, the value of X ranges from $1.2 \cdot 10^{-2}$ to about $1.0 \cdot 10^{-2}$, which is 1 order of magnitude smaller than 0.13. This is consistent with primarily intra-particle diffusion control of the desorption rate of pore-PG. Furthermore, the fact that the parameter L calculated from Eq. 2.34 ranges from 54 to 98 for the flowrates used indicates that the flowrate is fast enough to meet shallow-bed conditions and, thus, not to have a distorting effect on the desorption curve shape of pore-PG. For these reasons, particle diffusion is assumed to be the rate-limiting step. If there were no band broadening in the shallow bed apparatus, the instantaneous rate of desorption of PG would be relatively well described by Eq. 2.30 for spherical diffusion. In Fig. 5.5 B is shown the predicted desorption of pore PG, calculated with Eq. 2.30 using $D_{i,PG} = 2.4 \times 10^{-6} \, cm^2 \, s^{-1}$, and the particle radius of $r = 6.15 \, \mu m$, and scaled so that the area under the curve is equal to that obtained in Eq. 5.4. Only the first 10 terms of (Eq.2.30) are used. Fig 5.5 B is deemed to be a reasonable approximation of what the pore-PG curve would look like at the detector in the absence of band broadening in the shallow-bed apparatus.

However, to determine the shape of the curve seen by the detector it is necessary to account for the band broadening on the way to the detector and in the detector window. This is done by a series of successive approximations starting with convolution of Fig. 5.5 B with the IRF function that is obtained by taking the negative derivative of the IRF-Marker curve (PG curve in Fig. 5.5 A), as defined by Eq. 2.27. Successive approximations are necessary because the PG curve in Fig. 5.5 A also needs correction for pore-PG, and consequently so does the IRF function. This method is described in Fig.

173

5.6. First it is assumed that the initial IRF peak, obtained by taking the negative derivative of the observed PG curve is close to the real IRF waveform. This $IRF_{initial}$ (curve II in Fig. 5.6 A) is convolved with the predicted pore-PG curve from Fig. 5.5 B (curve I in Fig. 5.6 A) to obtain the approximate shape of the pore-PG at the detector (curve IV in Fig. 5.6 A). Curve IV is then subtracted from the initially observed PG curve (curve III in Fig. 5.6 A) in order to obtain the corrected PG curve after the first iteration (curve V in Fig. 5.6 A). When the negative derivative is taken of Curve V the corrected IRF-curve, first iteration, is obtained (curve VI in Fig. 5.6 A). The first iteration ends with a new PG curve and a new IRF peak, which have been approximately corrected for pore-PG. To compare them to the initial PG and IRF peaks, see Fig. 5.6 C and 5.6 D. It is apparent that they look almost the same. The center of gravity (first statistical moment) of the corrected IRF is 0.04810 sec, as compared to 0.4916 sec of the original IRF, a relative difference of just over 2%. So far, this is consistent with the assumption that the initial IRF is close to the real one.

The second iteration is shown in Fig. 5.6 B. The new, corrected IRF (curve VI) is convolved again with curve I (the modeled pore-PG assuming spherical diffusion and no band broadening), to obtain a better estimate of pore-PG at the detector (curve VII in Fig. 5.6 B). This pore PG curve is subtracted from the initial PG curve (curve III, not curve V) to yield the corrected PG curve after the second iteration (curve VIII in Fig. 5.6 B). When the negative derivative of Curve VII is taken, the corrected IRF-curve, second iteration, is obtained (curve IX in Fig. 5.6 B). The second iteration ends with a new PG curve and the new IRF peak, which have been corrected for pore-PG to a slightly larger

174
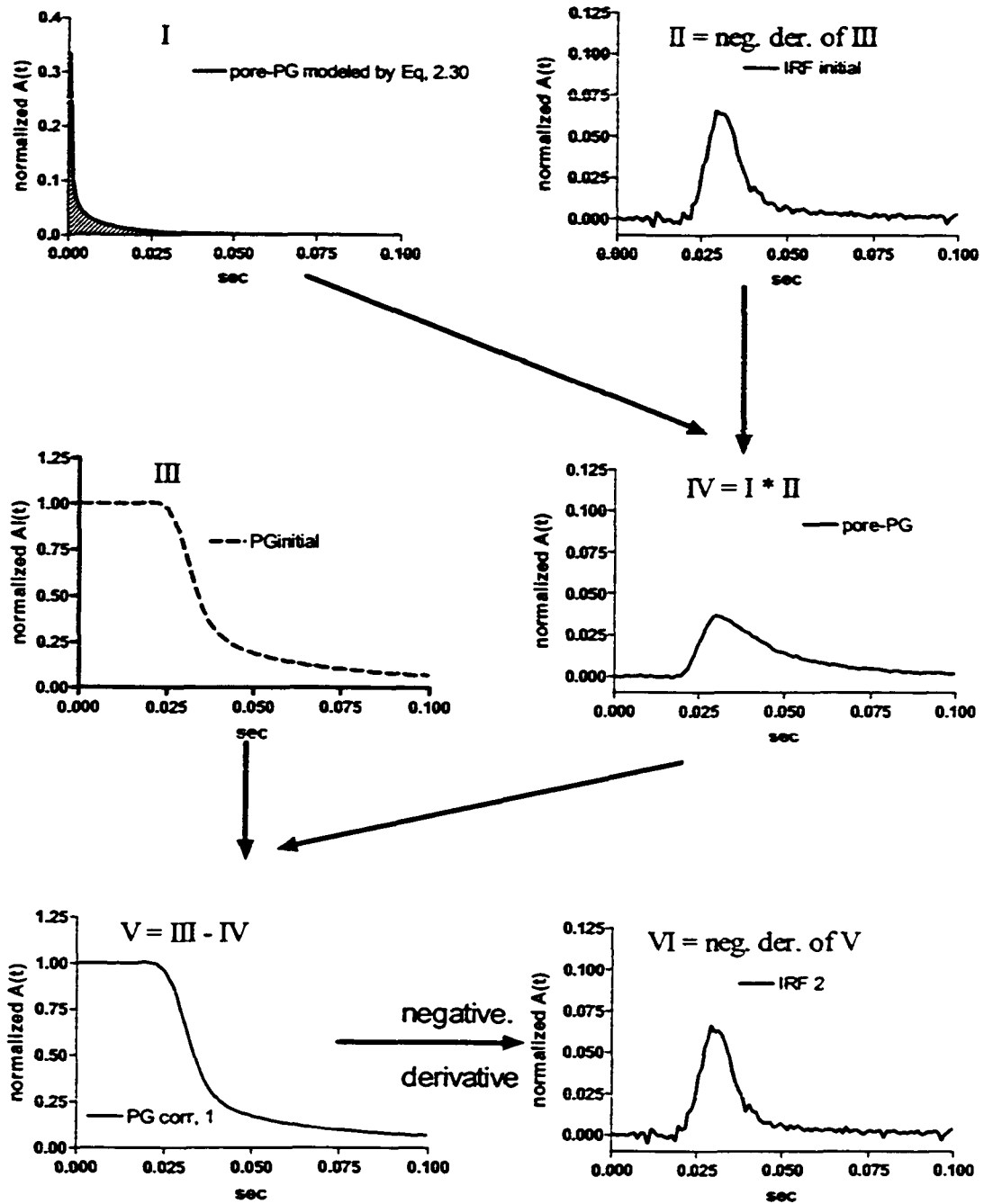
Fig. 5.6 A. Pore-PG correction. First iteration of the correction for pore PG. The predicted pore-PG desorption curve is convolved with the preliminary IRF function to obtain an estimate of the pore-PG curve which the detector would see (IV). This curve IV is then subtracted from the observed PG curve III to yield a corrected PG curve. From the corrected PG curve a new IRF is obtained. The new IRF will serve as the initial IRF in the second iteration.

175
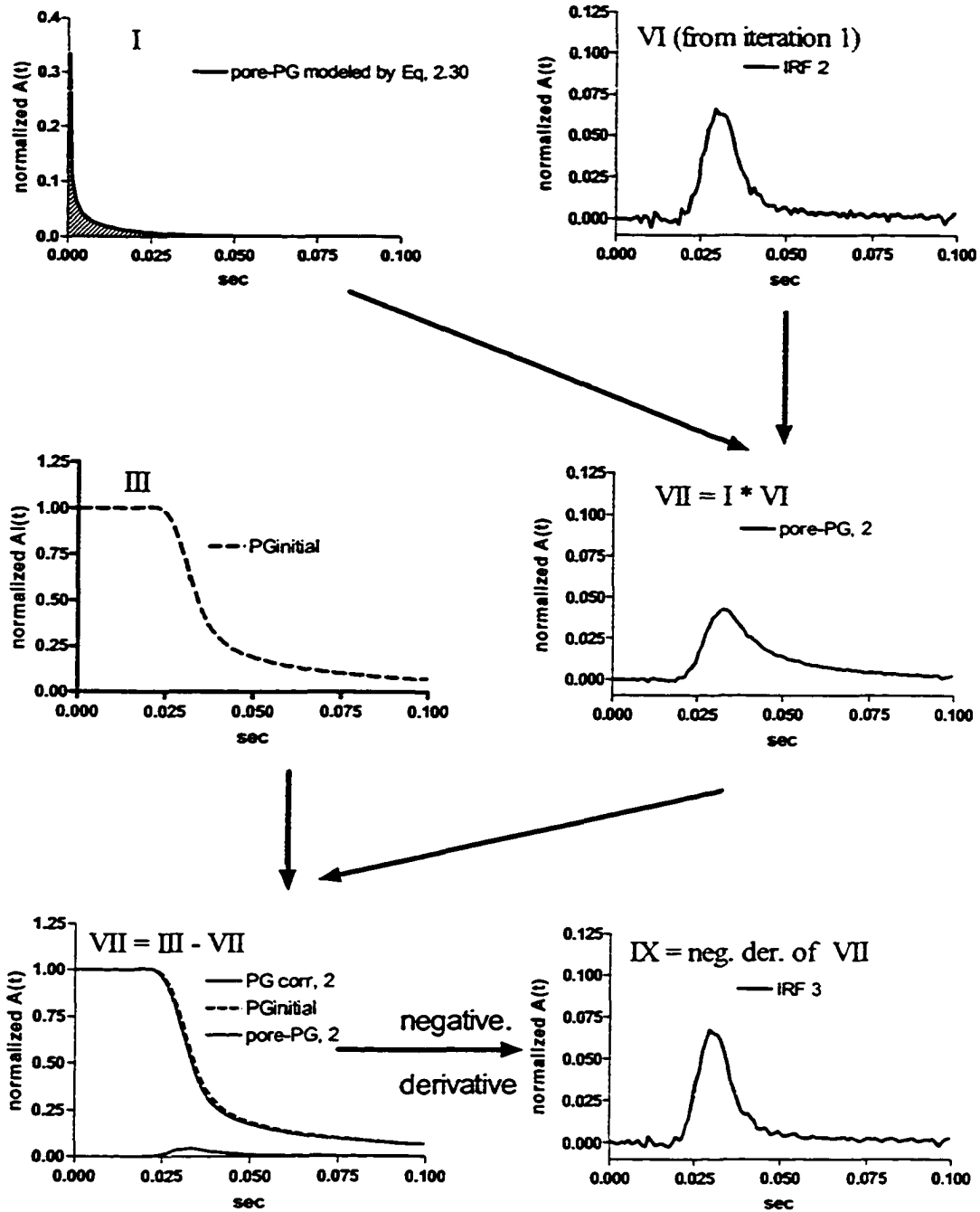
Fig 5.6 B. Pore-PG correction. Second iteration of the correction for pore PG. Curves I and III are the same as in Fig 5.6A. The same operation as is carried out as in Fig. 5.6 A, except that a new, corrected IRF from iteration 1 is used as the initial IRF. The iteration ends, with a new, more accurately corrected PG curve, and a new, more accurately corrected IRF function. Curves I and III are the same as the solid and dashed curves in Fig. 5.5 B and 5.5 A, respectively.

176
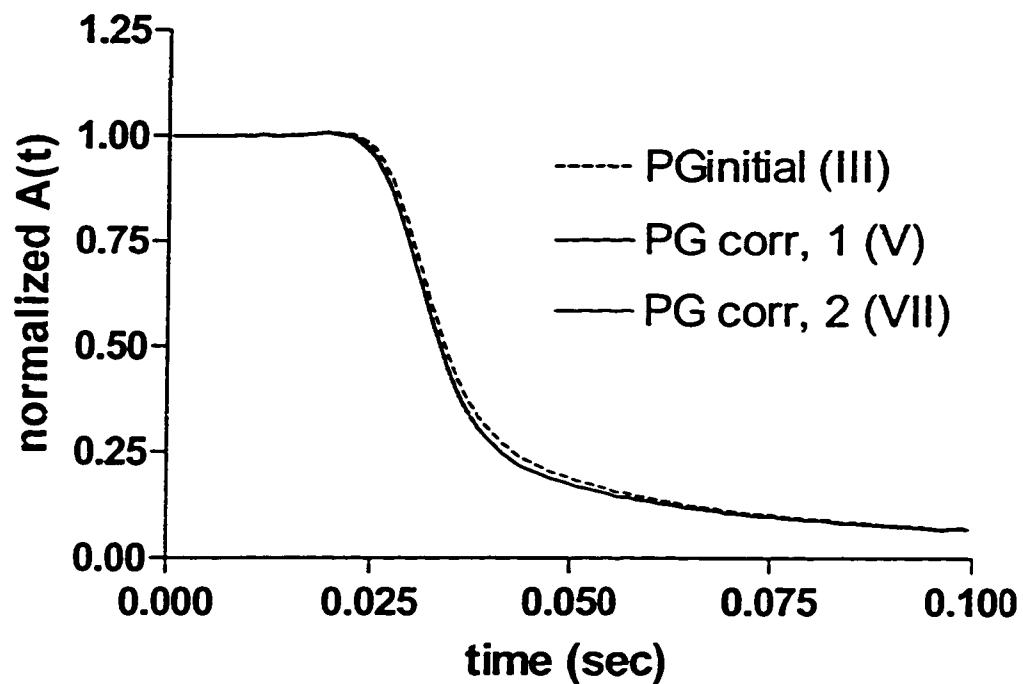
Fig. 5.6 C. Pore-PG correction. Comparison of the initial PG curve, and the pore-PG corrected curves after the first and second iterations. The numbers in the brackets indicate the curve numbering from Fig. 5.6. A and B. Curves V and VII are practically indistinguishable from one another.

177
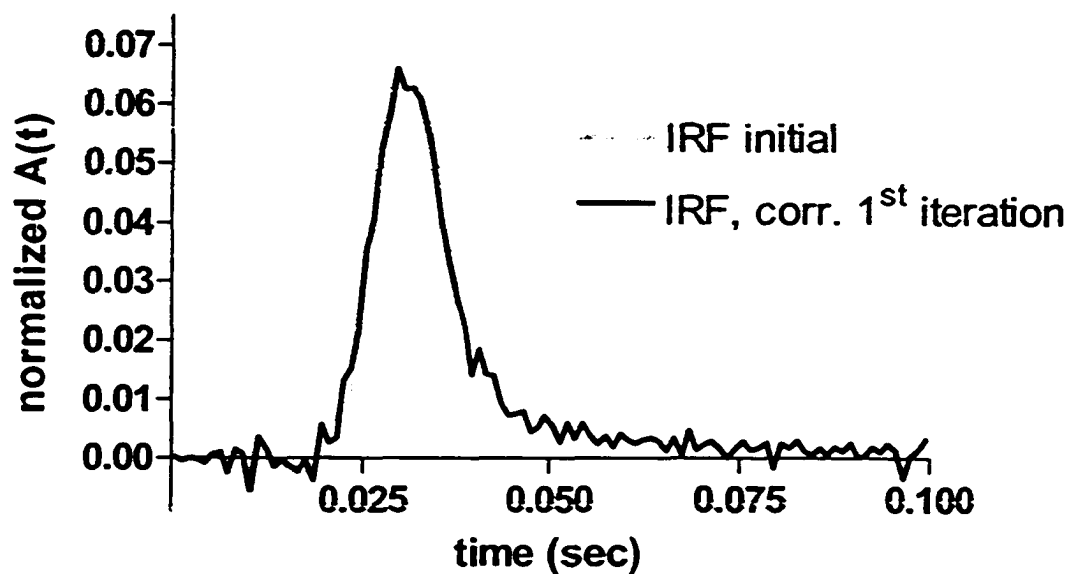
Fig 5.6 D. Pore-PG correction. Comparison of the initial IRF peaks before and after the first and the IRFs after pore-PG correction, first iteration. The IRF peak after the second iteration is not shown, because it is too similar to the IRF after the first iteration, and cannot be distinguished from it.

178

degree than after the first iteration. However, the corrected PG curve after the second iteration is virtually the same as after the first iteration, as can be seen in Fig. 5.6 D. The same is true for the corrected IRF peaks: the IRF obtained from the corrected PG-curve, second iteration, is the same as the IRF obtained after first iteration. The center of gravity of curve IX is calculated to be 0.4809, which is almost exactly the same as that of curve VI. The iteration process is therefore finished and the PG curve and the IRF are corrected as much as possible with this method. This method is applied to Runs 2 and 3 as well (not shown in Fig. 5.6), and in all cases only two iterations are needed to demonstrate convergence.

The largest source of error in this method lies in the fact that the pore diffusion coefficient is approximated first via both the Wilke-Chang equation [99], and then by the estimation of the tortuosity (see Chapter 1, sections 1.3.2 and 1.5.2) and the hindrance parameter [27]. However, since the pore-PG is only a small fraction of the total sorbed solute (less than 3%), these errors become very small.

From now on curve VII (corrected PG after the second iteration) and curve IX (the corrected IRF after the second iteration) will be used in place of the initial curves (Curve III and curve II in Fig. 5.6). Also, whenever the IRF-Marker curve and the IRF peak for Bed 2 are mentioned subsequently in this chapter, they refer to the corrected curves after the second iterations, unless stated otherwise. The IRF-Marker for Bed 1 is not corrected for pore-PG because of complicating factors, as revealed in section 5.3.5 below.

5.3.4 Instantaneous rate curves

Two shallow beds were prepared from the mixed-slurry of Luna C-18 and glass beads. Three DMNB desorption Runs were performed for each bed at varying flowrates. The A(t) vs t data for each Run were obtained by averaging 4-7 sets of 5 cycles (20-35 cycles) for DMNB and the same number of cycles for PG.

As an example of the data treatment, data for the first 1 sec in a typical experiment (Run 1, Bed 2) on DMNB and on the IRF-Marker (Pore-PG corrected) are shown in Fig. 5.7. Fig. 5.7 A shows the observed curve of normalized A(t) vs t for the desorption of DMNB as well as the curve for the IRF-Marker PG. Figure 5.7 B repeats the A(t) vs. t curve for the IRF-Marker curve, and also shows the negative derivative of this curve which serves as the IRF in accordance with the discussion of Section 2.2.5. All curves have been normalized so that the absorbance of the plateau at the start of the experiment is equal to 1. Figure 5.7 C results from subtracting the dashed line from the solid line of Fig. 5.7 A. Figure 5.7 D shows the result of deconvolution of 5.7 C with the solid line in 5.7 B. In order to clarify their significance, the solid curve in panel A, the dashed curve in panel A and B, the curve in C, and the curve in D of Fig. 5.7 may be compared, respectively, to the corresponding simulated curves: the solid line in Fig. 2.6 B, the dashed line in Fig. 2.6 B, the shaded part in Fig. 2.6 B, and the shaded part in Fig. 2.6 A.
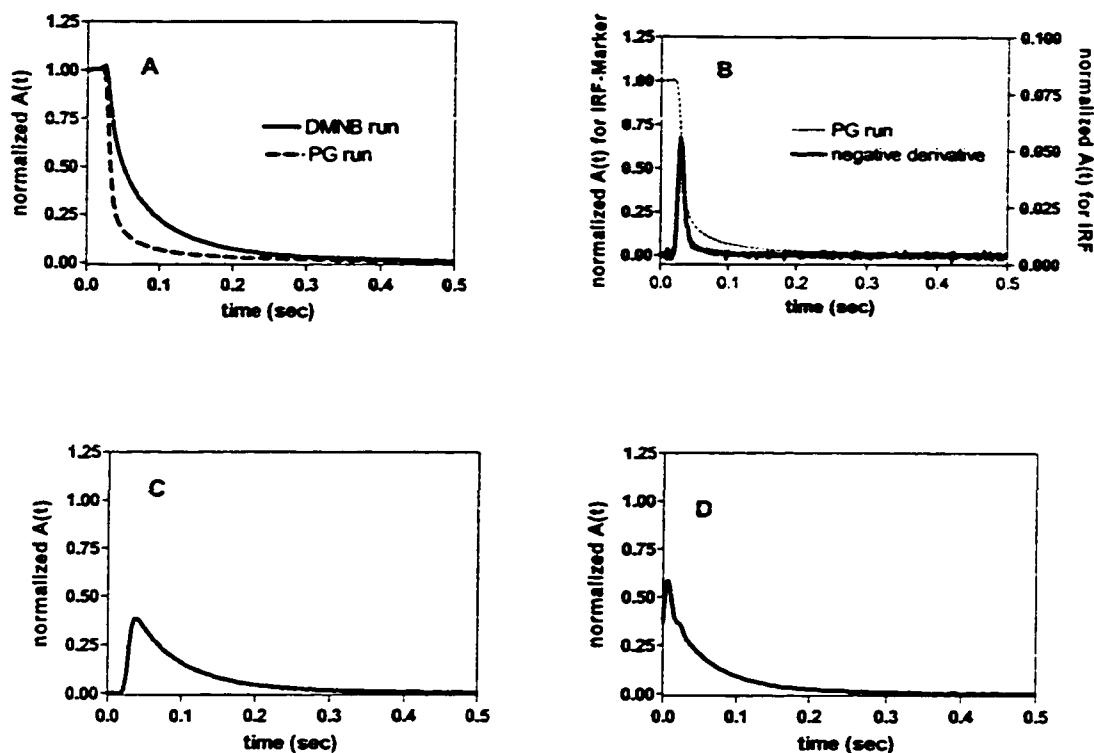
Fig 5.7. Correction for experimental artifacts of the instantaneous desorption rate curve for Run 1, Bed 2. Panel A contains the normalized A(t) values (or normalized concentrations in the detector) observed for the DMNB run (solid line, average of 20 cycles) and the PG run (dashed line also an average of 20 cycles, after Pore-PG correction). Fig 5.7 B shows the PG run again (thin dashed line) and its negative derivative which is used as the IRF (solid line, the y-axis scale for this line is on the right of the panel) Fig 5.7 C shows the difference of the subtraction of the PG curve from the DMNB curve from panel A. Fig 5.7 D shows the result of the deconvolution of the difference curve in panel C with the IRF in panel B. All runs are shown from 0-0.5 sec.

181

Deconvolution and digital filtering in the Fourier domain were performed by the following steps, which are described in more detail in Chapter 2, section 2.3 [88-90]: complex division of the Fourier transform of curve 5.7 C by the Fourier transform of the solid line in 4.7 B of the normalized PG curve; multiplication of the quotient of this complex division by the trapezoidal filter function ({0,1}, {0,1}, {49.80,1}, {69.34,0}) [88] in order to remove high frequency noise (>69.34 Hz); and inverse Fourier transformation to produce the deconvolved data in the time domain in Fig. 5.7 D.

5.3.5 Cumulative rate curves for Bed 1; demonstration of the need to remove PDMS

Experiments involving Bed 1 of Luna C-18 were found to exhibit an artifact that has not yet been discussed in this thesis. The characterization of this type of artifact on Bed 1 led to the improved procedure for packing Bed 2. The Bed 1 results will be discussed first. The deconvolved instantaneous rate curves were digitally integrated between 0 and 10 sec for all three experimental runs obtained from Bed 1 using Excel software. The average absorbance between 4 and 5 sec was taken as baseline and the results of the integrations were multiplied by $F/\varepsilon_i l$ in order to obtain the cumulative rate curves for desorption of NA, as described by Eq. 2.29. The curves for Runs 1-3 are shown in Fig. 5.8 as solid lines, each one of which is actually composed of 4000 data points. Prism Software Version 4.00 (GraphPad Software, San Diego, CA) was used to fit the data to Eq. 2.1, describing spherical diffusion (20 exponential terms), starting at 0.01 sec. The fit is the thin dashed line and in Fig. 5.8 and it is obvious that the fit to Eq. 2.1 is quite poor,

182
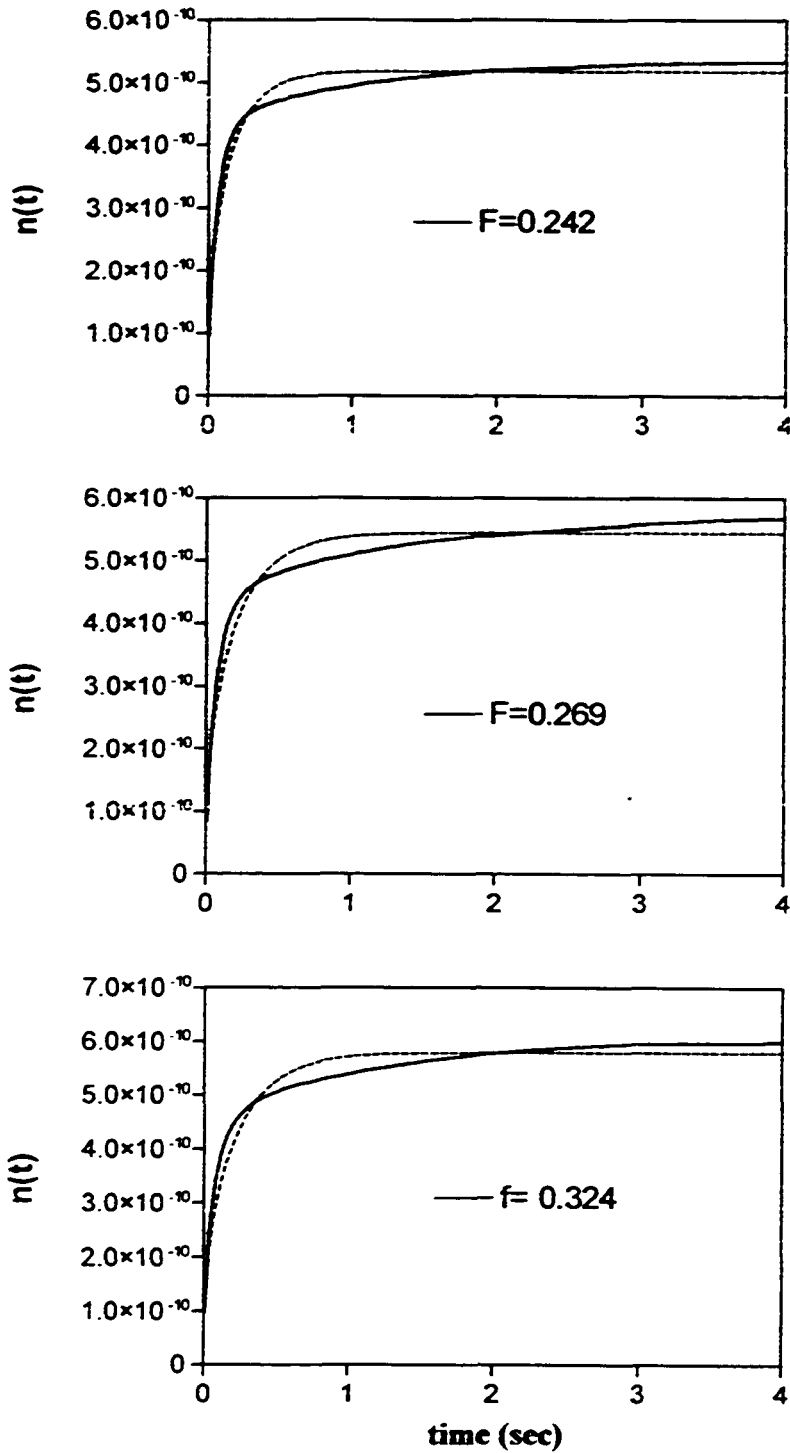
Fig 5.8. Cumulative desorption curves of DMNB from Luna C-18 for Bed 1, Runs 1-3. Solid line is the data, actually made up of 4000 data points. The thin dashed line is the fit to Eq. 2.1, (spherical diffusion) while the grey line is the fit to Eq. 5.6, which accounts for spherical diffusion and an additional planar diffusion process occurring in parallel.

183

with R^2 values ranging from 0.8810 to 0.8912. This could mean that there are two desorption processes of different origin inside ODS. However, it has to be investigated whether this could instead, be the caused by an instrument artifact such as the sorption of DMNB by the PDMS film or the glass beads.

To determine whether there are any sorptive materials present, in addition to the Luna C-18, DMNB and PG desorption runs were carried out with blank shallow beds, which did not contain Luna C-18 particles. The first blank shallow bed was prepared in exactly the same way as Bed 1, except that it was packed with glass beads only. The data treatment for this bed is the same as for Bed 1, including the treatment of section 5.3.4. (The Pore-PG correction, described in Section 5.3.3, was not performed since the glass beads used are non-porous). The cumulative DMNB desorption curve from this blank shallow bed is shown in Fig. 5.9 as the thick solid line. If there are no materials which exhibit any capacity for sorption of DMNB this curve should have a value of zero at all times. However, the desorption curve is clearly non zero, and it approaches a plateau value which is almost 20% of that of Bed 1 in Fig. 5.8. Clearly, there is an additional sorbing material other than the ODS particles.

Another blank shallow bed was prepared, but this time the space previously filled by the particles and silicon grids was filled with a porous Teflon membrane (Zitex, 30-60 μm pore size). As well, the Nickel mesh (see Fig. 4.4) is not used in this blank bed. The data were obtained in exactly the same way as for the first blank bed. The cumulative DMNB desorption curve from the Teflon-packed bed is shown as the thick dashed line in Fig.

184
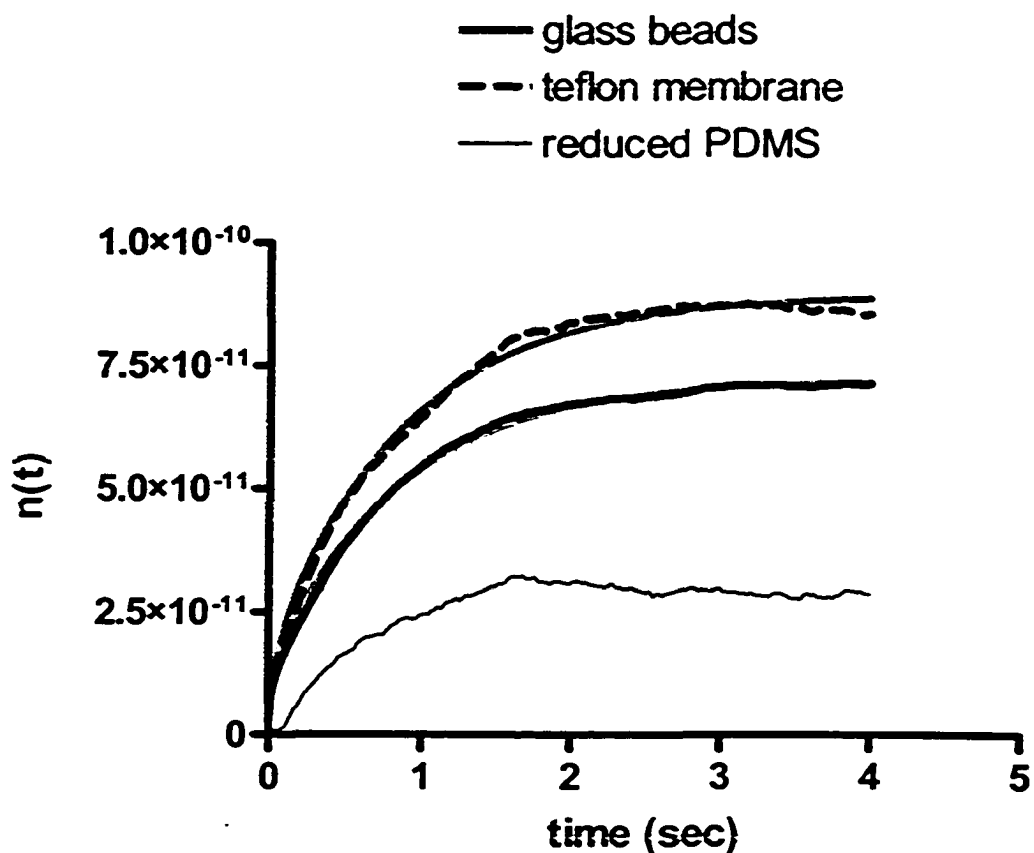
Best Fit Parameters	Glass beads	Teflon membrane
$n_{i,0,film}$ ($\times 10^{11}$ mol)	0.723 ± 0.001	0.895 ± 0.001
β_{film} (s^{-1})	1.175 ± 0.002	1.135 ± 0.03
R^2	0.9968	0.9932

Fig. 5.9. The cumulative desorption rate curves of DMNB from blank beds which do not contain Luna C-18. The solid line represents data for bed packed with glass beads only, while the thick-dashed line represents data for a different blank bed, only containing a porous teflon membrane, with no glass beads or ODS packing. The grey lines are the best fit lines of Eq. 5.5 to the data. The thin solid line corresponds to a blank bed packed only with a porous teflon, but which had PDMS partially scraped off some of its surfaces.

185

5.9. It is very similar in size and shape to that of the first blank bed. This result confirms that there is residual sorption in the shallow bed as prepared, but it eliminates the possibility that the glass beads (or the silicon grids and Ni mesh) are the source.

The next thing to consider is the possibility that the thin film of PDMS used to enable the seal between the s.s. washers (See Fig. 4.4, and Fig. 5.2) acts as a sorbing material for DMNB. This is a likely source since the phenomenon of small molecules being sorbed into the bulk of PDMS-stamps in microcontact printing is well known [110]. Even though it is not visible to the naked eye, a thin film of PDMS was found to exist on the walls in the hole of the s.s. washers. This was seen when the walls of the washers were scraped, causing the PDMS film come off and form visible, rolled-up regions. To test the possibility that the residual PDMS is sorbing DMNB, the PDMS was **partially** scraped off the inside walls of the s.s. washers as well as from the area up to around 0.2 mm from the inside edge (See Fig. 5.2). After this step, another blank bed was prepared using the porous Teflon membrane. The resulting cumulative desorption curve is shown as the thin dashed line in Fig. 5.9, from which it is clear that the amount of sorbed DMNB has been reduced.

Another piece of evidence supporting the hypothesis that residual films of PDMS sorb DMNB is the fitting of the desorption curves from the blank beds in Fig. 5.9. If PDMS film is involved, then the desorption curve should be best described by the equation for a plane sheet, and not by spherical diffusion equation (Eq. 2.1) or by any other form, such

186

as a single exponential equation (Eq. 2.6). The curves in Fig. 5.9 were fit to Eq. 5.5 describing diffusion from a planar film of material

$$n_{t}(t) = n_{t,0}\left(1 - \frac{8}{\pi^2}\sum_{j=0}^{\infty}\frac{1}{(2j+1)^2}e^{-(2j+1)^2\beta_{film}t}\right)$$ (5.5)

Where β_{film} is defined as

$$\beta_{film} = \frac{\pi^2 D_{film}}{\ell^2_{film}}$$ (5.5a)

and where D_{film} and ℓ_{film} are the diffusion coefficient of DMNB inside PDMS and the thickness of the film, respectively.

The curves in Fig 5.9 were also fit to the spherical diffusion Equation (Eq. 2.1) and the single exponential equation (Eq. 2.6). It is found that the best fit is obtained with Eq. 5.5 with R^2 coefficients of (0.9968 and 0.9932 for the glass beads and Teflon membrane, respectively). The best fit lines, along with a table showing the best fit parameters, are shown in Fig. 5.9. The fits of Eq. 2.1 (R^2 = 0.9810 and 0.9750) and Eq. 2.7 (R^2 = 0.9905 and 0.9879) were significantly poorer, and are not shown in Fig. 5.9.

With the knowledge that there is an extra signal from a film of PDMS which is in contact with the flowing solution, the DMNB desorption curves from Luna C-18 shown in Fig. 5.8 were re-fit to the following equation which describes the sum of spherical diffusion and planar diffusion process, which are independent of each other, under infinite bath conditions:

187

$$n_i(t) = n_{i,0,sph}\left(1 - \frac{6}{\pi^2}\sum_{j=1}^{\infty}\frac{1}{j^2}e^{-j^2\beta t}\right) + n_{i,0,film}\left(1 - \frac{8}{\pi^2}\sum_{j=0}^{\infty}\frac{1}{(2j+1)^2}e^{-(2j+1)^2\beta_{film}t}\right) \qquad (5.6)$$

where $n_{i,0,sph}$ is the total moles of DMNB in the spherical packing at sorption equilibrium, and $n_{i,0,film}$ is the total moles in the PDMS film at sorption equilibrium. The values of β and β_{film} are defined by Eq. 2.3 and 5.5a, respectively. Eq. 5.6 is derived by addition of Eq. 2.1 and Eq. 5.5. The fits to Eq. 5.6 are shown as the thick grey lines in Fig. 5.8 and the fitting parameters along with the R^2 values are shown in Table 5.1. It is quite obvious that this equation fits the data much more closely than the simpler spherical diffusion equation. The average values of $n_{i,0,sph}$, D_i, along with the standard deviations, based on the three runs of Bed 1, are $n_{i,0,sph} = (4.26 \pm 0.02) \times 10^{-10}$ mol, and $D_i = (3.5 \pm 0.3) \times 10^{-7}$ cm^2 s^{-1}, for spherical diffusion. The best fit parameters for planar diffusion of DMNB from the PDMS film are less reproducible, possibly due to the lower S/N ratio of this process and the fact that they describe the minor component of the desorption data (the desorption of DMNB from the film is significantly slower than from Luna C-18, and that the PDMS film contains less DMNB solute, which should decrease its signal to noise ratio according to the discussion in Chapter 2, section 2.3). Their values are $n_{i,0,film} = (1.5 \pm 0.3) \times 10^{-10}$ mol, and $\beta_{film} = (0.7 \pm 0.1)$ s^{-1}. They can be compared to values from Fig. 5.9 obtained on blank shallow beds containing a PDMS film, where the average values are $n_{i,0,film} = (0.8 \pm 0.1) \times 10^{-10}$ mol, and $\beta_{film} = (1.16 \pm 0.02)$ s^{-1}. The two sets of results are of the same order of magnitude. Results from Bed 1 have larger $n_{i,0,film}$ values and smaller β_{film} values, both of which suggest a thicker PDMS film than is present in the blank experiments. This is not surprising, since the application of PDMS film is not a tightly controlled process.

188

Table 5.1. Parameters from non-linear regression fit of Eq. 5.6, describing independent, simultaneous, spherical diffusion (in Luna C-18) plus planar diffusion (in the residual film of PDMS) processes, to the cumulative desorption rate curves of DMNB ($n_{i,0,sph}$, $n_{i,0,film}$, β and β_{film} are fitting parameters). Fitting curves are shown in Fig 5.8.

Result/Parameter	Run 1	Run 2	Run 3
m_{SB} ($\times 10^3$ g)[a]	-	-	-
$[i]_{MP}$ ($\times 10^4$ mol/L)	0.61	0.61	0.61
F ($\times 10^5$ L/s)	24.2	26.9	32.4
$n_{i,0,sph}$ ($\times 10^{10}$ mol)[b]	4.27 ±0.01	4.23 ±0.01	4.27 ±0.01
$n_{i,0,film}$ ($\times 10^{10}$ mol)[b]	1.54 ±0.01	1.15 ±0.01	1.80 ±0.01
β (s^{-1})[b]	8.92 ±0.04	10.52 ±0.05	9.688 ±0.04
β_{film} (s^{-1})[b]	0.565 ±0.007	0.782 ±0.09	0.791 ±0.06
R^2	0.9949	0.9941	0.9963
D_i ($\times 10^7$ cm^2/s)[c] (spherical)	3.25	3.84	3.53

[a]   The mass of the ODS packing is unknown (see section 5.2.2.2)
[b]   The standard deviation of numbers are based on the individual non-linear regression results.
[c]   The diffusion coefficient for DMNB is obtained from β via Eq. 2.3 using 1.0×10^{-3} cm for particle radius. Mean value for Runs 1-3 is $D_i = (3.5 \pm 0.3) \times 10^{-7}$ cm^{2}s^{-1}

189

5.3.6 Cumulative curves for Bed 2 fit to spherical diffusion equation

With the knowledge gained from the Bed 1 experiments, that PDMS needs to be eliminated from the parts of the s.s. washers which are in contact with the solutions during the shallow-bed experiments, the preparation of Bed 2 included the extra step of carefully scraping off the PDMS from the problem areas, as shown in Fig. 5.2 and discussed in Section 5.2.3.3.

The instantaneous rate curves (*e.g.* Fig. 5.7) from Bed 2 were treated in almost exactly the same way to that for Bed 1. The differences include the fact that Pore-PG correction was applied. The average absorbance between 2.5 and 3.5 sec was taken as baseline. The curves for Runs 1-3 are shown in Fig. 5.10 A-C, respectively, as solid lines, each one of which is actually composed of 4000 data points. It is apparent from comparing Fig. 5.10 to Fig. 5.8 that the slow part due to the presence of PDMS has been eliminated. Prism Software Version 4.00 (GraphPad Software, San Diego, CA) was used to fit the data to Eq. 2.1, describing spherical diffusion (15 exponential terms). The goodness of fit is much better than for Bed 1. The fits to these curves are shown in Fig. 5.11, which plots the same curves from 0-0.5 sec, in order to better visualize the goodness of fit. Only data from 0.01 sec are used, as justified by the use of 15 terms in Eq. 2.1. The results are shown in Table 5.2. The average values of $n_{i,0,sph}$, D_i, along with the standard deviations, based on the three runs of Bed 2, are $n_{i,0} = (5.43 \pm 0.06) \times 10^{-10}$ mol, and $D_i = (3.9 \pm 0.2) \times 10^{-7}$ cm^{2}s^{-1}. This value is statistically indistinguishable from the spherical diffusion parameter for Bed 1 (*i.e.* $D_i = (3.5 \pm 0.3) \times 10^{-7}$ cm^{2}s^{-1}, see Table 1) obtained by fitting
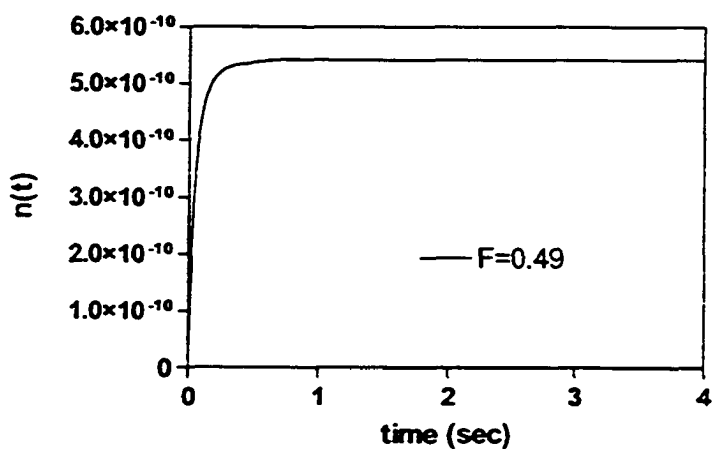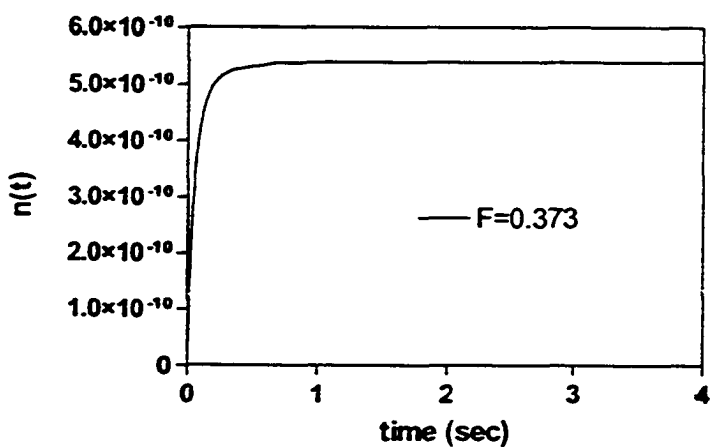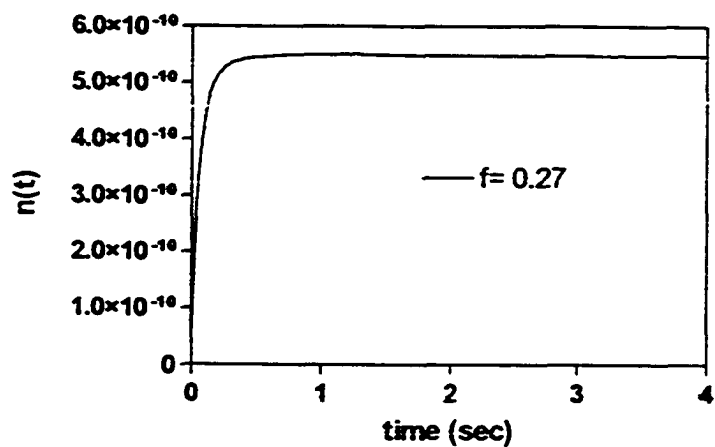
Fig 5.10 Experimental cumulative desorption rate curves of DMNB from Luna C-18 for Bed 2, Runs 1-3. The curves plateau before 1 sec has passed, suggesting that DMNB does not enter PDMS.

191
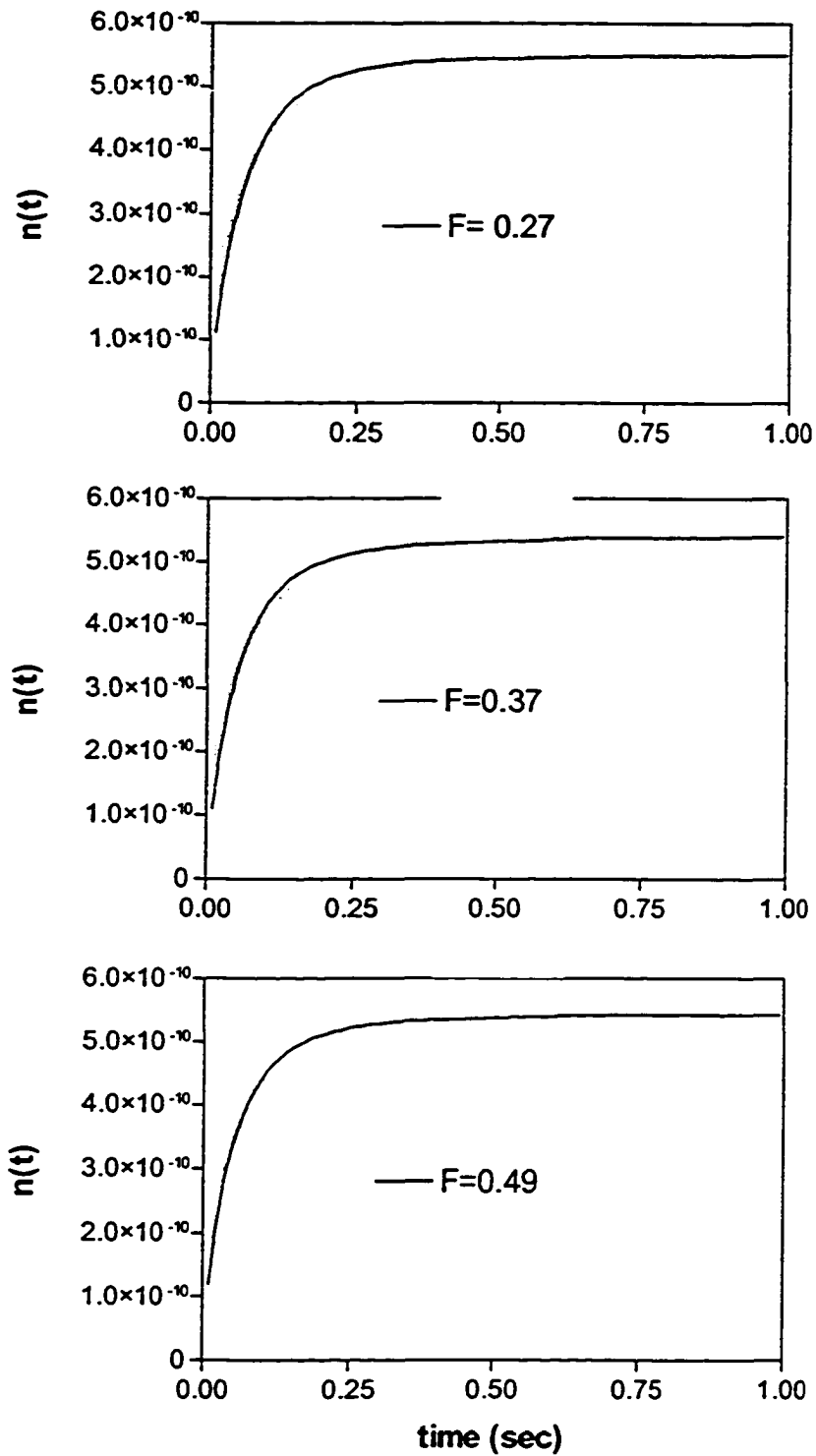
Fig. 5.11. Fit of Eq. 2.1 (pure spherical diffusion) to Runs 1-3 of Bed 2. Solid dark lines are experimental data points (same data as in Fig. 5.10) and gray line is for the best fit line. The fitting parameters are reported in Table 5.2.

192

Table 5.2. Parameters from non-linear regression fit of Eq. 2.1, describing spherical diffusion, to the cumulative desorption rate curves of DMNB from Luna C-18, Bed 2 ($n_{i,0}$ and β are fitting parameters). The fitting curves are shown in Fig. 5.11

Result/Parameter	Run 1	Run 2	Run 3
m_{SB} ($\times 10^3$ g)[a]	-	-	-
$[i]_{MP}$ ($\times 10^4$ mol/L)	0.61	0.61	0.61
F ($\times 10^5$ L/s)	27.5	37.3	49.0
$n_{i,0}$ ($\times 10^{10}$ mol)[b]	5.50 ± 0.01	5.37 ± 0.01	5.41 ± 0.01
β (s^{-1})[b]	9.84 ± 0.04	10.06 ± 0.05	10.99 ± 0.04
D_i ($\times 10^7$ cm^2/s)[c]	3.77	3.86	4.21
R^2	0.9839	0.9843	0.9860

[a]   The mass of the ODS packing is unknown (see section 5.2.2.2)
[b]   The standard deviation of numbers are based on the individual non-linear regression results.
[c]   The diffusion coefficient for DMNB is obtained from β *via* Eq. 2.3 using 6.15 × 10^{-4} cm for particle radius. Mean value for Runs 1-3 is $D_i = (3.9 \pm 0.2) \times 10^{-7}$ cm^2 s^{-1}

193

with Eq. 5.5 (the sum of spherical plus planar diffusion). The two values pass the t-test at the 95% confidence level. The $n_{i,0}$ values are not indistinguishable, but they are not expected to be, since the amount of ODS in the two beds are not known and are not expected to be the same (See Section 5.2.3.2). While the fit of the data from Bed 2 with the spherical diffusion equation (Eq. 2.1) is reasonable, with $R^2 \approx 0.98$, deviations are visible in Fig 5.11 at times under 0.3 sec. These deviations could be caused by the flowrate being too slow to achieve shallow-bed conditions at short times or by the occurrence of slow external film diffusion, in addition to intra-particle diffusion, as a rate-determining step. These possibilities are explored in the next section.

5.3.7 Cumulative rate curves for Bed 2 fit to models accounting for film resistance and slow flowrate

Fig. 5.12, panels A-C, shows the fit of Runs 1-3 of Bed 2 to Eq. 2.32, which applies to spherical diffusion if shallow bed conditions have not been fully met or when external film diffusion contributes as the rate-limiting step, or when both are true. The curves were fit using Microsoft Excel solver, and the best fit values are reported in Table 5.3. It is apparent from the high R^2 values that the fit of the data to this equation is significantly better than the fit to a simple spherical diffusion equation (Table 5.2). Equation 2.32 has three fitting parameters: $n_{i,0}$, D_i, and L. The best fit values for the three runs give $D_i = (8.8 \pm 0.3) \times 10^{-7} \text{ cm}^2 \text{ s}^{-1}$. The three D_i values are close in magnitude, regardless of the flowrate used. The best fit values of L are 4.1, 4.1 and 4.5 for Runs 1-3, respectively. A low value of L (less than ≈ 25) means there is a significant deviation from the shape of the simple spherical diffusion, defined by Eq. 2.1. The two possible causes for the low

194

Fig. 5.12. Fit of Eq. 2.32 to Runs 1-3 of Bed 2. Solid dark lines are experimental data points (same data as in Fig. 5.10) and gray line is for best fit line. The fitting parameters are reported in Table 5.3.

Table 5.3. Parameters from non-linear regression fit of Eq. 2.32, to the cumulative desorption rate curves of DMNB from Bed 2 ($n_{i,0}$, D_i and L are fitting parameters). The fitting curves are shown in Fig. 5.12

| Result/Parameter	Run 1	Run 2	Run 3
m_{SB} ($\times 10^3$ g)[a]	-	-	-
$[i]_{MP}$ ($\times 10^4$ mol/L)	0.61	0.61	0.61
F ($\times 10^5$ L/s)	27.5	37.3	49.0
$n_{i,0}$ ($\times 10^{10}$ mol)[b]	5.42	5.28	5.34
D_i ($\times 10^7$ cm^2/s)	8.6	9.0	9.1
L	4.1	4.1	4.5
δ ($\times 10^4$ cm)[c]	0.51	0.49	0.44
R^2	0.999795	0.999578	0.999466

[a] The mass of the ODS packing is unknown (see section 5.2.2.2)
[b] The standard deviation was not obtained from the fit because Microsoft Excel Solver does not calculate them automatically, unless a specific macro is written. Mean value for Runs 1-3 is $D_i = (8.8 \pm 0.3) \times 10^{-7}$ cm^2 s^{-1}
[c] δ was obtained from L and D_i through Eq. 5.8.

value of L are failure to meet shallow-bed conditions and film diffusion. To find which one of these processes is dominant, it is useful to plot the dependence of the value of L on flowrate. If failure to meet shallow-bed conditions is the reason for low L, then the value of L obtained from the fit to the data should vary linearly with flowrate, according to Eq. 2.34. Conversely, if film diffusion is the primary cause of the deviation, L should be proportional to (flowrate)$^{1/3}$, according to the theoretical relationship developed in Chapter 2, Section 2.4 :

$$L = \frac{Sh\,[i]_{MP}\,D_{MP}}{2\,[i]_{part}\,D_i} = \frac{1.09}{\varepsilon_{inter}} \left(\frac{2\,u_s\,r}{D_{MP}} \right)^{1/3} \frac{[i]_{MP}\,D_{MP}}{2\,[i]_{part}\,D_i} \qquad \text{(Eq. 2.36)}$$

In Eq. 2.36 the effect of flowrate is represented by the effect of superficial velocity u_s which is a proportional quantity. Fig. 5.13 A plots the values of L *vs.* flowrate and fits them to both Eq. 2.34 or Eq. 2.36. It is apparent that the fit to Eq. 2.36 is the better fit of the two, suggesting that film diffusion, and not slow flowrate is the primary cause of the deviation from pure spherical diffusion described by Eq. 2.1.

To further investigate the possibility of external film diffusion being the primary cause of low value of L, the best fit values of L can be compared with the predicted values of L, as discussed in Section 2.4. However, it is instead preferred here to compare the predicted and experimental values of the *diffusion-film thickness* δ, since δ is easier to interpret. The experimental value of δ can be extracted from the value of L by combining Eq. 2.35 and 2.7.

197
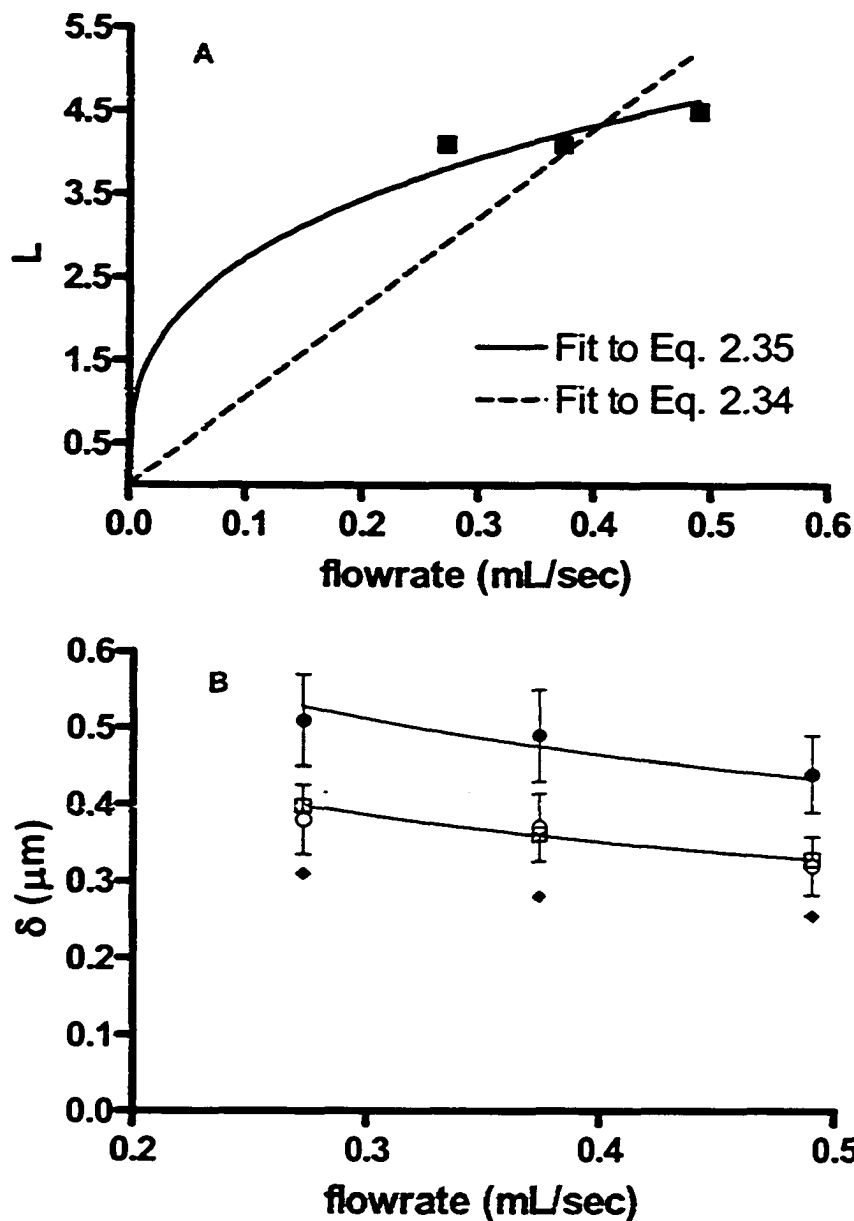
Fig. 5.13. Evidence for film diffusion being the primary distortive effect in Bed 2. A: Dependence of the parameter L on flowrate. The experimental values of L for Runs 1-3 of Bed 2 (filled squares) are from Table 5.3. Dashed line is the fit to Eq. 2.34 (non-ideal shallow bed conditions) and the solid line is the fit to Eq. 2.35 (film diffusion). B: Dependence of the diffusion film thickness δ on flowrate. Filled circles, are δ_{expt} calculated from Eq. 5.8. The open circles are δ_{expt} calculated from Eq. 5.9. The error bars are the standard deviations. The solid lines are fits of equation δ_{expt} = constant · (flowrate)$^{-1/3}$. The open squares and the filled diamonds are $\delta_{predicted}$ values from Eq 5.10 and 5.11, respectively. See text for details.

198

$$\delta_{expt} = \frac{r[i]_{MP} D_{MP}}{L_{expt} [i]_{part} D_i}$$

(5.8)

The subscripts 'expt' in the above equation signify that the value of L and δ are obtained from fitting the *experimental data* with Eq. 2.32, which distinguishes them from predicted values to be discussed later. The values for δ_{expt} obtained *via* Eq. 5.8 from the best-fit values of D_i, L, and from $[i]_{MP}/[i]_{part} = 0.05925$, $D_{MP} = (5 \pm 0.6) \cdot 10^{-6}$ cm^2/s (Wilke-Chang correlation), $r = 6.15 \times 10^{-4}$ cm. The values obtained are $\delta_{expt} = 0.51 \pm 0.06$, 0.49 ± 0.06 and 0.44 ± 0.05 μm for Runs 1-3, respectively. (The standard deviations are taken to be 12%, to match the standard deviation associated with the value of D_{MP} [99], which is assumed have the largest amount of uncertainty compared to other parameters used to calculate δ). The experimental values of δ_{expt} are shown in Fig 5.13 B as the filled circles, along with the standard deviations.

If one assumes that shallow bed conditions are met and only film diffusion acts to slow down the desorption-rate from the particle, there is another way of obtaining δ_{expt}. It involves fitting the experimental data to Eq. 2.15, described in Section 2.1.3. Fig. 5.14, panels A-C, shows the fit of Eq. 2.15 to Runs 1-3 of Bed 2. The curves were fit using Microsoft Excel solver, and the best-fit values are reported in Table 5.4. The fit of this equation is also very good and it displays very high R^2 values. Eq. 2.15 has three fitting parameters: $n_{i,0}$, D_i, and θr. The average value of D_i for the three runs is $(7.4 \pm 0.3) \times 10^{-7}$ cm^2 s^{-1}, which is close to that obtained from fitting with Eq. 2.32 above. This is expected since, when film diffusion is the primary cause of deviation from spherical diffusion, Eq.
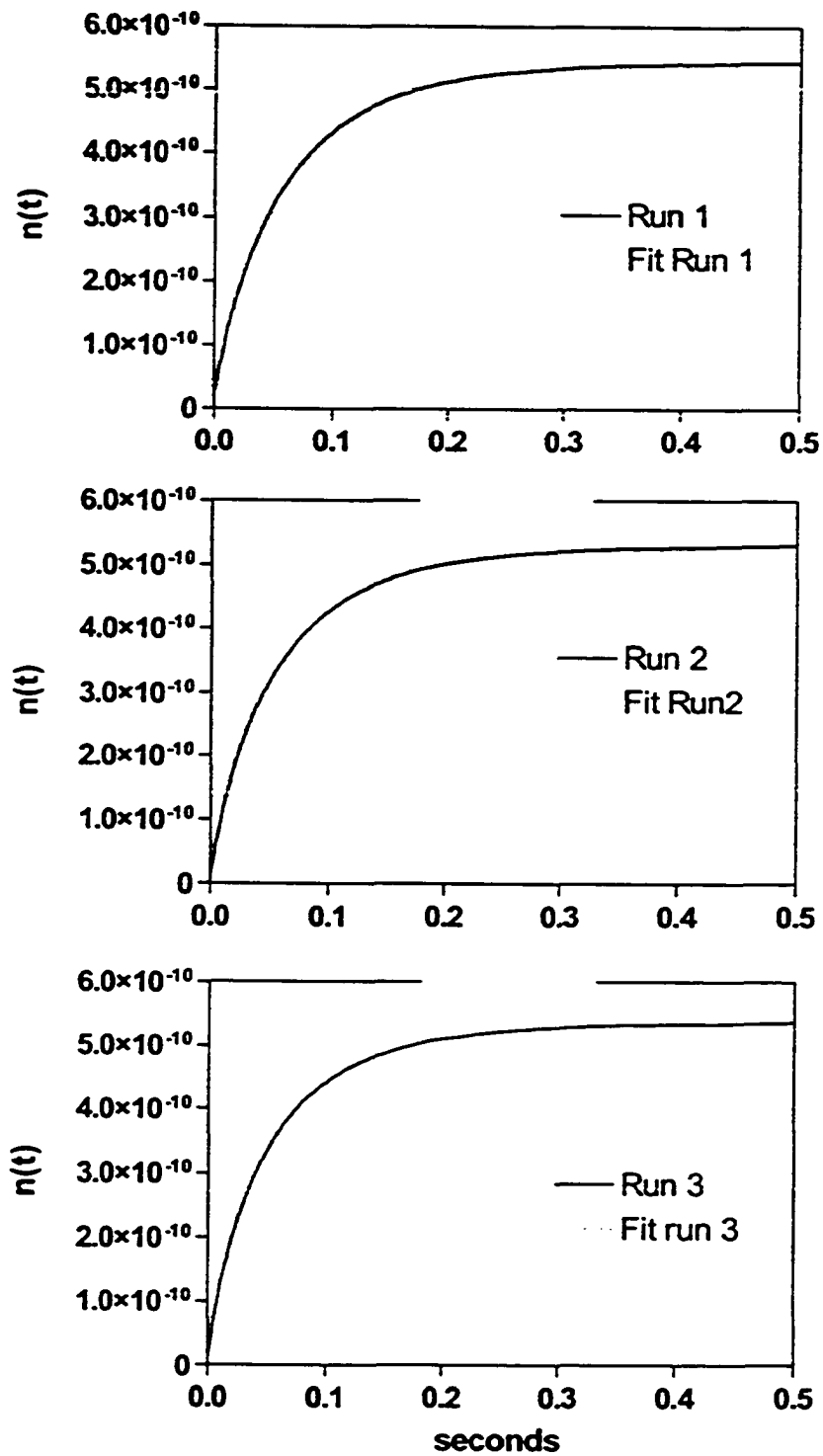
199
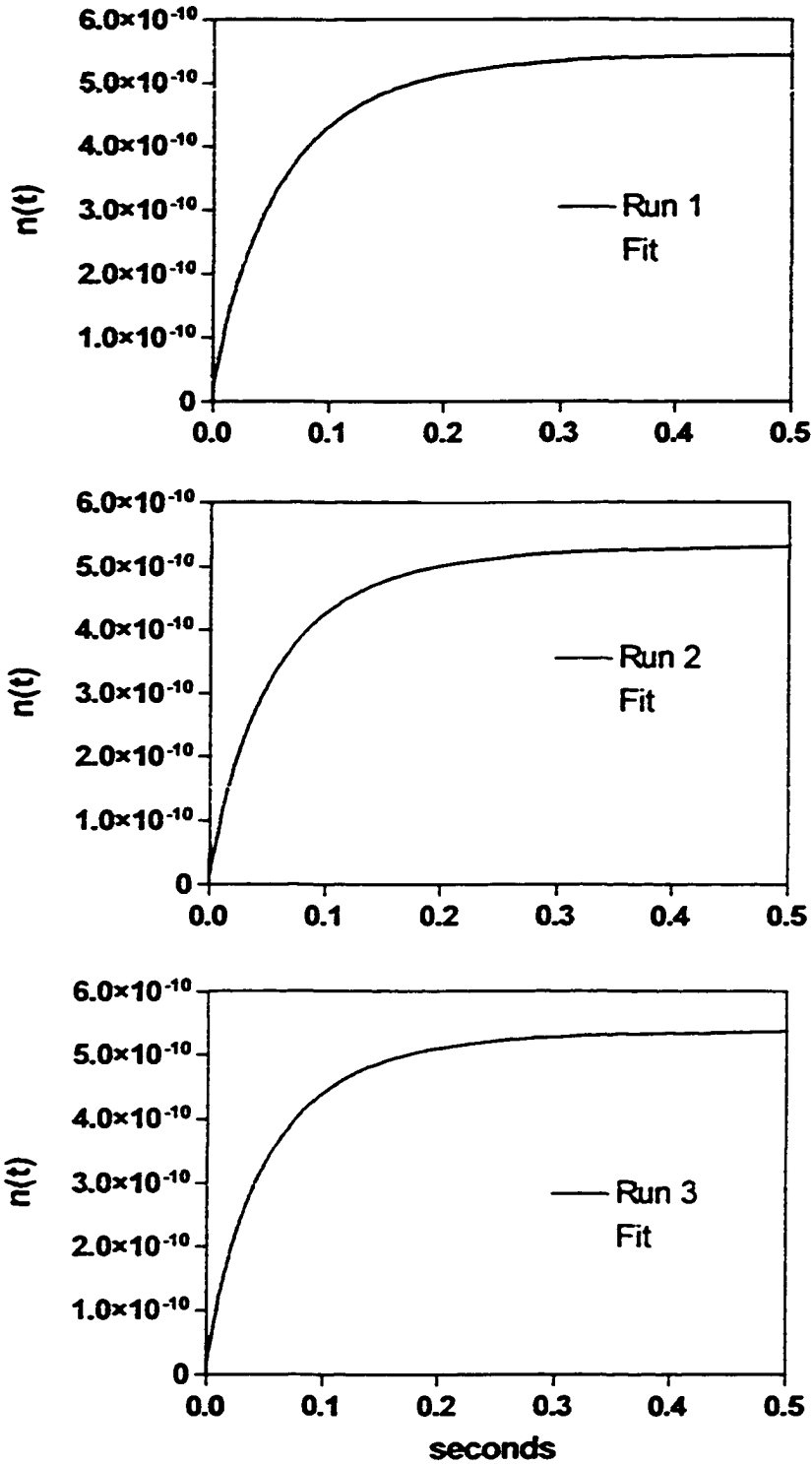
Fig. 5.14. Fit of Eq. 2.15 (film/spherical particle diffusion) to Runs 1-3 of Bed 2. Solid dark lines are experimental data points (same data as in Fig. 5.10) and gray line is for best fit line. The fitting parameters are reported in Table 5.4.

200

Table 5.4. Parameters from non-linear regression fit of Eq. 2.15, describing desorption from a sphere with partially-limiting external film diffusion, to the cumulative desorption rate curves of DMNB from Bed 2 ($n_{i,0}$, D_i and δ are fitting parameters). The fitting curves are shown in Fig. 5.14

Result/Parameter	Run 1	Run 2	Run 3
m_{SB} ($\times 10^3$ g)[a]	-	-	-
$[i]_{MP}$ ($\times 10^4$ mol/L)	0.61	0.61	0.61
F ($\times 10^5$ L/s)	27.5	37.3	49.0
$n_{i,0}$ ($\times 10^{10}$ mol)[b]	5.42	5.28	5.34
D_i ($\times 10^7$ cm^2/s)[b]	7.14	7.50	7.68
θr (from Eq. 2.15)[h]	6.65	6.55	7.35
δ ($\times 10^5$ cm)[c]	3.84	3.71	3.23
R^2	0.99969	0.99951	0.99945

[a]   The mass of the ODS packing is unknown (see section 5.2.2.2)
[b]   The standard deviation for the fitting parameters was not obtained from the fit because Microsoft Excel Solver does not calculate it automatically, unless a specific macro is written. Mean value for Runs 1-3 is $D_i = (7.4 \pm 0.3) \times 10^{-7}$ cm^2 s^{-1}
[c]   The value of δ was obtained from θ via Eq. 5.9 by using $[i]_{MP}/[i]_{part} = 0.05925$ (calculated using R=32.40, and particle porosity $\varepsilon_{pp} = 0.505$), $D_{MP} = 5 \times 10^{-6}$ cm^2/s, and the best fit values for D_i and θr (r = 6.15 $\times 10^{-4}$ cm).

201

Eq. 2.15 should be an alternative form of Eq. 2.32. The values for δ_{expt} are obtained *via* a modified form of Eq. 2.15 b:

$$\delta_{expt} = \frac{[i]_{MP} \, D_{MP} \, r}{[i]_{part} \, D_i \, \theta \, r} \tag{5.9}$$

Using the best-fit values of D_i and θr, and from $[i]_{MP}/[i]_{part} = 0.05925$, $D_{MP} = (5 \pm 0.6) \times 10^{-6}$ cm^2/s (Wilke-Chang correlation), $r = 6.15 \times 10^{-4}$ cm, the values of $\delta_{expt} = 0.38 \pm 0.05$. 0.37 ± 0.04 and 0.32 ± 0.04 μm are obtained for Runs 1-3, respectively. (The standard deviations are taken from the average deviation associated with D_{MP} which, at 12% is assumed have the largest amount of uncertainty as compared to other parameters used to calculate δ_{expt} from Eq. 2.15). These values of δ_{expt} are also shown in Fig 5.13 B as open circles.

As mentioned above, the values of δ can also be **predicted**, which is done using the following correlations. The first correlation is obtained after combining and rearranging Eq, 2.7 and Eq. 2.12.

$$\delta_{predicted} = \frac{2 \, r \, \varepsilon_{inter}}{1.09} \left(\frac{2 \, u_s \, r}{D_{MP}} \right)^{-1/3} \tag{5.10}$$

The second correlation is obtained after combining Eq, 2.7 and 2.13

$$\delta_{predicted} = \frac{2 \, r}{1.85} \left(\frac{1 - \varepsilon_{inter}}{\varepsilon_{inter}} \right)^{-1/3} \left(\frac{2 \, u_s \, r}{D_{MP}} \right)^{-1/3} \tag{5.11}$$

202

Values obtained by the use of Eq. 5.10 are 0.31, 0.28, and 0.255 μm, while those

obtained with Eq. 5.11 are 0.398, 0.36, and 0.328 for Runs 1-3 respectively. These

values are based on $r = 6.15 \times 10^{-4}$ cm, $\varepsilon_{inter} = 0.4$, and assuming that the open fraction of

the shallow bed (the area not taken up by the walls of the silicon grids) is 0.7. Fig 5.13 B

shows the $\delta_{predicted}$ values obtained from Eq. 5.10 as open squares and the $\delta_{predicted}$ values

obtained from Eq. 5.11 as filled diamonds.

The predicted and experimental values of δ plotted in Fig. 5.13 B and presented in Table

5.5 are of the same order of magnitude. Also, when the values of δ_{expt} are fit with an

equation :

$$\delta_{expt} = (\text{constant}) \cdot (\text{flowrate})^{-1/3} \tag{5.12}$$

which is the expected dependence of δ, the fit is reasonable. (The fit line to the *predicted*

values is not shown, because, by definition, they give a perfect fit to an equation such as

constant $\cdot$ (flowrate)$^{-1/3}$, *i.e.* see Eq. 5.10 and 5.11) In addition, it is very likely that the

$\delta_{predicted}$ values are even closer to the values of δ_{expt}, because of a systematic error in the

present use of Eqs 5.10 and 5.11: the particle radius that is used in the prediction of δ is

that of Luna C-18 particles, but in fact the bed was prepared with a mixed-particle slurry.

The glass beads have larger diameters (from 10-20 μm, with the majority having

diameters closer to 20 μm, by microscopic inspection). It is therefore likely that $\delta_{predicted}$

values should be larger. It is not clear how much larger this value should be, however it

203

Table 5.5. Summary of experimentally obtained (δ_{expt}) and predicted ($\delta_{predicted}$) diffusion thicknesses plotted in Fig. 5.13 B.

Method of obtaining δ_{expt} or $\delta_{predicted}$	Run 1	Run 2	Run 3
δ_{expt} (from Table 5.3)	0.51 ± 0.06 [a]	0.49 ± 0.06	0.44 ± 0.05
δ_{expt} (from Table 5.4)	0.38 ± 0.05	0.37 ± 0.04	0.32 ± 0.04
$\delta_{predicted}$ via Eq. 5.10	0.310 [b]	0.280	0.255
$\delta_{predicted}$ via Eq. 5.11	0.398 [b]	0.360	0.328

[a] The ± signs are standard deviations

[b] The uncertainty in the values of $\delta_{predicted}$ could not be easily calculated. Instead, the differences between the two predicted values provide a sense of the possible uncertainty.

204

could be on the order of 10-20%. For example if it is assumed that the volume-averaged particle diameter of the glass beads is on the order of 16 μm, and that the volume fraction of the glass beads in the shallow bed is about 35%, according to discussion is Section 5.2.3.2, then the volume-averaged particle diameter in the bed is $12.3 \cdot 0.65 + 16 \cdot 0.35 = 13.9$ μm, which is 10 % higher than the diameter of Luna C-18 packing of 12.3 μm.

In summary, the δ_{expt} and $\delta_{predicted}$ values are close in magnitude, especially when taking into account that $\delta_{predicted}$ values should be slightly larger. As well, δ_{expt} values give a reasonable fit to an Eq. 5.12. These facts give further support to the view that the desorption rate from Luna C-18 is slowed-down primarily by film diffusion, and not the failure to meet shallow bed conditions.

5.3.8 Shallow-bed conditions

The requirements which need to be met for the achievement of shallow-bed conditions have already been discussed in Sections 2.4 and 3.3.4. In short, shallow-bed conditions can be effectively achieved if the maximum desorbing solute concentration never exceeds a very small fraction of the feed-solution concentration. For this purpose it is useful to refer to Fig. 5.7, which has been normalized so that the absorbance (or concentration) of the feed solution is equal to 1. The plot of the normalized, deconvolved desorbing concentration for Run 1 is shown in Fig. 5.7 D. At small times, the maximum desorbing concentration is 59% of the feed concentration. The maximum desorbing concentrations leaving the bed are 47% for Run 2 and 40% for Run 3 (not shown). They are lower

205

because of the increased flowrate. According to this criterion alone, it seems that shallow bed conditions are not fully met.

However, the results from the previous section suggest that shallow-bed conditions are nearly met and that film diffusion is the dominant effect causing the distortion of the observed desorption-rate curve

Finally, if one is only interested in obtaining the value of the diffusion coefficient inside the packing (D_i) it is not necessary to achieve strict shallow bed conditions because Eq. 2.32 accounts for the effects of slow flowrate and/or external film diffusion. In addition, errors associated with failure to meet shallow bed conditions (and with film diffusion) affect the data at short times, and to a lesser extent at longer times, so only looking at long-time data would lessen their effect. However, it is desirable to keep flowrates as large as possible, so that the distortion due to small velocities does not become the major contributor to the observed desorption curves; extracting diffusion coefficients in such cases would be prone to large errors.

5.3.9 Film *vs* particle diffusion

The issue of film diffusion being partially rate limiting to the desorption kinetics from Luna C-18 has already been explored in Section 5.3.7, where it was shown that film diffusion is the primary reason for the fact that the desorption data do not follow pure spherical particle diffusion. In this section, the relative contributions of particle diffusion

206

and film diffusion are quantified with the use of Eq. 2.14. For DMNB, D_{MP} is 5×10^{-6} $cm^2 s^{-1}$ and D_i can be obtained from Table 5.3, and the ratio $[i]_{part}/[i]_{MP}$ is equal to 16.9, and the values of δ are obtained from the correlations as described in Section 5.3.7. The value of X ranges from 0.17 to 0.14 for the slowest to the highest flowrates used for Bed 2. These values are very close to 0.13, suggesting that both film - and particle diffusion resistances contribute significantly to mass-transfer in this study.

5.3.10   Pore vs. surface diffusion of DMNB in Luna C-18

The intra-particle diffusion coefficient for DMNB in Luna C-18 obtained from fitting Eq. 2.32 to the cumulative desorption rate data is $D_i = (8.8 \pm 0.3) \cdot 10^{-7} cm^2 s^{-1}$. If DMNB were to diffuse inside the mesopores of LUNA C-18 *via* sorption-retarded pore diffusion (SRPD), the D_i for DMNB can be predicted *via* Eq 1.16 using the values: $D_{MP} = (5 \pm 0.6)$ $\cdot 10^{-6} cm^2 s^{-1}$ for DMNB in 50/50 $MeOH/H_2O$ (from the Wilke-Chang correlation [99]). The parameter R in Eq. 1.16, which is the ratio of moles DMNB in the pores to the moles adsorbed on the pore walls, was calculated to be 32.4. Tortuosity is assumed to have the value of 2 ± 0.5, as discussed in Sections 1.3.2 and 1.5.2. The hindrance parameter for DMNB inside the mesopores of LUNA C-18 (average pore size of 100 Å) is estimated to be 0.8 ± 1 [27, 30, 31]. The estimated D_i for DMNB assuming SRPD mechanism is then calculated via Eq. 1.16 to be $(6 \pm 2) \cdot 10^{-8} cm^2 s^{-1}$. This value is more than an order of magnitude smaller than the observed diffusion coefficient showing that pore diffusion alone cannot explain the observed value, and surface diffusion is the dominant mode of mass transfer in Luna C-18. The surface diffusion coefficient for DMNB inside Luna C-

18 is calculated by rearranging Eq. 1.11 and using parameters calculated above, to yield $D_S = (8.5 \pm 0.5) \cdot 10^{-7}$ cm^2 s^{-1}. Since, in Eq. 1.11 the tortuosity for surface diffusion coefficient is lumped into D_S, the surface diffusivity along the pore walls is more likely to be around $(3 \pm 1) \cdot 10^{-6}$. This value is in agreement with surface diffusivities on C-18-derivatized flat fused silica obtained from luminescence methods where they range from about $2.5 \cdot 10^{-7}$ to $6.5 \cdot 10^{-6}$ cm^2/sec. (See section 1.5.2)

5.3.11 Sources of error

There are a number of sources of error in this analysis, but it will be shown that they don't contribute a large systematic error in the determined values of the intraparticle diffusivity.

(1) **Pore-PG correction**: Table 5.6 shows the results of the fit of Eq. 2.32 to the cumulative desorption curves for Runs 1-3 when the correction for pore-PG is not carried out prior to the data processing steps. To determine the importance of the pore PG-correction, these values are compared with the values in Table 5.3. One obvious difference is in the $n_{i,0}$ values, which are all consistently 3% lower. This is of course expected, since the amount of pore-solute is 3% of that of the sorbed solute at equiluilibrium. However, there is very little change in the actual mass-transfer parameters obtained from the fit to Eq. 2.32. The average value of D_i is $(9.4 \pm 0.4) \cdot 10^{-7}$ cm^2 s^{-1}, which is statistically indistinguishable (t-test, 95% confidence level) from the

208

Table 5.6. Parameters from non-linear regression fit of Eq. 2.32, the cumulative desorption rate curves of DMNB from Bed 2, which were *not* corrected for pore-PG ($n_{i,0}$, D_i and L are fitting parameters).

Result/Parameter	Run 1	Run 2	Run 3
m_{SB} ($\times 10^3$ g)[a]	-	-	-
$[i]_{MP}$ ($\times 10^4$ mol/L)	0.61	0.61	0.61
F ($\times 10^5$ L/s)	27.5	37.3	49.0
$n_{i,0}$ ($\times 10^{10}$ mol)[b]	5.23	5.09	5.15
D_i ($\times 10^7$ cm²/s)	8.9	9.6	9.6
L	3.8	3.6	4.1
δ ($\times 10^4$ cm)[c]	5.4	5.1	4.7
R^2	0.999688	0.999411	0.999347

[a] The mass of the ODS packing is unknown (see section 5.2.2.2)
[b] The standard deviation could not be obtained from the fit
[c] δ was obtained from L and D_i through Eq. 2.35.

209

value of D_i obtained after the correction $((8.8\pm 0.3) \cdot 10^{-7} \text{ cm}^2 \text{ s}^{-1})$. As well, the values of δ (0.54, 0.53, and 0.47 μm for Runs 1-3 of Bed 2) are very close to the ones obtained by fitting the corrected data (0.52, 0.50, and 0.44 μm). It seems that the uncorrected IRF-marker curve yields almost the same parameter values as the corrected one. This is true because the DMNB solute is strongly retained under the conditions $(k' = 15.0, R = 32.4)$ and the pore solute contributes only a small fraction to the total solute in the particle at sorption equilibrium. For solutes which are less strongly sorbed, the Pore-PG would be larger. The best policy, however, would be to use an IRF-Marker which is totally excluded from the porous particles. It was already discussed that high-molecular weight Blue Dextran is not suitable here for practical reasons. Another possible type of excluded IRF-Marker, which was not explored in this study, might be UV-absorbing anions, in the absence of any buffer. When the concentration of anions in the unbuffered solvent is small, the ionic strength is small, and the Donnan Potential inside the negatively-charged silica particles has an excluding effect on the anions. For example, anions such as nitrate have been used for the purpose of marking of the interparticle porosity [44, 111, 112].

(2) **Presence of PDMS**: The second significant source of possible uncertainty is the presence of PDMS on the parts of the shallow bed directly in contanct with the flowing solvent. As was shown for Bed 1 in Section 5.3.5, the solute sorbed by the film of PDMS adds an undesirable contribution to the overall desorption curve. Removal of the PDMS film was found to eliminate the problem. However, if complete removal of the film is not possible its contribution can be subtracted. We have already seen that the diffusion coefficients inside Luna C-18 obtained from Bed 1 (after fitting with Eq. 5.6,

210

accounting both for spherical diffusion plus the undesirable diffusion from the PDMS film) and from Bed 2 (after fitting with Eq. 2.1, describing spherical diffusion only) are very close in value and are statistically indistinguishable. This suggests that for Bed 1 the slow part seems to be well accounted for by the planar diffusion term of Eq 5.6. But the fast part, which is due to the desorption from Luna C-18, is not properly accounted for by the spherical diffusion term of Eq. 5.6, because of the presence of the external film resistance as well as non-shallow bed conditions. It is therefore necessary to fit the fast desorption data to Eq. 2.32, which accounts for both of those effects. This can be done if, prior to the fitting, the undesirable part of the curve is subtracted. To do this, one simply subtracts the best-fit line for the slow part, described by the parameters $n_{i,0,film}$ and β_{film} from Table 5.1. When this is done, and the resulting desorption curves for Bed 1 are fit to Eq. 2.32, the fitting parameters of D_i and L, along with the corresponding value δ are also close to those from Bed 2. The fitting parameters are shown in Table 5.7. The average D_i is $(8.8 \pm 0.8) \cdot 10^{-7}$ cm^{2}s^{-1}, which is indistinguishable from the value obtained for Bed 2 (Table 5.3). The values of L and δ are also similar, though the results are slightly more scattered.

Thus, it seems that the undesirable contribution from PDMS can be successfully subtracted from the cumulative desorption curve. Nevertheless, it is preferable to avoid direct contact of the flowing solutions with PDMS altogether, since it is a complicating factor. The method used to achieve this (scraping the extra PDMS off) is crude and time-consuming, but better methods of applying the liquid elastomer can no doubt be developed. As well the use of elastomers similar in their physical properties to PDMS

Table 5.7. Parameters from non-linear regression fit of Eq. 2.32, to the fast part of the cumulative desorption rate curves of DMNB from Bed 1. No Pore-PG correction for has been made. ($n_{i,0}$, D_i and L are fitting parameters).

Result/Parameter	Run 1	Run 2	Run 3
m_{SB} ($\times 10^3$ g)[a]	-	-	-
$[i]_{MP}$ ($\times 10^4$ mol/L)	0.61	0.61	0.61
F ($\times 10^5$ L/s)	27.5	37.3	49.0
$n_{i,0}$ ($\times 10^{10}$ mol)[b]	4.18	4.19	4.21
D_i ($\times 10^7$ cm^2/s)	9.5	8.8	8.0
L	3.8	3.5	4.5
δ ($\times 10^4$ cm)[c]	0.50	0.59	0.51
R^2	0.999675	0.999586	0.999308

[a] The mass of the ODS packing is unknown (see section 5.2.2.2)
[b] The standard deviation could not be obtained from the fit
[c] δ was obtained from L and D_i through Eq. 2.35.

212

but without the strong sorbent properties of PDMS could be used in the future. One such material, presently being developed, is 'liquid' Teflon [113].

(3) **Effect of PDMS on desorption data in Chapter 4.** In the studies reported in Chapter 4 there also was exposure of the flowing liquids to the PDMS-lined walls of the s.s. washer, and no attempts were made to scrape it off. However a separate study with a blank bed containing unscraped PDMS (a porous Teflon membrane in place of PRP-1, see section 5.3.5) was carried out in 85/15 MeOH/H$_2$O (the solvent used in Chapter 4) and it was determined that amount of solute (NA) present inside the PDMS was less than 2% of the total, its contribution was present in only the first 1 sec of the desorption curve. The reasons for the very slight effect of PDMS in the PRP-1 study are most likely the more hydrophobic nature of the eluent (85% MeOH, as opposed to 50%) as well as a larger amount of solute sorbed onto the actual stationary phase. The latter would make the amount of NA sorbed into the PDMS relatively smaller. (NA is only slightly more hydrophobic than DMNB.)

(4) **Flowrate too slow:** Another source of error is the fact that the flowrate is too slow to fully achieve shallow bed conditions. It was shown in section 5.3.7 and 5.3.8 that this is not a large source of uncertainty (*i.e.* that the flowrate is sufficiently fast, and therefore the use of Eq. 2.32, gives a good estimate of D$_i$ in Luna C-18). However, if the flowrate is made faster, this potential source of error would be further diminished. This is possible with this apparatus. It will suffice to simply use less Luna C-18 and more glass beads in the mixed particle slurry used to pack the shallow bed. If the amount of Luna C-18 is

213

decreased twofold, the flowrate is expected to rise (a reasonable guestimate would be from 1.5 to 2 times, based on experience) and the molar desorption rate would be halved, making the concentration decrease 3-4 fold. Eventually, it will not pay to decrease the amount of stationary phase further, because the absorbance due to the desorbing solute will become too small, decreasing the S/N.

5.3.12 Predicting the contributions of particle mass transfer in Luna C-18 to band broadening in a chromatographic column

The plate height associated with band broadening due sorption/desorption kinetics and other effects can be calculated *via* equations outlined in Chapter 1, and it can be compared to the plate height of the DMNB peak which has been observed on a Luna C-18 HPLC column (4.6 mm ID, 25 cm long), 50/50 MeOH/H$_2$O, 2mL/min flowrate (0.292 cm/sec velocity of unretained component), packed with the same batch of Luna C-18 as that used in the kinetic studies.

First the observed plate height is discussed. Three different chromatograms of DMNB are shown in Fig. 5.15. The fits of a Gaussian curve are superimposed. The table in Fig. 5.15 shows the best-fit parameters, such as the center of gravity and the standard deviation of the Gaussian peak. The observed plate height is calculated *via* the following equation:

$$H_{obs} = \left(\frac{\sigma}{t_R}\right)^2 \times Z \tag{5.13}$$

214
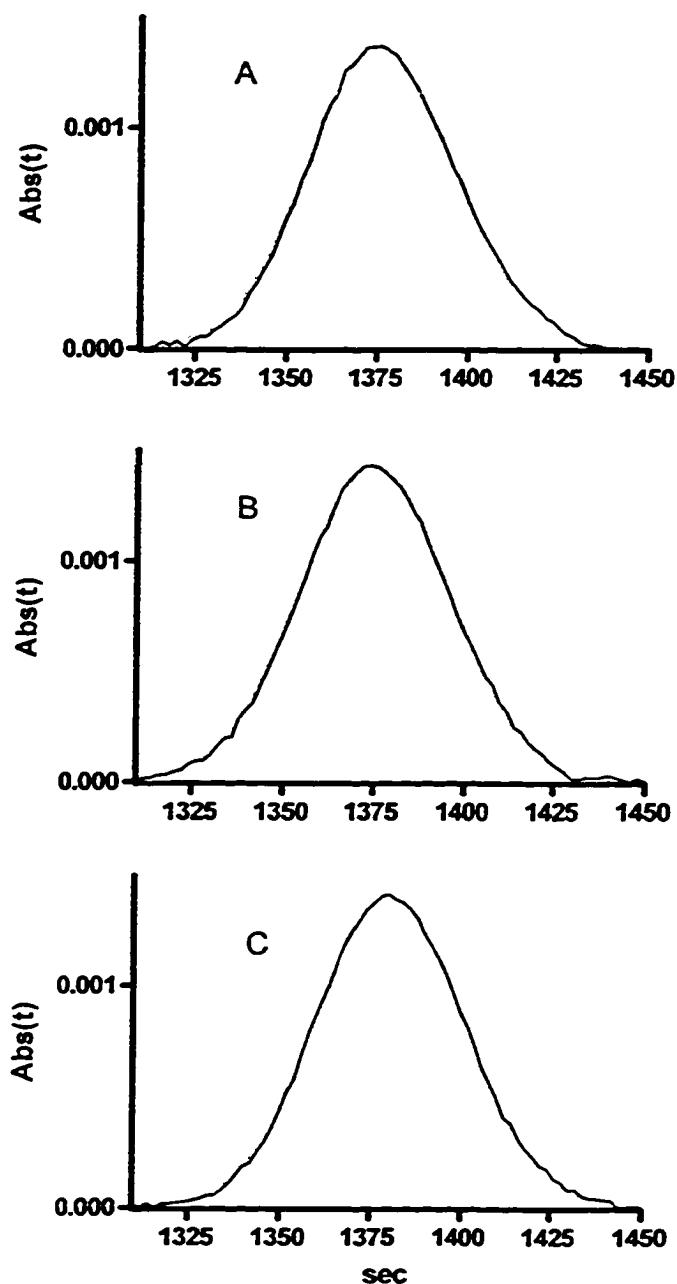
	A	B	C
σ (s)	20.2	20.6	20.2
t_R (s)	1376	1375	1380
H_{obs} (cm)	0.00536	0.00562	0.00535

Fig.5.15. Gaussian fits to three elution chromatograms of DMNB. The data is the solid black line while the fit is the grey line.

215

where Z is the length of the column and t_R is the retention time of the elution peak. The value of H_{obs} for DMNB at 2mL/min is 54 ± 2 µm.

Next, prediction of the plate-height will be carried out using equations from Chapter 1. There are several contributors to band broadening, and thus to the overall plate-height: contribution from longitudinal diffusion (H_{LD}), the coupled term of liquid chromatography (H_{couple}), the diffusion through the stagnant mobile phase of the particles, including surface diffusion (H_{SM}), the kinetics of the chemical interaction with the stationary phase (H_S), and film diffusion (H_{film}). The contributions of all these processes can be represented via the following equation.

$$H_{total} = H_{LD} + H_{couple} + H_{SM} + H_S + H_{film} \tag{5.14}$$

First, the contribution of H_{LD} is calculated. According to Eq. 1.4 H_{LD} is:

$$H_{LD} = \frac{2 \, \gamma \, D_{MP}}{u} \tag{1.4}$$

where D_{MP} is the diffusion coefficient of the solute in the mobile phase (cm^2/sec) and u is the linear velocity of the mobile phase (i.e. the velocity with which an unretained component moves axially through the column). The obstruction factor, γ, is about 0.5 to 0.8. At the flowrate of 2 mL per minute (u = 0.292 cm/sec) H_{LD} is equal to ~ 0.3 µm, which is small enough to make it negligible.

The value of H_{couple} is given by Eq. 1.7:

216

$$H_{couple} = \left(\frac{1}{H_{Eddy}} + \frac{1}{H_{MP}} \right)^{-1} = \left(\frac{1}{\lambda \, d_p} + \frac{D_{MP}}{\omega \, d_p^2 \, u} \right)^{-1} \qquad (1.7)$$

where d_p^2 is the particle diameter of the packing and λ and ω are a packing parameters in the H_{Eddy} and H_{MP} terms, respectively. The values of λ and ω, are 2.5 and 5 for a well-packed column (the smallest packing parameters possible) [1]. Using Eq. 1.7, H_{couple} is calculated to be around 30 μm. This value can be confirmed by calculating H_{couple} from similar equations, such as equation 2.47 in reference [1], which gives a value of 29 μm. The error in H_{couple} depends on how well the column is packed and its value could range from 30 to 60 μm.

The value of H_{SM} is calculated via Eq. 1.17:

$$H_{SM} = \frac{(1-f+k')^2}{30(1-f)(1+k')^2} \frac{d_p^2 \, u}{\left(D_P + \dfrac{k' D_S}{f} \right)} \qquad (1.17)$$

where k' is the retention factor of the solute i, and f is defined in Eq. 1.13 to be the fraction of the total porosity of the column which is occupied by the stagnant mobile phase in the pores of the particles. H_{SM} is calculated to be 10 ± 1 μm (using the values of k' = 15.0, f = 0.46, $D_P = (2 \pm 0.5) \cdot 10^{-6}$ cm^2 s^{-1}, and $D_S = (8.45 \pm 0.3) \cdot 10^{-7}$ cm^2 s^{-1}). In conventional chromatography, the contribution of surface diffusion is usually neglected (primarily because band broadening studies are carried out for small retention factors where surface diffusion is less important). If surface diffusion was to be ignored here by making $D_S = 0$, the value of H_{SM} obtained via Eq. 1.7 would be equal 148 μm, or about 15 times larger (i.e. worse).

217

The next parameter, H_S, arises when the rate of the chemical step of sorption/desorption onto/from the stationary phase is slow. As discussed in Chapter 1, Section 1.3.1, ODS stationary phases exhibit extremely fast chemical kinetics, making the term Hs negligible. For this reason, it will not be discussed further here.

The value of H_{film} is calculated via Eq. 1.22:

$$H_{film} = \frac{\xi\,(k_0 + k' + k_0 k')^2}{(1 + k_0)^2\,(1 + k')^2}\,\frac{d_p^{5/3}\,u_{inter}^{2/3}}{D_{MP}^{2/3}} \tag{1.22}$$

where ξ is a packing factor, and k_0 is defined in Eq. 1.23 as the ratio of the intraparticle and interparticle porosities inside the HPLC column. H_{film} is calculated (using the values $\xi = 15$ [2] and $k_0 = 0.86$) to be $20.0 \pm 2\ \mu m$. The fact that H_{film} is greater than H_{SM} (including the effect of surface diffusion on H_{SM}) is reasonable in view of the fact that at 2 ml/min ($u = 0.292$ cm/sec) in the HPLC column the film thickness is about 4 times larger than during the shallow bed experiments, while intraparticle diffusivity is assumed to remain unchanged. Since film and particle diffusion had approximately equal contributions during the shallow-bed experiments, film diffusion should be rate-limiting in HPLC experiments in this case. The contribution due to film diffusion is generally ignored by chromatographers studying band broadening [1, 2]. This is usually a reasonable assumption as the value of H_{film} is often small when compared to H_{SM} at small retention factors. (Recall that, at small retention factors, surface diffusion is thought to have a negligible contribution to H_{SM}.) For example the value for H_{SM} calculated above neglecting surface diffusion is 148 μm.

218

Putting together the information gathered above, it is concluded that the values of H_{LD}, and H_S are negligible, but the effects of surface diffusion (in addition to the stagnant mobile phase diffusion) and of film diffusion should be included. H_{total} becomes:

$$H_{total} = H_{couple} + H_{SM} + H_{film}$$

$$= \left(\frac{1}{\lambda d_p} + \frac{D_{MP}}{\omega d_p^2 u} \right)^{-1} + \frac{(1-f+k')^2}{30(1-f)(1+k')^2} \frac{d_P^2 u}{(D_P + \frac{k'D_S}{f})} + \frac{\xi(k_0 + k' + k_0 k')^2}{(1+k_0)^2 (1+k')^2} \frac{d_p^{5/3} u_{inter}^{2/3}}{D_{MP}^{2/3}}$$

$$= \quad 30 \, \mu m \; + \; 10 \, \mu m \; + \; 20 \, \mu m \tag{5.15}$$

The predicted value of H_{total} is calculated to be around 60 μm, which is in good agreement with the observed value ($H_{obs} = 54$ μm). The conventional way to predict plate height also neglects H_{LD}, and H_S. In addition, the contribution of surface diffusion and film diffusion are also neglected, and H_{total} becomes:

$$H_{total} = H_{couple} + H_{SM}$$

$$\tag{5.16}$$

$$= \left(\frac{1}{\lambda d_p} + \frac{D_{MP}}{\omega d_p^2 u} \right)^{-1} + \frac{(1-f+k')^2}{30(1-f)(1+k')^2} \frac{d_P^2 u}{D_P} = 30 + 148$$

The value of H_{SM}, is calculated via Eq. 5.16 $H_{total} = 178$ μm. Even though this value is in agreement with the plate height which would be calculated from literature (For example, H_{total} from equations 2.47 and 2.48 in reference [1] is predicted to be 140 μm) it is almost 3 times larger (*i.e.* worse) than the observed value of 54 μm. The two predictions are further illustrated in Fig.5.16, where equations 5.15 and 5.16 are plotted over a large span of velocities in the column and are compared to the observed value.

219
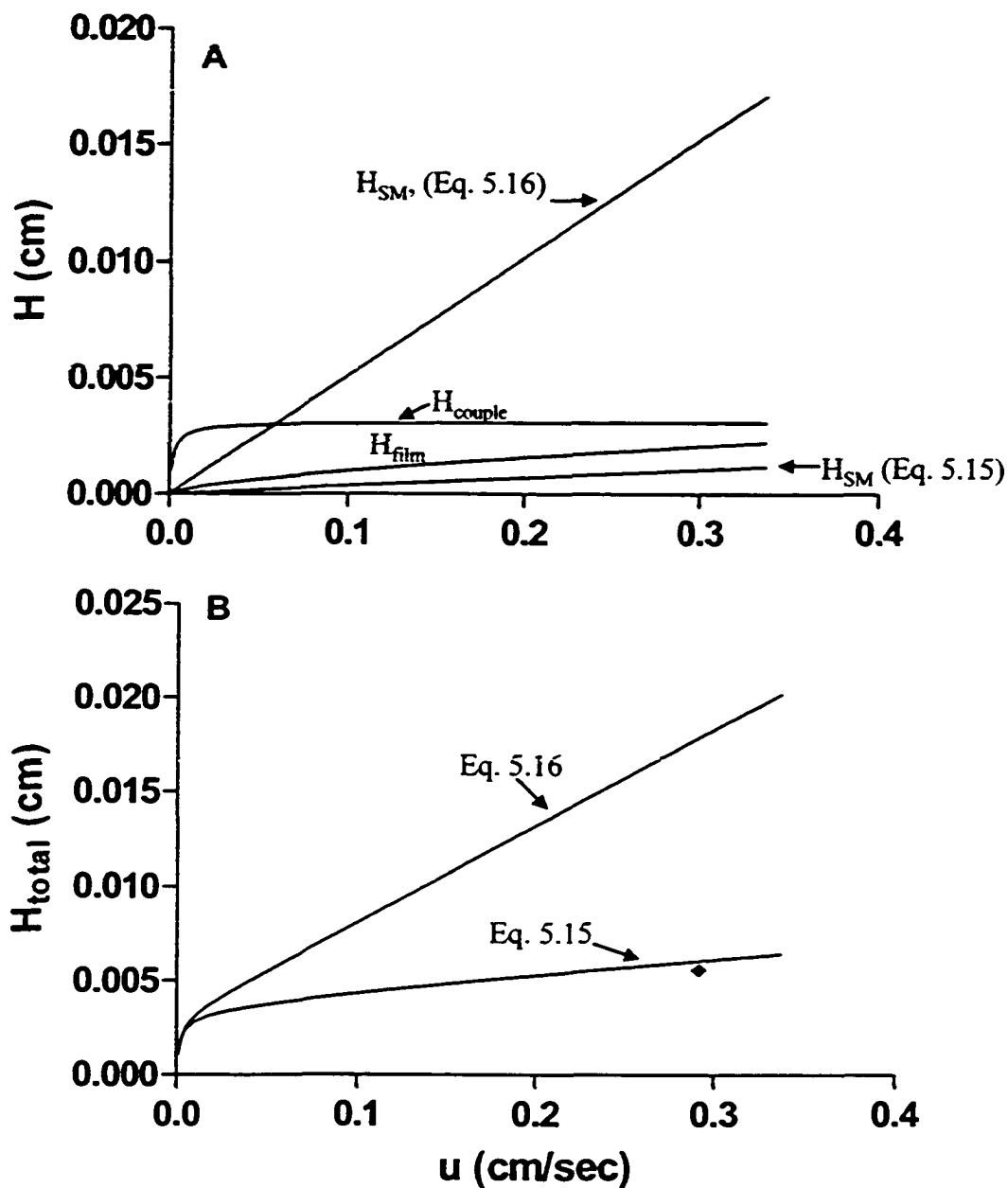
Fig 5.16 Predicted H vs. u curves for DMNB on a column of 12 μm Luna-C18. A: The contribution of each term in Eqs 5.15 and 5.16. The top H_{SM} line is calculated neglecting surface diffusion (Eq. 5.16), while the bottom H_{SM} line is calculated including it (Eq. 5.15). The contribution of H_{LD} is not plotted. B: H_{total} vs. u curves calculated neglecting surface diffusion and film diffusion (Eq.5.16), and including them (Eq.5.15). The diamond-shaped point in panel B the experimental plate height H_{obs} which was obtained at 0.292 cm/sec.

220

Fig. 5.17 shows the experimental elution peak of DMNB on a Luna C-18 column at 2 mL/min along with elution peaks predicted via Eq. 5.15 and Eq. 5.16. It is clear that, in this case, the contribution of surface diffusion and film diffusion should not be neglected.

It is important to point out the fact that DMNB is strongly sorbed onto the stationary phase under the present experimental conditions. Retention factors which are this large are generally avoided in isocratic HPLC analyses in order to speed up separations and to keep the signal at a reasonable value. Since the effect of surface diffusion is less for compounds with smaller retention factor, Eq. 5.16, rather than Eq. 5.15, is usually used to describe bandbroadening in analytical chromatographic literature. However, since there is some evidence that surface diffusion coefficients may increase as the strength of retention decreases [44], there may still be cases, where Eq. 5.16 would better describe bandbroadening, even for compounds with relatively low. Kinetic studies at low retention factors could shed more light on the importance of this phenomenon in practical HPLC.

221

observed curve

------ predicted neglecting surface and film diffusion

—— predicted including surface and film diffusion
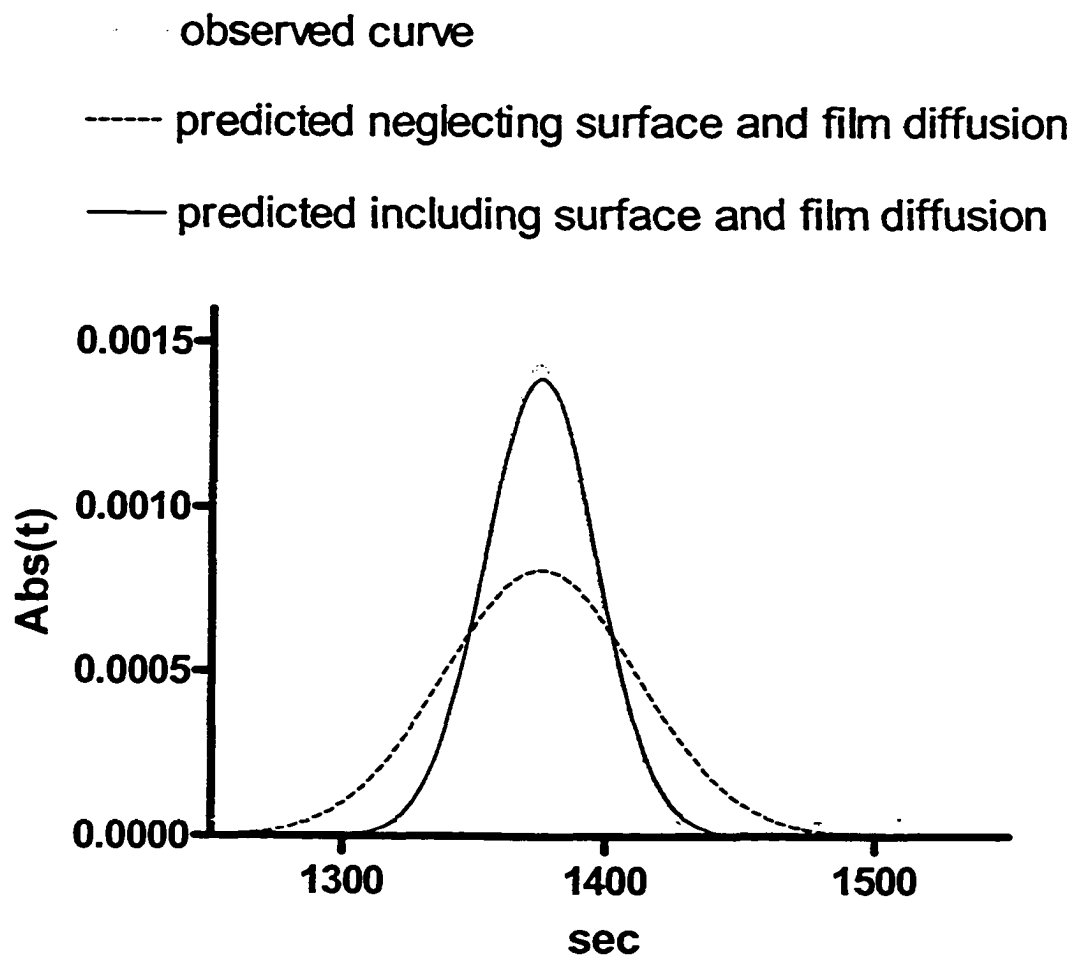
Fig. 5.17. Predicted and observed elution peaks. The grey line is the experimental curve (from Fig 5.15 A). The solid black line is the curve predicted with Eq. 5.15, which includes the effects of surface and film diffusion. The dashed line is the peak predicted with Eq. 5.16, a more conventional equation which excludes surface and film diffusion.

222

Chapter 6: Sources of extra-bed band broadening in Type II apparatus

6.1 Introduction

The role of instrument (extra-bed) band broadening and the correction for it, which includes subtraction of the IRF-Marker and deconvolution, was outlined in Chapter 2, Section 2.2. For the Type II apparatus the correction is outlined in Section 2.2.5. Despite our ability to correct for it, the instrument band broadening (also called dispersion) is an unwanted phenomenon, and it is desirable to minimize it as much as possible. Therefore, it is useful to obtain a general idea about what instrument band broadening processes are the most important. For the purpose of the following discussion, see Section 4.2.2 and Fig. 4.1, Fig. 4.2, and Fig. 4.4.

6.1.1 Parts of the apparatus through which an IRF-Marker flows during the desorption step

Fig. 6.1 shows the close up of part of the shallow-bed assembly in the Type II apparatus described in Chapter 4, focusing on the shallow bed and those components where band broadening occurs during the desorption step. It is presumed that just before the desorption step, the solute-containing eluent is present above (*i.e.* downstream of) the bottom s.s. screen, while below this screen, only solute-free eluent is present as the result of the flush step. The solution containing desorbed solute goes through several components on its way to the detector: First, the desorbed solute has to travel through the empty 200 μm - thick silicon grid, followed by the 5 μm – thick nickel mesh, and then the

223

600 µm particle-packed shallow bed. After the bed, it passes through the top nickel mesh, and flows through another empty silicon grid. It then passes through the woven s.s. screen, and finally enters the 2 mm i.d. quartz-tube flow-cell. The bottom edge of the 2 mm –long detector window is located a short way downstream (about 0.5 mm).

6.1.2 Band broadening processes which can occur during the flow of an IRF-Marker

First, consider the band broadening in the shallow bed. Because we are considering the band broadening which occurs due to the processes occurring *outside* the particles, the particles are assumed to be non-porous and non-sorbing. It also has to be remembered that the fluid velocity between the particles is 2 orders of magnitude higher than in conventional HPLC. The main dispersion process should thus be controlled by eddy diffusion (See Eq. 1.7, Section 1.2), while molecular diffusion should have a negligible
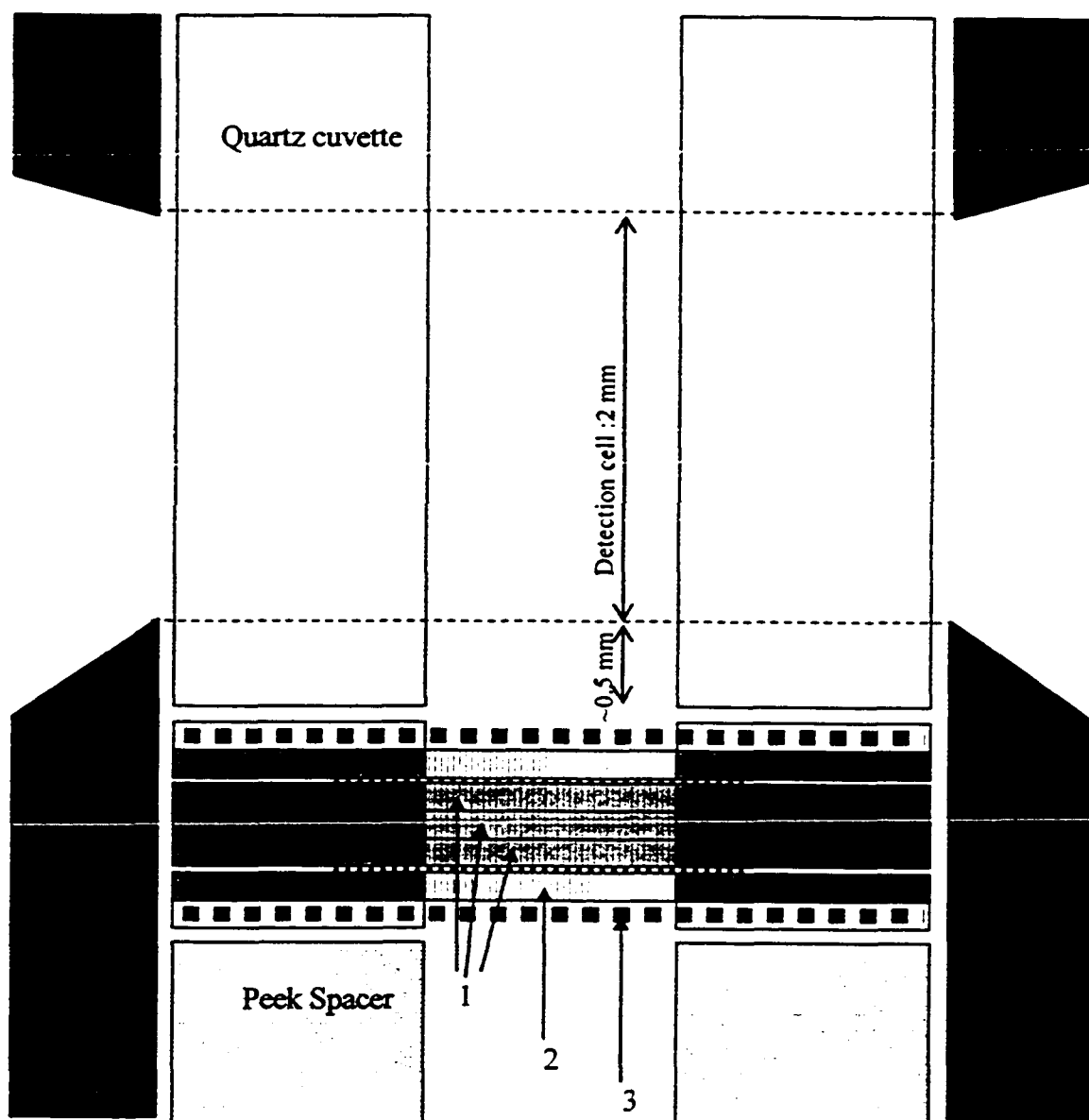
Fig. 6.1: Schematic of the particle-packed shallow-bed and other parts where band spreading may occur during the desorption run. Roughly to scale. For more detail see Fig. 4.2 and 4.4. 1: particle-packed silicon grids comprising the shallow bed. 2: Empty silicon grids. 3: bottom s.s. screen – the presumed boundary between the solute-containing solvent and pure solvent after the end of the flush step and just before the desorption step (see Fig. 4.1 and 4.2 for a reminder about the flush and desorption steps).

225

contribution to dispersion. However, Eq. 1.7 cannot be used to calculate the likely shape of the elution profile from this bed, because Eq. 1.7 applies for long columns. The volume of the shallow bed through which the fluid flows is calculated to be ~ 0.5 μL, based on the height (0.6 mm), the radius (1 mm), the open area not taken up by the walls of the silicon grids (~0.69) and the void fraction (~0.4).

Next consider the flow through the quartz tube and the empty silicon grids above and below the packed shallow bed. The holes in the empty silicon grids can be treated as an assembly of very short open tubes. The quartz tube above the shallow bed is a single channel. Band broadening processes inside open tubes are going to be considered in the following paragraphs. The volume of the holes in the two empty silicon grids is about 0.9 μL. The volume in the quartz tube from the top of the s.s. screen to the top of the detection window is 7.8 μL, assuming the distance between the s.s. screen and the bottom of the detection window is 0.5 mm. Thus the volume of the quartz tube is almost 10 times the volume of the holes in the silicon grids, which makes it very likely that it is the quartz tube which is responsible for most of the dispersion from the two components. The volume of the quartz tube is also 16 times the volume of the shallow bed. Moreover, the relative band broadening in a packed tube is much smaller than that associated with open, unpacked tubes [55, 91]. This means that the contribution to dispersion from the shallow bed is also negligible compared to that from the quartz tube.

Band broadening in the nickel mesh and the s.s. screens will be ignored here, because their volumes are negligible compared to the above parts.

226

The last source of band broadening that may need to be considered comes from the region directly below (upstream) the bottom s.s. screen in Fig. 6.1. However, it is likely that this region is free of solute at the beginning of the desorption step because it has been flushed out during the flush step (See Fig 4.2). Convection underneath the screen likely occurs via a recirculation zone depicted in Fig 4.2 C [104-106]. The s.s. screen, along with the silicon grids, act as a barrier which prevents convection by recirculation within them and above them. Prior to conducting all the desorption experiments, it was part of the procedure to demonstrate this by increasing the flush time until the A(t) signal observed in the desorption step did not change. (In all cases, flush times of 1 second met and exceeded this criterion). This demonstrates that convection completely removes the solute from underneath the bottom s.s. screen, while the solute above that screen remains unflushed, as is desired. Thus, band broadening processes that would occur if the solute was there at the start of the desorption step need not be considered.

The above discussion shows that instrument band broadening is mainly occurring in the quartz flowcell, with possibly a small contribution from the empty silicon grids. Therefore, it will be necessary to consider the dispersion equations for flow through an open tube. This involves first determining whether the flow through the flowcell is likely to be laminar (viscous) or turbulent. The Reynolds number, R_e, is:

$$R_e = \frac{\rho\, U\, d}{\eta} \qquad\qquad (6.1)$$

227

where U is defined as the average linear velocity in the tube (cm/sec), ρ is the density (g/cm^3) of the following liquid, d is the internal diameter of the tube, and η is the viscosity of the liquid (Poise). For straight tubes, the flow is laminar when $R_e < 2100$, meaning that all the streamlines are parallel to the walls of the tube. At $R_e > 2100$, the flow develops turbulence [114]. In all the studies carried out on the type II apparatus in Chapter 4 and 5, the fastest flowrate was 0.49 mL/sec, giving the average linear velocity in the quartz tube of 15.6 cm/s, resulting in a Reynolds number of around 200. Later in this chapter, Reynolds number as high as 1000 will be reported, but this is still a value well below the transition region. The Reynolds number is much smaller inside the holes of the empty silicon grids because of the smaller hole-diameter (the holes are actually squares, but that doesn't affect the current discussion). Thus, it is safe to conclude that the flow within the quartz tube is laminar.

For laminar flow, several mathematical models have been developed to quantify dispersion. For a long, straight piece of tubing, the laminar flow profile is parabolic [1, 3, 55, 79, 91, 114, 115], meaning that the velocity of the moving fluid is largest in the center, and it decreases as a parabolic function of the radial coordinate until it achieves the value of zero at the wall. This is depicted in Fig 6.2 A. Such a flow profile is a source of band broadening, since the solute molecules in the middle of the tube move faster than the solute molecules closer to the walls. The only relaxation of the solute band broadening arising from this non-uniform flow profile is provided by lateral diffusion, because as the molecules diffuse towards and away from the wall, they sample different velocities, and can thus average out their overall velocity through the column. If the tube

228

is long enough, the process of diffusion to and from the wall happens many times, and the eluting zone will adopt a Gaussian peak shape [1, 6]. When the tube is made shorter, or as the flow is made faster, or when the tube –diameter is made larger, radial diffusion has progressively less time to act as an averaging mechanism, and the eluting peaks start to deviate from the Gaussian peak shape, becoming progressively more asymmetric [96-98].

However, in the present case it is obvious that the tube is extremely short. The length from the bottom of the quartz tube (end of the s.s. screen) to the top of the detection window is only slightly larger than the tube diameter itself. Moreover, the I.D. of the tube is quite large – 2 mm, and the average time that a solute needs to flow from the s.s screen to the end of the detector is measured in milliseconds (from 26 milliseconds in Run 3, bed 2 of Chapter 5 to approximately 200 milliseconds in the slowest run in Chapter 4). Using the Einstein equation [1, 3, 6, 56, 57], the average diffusion distance in those instances for a small molecule such as PG (taking into account the diffusion coefficients in different fluids) are 5 and 21 μm, respectively, which is only 0.5% and 2% of the tube radius. Thus, lateral diffusion has almost no time to relax the flow profile. The experiments carried out in this chapter aim to determine if this is the case.

229
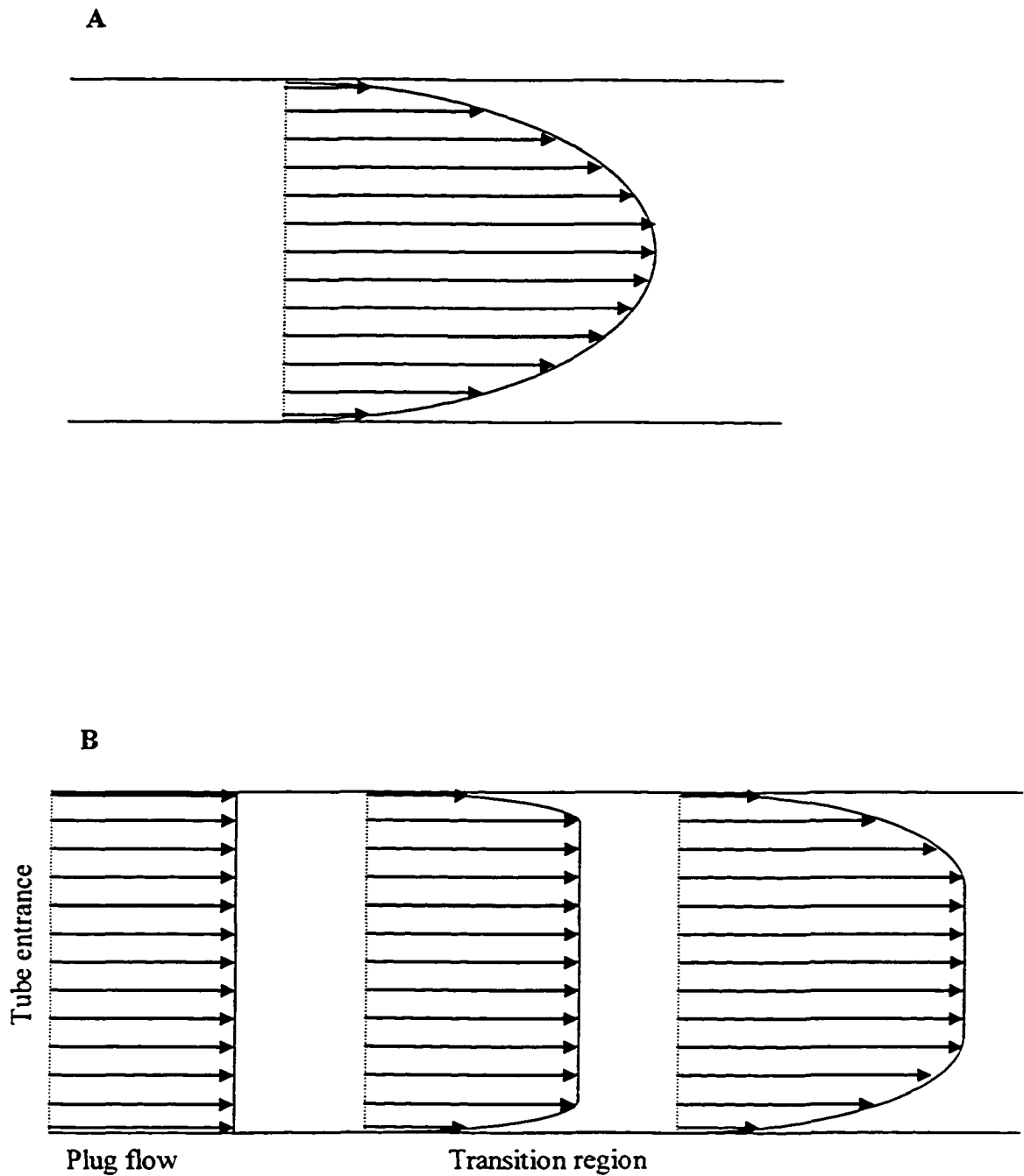
Fig 6.2 Schematic representation of fully developed parabolic flow profile (6 A), and flow profiles at the entrance region of a tube (6 B). The flow profiles are not those calculated from theoretical equations, but are merely schematic aids.

230

6.1.3 Band broadening due to the detector

The last source of band broadening relevant here is due to the detector and the detector window. The detector response-time often distorts the true waveform passing through it. The IRF function associated with this phenomenon is an exponential-decay function, where the response time equals the response time of the detector. In the present case, the response time was always chosen to be 0.3 milliseconds. This is enough not to cause significant contribution to the observed A(t) signal. A much more serious problem is the fact that the detection window in the present apparatus is almost as long as the relevant length of the quartz tube itself. The IRF due to the detection window is often defined as a rectangular signal whose variance is, in volume units [1]:

$$\sigma^2 = (V_d)^2 / 12 \qquad\qquad (6.2)$$

and in time units

$$\sigma^2 = (t_d)^2 / 12. \qquad\qquad (6.3)$$

Here, V_d and t_d are the volume of the detector cell, which is a portion of the quartz cuvette that is viewed through the window, and the time needed to pass through the detector cell, respectively. Even though this relationship seems simple at first glance, it is important to realize that solute molecules which flow along different radial coordinates in the quartz tube have different velocities. While t_d may be very short for solutes traveling through the center of the tube, it will be much longer for those traveling next to the walls. In other words, the effect of the detector window varies for different radial

231

distances within a tube. This phenomenon will not be dealt with further here, but it is important to keep in mind.

6.1.4 Goal of the experiments

The experiments in this chapter deal with the observation of the $A(t)$ curves for the reverse fronts of two IRF-Marker solutes eluted from a bed packed with non-porous beads in order to characterize the dispersion in the apparatus. One IRF-Marker is PG, a small molecule, while the other is Blue Dextran, a very large co-polymer molecule (2,000,000 Daltons). Their different sizes give them vastly different diffusion coefficients. By comparing the differences between the shapes of their IRF peaks, the role that molecular diffusion plays in the apparatus can be elucidated. It will become apparent that molecular diffusion plays a virtually negligible role in dispersion in the current system. Further interpretation of the data will not be possible, because of many complicating factors.

6.2 Experimental

6.2.1 Reagents, solvents, and sorbent

Phloroglucinol (PG) (1,3,5 trihydroxybenzene, Fluka, $\geq 99\%$) and Blue Dextran (Sigma-Aldrich #D 5751) were was used without further purification. The solvent (mobile phase, or eluent) used in this study, both for making solutions of PG and Blue Dextran, was filtered, deionized H_2O. Water and its PG and Blue dextran solutions were sparged with helium before the experiments. The non-porous glass beads used to pack the shallow bed have been described in Chapter 5, Section 5.2.1

232

6.2.2 Apparatus

The apparatus used was exactly as described in Chapter 4, Section 4.2.2

6.2.3 Procedure for the measurement of the reverse front shapes

The procedure is exactly the same as that outlined in Chapter 4, Section 4.2.3. The only

difference is that the equilibration time was 10 sec and the desorption step lasted 2.5 sec.

Also, it wasn't necessary to adjust the pressure after each set of five cycles, because the

resistance of the glass-bead packed bed was constant, and, consequently, so were the

flowrates.

6.3 Results and Discussion

This section discusses the role of molecular diffusion *vs.* convection in the present

apparatus, and the nature of the flow profile inside the quartz tube

6.3.1 Determination of the role of diffusion in the instrument band broadening in Type II apparatus.

Shown in Fig. 6.3 A are the normalized A(t) curves of the reverse fronts for a small

molecule (PG, 126 Daltons) and a large molecule (Blue Dextran, 2,000,000 Daltons)

from the bed packed with non porous glass beads at a flowrate of 1.63 mL/min (51

cm/sec) in water. Both of the curves are an average of 30 cycles (6 sets) each. The

experiment has been carried out in the same manner as in Chapters 4 and 5, but in this

case no desorption kinetic information is obtained; both compounds act as unretained,

233

excluded solutes (IRF-Markers). The diffusion coefficient of PG in water is $8.6 \cdot 10^{-6}$ $cm^2 s^{-1}$, according to the Wilke-Chang correlation for small molecules, while the macromolecule Blue Dextran has the diffusion coefficient of $2.4 \cdot 10^{-8}$ $cm^2 s^{-1}$ (according to the Stokes-Einstein equation [3, 27, 52]). The two coefficients differ by more than 2 orders of magnitude. If molecular diffusion plays a significant role in the band broadening experienced in the present system it should make a large difference to the shape of the two desorption curves. For example, if they were injected into a long tube, the Gaussian peak of the PG curve would be about 19 times narrower than the Blue Dextran curve [1, 6]. Fig 6.3 A however shows that the two curves are virtually identical. Fig 6.1 B shows the IRF peaks obtaining by taking the negative derivative of the curves in Fig. 6.1 A, according to Eq. 2.27. Table 6.1 shows the values of the elution time (the first statistical moment) and the variances (the second statistical moment). It also tabulates the results obtained at two other flowrates. The elution times for Blue Dextran are only a few percent larger than for PG. This is due to the fact that the viscosity of the Blue Dextran solution (concentration of 0.125 g/L) is slightly larger than that of the PG solution, which causes a slightly slower flowrate [109]. The lower flowrates for Blue Dextran cause the slightly delayed elution times and wider widths of elution peaks. (No correction for Dextran viscosity was attempted because it is impossible to determine the exact magnitude of it in the present apparatus, even if the relative viscosities are known) The change in viscosity causes the PG and Blue Dextran values not to be statistically different at the 95 % C.I., but they are still remarkably close. This agreement between the two sets of data confirms the fact that diffusion does not contribute significantly to

234
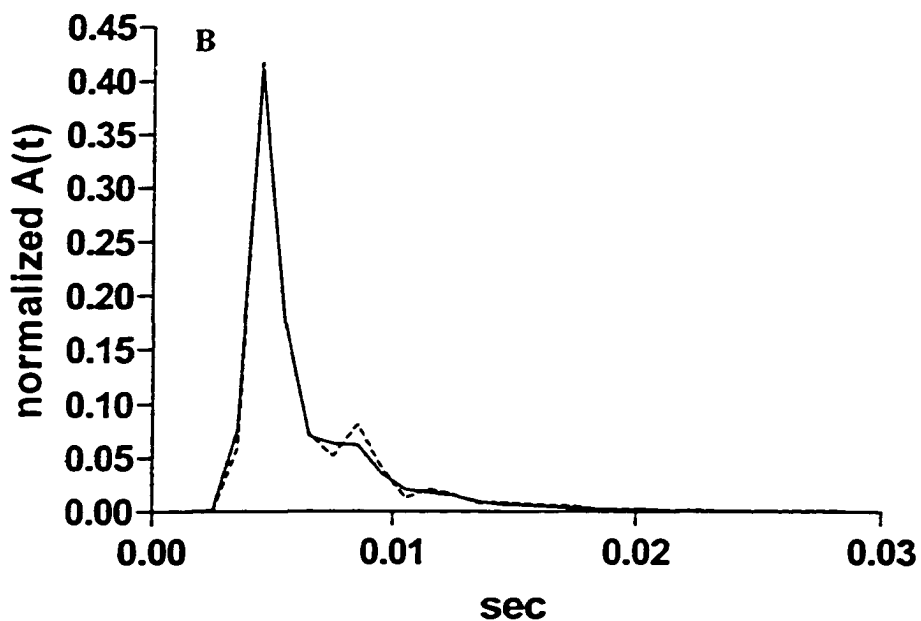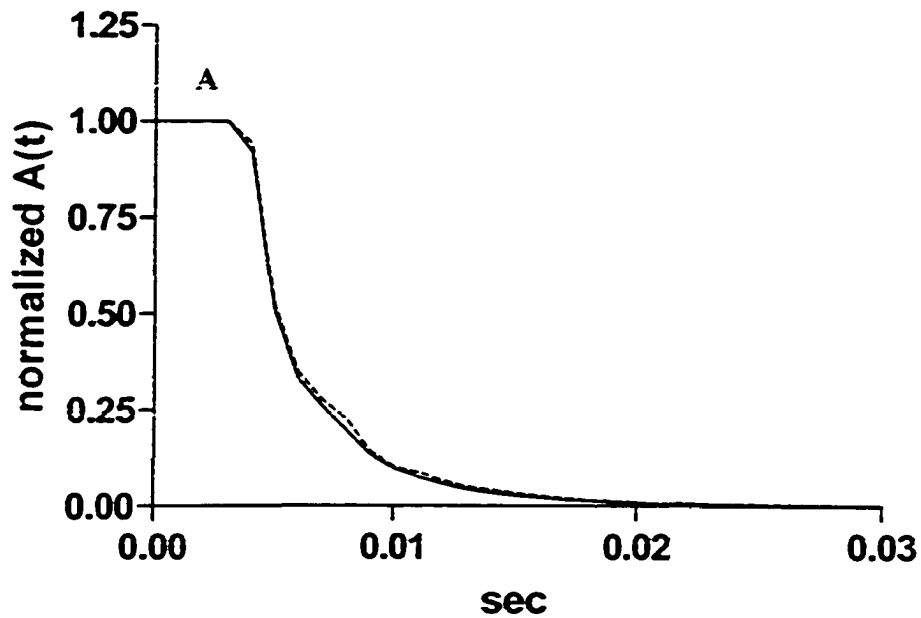
Fig. 6.3. Comparison of band broadening for PG (solid lines, 126 Daltons) and Blue Dextran (dashed line, 2,000,000 Daltons) at 1.63 mL/sec. A: The reverse-fronts. Both curves are averages of 30 cycles each. The sampling frequency is 1000 Hz, *i.e.* there are 30 data points per curve on the graph. B: The IRF peaks which are obtained by taking the negative derivative of the reverse frontal curves. PG IRF is the solid line while the Blue Dextran IRF is the dashed line.

235

Table 6.1. The elution times, variances, and standard deviations of the IRF peaks for PG
and Blue Dextran obtained from reverse fronts on non-porous packing.

Table 6.1 A: 1.06 mL/sec (33.7 cm/sec)

	PG	Blue Dext.
$t_{elution}$ ($\times 10^3$ s)	8.86 ± 0.002 [a]	9.09 ± 0.003
σ^2 ($\times 10^5$ s^2)[a]	5.03 ± 0.17	5.6 ± 0.16
σ ($\times 10^3$ s)[a]	7.1 ± 0.1	7.5 ± 0.1

Table 6.1 B: 1.40mL/sec (44.6 cm/sec)

	PG	Blue Dext.
$t_{elution}$ ($\times 10^3$ s)	7.28 ± 0.003	7.56 ± 0.003
σ^2 ($\times 10^5$ s^2)	2.1 ± 0.24	2.72 ± 0.22
σ ($\times 10^3$ s)	4.6 ± 0.3	5.2 ± 0.2

Table 6.1 C: 1.63 mL/sec (51.9 cm/sec)

	PG	Blue Dext.
$t_{elution}$ ($\times 10^3$ s)	6.47 ± 0.003	6.66 ± 0.003
σ^2 ($\times 10^5$ s^2)	1.63 ± 0.26	1.83 ± 0.26
σ ($\times 10^3$ s)	4.0 ± 0.3	4.3 ± 0.3

[a]   The $\pm$ signify the standard deviations of values in the table are based on 21
repetitive calculations of the value with different integration times, n = 20. The symbols
σ^2 and σ are the variance and the standard deviation of the IRF peak.

236

the shape of the IRF. This is very good news when it comes to choosing the IRF-Marker, because it identifies convective processes as the primary determinant of dispersion in the present Type II apparatus, and allows us to choose an IRF-Marker having a diffusion coefficient which is significantly different from the solute.

6.3.2 Possible flow patterns in the apparatus

It is now established that the band broadening in the present apparatus is primarily affected by the flow patterns. It was also shown in the introduction that little or no turbulence is expected to occur. There are three things to consider when trying to determine the possible flow patterns inside the apparatus.

1. The shape of the velocity profile exiting the shallow bed and entering the quartz tube. Under laminar conditions, the flow profile in straight, cylindrical tubes eventually becomes parabolic. However, as discussed in Section 6.1.2, it is unlikely that a parabolic flow profile exists in the quartz tube. The presence of the packed shallow-bed, the s.s. screens, and the empty silicon grids, is very likely to change the velocity profile along the radial coordinate. In the best-case scenario (when it comes to band broadening) the radial distribution of the axial velocity could be made to approach a plug-flow profile at the entrance into the quartz tube, just above the top s.s. screen in Fig 6.1. A plug profile simply means that all the velocities are equal, regardless of the position along the radius of the quartz tube.

2. The amount of band broadening occurring in the quartz tube itself. The flow – profile entering the quartz tube could be parabolic (Fig. 6.2 A), plug (Fig. 6.2 A), or it

237

could have any shape in between those two. If a fully parabolic flow-profile were to exit the top s.s. screen (See Fig. 6.1) and enter the quartz tube, it would also remain parabolic in the tube. For this profile, the velocity in the center is twice the average fluid velocity through the tube, and is zero at the walls. The IRF expected from injecting an infinitely narrow zone of solute into a straight tube displaying a parabolic flow profile in the absence of molecular diffusion is given by [91]:

$$A(t)_{IRF\text{-}parabolic} = \frac{1}{2\left(t/t_{cg}\right)^3} \quad \text{for} \quad t_{cg}/2 < t < \infty$$

$$(6.4)$$

$$= 0 \qquad \text{everywhere else}$$

where t is time and t_{cg} is the center of gravity of the peak.

If, on the other hand, a plug flow-profile was to enter the quartz tube, it would not remain perfectly flat because the viscous drag from the stationary walls of the quartz tube. This drag would cause the profile to gradually become parabolic further down the tube, as depicted in Fig 6.2 B. The length of the tube needed for this transition is called the entrance length of the tube. It can be estimatied *via* the following equation [114]:

Entrance region length $\sim 0.1 \cdot r \cdot R_e$ $\qquad\qquad$ (6.5)

For a flowrate of 1.63 mL/sec (51 cm/sec in the quartz tube and about 180 cm/sec between the particles in the shallow bed) in water (the fastest used in this thesis, the data for which are shown in Fig. 6.3) this tube has an entrance region of about 100 mm while for the flowrate of 0.11ml/sec (3.5 cm/sec in the quartz tube and about 12 cm/sec

238

between the particles in the shallow bed) in 85/15 MeOH/H$_2$0 (the slowest used in this thesis for Type II apparatus in Chapter 4) it is 7 mm. Another method of calculating the entrance length gives very similar results [115]. This calculation shows that, if the starting profile was indeed flat, in all cases the detector cell would be well within the entrance region of the tube. The velocity distributions in the entrance region can be numerically simulated using reference [114] (equation 3.39 and chapter II, section 20 therein). Other methods of simulating the flow in the entrance region of a tube exist in the literature [115].

3. The effect of the finite detector cell length on the observed curves. In the present apparatus the volume of the detector cell comprises 80% of the volume associated with the quartz tube. This adds a large degree of complexity when it comes to interpreting the data. The only quantitative statement which can be made about this effect is that the detector should broaden the expected theoretical curves significantly. As well, the presently discussed A(t) signal changes so rapidly that the detector time-constant (the rise time) also contributes to the band broadening of the experimental data.

It could be potentially useful to produce theoretical A(t) *vs* t curves for the IRF peak inside the shallow bed apparatus based on both the parabolic and plug entrance velocity profiles in the quartz tube and compare them to experimental curves. Before this is done however, it is important to list certain cautionary statements against overinterpreting the data. The unknown effect of the detector window has been already mentioned above. There is however, one other issue: the Delay time of the electronic valves. The flow in

239

the present apparatus is controlled by an arrangement of computer-controlled electronic valves. The time required for those valves to fully switch positions is specified by the manufacturer as "5 milliseconds or less". This gives rise to a *Delay time*, meaning that the flow does not start at 0 milliseconds. Moreover, in the few milliseconds during which the valves switch, the valve is partially open, causing partial flow to occur. In order to simplify this problem it will be assumed that there are two distinct times – the Delay Time (no flow) and the time during which flow does occur. The center of gravity of the peak measured from the end of the Delay time to the time where the middle of the peak reaches the detector is defined as t_{cg}. This definition means that the elution time observed by the detector is equal to Delay time + t_{cg}.

$$\text{Elution time} \equiv \text{Delay time} + t_{cg} \tag{6.6}$$

Figure 6.4 A shows two predicted curves modeled assuming a fully-developed parabolic flow profile (Eq. 6.4). The first curve is calculated based on Delay Time = 0 and t_{cg} = 6.5 msec. The second curve is calculated based on Delay time = 3.5 msec and t_{cg} = 3 msec. The sum of delay time and t_{cg} for the predicted peaks add up to 6.5 msec, in order to match them with the elution time of the experimental IRF peak obtained for PG at 1.63 mL/sec, (See Fig. 6.3 B and Table 6.1 C). Fig. 6.4 B shows two curves predicted assuming that the flow is occurring in the entrance region where the flow profile is evolving from a plug towards a parabolic shape. The first curves in both A and B are the

240
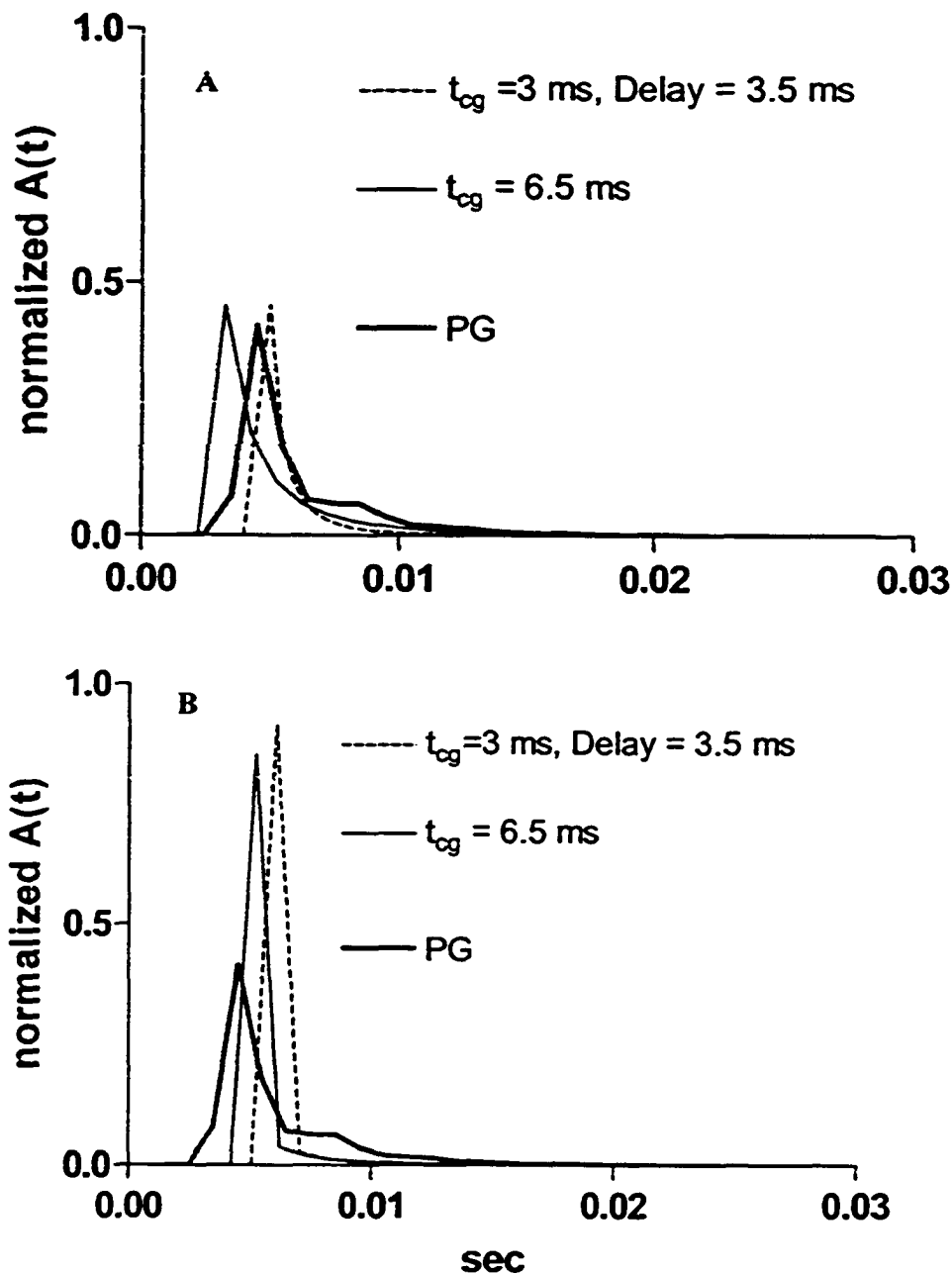
Fig 6.4. Theoretical A(t) vs. t curves for the IRF superimposed onto the experimental curve for PG at 1.63 mL/sec. All curves are made to have the same elution time (first statistical moment). The t_{cg} means the center of gravity of a peak measured from the end of the Delay Time of the valves used. The sampling frequency for both modeled and experimental curves is 1000 Hz, i.e. there are 30 data points per curve on the graph. A: Curves predicted using Eq.6.4 for a parabolic flow profile. B: Curves predicted for the entrance region of a tube, assuming plug-flow as the starting flow profile. The effect of detector flow profile has not been accounted for in the predictions.

241

ones calculated based on Delay time = 0 and t_{cg} (center of gravity) = 6.5 msec. The second curves are calculated based on Delay time = 3.5 msec and t_{cg} = 3 msec. They are again compared with the observed PG curve. Even though the predicted curves from the laminar flow profile seem to fit the observed curves better in terms of the overall width and peak height it has to be pointed out again that detector band broadening effects have not been taken into account here. These effects would serve to lower and broaden the predicted peaks. It is important to observe that both sets of the predicted eluting peaks develop a tail, just like the observed peak. Based on such preliminary results it is not possible to exclude the existence of either flow regime.

To summarize there are three effects to be considered: the shape of the flow profile exiting the shallow bed and entering the quartz tube, the flow profile in the quartz tube itself (whether it is parabolic, or whether it is evolving towards a parabolic profile from some starting profile), and the finite cell (window) length, which contributes to band broadening and makes interpretation of experimental results difficult. The present analysis does not allow characterization of the flow inside the instrument. However, it stands to reason that the closer the flow profile that exits the shallow bed is to plug flow, the less band broadening will be created. Also, the shorter the length of the quartz tube between the bed and the detector, the shorter the time for the solute to reach the detector, which will result in a decrease of system band broadening,. Increasing the flowrate can have the same effect as decreasing this distance (this is confirmed experimentally in Table 6.1). Finally, decreasing the length of the detection cell will reduce band broadening.

242

Chapter 7: Summary and future work

7.1 Summary

The purpose of this work was to develop an instrument based on the shallow-bed method which measures the desorption rates from chromatographic packings in a continuous fashion – *i.e.* which can obtain the entire rate curve in a single run. The first part of the work (Chapter 3) was to confirm the feasibility of the technique and to develop the appropriate data processing steps. The desorption of naphthalene from 20 μm polymeric particles of PRP-∞ in 70/30 MeOH/H$_2$O was chosen as the solute-sorbent-solvent system to be studied. The reasons were that the diffusion coefficient of naphthalene inside the matrix of the gel-like PRP-∞ particle is slow, and that it was previously measured. This made the design of the instrument simpler and it allowed comparison of the observed intraparticle diffusion coefficient to the literature value. The digital data processing techniques such as deconvolution and filtering allowed corrections for experimental artifacts due to instrument band broadening and extra-particle solute, after running a separate desorption experiment on an unretained, excluded compound, phloroglucinol. The results were fit with a spherical diffusion model (Eq. 2.1), and the measured particle diffusivity of 5×10^{-11} cm^2 sec^{-1} was found to be statistically indistinguishable from the observed literature value. This successfully demonstrated the feasibility of the instrumental and data-processing approach.

The second, more difficult part of the work was to develop an instrument capable of measuring sub-second desorption kinetics, in order to advance the shallow-bed method.

243

Considerable experimental challenges existed: (i) Placing the detector very close to the shallow bed (about a millimeter), while maintaining dependable seals. (ii) Allowing for efficient and sharp transition between the flow of the solute-containing solvent used in equilibration and the solute-free solvent used in the desorption step. (iii) Acquiring data very rapidly. (iv) Maintaining the geometrical integrity of the shallow bed, i.e. preventing the bed from collapsing. (v) Preventing the stabilized shallow bed from changing resistance to flow (even if the bed doesn't collapse and no voids develop in the packing, the resistance to flow can change due to consolidation). (vi) Developing a new data analysis technique to correct for experimental artifacts due to instrument band broadening and extra-particle solute. (vii) Developing a way to deal with the difficulty of finding an excluded compound for porous particles. (viii) Finding and applying the proper theoretical models to describe the mechanism of the desorption process and the departures from true shallow bed conditions (i.e. the concentration of the desorbing solute becoming significantly larger than zero).

The first three challenges were solved by modifying an existing instrument that is used for homogeneous kinetic measurements. The stopped-flow instrument was designed to withstand pressures of 150 psi. It already contained the optics needed to focus light through a small-volume flow cell and the electronics needed to record fast-changing signals (down to a sub millisecond scale). The modifications made to the instrument were extensive and are described in Chapter 4 and Chapter 5 in the experimental section. They included designing a flow-channel block that would house the shallow bed less than a millimeter upstream from the flow cell, and which replaced the "mixer" used in the

244

stopped flow experiments. Also, commercial electronic valves were purchased and were positioned to achieve the proper flow sequence needed for the desorption experiment. They are controlled with a computer *via* a program written in Labview, which also allows for fast data acquisition from the UV-Vis absorbance detector. Constant pressure pumps were connected to the inlets of the stopped-flow apparatus, so that the proper solutions could be delivered. The instrument can also be thermostatted at a wide range of different temperatures (from 0 to 60 Celsius).

The fourth challenge (preventing the shallow bed from collapsing) proved most difficult. The first design that prevented the bed from collapsing is shown in Chapter 4, Fig. 4.4, and it involved the use of microfabricated silicon grids. It is thought that the silicon grids stabilize the bed by "fencing – in" the particles, which prevents large lateral shifts of particulate material. It was also found that for the bed to be stable inside the instrument it had to be more than 0.2 mm long. The bed-length used subsequently was 0.6 mm long. The fifth challenge (maintaining a constant resistance to flow of the shallow bed) was solved in Chapter 5 by using a mixed-particle slurry, where the ODS-silica sorbent was mixed with larger porous glass beads. The reason for this could be that the glass beads were more wetted by the relatively polar solvent used. An important additional benefit of the larger-diameter glass beads is that higher flowrates are achieved.

Challenge six was overcome when the proper expression was found in the literature to obtain the IRF signal by differentiating the observed curve for the excluded compound in the apparatus (See Eq. 2.27, section 2.2.5). Challenge seven was solved by using an

245

unretained, but not excluded, compound and developing a correction for it (See Section 5.3.2). Challenge eight was solved by finding the proper theoretical equations in the chemical-engineering literature, and developing Microsoft Excel spreadsheets which allow for fitting the rate date with those equations using Microsoft Excel Solver.

Overall, the instrument which was built, combined with the novel data-analysis techniques, is capable of measuring the fastest kinetics yet observed *via* the shallow-bed method (*i.e.* processes which are complete in 0.5 seconds), and its development significantly advances the technique. It displays the potential of observing even faster kinetics. Another significant feature is the capability of computer control, which readily allows for signal averaging and for checking of the reproducibility of the data (the reproducibility between cycles and in between sets of cycles is excellent). Finally, the detector used is a UV-Vis absorbance detector, which allows for measurements of a large class of analytes.

The first solute / particle / solvent studied with the Type II instrument was naphthalene / PRP-1 / 85% MeOH. PRP-1 is an HPLC polymeric sorbent, 10 µm particle diameter. Fitting the kinetic data with Eq. 2.4 (biporous spherical diffusion) revealed that there are two intraparticle diffusivities. The first is for mesoporous diffusion, which is the faster one of the two. The application of Eq. 2.32, which applies when there are significant deviations from shallow-bed conditions, revealed that the mesoporous diffusion coefficient inside the packing is much higher than that obtained with Eq. 2.4, and, from best-fit parameters it was measured to be approximately 3×10^{-7} cm^2 sec^{-1}. This value

suggests that both pore and surface diffusion may be significant contributors to mass transfer inside the mesopores. As well, it was shown that film diffusion, in addition to mesoporous particle diffusion, also contributes to the observed desorption rate for the faster process. The kinetic data for the mesoporous diffusion coefficient contained a much larger amount of information than literature data, which was obtained with a less-advanced shallow bed method. The new data (and theoretical methods) allowed for the better estimate of the mesoporous diffusivity and identification of film diffusion as partially rate limiting. The slower process involved matrix diffusion through the skeleton made up of microspherical aggregates of the cross-linked polymer. The diffusion through this matrix was found to be very hindered, giving an estimated diffusivity of 2×10^{-15} cm^2 sec^{-1}. A Low S/N ratio was found to introduce a large uncertainty (a range of $\pm$ 50%) in the determination of this diffusivity.

The second and final solute / particle / solvent system studied was 1,2-dimethyl-4-nitrobenzene /Luna C-18 / 50% aqueous MeOH. Luna C-18 is a porous ODS packing, with a particle size of 12 μm. The resulting curves were fit with Eq. 2.32 and Eq. 2.15 and it was found that particle and film diffusion were both rate-limiting under the conditions studied. The intraparticle diffusivity was measured as 8.8×10^{-7} cm^2 sec^{-1}. The entire process was completed in about 0.5 sec. It was determined that surface diffusion comprises more than 90% of intraparticle transport for a compound with a high retention factor. After the determination of the surface diffusion coefficient, its effect on band broadening of elution peaks in column chromatography was studied by comparison of predicted and experimental elution peaks obtained in a 25-cm long HPLC column.

247

Theoretical band broadening equations were used to predict the plate height of the overall peak for two cases. In the first case surface diffusion and film diffusion were ignored, while in the second case they were accounted for. It was found that in the second case the predicted and observed peak shapes and plate heights were in close agreement, while in the first case the agreement was poor. This showed that surface and film diffusion have a significant effect on the band broadening in the column, and that the effect of surface diffusion was to decrease band broadening at high flowrates, compared with what is predicted with conventional versions of HPLC band broadening theory.

7.2 Future work

Future work can be grouped into two categories. The first is the kinetic studies which could be carried out with the present system. The second category relates to some possible improvements to the existing Type II apparatus.

Kinetic Studies which could be pursued with the present system. Fundamental, systematic kinetics studies can be carried out on the present instrument with a wide variety of packings, solvents, and solutes.

As early as 40 years ago, J. C. Giddings wrote about the potential importance of surface diffusion on chromatographic band broadening [3, 44]. However, to date, no systematic fundamental studies of surface diffusivities in HPLC have been performed. The dependence of intraparticle diffusivities on parameters such as the mobile phase

248

composition, temperature, and retention could be measured with the present apparatus to obtain data which could lead to deeper understanding of the nature of surface diffusion and to illuminate further its effect on band broadening in chromatography.

The present method could also be used to study the kinetics of other types of sorption mechanisms, including ion exchange [50], affinity chromatography (using, for example, protein/ligand interactions [18], aptamers [116], or molecularly imprinted polymers [117]), and metal-ligand interactions [118]. This instrument could also be applied in measuring the rates of extraction/release of solid - phase extraction membranes [119].

Improvements to the present type II apparatus. Further improvements to the apparatus would include, but are not limited to the following. (i) Better infrastructure for packing the shallow bed. The present methods of bed packing involve a high degree of manual labor and a fair amount of dexterity (See Fig. 4.5, 5.1, and 5.2). A proper design would surely decrease the difficulties associated with the procedure. Also, proper design of the use of PDMS to improve the seals but to prevent unwanted sorption into it would greatly decrease the amount of labor involved. (ii) Higher Flowrates. Higher flowrates will allow for study of faster processes. They could be achieved with proper ratios of the non-porous glass-beads in the mixed particle slurry. Also, pressures could be raised beyond 250 psi, which is the current rating of the apparatus. A different design of sealing materials may be needed. (iii) The use of a high-flowrate constant-displacement pump instead of constant pressure pumps during the flush and desorption step. The instrument can be adapted for the use of constant displacement pumps, with only minor adjustments

249

necessary. Special pump systems would have to be used to deliver high flowrates (Waters 2525 Binary Gradient Module, which is capable of delivering up to 150 mL/min. is one example of such a pump). This would create several advantages. First, the reproducibility of the runs could be increased even further. Moreover, the use of high-molecular-weight excluded compounds for IRF-Markers could be made more feasible, because the slight viscosity change that is common to their solutions would not change the flowrate. (iv) Finding better (excluded) IRF-Markers. The current approach of using an imperfect IRF-Marker (an unretained, but not excluded compound) and applying a correction works very well because of highly retentive conditions. There could be considerable interest in studying surface diffusivities at low – retention conditions and even of studying pore diffusion under non-retentive conditions. For such studies, the use of an excluded compound would become imperative. The use of low ionic strength solutions of anionic UV - absorbers should be investigated as they can be excluded due to the Donnan potential.

References

1.	Neue, U.D., *HPLC Columns: Theory, Technology, and Practice.* 1997, Chapter 4., New York: Wiley - VCH.

2.	Horvath, C. and H.J. Lin, *Band Spreading in Liquid-Chromatography - General Plate Height Equation and a Method for Evaluation of Individual Plate Height Contributions.* J. Chromatogr., 1978. 149(FEB): p. 43-70.

3.	Giddings, J.C., *Dynamics of Chromatography.* 1965, New York: Marcel Dekker.

4.	Crombeen, J.P., H. Poppe, and J.C. Kraak, Chromatographia, 1986. 22: p. 319.

5.	Snyder, L.R. and J.J. Kirkland, *Introduction to Modern Liquid Chromatography.* 1982, Wiley: Toronto. p. Chapter 19.

6.	Karger, B.L., L.R. Snyder, and C. Horvath, *An Inroduction to Separation Science,* in *An Inroduction to Separation Science.* 1973, John Wiley & Sons, Inc: Toronto. p. 135-155.

7.	Chen, J.C. and S.G. Weber, Anal. Chem., 1983. 55: p. 127.

8.	Giddings, J.C., L.M. Bowman, and M.N. Myers, *Isolation of Peak Broadening Factors in Exclusion (Gel) Chromatography.* Macromolecules, 1977. 10(2): p. 443-449.

9.	Gzil, P., Vervoot, N., Baron, G.V., Desmet, G., *Advantages of Perfectly Ordered 2-D Porous Pillar Arrays over Packed Bed Columns for LC Separations: A Theoretical Analysis.* Analytical Chemistry, 2003. 75.

251

10. Knox, J.H. and H.P. Scott, *B-Term and C-Term in the Vandeemter Equation for Liquid-Chromatography.* Journal of Chromatography, 1983. 282(DEC): p. 297-313.

11. Lenhoff, A.M., *Significance and Estimation of Chromatographic Parameters.* J. Chromatogr., 1987. 384: p. 285-299.

12. Stout, R.W., J.J. Destefano, and L.R. Snyder, *High-Performance Liquid-Chromatographic Column Efficiency as a Function of Particle Composition and Geometry and Capacity Factor.* Journal of Chromatography, 1983. 282(DEC): p. 263-286.

13. Broske, A.D., R.D. Ricker, B.J. Permar, W. Chen, and M. Joseph, *The influence of Sub-Two Micron Particles on HPLC Performance.* 2003, Agilent Technologies: Wilmington.

14. Colon, L.A., Cintron, J.M., Anspach, J.A., Fermier, A.M., Swinney,K.A, *Very high pressure HPLC with 1 mm id columns.* Analyst, 2004. 129(6): p. 503-504.

15. Giddings, J.C., Anal. Chem., 1963. 35: p. 1999.

16. Muller, A.J. and P.W. Carr, *Examination of Kinetic Effects in the High-Performance Liquid Affinity-Chromatography of Glycoproteins by Stopped-Flow and Pulsed Elution Methods.* Journal of Chromatography, 1984. 294(JUN): p. 235-246.

17. Muller, A.J. and P.W. Carr, *Chromatographic Study of the Thermodynamic and Kinetic Characteristics of Silica-Bound Concanavalin-A.* Journal of Chromatography, 1984. 284(1): p. 33-51.

252

18. Muller, A.J. and P.W. Carr, *Examination of the Thermodynamic and Kinetic Characteristics of Microparticulate Affinity-Chromatography Supports - Application to Concanavalin-A.* Journal of Chromatography, 1986. 357(1): p. 11-32.

19. Bogar, R.G., J.C. Thomas, and J.B. Callis, *Lateral Diffusion of Solutes Bound to the Alkyl Surface of C-18 Reversed-Phase Liquid-Chromatographic Packings.* Analytical Chemistry, 1984. 56(7): p. 1080-1084.

20. Marshall, D.B., J.W. Burns, and D.E. Connolly, *Direct Measurement of Liquid-Chromatographic Sorption Desorption-Kinetics and the Kinetic Contribution to Band Broadening.* J. Chromatogr., 1986. 360(1): p. 13-24.

21. Marshall, D.B., J.W. Burns, and D.E. Connolly, *Determination of the Interaction Free-Energy Dispersion in Sorptive Systems by Relaxation Kinetics Methods.* J.Am. Chem. Soc., 1986. 108(5): p. 1087-1088.

22. Ludes, M.D., S.R. Anthony, and M.J. Wirth, *Fluorescence Imaging of the Desorption of Dye from Fused Silica versus Silica Gel.* Anal. Chem., 2003. 75(13): p. 3073-3078.

23. Waite, S.W., D.B. Marshall, and J.M. Harris, *Temperature-Jump Investigation of Sorption/Desorption Kinetics at Reversed-Phase Chromatographic Silica Solution Interfaces.* Anal. Chem., 1994. 66(13): p. 2052-2061.

24. Shield, S.R. and J.M. Harris, *Triplet-state photoexcitation dipole-jump relaxation method to observe adsorption/desorption kinetics at a reversed-phase silica/solution interface.* Anal. Chem., 2002. 74(10): p. 2248-2256.

253

25. McGuffin, V.L. and C. Lee, *Thermodynamics and kinetics of solute transfer in reversed-phase liquid chromatography.* J. Chromatogr. A, 2003. 987(1-2): p. 3-15.

26. Komiyama, H. and J.M. Smith, *Surface Diffusion in Liquid-Filled Pores.* Aiche Journal, 1974. 20(6): p. 1110-1117.

27. Grathwohl, P., *Diffusion in Natural Porous Media: Contaminant Transport, Sorption/Desorption and Dissolution Kinetics.* Topics in Environmental Fluid Mechanics. 1998, Norwell, Massachusetts: Kluwer Academic Publishers.

28. Li, J.Y. and F.F. Cantwell, *Intra-particle sorption rate and liquid chromatographic bandbroadening in porous polymer packings .3. Diffusion in the polymer matrix as the cause of slow sorption.* J. Chromatogr. A, 1996. 726(1-2): p. 37-44.

29. Ruthven, D.M., *Principles of Adsorption and Adsorption Processes.* 1984, New York: Wiley.

30. Beck, R.E. and J.S. Schultz, *Hindrance of Solute Diffusion within Membranes as Measured with Microporous Membranes of Known Pore Geometry.* Biochimica Et Biophysica Acta, 1972. 255(1): p. 273-&.

31. Deen, W.M., *Hindered Transport of Large Molecules in Liquid-Filled Pores.* Aiche Journal, 1987. 33(9): p. 1409-1425.

32. Coffman, J.L., E.N. Lightfoot, and T.W. Root, *Protein diffusion in porous chromatographic media studied by proton and fluorine PFG-NMR.* Journal of Physical Chemistry B, 1997. 101(12): p. 2218-2223.

254

33.   Gibbs, S.J., E.N. Lightfoot, and T.W. Root, *Protein Diffusion in Porous Gel-Filtration Chromatography Media Studied by Pulsed Field Gradient Nmr-Spectroscopy*. Journal of Physical Chemistry, 1992. 96(18): p. 7458-7462.

34.   Lorenzanoporras, C.F., P.W. Carr, and A.V. McCormick, *Relationship between Pore Structure and Diffusion Tortuosity of ZrO₂ Colloidal Aggregates*. J. Colloid. Interf. Sci., 1994. 164(1): p. 1-8.

35.   Lorenzanoporras, Annen, M.J., Flickinger, M.C., C.F., P.W. Carr, and A.V. McCormick, *Pore Structure and Diffusion Tortuosity of Porous ZrO₂ Synthesized by 2 Different Colloid-Aggregation Processes*. J. Colloid. Interf. Sci., 1995. 170(2): p. 299-307.

36.   Tallarek, U., F.J. Vergeldt, and H. Van As, *Stagnant mobile phase mass transfer in chromatographic media: Intraparticle diffusion and exchange kinetics*. J. Phys. Chem. B, 1999. 103(36): p. 7654-7664.

37.   Sekine, T. and K. Nakatani, *Intraparticle diffusion and adsorption isotherm for sorption in silica gel studied by single-microparticle injection and microabsorption methods*. Langmuir, 2002. 18(3): p. 694-697.

38.   Bujalski, R. and F.F. Cantwell, *Comment on "Direct analysis of intraparticle mass transfer in silica gel using single-microparticle injection and microabsorption methods"*. Langmuir, 2001. 17(24): p. 7710-7711.

39.   Sekine, T. and K. Nakatani, *Nanometer pore size dependence of intraparticle diffusion in silica gel*. Chem. Lett., 2004. 33(5): p. 600-601.

255

40. Kovaleski, J.M. and M.J. Wirth, *Lateral Diffusion of Acridine-Orange at Liquid-Hydrocarbon Water Interfaces.* Journal of Physical Chemistry, 1995. 99(12): p. 4091-4095.

41. Kovaleski, J.M. and M.J. Wirth, *Lateral diffusion of an adsorbate at chromatographic octadecylsiloxane/water interfaces of varying hydrocarbon density.* Journal of Physical Chemistry B, 1997. 101(28): p. 5545-5548.

42. Swinton, D.J. and M.J. Wirth, *Lateral diffusion of 1,1 '-dioctadecyl-3,3,3 ' 3 '-tetramethylindocarbocyanine perchlorate at the interfaces of C-18 and chromatographic solvents.* Analytical Chemistry, 2000. 72(16): p. 3725-3730.

43. Wirth, M.J., D.J. Swinton, and M.D. Ludes, *Adsorption and Diffusion of Single Molecules at Chromatographic Interfaces.* J. Phys. Chem. B, 2003. 107: p. 6258-6268.

44. Miyabe, K. and G. Guiochon, *Measurement of the parameters of the mass transfer kinetics in high performance liquid chromatography.* Journal of Separation Science, 2003. 26(3-4): p. 155-173.

45. Gowanlock, D., R. Bailey, and F.F. Cantwell, *Intra-particle sorption rate and liquid chromatographic bandbroadening in porous polymer packings .1. Methodology and validation of the model.* J. Chromatogr. A, 1996. 726(1-2): p. 1-23.

46. Li, J.Y., L.M. Litwinson, and F.F. Cantwell, *Intra-particle sorption rate and liquid chromatographic bandbroadening in porous polymer packings .2. Slow sorption rate on a microparticle packing.* J. Chromatogr. A, 1996. 726(1-2): p. 25-36.

256

47.   Nevejans, F. and M. Verzele, *On the Structure and Chromatographic Behavior of Polystyrene Phases.* J. Chromatogr., 1987. 406: p. 325-342.

48.   Liang, C., S. Dai, and G. Guiochon, *A Graphitized-Carbon Monolithic Column.* Anal. Chem., 2003. 75: p. 4904-4912.

49.   Ells, B., *Bandbroadening on Polymeric HPLC packings.* 1998, Thesis, University of Alberta: Edmonton.

50.   Helfferich, F.G. and Y.L. Hwang, eds. *Ion Exchange kinetics.* Ion Exchangers, ed. D. K. 1991, Walter de Gruyter: Berlin. 1277-1310.

51.   Helfferich, F., *Ion Exchange.* 1962, Chapters 6 and 9, New York: McGraw-Hill.

52.   Cussler, E.L., *Diffusion Mass Transfer in Fluid Systems.* 1984: Cambridge University Press.

53.   Bird, R.B., W.E. Stewart, and E.N. Lightfoot, *Transport Phenomena.* 2002, New York: John Wiley & Sons.

54.   Sternberg, J.C., in *Advances in Chromatography, Vol 2*, J.C. Giddings and R.A. Keller, Editors. 1966, Chapter 6, Marcel Dekker: New York.

55.   Ruzicka, J. and E.H. Hansen, *Flow Injection Analysis.* 1981, New York: John Wiley. Chapter 3.

56.   Guiochon, G., S. Golshan-Shirazi, and A.M. Katti, *Fundamentals of Preparative and Nonlinear Chromatography.* 1994, Academic Press, Inc.

57.   Conder, J.R. and C.L. Young, *Physicochemical Measurement by Gas Chromatography.* 1979, Chichester: John Wiley & Sons.

257

58. Vonmeerwall, E.D., *Diffusion in Polymer Systems, Measured with the Pulsed-Gradient NMR Method.* Journal of Non-Crystalline Solids, 1991. 131: p. 735-741.

59. Karger, J. and D.M. Ruthven, *Diffusion in Zeolites and Other Microporous Solids.* 1992, New York: Wiley.

60. Viel, S., F. Ziarelli, and S. Caldarelli, *Enhanced diffusion-edited NMR spectroscopy of mixtures using chromatographic stationary phases.* Proceedings of the National Academy of Sciences of the United States of America, 2003. 100(17): p. 9696-9698.

61. Tallarek, U., M. Paces, and E. Rapp, *Perfusive flow and intraparticle distribution of a neutral analyte in capillary electrochromatography.* Electrophoresis, 2003. 24(24): p. 4241-4253.

62. Hunter, A.K. and G. Carta, *Protein adsorption on novel acrylamido-based polymeric ion- exchangers III. Salt concentration effects and elution behavior.* J. Chromatogr., 2001. 930(1-2): p. 79-93.

63. Suzuki, M., *Adsorption Engineering.* 1990, Amsterdam: Elsevier.

64. Lewus, R.K., F.H. Altan, and G. Carta, *Protein adsorption and desorption on gel-filled rigid particles for ion exchange.* Ind. Eng. Chem. Res., 1998. 37(3): p. 1079-1087.

65. Nakatani, K. and T. Sekine, *Direct analysis of intraparticle mass transfer in silica gel using single-microparticle injection and microabsorption methods.* Langmuir, 2000. 16(24): p. 9256-9260.

258

66. Tetenbaum, M. and H.P. Gregor, *Self-diffusion of cations, non-exchange anions and solvent in a cation exchange resin system.* J. Phys. Chem., 1954. 58: p. 1156-1163.

67. Costa, C. and A. Rodrigues, *Design of Cyclic Fixed-Bed Adsorption Processes. Part I: Phenol Adsorption on Polymeric Adsorbents.* AIChE J., 1985. 31: p. 1645.

68. Du Domaine, J., R.L. Swain, and O.A. Hougen, *Cation-Exchange Water Softening Rates.* Ind. Eng. Chem., 1943. 35: p. 546-553.

69. Boyd, G.E., A.W. Adamson, and L.S. Myers Jr., *The Exchange Adsorption of Ions from Aqueous Solutions by Organic Zeolites. II. Kinetics.* J. Am. Chem. Soc., 1947. 69: p. 2836-2848.

70. Bieber, H., F.E. Steidler, and W.A. Selke, *Ion Exchange Rate Mechanism.* Chem. Eng. Progr. Symp. Ser., 1954. 50: p. 17-21.

71. Ells, B., Y. Wang, and F.F. Cantwell, *Influence of solvent uptake and swelling by poly(styrene- divinylbenzene) column packings on sample sorption rate and band broadening in reversed-phase liquid chromatography.* J. Chromatogr. A, 1999. 835(1-2): p. 3-18.

72. Brandani, S. and D.M. Ruthven, *Analysis of Zlc Desorption Curves for Liquid-Systems.* Chem. Eng. Sci., 1995. 50(13): p. 2055-2059.

73. Ruthven, D.M. and P. Stapleton, *Measurement of Liquid-Phase Counter-Diffusion in Zeolite Crystals by the ZLC Method.* Chem. Eng. Sci., 1993. 48(1): p. 89-98.

259

74. Eic, M. and D.M. Ruthven, *A New Experimental Technique for Measurement of Intracrystalline Diffusivity*. Zeolites, 1988. 8(1): p. 40-45.

75. Sanders, M.S., J.B. Vierow, and G. Carta, AIChE J., 1989. 35: p. 53-68.

76. Fernandez, M.A., W.S. Laughinghouse, and G. Carta, *Characterization of protein adsorption by composite silica- polyacrylamide gel anion exchangers .2. Mass transfer in packed columns and predictability of breakthrough behavior*. Journal of Chromatography A, 1996. 746(2): p. 185-198.

77. Crank, J., *The Mathematics of Diffusion*. Second ed. 1975, New York: Oxford University Press.

78. Ruckenstein, E., A.S. Vaidyanathan, and G.R. Youngquist, *Sorption by Solids with Bidisperse Pore Structures*. Chemical Engineering Science, 1971. 26(9): p. 1305-&.

79. Golay, M.J.E., *Height Equivalent to a Theoretical Plate of Tubular Gas Chromatographic Columns Lined with a Porous Layer*. Nature, 1963. 199(489): p. 370-&.

80. Golay, M.J.E., *Height Equivalent to a Theoretical Plate of an Open Tubular Column Lined with a Porous Layer - a Generalized Equation*. Analytical Chemistry, 1968. 40(2): p. 382-&.

81. Wilson, E.J. and Geankoplis, C.J, *Liquid Mass Transfer at Very Low Reynolds Numbers in Packed Beds*. Industrial & Engineering Chemistry Fundamentals, 1966. 5(1): p. 9-&.

82. Katoka, T., H. Yoshida, and K. Ueyama, J. Chem. Eng. Jpn., 1972. 5: p. 132-136.

83. Gilliland, E.R. and R.F. Baddour, *The Rate of Ion Exchange*. Ind. Eng. Chem., 1953. 45(2): p. 330-337.

84. Glueckauf, E., *Principles of Operation of Ion-Exchange Columns*, in *Ion Exchange and Its Applications*. 1955, Society of Chemical Industry: London. p. 34-46.

85. Sha'afi, R.I. and S.M. Fernandez, eds. *Fast methods in physical biochemistry and cell biology*. 1983, Elsevier: Amsterdam, New York.

86. Hiromi, K., *Kinetics of fast enzyme reactions : theory and practice*. Hiromi, Keitaro, New York: Wiley.

87. Horlick, G., *Resolution Enhancement of Line Emission Spectra by Deconvolution*. Appl. Spectrosc., 1972. 26(3): p. 395-399.

88. Horlick, G. and G. Hieftje, *Correlation Methods in Chemical Data Measurement*, in *Contemporary topics in analytical and clinical chemistry, Vol 3*, D.M. Hercules, et al., Editors. 1978, Chapter 4., Plenum Publishing Corporation: New York.

89. Economou, A., P.R. Fielden, and A.J. Packham, *Deconvolution of overlapping chromatographic peaks by means of fast Fourier and Hartley transforms*. Analyst, 1996. 121(2): p. 97-104.

90. Yamane, T., S. Katayama, and M. Todoki, *Application of a Deconvolution Method to Kinetic-Studies with Conduction Type Microcalorimeters*. Thermochim. Acta, 1991. 183: p. 329-338.

91. Levenspiel, O., *Chemical Reaction Engineering*. 1972, John Wiley: New York. p. Chapter 9.

92. Brandrup, B.A. and E.H. Immergut, *Polymer Handbook*. 1975, New York: Wiley.

93. Tanaka, N., T. Ebatta, K. Hashizume, K. Hosoya, and M. Araki, J. Chromatogr., 1989. 475: p. 195.

94. Personal communication, Dan Lee, Hamilton Corp., Reno, NV.

95. Fossey, L. and F.F. Cantwell, Anal. Chem., 1982. 54: p. 1693.

96. Golay, M.J.E. and J.G. Atwood, *Early phases of the dispersion of a sample injected in Poiseuille flow*. J. Chromatogr., 1979. 186: p. 353-370.

97. Gill, W.N. and V. Ananthakrishnan, *Laminar Dispersion in Capillaries*. AIChE J., 1967. 13(4): p. 801-807.

98. Maycock, K.P., J.M. Tarbell, and J.L. Duda, *Numerical Simulation of Solute Dispersion in Laminar Tube Flow*. Separ. Sci. Technol., 1980. 15(6): p. 1285-1296.

99. Wilke, C.R. and P. Chang, *Correlation of Diffusion Coefficients in Dilute Solutions*. AIChE J., 1955. 1: p. 264.

100. Gailer, J., G.A. Buttigieg, and M.B. Denton, *Simultaneous arsenic-and selenium-specific detection of the dimethyldiselenoarsinate anion by high-performance liquid chromatography-inductively coupled plasma atomic emission spectrometry*. Appl. Organomet. Chem., 2003. 17(8): p. 570-574.

101. He, P. and Y. Yang, *Studies on the long-term thermal stability of stationary phases in subcritical water chromatography*. J. Chromatogr. A, 2003. 989(1): p. 55-63.

102. Hubbuch, J., T. Linden, E. Knieps, A., Ljunglof, J. Thommes, and M.R. Kula, *Mechanism and kinetics of protein transport in chromatographic media studied by confocal laser scanning microscopy - Part I. The interplay of sorbent structure and fluid phase conditions.* Journal of Chromatography A, 2003. 1021(1-2): p. 93-104.

103. Kondo, T. and Y. Yang, *Comparison of elution strength, column efficiency, and peak symmetry in subcritical water chromatography and traditional reversed-phase liquid chromatography.* Anal. Chim. Acta, 2003. 494(1-2): p. 157-166.

104. Hayes, R.E., K. Nandakumar, and H. Nasr-El-Din, *Steady Laminar-Flow in a 90-Degree Planar Branch.* Comput. Fluids, 1989. 17(4): p. 537-553.

105. Moser, K.W., E.C. Kutter, J.G. Georgiadis, R.O. Buckius, H.D. Morris, J.R. Torczynski, *Velocity measurements of flow through a step stenosis using Magnetic Resonance Imaging.* Experiments in Fluids, 2000. 29(5): p. 438-447.

106. Trevelyan, P.M.J., S. Kalliadasis, J.H. Merkin, S.K. Scott, *Circulation and reaction enhancement of mass transport in a cavity.* Chem. Eng. Sci., 2001. 56(17): p. 5177-5188.

107. Savitzky, A. and M.J.E. Golay, *Smoothing and Differentiation of Data by Simplified Least Squares Procedures.* Anal. Chem., 1964. 36(8): p. 1627-39.

108. Cantwell, F.F. and D.W. Brown, *Liquid Chromatographic Determination of Nitroanilines.* J. Chem. Educ., 1981. 58: p. 820-823.

109. Kulicke, W.-M. and C. Clasen, *Viscosimetry of Polymers and Polyelectrolytes.* 2004, Heidelberg: Springer-Verlag. 121.

263

110. Delamarche, E., H. Schmid, A. Bietsch, N.B. Larsen, H. Rothuizen, B. Michel, and H. Biebuyck *Transport Mechanisms of Alkanethiols during Microcontact Printing on Gold.* j. phys. Chem. B, 1998. 102: p. 3324-3334.

111. Wells, M.J.M. and C.R. Clark, *Liquid-Chromatographic Elution Characteristics of Some Solutes Used to Measure Column Void Volume on C-18 Bonded Phases.* Analytical Chemistry, 1981. 53(9): p. 1341-1345.

112. Rimmer, C.A., C.R. Simmons, and J.G. Dorsey, *The measurement and meaning of void volumes in reversed-phase liquid chromatography.* Journal of Chromatography A, 2002. 965(1-2): p. 219-232.

113. Rolland, J.P., R.M. Van Dam, D.A. Schorzman, S.R. Quake and J.M. DeSimone, *Solvent-Resistant Photocurable "Liquid Teflon" for Microfluidic Device Fabrication.* J. AM. CHEM. SOC., 2004. 126: p. 2322-2323.

114. Levich, V.G., *Physicochemical Hydrodynamics.* 2 ed. 1962, Englewood Cliffs, N.J.: Prentice - Hall.

115. Langhaar, H.L., *Steady Flow in the Transition Length of a Straight tube.* Journal of Applied Mechanics, 1942: p. A55-A58.

116. Deng, Q., C.J. Watson, and R.T. Kennedy, *Aptamer affinity chromatography for rapid assay of adenosine in microdialysis samples collected in vivo.* J. Chromatogr. A, 2003. 1005(1-2): p. 123-130.

117. Sajonz, P., M. Kele, G.M. Zhong, B. Sellergren, and G. Guiochon, *Study of the thermodynamics and mass transfer kinetics of two enantiomers on a polymeric imprinted stationary phase.* J. Chromatogr. A, 1998. 810(1-2): p. 1-17.

264

118. Ren, D.Y., N.A. Penner, B.E. Slentz, H.D. Inerowicz, M. Rybalko and F.E. Regnier, *Contributions of commercial sorbents to the selectivity in immobilized metal affinity chromatography with Cu(II)*. J. Chromatogr. A, 2004. 1031(1-2): p. 87-92.

119. Green, C.E. and M.H. Abraham, *Investigation into the effects of temperature and stirring rate on the solid-phase extraction of diuron from water using a C-18 extraction disk*. J. Chromatogr. A, 2000. 885(1-2): p. 41-49.

265

Appendix 1   Labiew file used for data acquisition with Type I instrument

Figure A1.1 below shows the Labview 4.1 program which instructs the National

Instruments I/O board (PCI-MIO-16XE-50) to acquire signal from the Waters Lambda

Max 481 LC detector used in Chapter 3 with the Type I apparatus. This file also allows

choosing the scan rate (Hz) and the gain of the I/O board. The program was written by

Eric Carpenter. The wiring used to connect the detector to the I/O board are shown

below in Fig A1.2.

Fig. A1.1 Labview (National Instruments, Austin, TX, USA) file for data acquisition .
This program has been Designed by Eric Carpenter from the department of Physics.
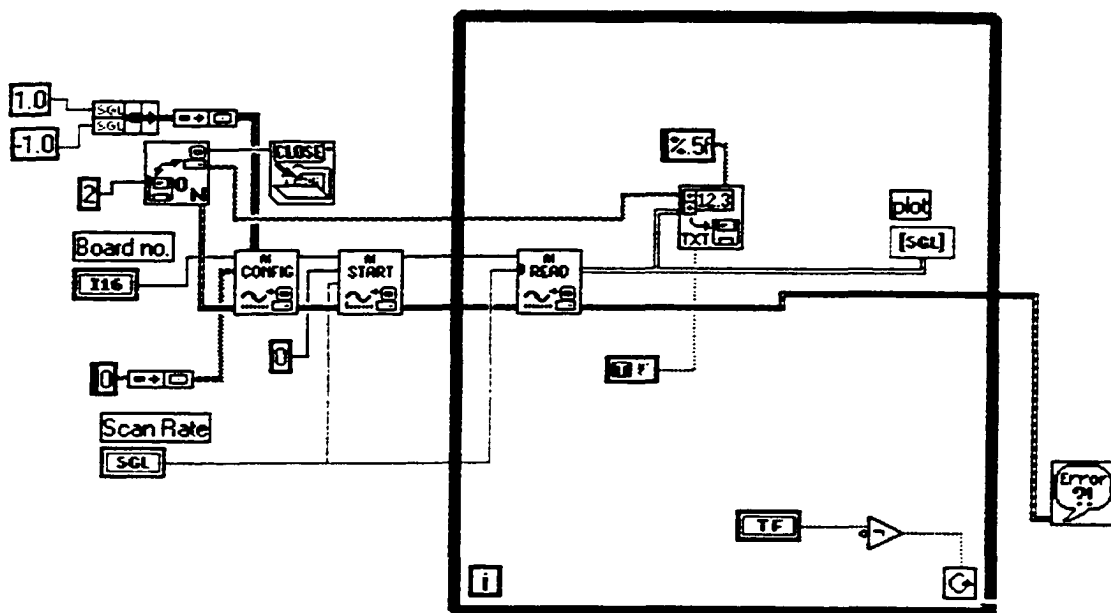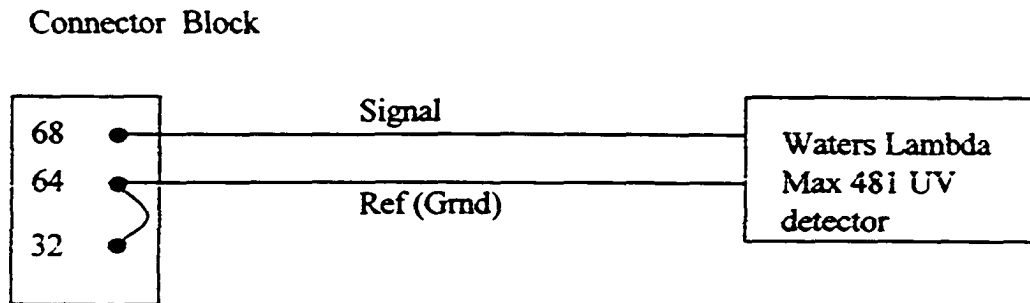

266

Fig. A1.2 Wiring between the Detector and the Connector block. The connector block is

connected directly into the I/O board. See Table A2. 1 for the functions of the pin

numbers

Connector Block

267

Appendix 2 Labview programs and the connections used to control the Type II apparatus in Chapters 4 and 5.

This appendix describes the Labview files used to control the valve sequences described in Fig. 4.1. The main Labview file, called "SingleFlowdirection2.vi" is shown on the next page in Fig. A2.1. This is the file which controls the timing of the counters on the National Instruments I/O board (PCI-MIO-16XE-50). Also, it defines the Data Acquisition window during a cycle. In addition it allows for choosing the number of cycles per set of runs (the number of cycles per set was always chosen to be 5). The main file is followed by a sub-file called "mergefiles.vi" shown in Fig. A2.2. This file takes the data from each cycle in a set and merges them into a single file with a user-defined name and directory.

The wirings needed to connect the National Instruments I/O board with the Valve Drivers (Part #090-0022-100-1 Parker Hannifin, General Valve Division, Fairfield, NJ) that control the valves are shown in Fig. A2.3. The left box shows the connections on the connector block. The connector block is wired directly into the port of the Data Acquisition board. The numbers on the left represent the pin numbers which were used. The grey area to the right of the connector block is an additional external circuit, which is needed to supplement the insufficient number of clocks on the I/O board. The components of the internal circuit include an OR gate and a falling edge triggered flip-flop toggle switch (actually, the parts used are a *rising* edge triggered flip-flop toggle switch with a NOT gate before the Toggle (T) input. Taken together the flip-flop and the

268

NOT gate give *falling*-edge triggering). The boxes on the right, above the dashed line, depict the wiring connections on the Valve Drivers (VD). The numbers represent the pin numbers of the individual valve drivers. VD1 controls valve 1, and VD2 and VD3 control valves 2 and 3, respectively (VD2 and VD3 are wired in exactly the same way). The box below the dashed line on the right represents the detector output device (called the RA 401 controller). The dashed line is an imaginary line which separates the connections that have to do with flow control from those that are involved in Data Acquisition. The following page contains Table A2.1 and A2.2 which gives the function or name of each pin on the connector block and the valve drivers, respectively.

The timing diagrams are shown for the outputs of different devices. The first four lines show the timing of the counters (CTR), the digital line, and the data acquisition clock. All these take place in the I/O board. The next line is the timing diagram of the falling edge triggered external flip-flop. The sixth trace from the top shows the timing diagram for the OR gate on the external circuit. Since the output of the OR gate is connected directly into VD1, the same timing diagram applies for the timing of valve # 1. When the output of the OR gate is high, valve #1 turns is in an energized state. The last trace shows the timing diagram for VD2 and VD3, and hence for valves # 2 and 3. Finally, the timing events are related to the different steps in the cycle: Equilibration, Time-out, Flush, and Run. The lengths of the individual steps are not related to the actual duration of the steps during the experiments. For example, the Equilibration and Desorption steps are much longer than the Time-out and Flush steps in reality.

269

Fig. A2.1 Diagram of the Labview (National Instruments, Austin, TX, USA) file "SingleFlowdirection2.vi" for flow control and data acquisition for the Type II apparatus.. The boxes with text contain comments. This program was written by Eric Carpenter of the Department of Physics
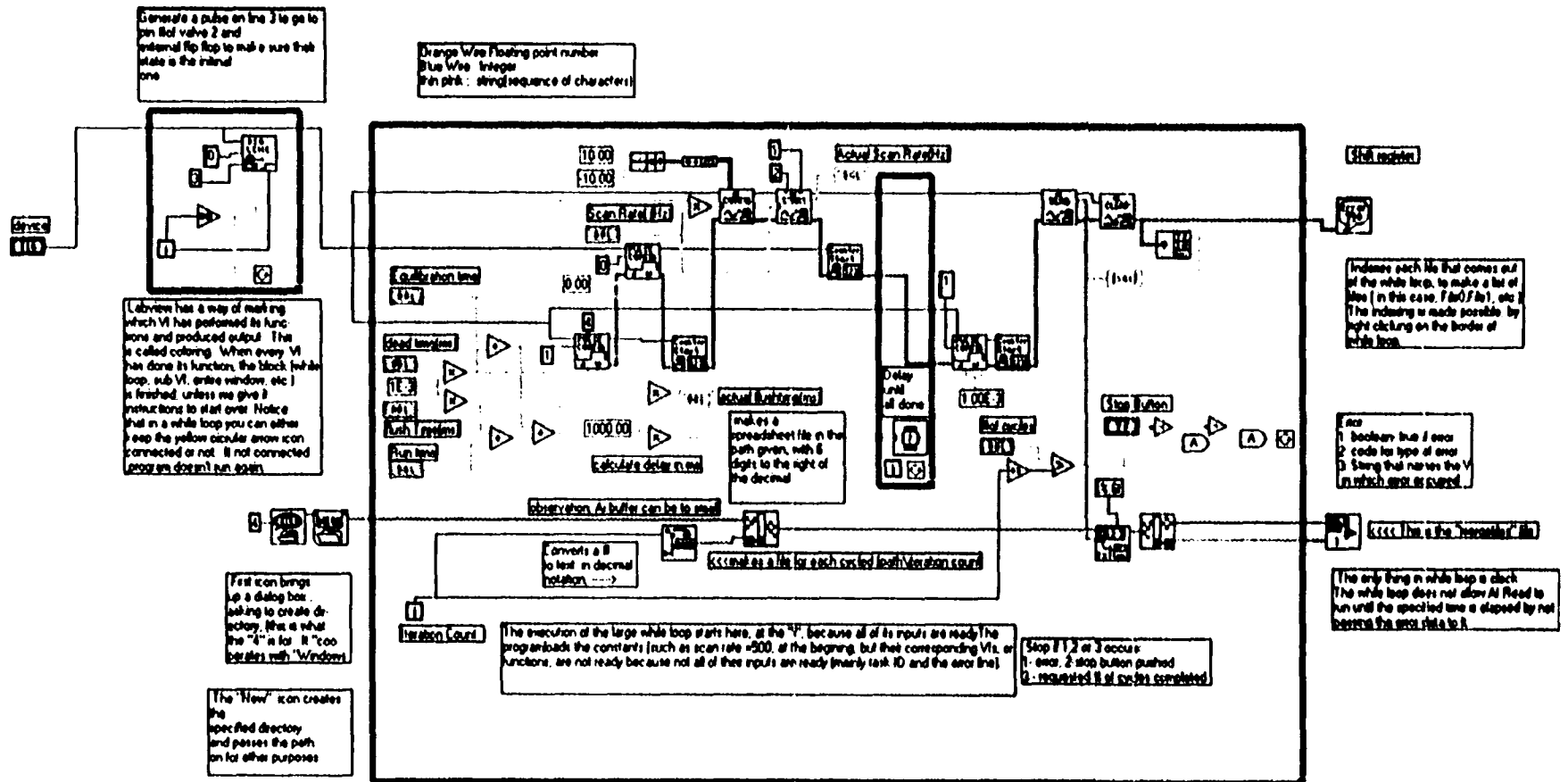
Fig. A2.2 Diagram of a subfile of "SingleFlowdirection2.vi", called "mergefiles.vi". The boxes with text contain comments. This program was written by Eric Carperter fof the Department of Physics
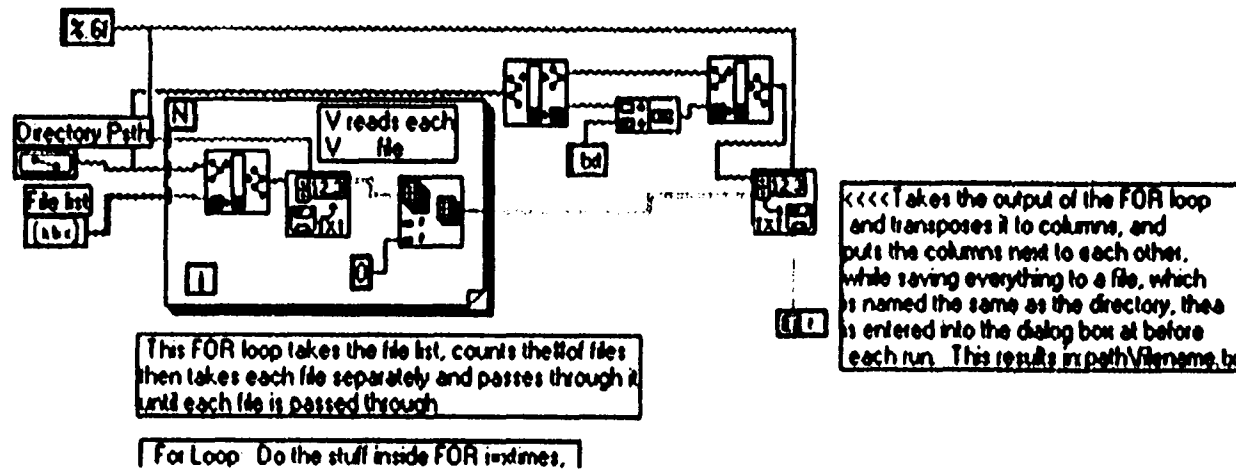
Fig. A2.3 External connections used in conjunction with the Labview files. The top part (above the thick dashed line) enables flow control by enforcing a sequence on the valve drivers, while the bottom part controls to data acquisition. The connector-block is wired directly to the NI DAQ board in the computer. The symbols V+ and V- symbolize the 5 V power supply to all the component of external logic circuit.
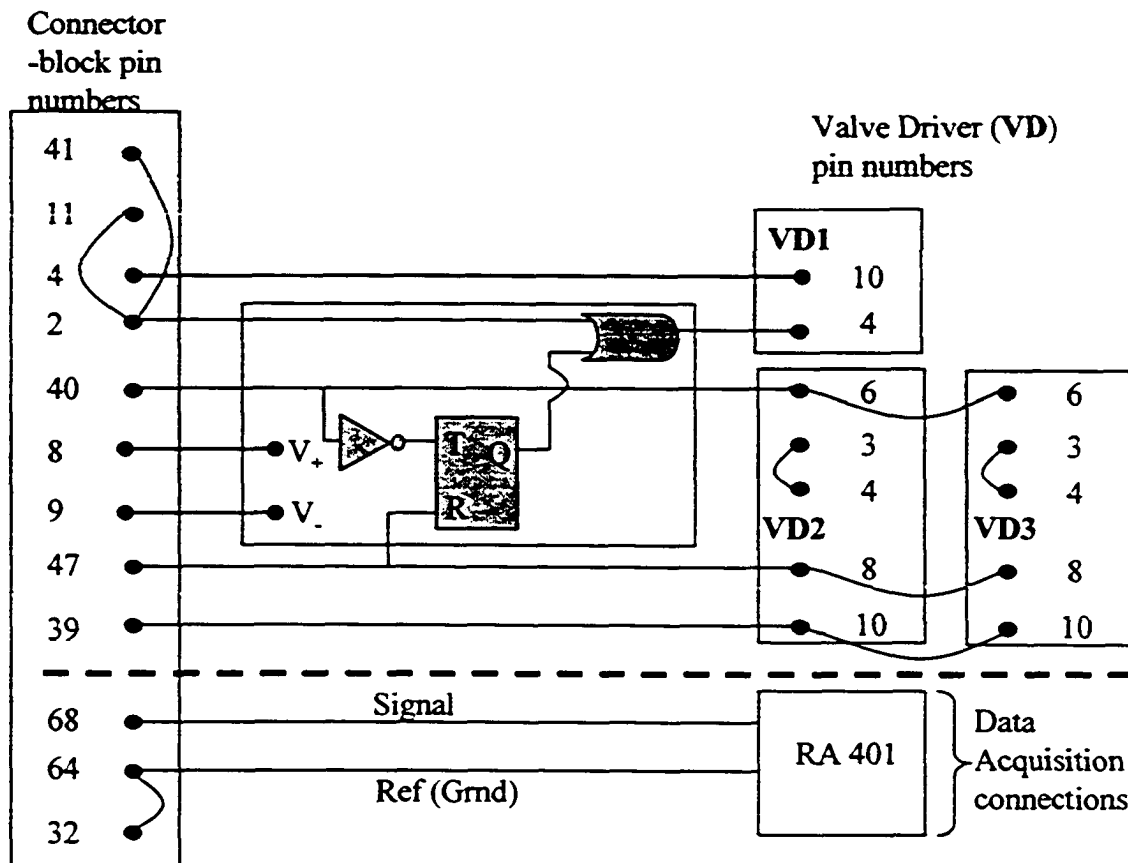
Legend

●   Pin connections (see next page for the function of each pin on the connector block)

NOT gate (Inverter)

Rising-edge triggered Toggle flip-flop switch – Resets on high. (If combined with the NOT gate, the together become a Falling-edge triggered Toggle flip-flop. T = toggle, R = Reset, Q = output

OR gate.

272

Table A2.1 Functions of each pin on the connector block used in Fig. A2.3

Pin #	Function*
41	PF/I4 GPCTR1_GATE
11	PF/IO TRIG 1
4	DGND
2	GPCTR0_OUT
40	GPCTR1_OUT
8	V+
9	V-
47	DIO3
39	DG GND
68	ACHO
64	AIGND
32	AIGND

*See a National Instruments " PCI-MIO E Series User Manual" for details

Table A2.2 Functions of each pin on the valve drivers in Fig. A2.3

Pin #	Function*
3	Toggle output ((internal to driver)
4	Positive logic input
3 jumpered to 4	necessary when using Toggle feature
6	Rising edge triggered flip-flop
8	Resets to de-energized state on rising edge
10	GRND

*See a Valve Driver II manual for details

273

Fig. A2.4 Timing diagram for the Counters (CTR), Digital input/output lines (DIO), and the data acquisition clock controlled by the Labview program (The top 4 lines). Also shown are the timing diagrams for the external circuit, visible as the grey area in Fig. A2.3(the flip-flop and the OR gate), as well as the timing diagrams for the valve drives 1-3 (VD1 – VD3). The text in the brackets names the device serving as the input (e.g. CTR 1) and the name of the input port (e.g. Toggle, Pin 6 etc.). The numbers at the bottom refer to the states of the valves from Fig. 4.1

CTR 0

CTR 1

DIO 3

Data Acquisition

Falling edge triggered
flip-flop (CTR1 to
Toggle; DIO 3 to Reset)

VD1 (OR gate to pin 4)
(flip-flop and DIO 3 to
OR gate)

VD1 and VD2
(CTR 1 to pin 6, DIO
3 to pin 8)

1   2   3   4

1 : Equilibration
2 : Time-out (no flow)
3 : Flush
4: Desorption